An Analytical and Experimental Investigation of Potential Mechanical Work Extraction from Supersonic Jet Flow on High Speed Mini Turbines

by

Ken Thye Lee

Submitted to the graduate degree program in Aerospace Engineering
and the Graduate Faculty of the University of Kansas School of Engineering
in partial fulfillment of the requirements for the degree of Master of Science

Committee:

_____

Dr. Ronald M. Barrett,
Associate Professor of Aerospace Engineering,
Chairperson

_____

Dr. Saeed Farokhi,
Professor of Aerospace Engineering

_____

Dr. Ray Taghavi,
Professor of Aerospace Engineering

Date Thesis Defended: _____

This Thesis Committee for Ken Thye Lee certifies that this is the approved Version of the following thesis:

An Analytical and Experimental Investigation of Potential Mechanical Work Extraction from Supersonic Jet Flow on High Speed Mini Turbines

Committee:

_____

Dr. Ronald M. Barrett,

Associate Professor of Aerospace Engineering,

Chairperson

_____

Dr. Saeed Farokhi,

Professor of Aerospace Engineering

_____

Dr. Ray Taghavi,

Professor of Aerospace Engineering

Date Approved: _____

ABSTRACT

In the present study, an inexpensive method of mechanical power extraction from supersonic jets was investigated. Detailed experiments were carried out to measure the mechanical torque generated by a 45^o planar bladed mini-turbine with a radius of 12.8 mm. The mini-turbine was exposed to supersonic flow of air exhausting from the exit of a sonic nozzle (diameter of 0.711 mm) into still air. Experiments were carried out by placement of the mini-turbine in various configurations with respect to the supersonic jet flow centerline. These experiments were conducted in the Adaptive Aerostructures Laboratory at the University of Kansas using compressed air with a supply pressure of around 6.12 to 6.80 atm. The mini-turbine was tested up to speeds of 50,000 RPM. In addition, the experiments were carried out to determine the mechanical shaft power of the mini-turbine and the overall efficiency of the power conversion from fluid aerodynamic power of the supersonic jet flow to the mechanical shaft power measured.

Ten different configurations were tested by positioning the mini-turbine at $x/D_{turbine} = 0.5$ and $x/D_{turbine} = 0.25$ ($x/D_{turbine}$ defined as the lateral distance of the supersonic jet from the mini-turbine centerline axis normalized by mini-turbine diameter), +/- 3^o and +/- 1.5^o inclination angle, and +/- 2.5^o and +/- 1.0^o directional angle offset relative to the nozzle exit supersonic jet centerline axis, respectively. The effect of nozzle exit area variation on mechanical shaft power extraction and aero-mechanical efficiency of power conversion in each of the test configurations was tested for three different areas; $A_e = 0.397\ \mu m^2$, $0.75A_e = 0.298\ \mu m^2$ and $0.5A_e = 0.199\ \mu m^2$. Additional studies were performed to determine the effect of varying the axial location (y/D_e) of the mini-turbine along the supersonic jet centerline axis measured downstream from the ejector

nozzle exit. These experiments were conducted for the three nozzle exit area cases mentioned above. Shadowgraph images were captured for the supersonic jet shock structure and jet spread at the three different nozzle exit areas specified.

Results obtained from the experimental runs showed that the mechanical shaft power of the mini-turbine was in the range of 1-2 W and the aero-mechanical efficiency of power conversion achieved were approximately 25% to 40% for the mini-turbine operating at speeds of approximately 35,000 to 50,000 RPM. The aero-mechanical efficiency of power conversion increased when the nozzle exit area was reduced and as the mini-turbine was placed further downstream of the nozzle exit, respectively. These results were attributed to the fact that the jet spread and shear layer growth rate increased at the far-field locations downstream of the nozzle exit. The flow images captured showed visible diamond shock structures in the near-field region for the underexpanded nozzle exit flow and the degree of underexpansion decreased as the nozzle exit area was decreased. Reasonable values of the mini-turbine shaft power extracted from supersonic jet flow and the aero-mechanical efficiency of power conversion were achieved from the present study.

ACKNOWLEDGEMENTS

First and foremost, I would like to thank the chair of my advisory committee, Dr. Ronald M. Barrett, for all his help and guidance throughout this project. This work was primarily funded and supported by the University of Kansas Transportation Research Institute and the Aerospace Engineering Department. I would also like to thank my committee members, Dr. Saeed Farokhi and Dr. Ray Taghavi for their support, guidance and dedicated teaching throughout my undergraduate and graduate education at the University of Kansas.

Second, I would like to thank Mr. Scott Cravens for his generosity in providing me with camera equipment for use in this research work. Without his camera, I would not be able to capture flow images to present in this document. I would also like to thank Mr. Richard Bramlette for his kind advice and knowledge which helped a great deal in revising and determining concepts to explain the fundamentals of aerodynamics and its correlation to the findings of this research.

Finally, I want to thank my family. This thesis is also written in dedication to their support and the unwavering love of my parents and siblings. Without them, I would not have had the strength and motivation to work through the long days and late nights at Learned Hall. Also, I would like to thank my girlfriend, Nancy Dinh, for her love and strength that pushed me through all obstacles faced while performing work for this research and completing this thesis.

TABLE OF CONTENTS

Page No.

Table of Contents (Cont'd)

Table of Contents (Cont'd)

NOMENCLATURE

Symbol	Description	Units
a	Local Gas Speed of Sound	m/s
A	Area	m^2
AR	Blade Aspect Ratio	~
c	Blade Chord	m
c_p	Specific Heat at Constant Pressure	J/kg-K
C_D	Discharge Coefficient	~
CO_2	Carbon Dioxide Gas	~
d	Moment Arm Distance	m
D	Diameter	m
h	Enthalpy	J/kg
$\dot{m}$	Mass flow rate	kg/s
M	Mach Number	~
NPR	Nozzle Pressure Ratio (p_0/p_{amb})	~
P	Pressure	N/m^2, Pa
$\wp$	Power	J/s or W
Q	Shaft Torque	N-m
R	Universal Gas Constant Radius	J/kg-K m
Re	Reynold's Number	~
s	Blade Spacing	m
S	Blade Area	m^2
t	Blade Thickness	m

NOMENCLATURE (Continued)

Symbol	Description	Units
T	Temperature	^{o}C or K
V	Local Gas Velocity	m/s
x	Lateral Distance Variation w.r.t. Nozzle Face	m
y	Longitudinal Distance Variation w.r.t. Nozzle Face	m
z	Height Variation of Turbine w.r.t. Nozzle Face	m

Greek Symbols	Description	Units
α	Inclination Angle	deg. or rad
β	Sideslip Angle	deg. or rad
γ	Ratio of Specific Heats	~
δ	Turbine Blade Angle	deg. or rad
ε	Jet Divergence Angle	deg. or rad
η	Mechanical Efficiency	~
θ	Deflection Angle	deg. or rad
φ	Turbine Blade Camber Angle	deg. or rad
μ	Dynamic Viscosity	kg/(m-s)
ρ	Gas Density	kg/m^3
σ	Turbine Blade Solidity	~
υ	Gas Kinematic Viscosity	m^2/s
ω	Shaft RPM	rev/min

NOMENCLATURE (Continued)

Subscripts	Description
0	Stagnation Conditions
1	Gas Chamber Properties
2	Exit Conditions
aero	Aerodynamic
amb	Ambient
be	Ratio of Ambient to Nozzle Exit Static Pressure (p_{amb}/p_e)
e	Exit
eff	Effective Area
fluid	Fluidic Power
m	At Pitchline Radius
mech	Mechanical
nominal	Nominal Area
root	Root
s	Shaft
t	Total or Stagnation Conditions
tip	Tip
turbine	Mini-Turbine

NOMENCLATURE (Continued)

Superscripts	Description
*	Sonic or Choked Conditions

Abbreviations	Description
Eq.	Equation
Fig.	Figure
min	Minutes
No.	Number
Pg.	Page
Ref.	Reference
rev	Revolutions
Vol.	Volume

Acronyms	Description
AC	Alternate Current
AIAA	American Institute of Aeronautics & Astronautics
CAD	Computer Aided Design
COP	Coefficient of Performance
DC	Direct Current
LCD	Liquefied Crystal Display
UG NX	Unigraphics CAD Software (NX 6.0 version)

LIST OF FIGURES

Page No.

LIST OF FIGURES (Cont'd)

Page No.

LIST OF FIGURES (Cont'd)

Page No.

LIST OF FIGURES (Cont'd)

Page No.

LIST OF FIGURES (Cont'd)

Page No.

LIST OF TABLES

Page No.

1.0 INTRODUCTION

A supersonic underexpanded free jet discharging from a sonic nozzle or orifice is one of the simplest flows to analyze and has a number of practical applications including the design of rocket propulsion systems to various industrial processes using high pressure gases. The inherent simplicity in the construction of conical convergent nozzles and the wide use of these nozzles as a means of converting pressure energy to kinetic energy is of great interest. Motivated by these considerations, an inexpensive method of mechanical power extraction from the sonic injection of a round underexpanded supersonic air jet into still air was studied. The above was achieved by developing a simple and economical method of power extraction using a planar bladed turbine assembly and determining reasonable percentages of power conversion from fluid aerodynamic power to mechanical shaft power of a supersonic jet emanating from the exit of a sonic plugged nozzle.

The above concept has marked similarities to the De Laval turbine configuration developed many decades earlier. De Laval proved that much of the energy present in steam could be converted to velocity through a convergent-divergent nozzle and a bucket-type turbine blade configuration. He was able to develop a very simple and economical method of power extraction from gas flow imparting on the blades of a turbine. The main goal in this research was to investigate analytically and experimentally the overall efficiency of power conversion when a simple planar mini-turbine was placed in various configurations with respect to a supersonic jet of air which exhausted into still air from a convergent type nozzle.

The first part of this research was centered on building a gas pressurization system to investigate the kinetic-energy related properties of very high pressure gas flows exiting from mm-scale plug nozzles into still air. A gas generator was designed and built to provide pressurized air flow which exhausts into ambient air though a convergent nozzle with a needle valve which formed a plug nozzle. The nozzle pressure ratio remained constant but the nozzle back pressure ratio was varied by means of a needle valve to control the area contraction of the convergent nozzle. The convergent nozzle was used to accelerate the working fluid to supersonic speeds as it exits the nozzle and into still air. A turbine assembly was placed in front of the nozzle flow to determine the mechanical work that was imparted by the pressurized air flow. Torque and turbine rotational speed (RPM) measurements were made by placing the turbine assembly in various positions relative to the jet entrainment to determine the shaft power of the turbine when exposed to the nozzle exit flow. The efficiency of the power conversion was measured by the ratio of mechanical work output to the aerodynamic power input from the pressurized fluid flow. In addition, studies were also performed to determine the effect of the sonic nozzle area contraction ratio on the efficiency of mechanical work conversion from aerodynamic fluidic power.

In the present investigation, shadowgraph techniques were used to visualize the shock structure of the sonic nozzle flow at three different nozzle area contraction ratios. The purpose of this investigation was to understand the shock structures formed from the micro sonic nozzles with a needle valve control and their effect on the potential for mechanical work extraction from high speed jets.

The literature review for the current study is presented in Chapter 2. An overview of the overall engine setup is described in Chapter 3 of this thesis. Chapter 4 provides a theoretical review of the theories and concepts used to analyze the aerodynamic fluid power through the orifice of the sonic nozzle and its conversion to mechanical work by means of a turbine. Chapter 5 will detail the experimental setup and procedures. In this section, the maximum pressure ratings, CAD drawings of the engine setup and turbine geometry, instrumentation and a description of the various positions for the turbine assembly relative to the nozzle jet are also presented. Results from the experiments conducted are presented in Chapter 6 of this document. The conclusion and the recommendations for further research activities are presented in Chapter 7.

2.0 LITERATURE REVIEW

In this chapter, a brief review of the past and current literature is presented to provide a perspective on the current investigation and to understand the different areas of research that have lead directly, or indirectly, to the development of the proposed engine concept under investigation.

2.1 De Laval Nozzle and Turbine

The potential of mechanical work extraction from pressurized fuel or gas flow can be achieved with the use of axial, radial or impulse turbines for shaft and/or electric power generation. The power derived can also be used to power pumps, generators and other waste energy recovery systems. In the present study, mechanical power derived from the kinetic energy of the high pressure flow of air was extracted by the concept of gas flow expansion through a convergent nozzle and of flow velocity imparted on an impulse turbine. The concept bears similar resemblance to the steam turbine engine designed by Carl Gustaf Patrik De Laval patented in 1894. De Laval designed an efficient means of converting the potential energy of the steam before it encounters a turbine wheel[1].

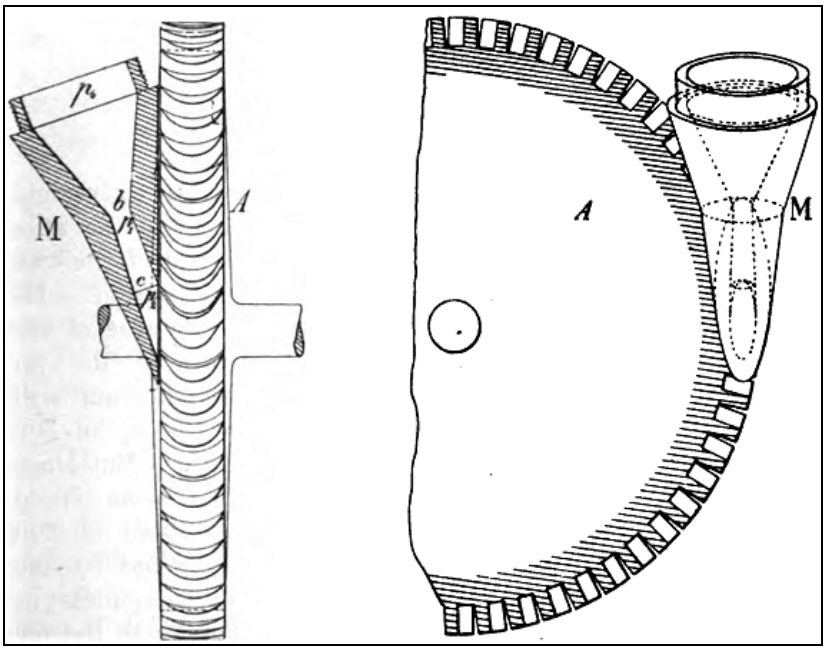

Figure 2.1 Patent Drawing of De Laval Turbine[2].

According to his invention, steam is expanded in a De Laval type nozzle and the pressure of steam is converted into velocity. The kinetic energy of the steam flowing past the nozzle exit reaches the turbine wheel in the expanded condition whereby the wheel is rotated by the fluid momentum imparted on the turbine wheel. The design of the nozzle for flow expansion is an important consideration. Figure 2.2 shows a schematic diagram of the discharge nozzle used in a De Laval steam turbine. The cross sectional area of a De Laval nozzle decreases in the converging section such that the gas velocity increases from subsonic speeds to sonic condition at the throat. The pressure of the gas is simultaneously decreasing as the gas velocity increases in the converging portion of the nozzle. The sonic condition is referred to as the "choked condition" where the nozzle cross sectional area is the minimum and the local gas velocity is sonic (M = 1). In the diverging portion of the nozzle, the gas experiences maximum expansion in which gas velocity is increased to supersonic speeds and gas pressure is further decreased.

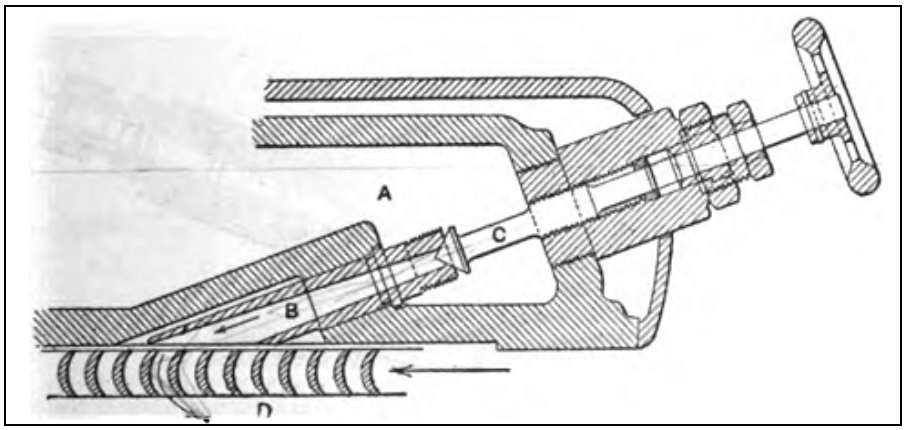

Figure 2.2 Patent Drawing of De Laval Nozzle and turbine wheel[3].

For the De Laval turbine, "most" of the potential energy invested in the steam is converted to velocity (kinetic energy)[1]. De Laval explained in his patent that the steam pressure was expanded to 57.7 per cent of its initial pressure at the throat section of the nozzle. Also, he stated that a nozzle with a throat diameter of 1/8 inches and a divergent nozzle length of 3 inches would expand the entering steam from 165 psi to 3 psi. The corresponding velocity exits the nozzle and impacts the turbine wheel in a single compact jet which will have no tendency to further expand[4]. This gas behavior, as explained by De Laval, will produce a jet that does not leak to the sides of the wheel (see Figure 2.1) but imparts entirely on the wheel itself. As the steam jet leaves the nozzle, the gas pressure is at a minimum and the maximum gas velocity impacts the buckets of a concave and convex cross section on the turbine wheel. De Laval had shown that at the above conditions, the wheel rotates at speeds higher than 15,000 revolutions per minute. A number of converging-diverging nozzles can also be positioned around the circumference of the turbine wheel to increase the efficiency of power conversion[4]. This practical conversion of steam pressure to velocity potential for turning the turbine wheel was a simple and economical design for power conversion.

A quantitative analysis of the total efficiency of conversion in a 300 hp De Laval turbine can be found in Reference 5. Stevens' and Hobart's book indicated that in a 300 hp De Laval turbine supplied with an absolute pressure of 13 metric atmospheres and with 50 ^{o}C of superheated steam, and exhausting to a condenser with 86.8 per cent vacuum, a steam consumption of 8 kg per brake horsepower is generally obtained. When the 300 hp De Laval turbine was coupled to a dynamo of 209 kW operating at the above conditions, it was found that 10 kg per kWh is required. In addition, the total energy conversion, from the total kinetic energy in the steam supplied, into the electrical energy from the dynamo, is approximately 59 per cent. The remaining 41 per cent was attributed to losses in the form of[2]:

- Nozzle losses
- Leakage losses
- Radiation losses
- Losses due to friction of the turbine wheel revolving in the steam
- Losses due to friction of the steam traveling over the vanes
- Losses in the speed reduction gearing
- Losses due to the bearing friction of the wheel
- Losses in the dynamo
- Losses due to the residual kinetic energy in the steam passing to the condenser

Based on the understanding of the De Laval turbine design concept, the importance of power conversion from gas expansion process, can be reiterated in the following statement made in his original patent[1], "My invention relates to an improvement in turbines which are set in motion by means of a current of steam; and the object of the improvement is to increase, by complete expansion, the velocity of the steam current, thus producing the relatively largest quantity of vis viva of the steam." More detailed descriptions of the De Laval turbine exist in the original patent claimed by De Laval himself as well as other pertinent texts on the design of the turbine.

2.2 Microturbines for Power Generation

Recent developments and advances have been made in the area of micro power generation systems. These types of systems combine the potential of shaft and electrical power generation from converting kinetic energy of pressurized gas flow and/or combustion energy of fuel. Micro-scale turbine expanders have also been tested experimentally to determine energy recovery capability.

In 2009, a paper was published in the ASME Turbo Expo on the development of a micro-scale turbine expander for energy recovery. Keding, Dudzinski, Tajmar, Wiliner and Kafer[4] developed a micro-scale turbine expander for work recovery in transcritical CO_2 heat pumps. The main drawback of transcritical CO_2 heat pumps is the lower COP (Coefficient of Performance) compared to conventional heat pumps and it originated from the non isothermal heat rejection process in the gas cooler[4]. Energy recovery could be performed by utilizing the pressure difference between the high pressure and low pressure regions of the heat pump. The authors suggested that work recovery can be feasible if a turbine expander

was used in place of the expansion valve that operated between the high and low pressure side of the heat pump. The type of turbine used in the proposed energy recovery system was a Pelton turbine with two-phase flow turbine blades (See Figure 2.3). The energy recovery device was connected to a small scale generator and thermodynamic simulation results yielded absolute micro-turbine power between 60 W and 150 W for a 2 kW heating system[4].

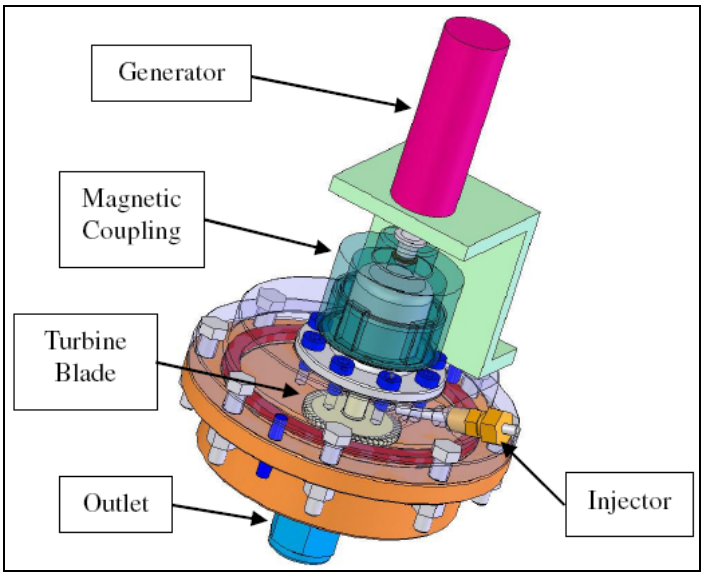

Figure 2.3 Turbine System Assembly (200 mm in Height and 100 mm in Diameter)[4].

Experiments were also performed in Switzerland by Krahenbuhl, Zwyssig, Horler and Kolar[5] on a 60 W compressed air-to-electric power system (See Figure 2.4). The power system was developed to utilize compressed air as a means to power a miniature single-stage axial impulse turbine. The turbine was rated at a rotational speed of 350,000 RPM and electrical power output of 60 W[5]. The paper described design considerations for such a power system and measurements were presented that showed maximum electric power output of 124 W and maximum system efficiency of 24% when connected to a permanent magnet generator[5]. This particular system is also useful in process applications where

pressure reduction takes place and heat is dissipated as a result. The energy could be further recovered by the implementation of a gas expander that produced electrical energy.

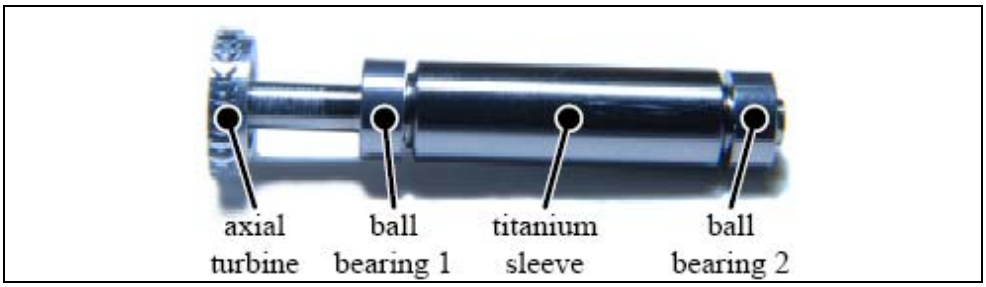

Figure 2.4 Impulse Turbine and Rotor with Assembled High Speed Bearings[5].

In 2009, Krahenbuhl, Zwyssig, Weser and Kolar[6] published a paper with theoretical and experimental results of a mesoscale electric power generation system from pressurized gas flow (Figure 2.5). The paper presented results for a miniature compressed air-to-electric power generating system with a turbine rotor diameter of 10.5 mm tested up to operating speeds of 490,000 RPM and a rated electrical power output of 150 W[6]. Furthermore, it was the first experimentally validated turbine-generator system which achieved a speed in excess of 600,000 RPM and a power output of more than 10 W. Measurements were also obtained for the turbine-generator system with a rated electrical power output of 170 W, maximum torque of 5.2 mN-m and a turbine efficiency of 52%.

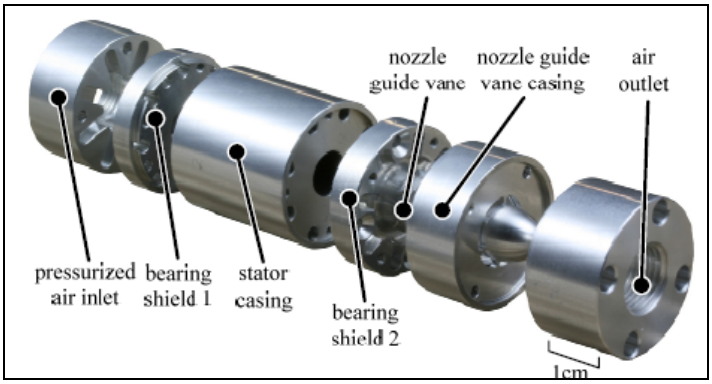

Figure 2.5 Picture of the Ultra Compact (22 mm x 60 mm) Pressurized Air-to-Power Demonstrator[5].

Further work in the development of axial microturbines for electric power generation had been realized in recent literature. Peirs, Reynaerts and Verplaetsen[7] developed a miniature single-stage axial impulse turbine (De Laval turbine) with a rotor diameter of 10 mm to generate electrical energy by power extraction of the kinetic energy available in compressed air flow. Experiments performed on the miniature turbine with compressed air showed that maximum mechanical work power of 28 W with a system efficiency of 18.4% was achieved when the turbine operated at speeds of approximately 160,000 RPM[7]. When the turbine was coupled with a small generator operating at rotational speeds of approximately 100,000 RPM, it was determined that 16 W of electrical power was generated and a corresponding system efficiency of 10.5% achieved[8]. System losses were found in the form of blade profile losses and exit losses. The authors proposed that efficiency can be increased and exit losses can be minimized by operating at higher speeds.

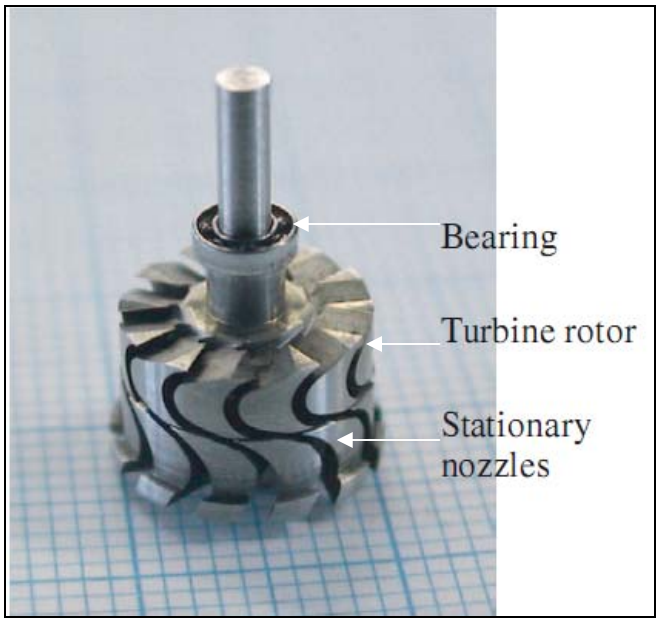

Figure 2.6 Turbine rotor picture of the Microturbine Developed by Peirs, Reynaerts and Verplaetsen[8].

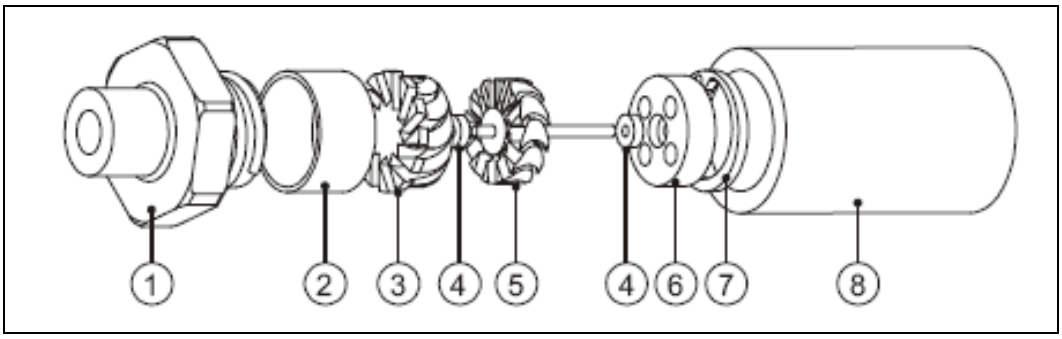

Figure 2.7 Exploded View of the Microturbine showing the Individual Components: 1. Pneumatic Connector, 2. Spacer Ring, 3. Nozzle Disc, 4. Bearings, 5. Rotor, 6. Outlet Disc, 7. Circlip, 8. Housing[7].

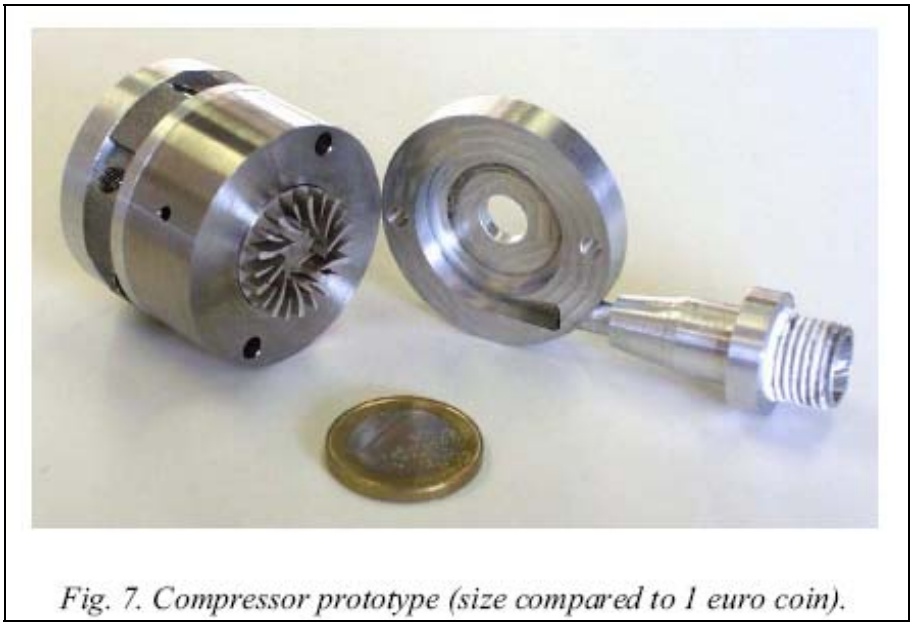

Fig. 7. Compressor prototype (size compared to 1 euro coin).

Figure 2.8 Compressor Prototype (Size Compared to 1 Euro Coin)[7].

In a different paper published, Peirs, Raynaerts, and Verplaetsen[9] also tested the same micro-turbine coupled to a small generator with compressed air up to speeds of approximately 160,000 RPM and elevated air supply temperatures up to 360 ^{o}C. The published results showed that the turbine generated 44 W of electrical power and system efficiency of 16%. Further work was developed in the fabrication and testing of a 20 mm centrifugal compressor with matched pressure and flow characteristics of the turbine[9]. Peirs,

Raynaerts and Verplaetsen[9] tested the miniature compressor-turbine gas generator with hot compressed air of 330 ^{o}C. The turbine was reported to have reached speeds of approximately 130,000 RPM and generated up to 50 W of mechanical power with efficiencies in the range of 20% to 24%. The electrical power output of 36 W was realized when the turbine was coupled with a small generator.

The current ongoing research and development of micro-turbines for power generation incorporating De Laval's original nozzle-turbine concepts and the miniaturization of current electrical power devices is of great interest for future power generating and energy recovery applications. These advances will fuel the need for future research in understanding the flow characteristics in miniature turbine gas generators.

2.3 Supersonic Nozzles and Microjets

2.3.1 Supersonic Flow Structure from Underexpanded Nozzles

The study of the structure of supersonic nozzles and emanating jets is more than a century old (Mach and Salcher, 1889; Hartman and Lazarus, 1941; Ladenburg et al., 1949; Love et. al, 1959; Adamson and Nicholls, 1959; Moe and Troesch, 1960; Abbett, 1971; Fox, 1974; Chang and Chow, 1974)[10]. A supersonic jet consists of an internal structure of shock waves which is highly dependent on the jet static pressure ratio (ratio of jet to ambient static pressure, $\frac{p_e}{p_{amb}}$)[10]. If the ratio is greater than 1, the supersonic jet emanating from a nozzle is said to be underexpanded. In contrast, if the ratio is equal to or greater than 1, the supersonic jet is referred to as perfectly expanded or overexpanded, respectively.

The structure of the supersonic flow behind an underexpanded nozzle is of great interest in the present study. Underexpanded jets have been easily studied experimentally and are more evident in practical applications as one often comes across a high pressure reservoir as the jet source and a lower pressure receiver (nozzle) into which the jet expands[10] such as, in the design of rocket propulsion systems and jet engine exhaust nozzles. The figure below is adapted from a paper by Adamson and Nicholls[11] (1958) and shows the flow structure in a highly underexpanded nozzle. Gas emerging from the nozzle exit, passes through Prandtl-Meyer expansion fans where the gas is expanded to the ambient pressure at the jet boundary. The underlying mechanism mentioned decreases the pressure to match the ambient pressure at the jet boundary. At this condition, the jet boundary is reflected back towards the flow axis. As the flow reverses direction along the jet boundary, compression waves formed at the intersection of expansion waves with the jet boundary are reflected back into the flow[11]. The expansion and compression waves coalesce to form the intercepting shock indicated in Figure 2.9.

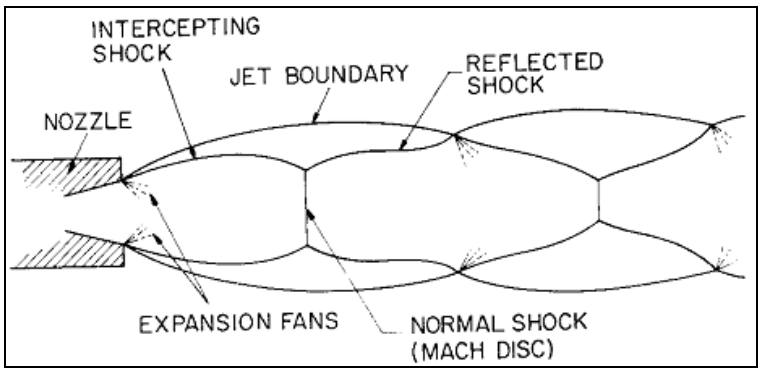

Figure 2.9 Sketch of jet structure behind a highly underexpanded nozzle[11].

In supersonic jets of moderate underexpansion, the intercepting shocks meet at the flow axis forming a diamond configuration. Increasing nozzle pressure ratios will cause the intercepting shocks to connect at the flow axis with a normal shock referred to as the

Mach disk as seen in Figure 2.9. In both cases mentioned, reflected shocks are formed and intersect with the jet boundary to reflect as expansion waves in a repetitive process. The repetition length of the said behavior continues until viscous effect dominates and the shock structure is no longer visible[11]. The study of underexpanded jets involves important parameters such as static pressure ratio at nozzle exit to ambient pressure, nozzle exit Mach number, and nozzle geometry and size. The results of such studies provide a wealth of information in relation to the jet boundary calculation, location of the first normal shock or Mach disk, and the length of the repeating shock structure.

Otobe, Kashimura, Matsuo, Setguchi and Kim[12] (2007) published results on a study performed to determine the influence of nozzle geometry on the near-field structure of a highly underexpanded sonic jet. The results indicated that the distance from nozzle exit to the first Mach disk and the shape of the jet boundary was an increasing function of nozzle exit to ambient static pressure ratio[12]. The diameter of the Mach disk was also an increasing function of the nozzle exit to ambient pressure ratio. The authors concluded that the near-field structure of highly underexpanded sonic free jets was only unique to the function of pressure ratio instead of the nozzle geometry.

Lee, Setoguchi, Matsuo and Kim[13] (2003) visualized underexpanded sonic jets using a shadowgraph optical method. The experimental studies presented shadowgraph pictures of supersonic free jets of varying NPR (Nozzle Pressure Ratio is defined as the ratio of nozzle total or stagnation pressure to static ambient pressure, $\frac{p_0}{p_{amb}}$). From the visualization results, one could observe the behavior of shock wave interaction with the jet boundary and the shock structure as the NPR was increased. The marked conditions

for overexpanded, perfectly expanded and underexpanded nozzles can also be observed. Lee, Setoguchi, Matsuo and Kim[13] (2003) also found that the diameter of the Mach disk increased as it became stronger and moved downstream as the NPR was increased. Figure 2.10 depicts shadowgraph pictures of the supersonic jets tested.

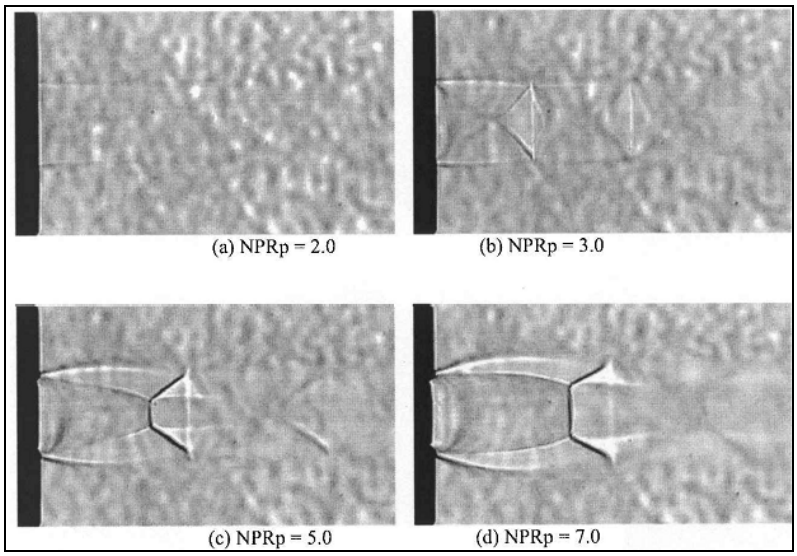

Figure 2.10 Shadowgraph pictures showing the supersonic free jets[13].

2.3.2 Supersonic Flow Visualization for Underexpanded Micorojets

Experimental studies were performed on supersonic microjets by Scroggs and Settles[14] (1996) and the results were compared to existing literature on large-scale underexpanded jets produced by supersonic nozzles (0.6 mm and 1.2 mm) of higher Reynold's numbers. It was found that the reduction in nozzle size produced notable effects on the transition to turbulence. Also, the use of one-dimensional isentropic compressible flow theory was proven to be valid for flow analysis of nozzles in the miniature scale. Scroggs and Settles[14] also showed that the Reynold's number and Mach

number dependence on supersonic length and core length correlated well with experimental data of large-scale supersonic jets.

The following figures are Schlieren images of a Mach 2.2 supersonic jet of 0.6 mm and 1.2 mm showing the effect of static ambient pressure to nozzle exit pressure ratio (overexpanded nozzles). Other important findings of Scroggs' and Settles' research[14] include the relation of the length of supersonic region as a function of increasing stagnation pressure. Increasing stagnation pressure in these microjets lowered the exit pressure ratio ($p_{be} = \frac{p_{amb}}{p_e}$, ratio of nozzle ambient to exit static pressure or the inverse of jet static pressure ratio) and increased the diameter of the shock cell to form a Mach disk at the first terminating shock cell from the nozzle exit[14].

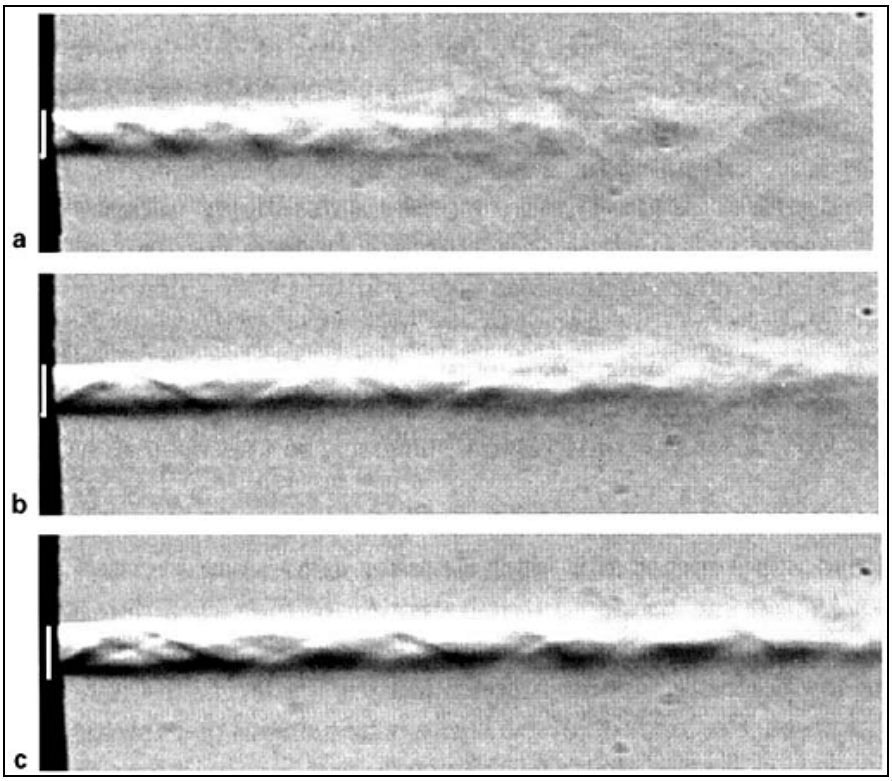

Figure 2.11 Schlieren Images of a Mach 2.2 Supersonic Jet of 0.6 mm diameter for (a) p_{be} = 2.0, (b) p_{be} = 1.0 and (c) p_{be} = 0.8[14].

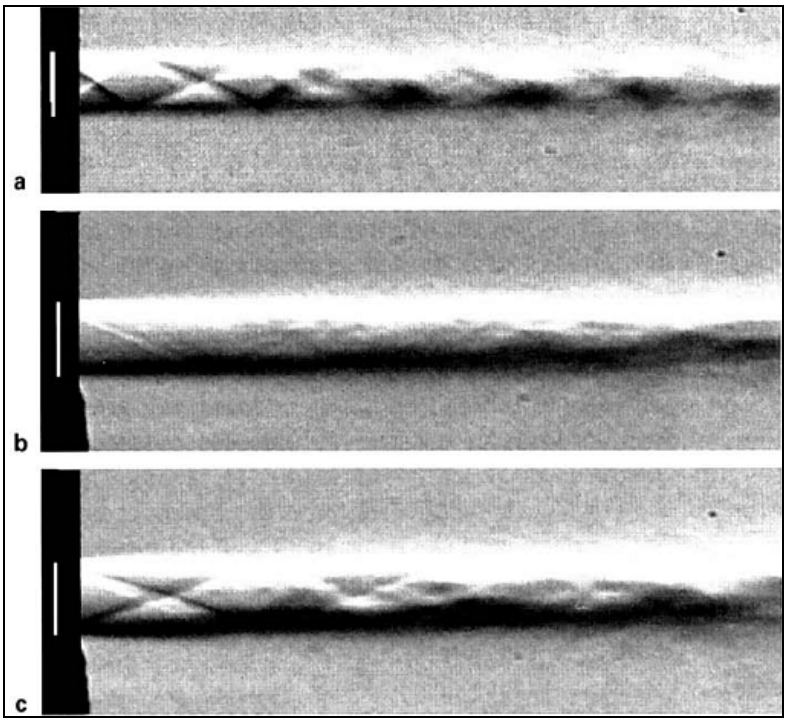

Figure 2.12 Schlieren Images of a Mach 2.2 Supersonic Jet of 1.2 mm diameter for (a) p_{be} = 2.0, (b) p_{be} = 1.0 and (c) p_{be} = 0.8[14].

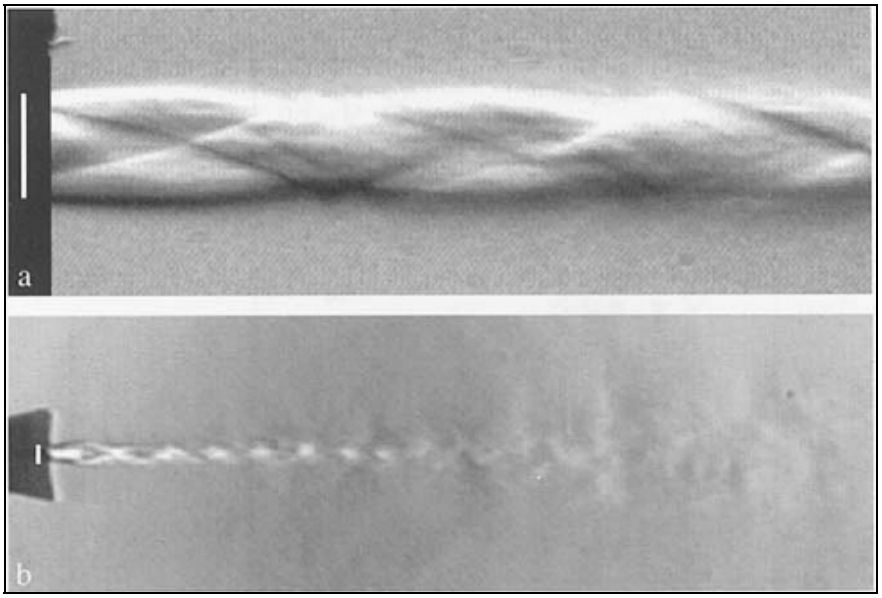

Figure 2.13 Images of Underexpanded M_e = 2.0 jets (a) High Magnification Showing Shear Layer Transition Under Strobed Illumination at p_{be} = 0.6 and (b) Constant Illumination Showing Far Field at p_{be} = 0.4[14].

The behavior of free and impinging supersonic microjets were studied by Phalnikar, Alvi and Shih[15] in 2001. The investigation examined supersonic microjets of 100-400 mm with exit velocities of 400-500 m/s. Micro-schlieren system was used to achieve effective magnifications of greater than 100x Schlieren images. These images clearly showed that the shock cell structures observed were similar to observations in large-scale jets. The supersonic microjets were evident as far as 10-12 diameters downstream of the nozzle. Phalnikar, Alvi and Shih[15] (2001) concluded that the properties of microjets were similar to larger supersonic jets operating at similar Reynold's number. However, viscous effects in microjets were predominant and lead to some differences.

Figure 2.14, 2.15 and 2.16 depict a series of Schlieren images of underexpanded flow from nozzles of 100 μm, 200 μm and 400 μm diameters. Plenum pressure was varied from 60 to 120 psia for each of these nozzles. Increasing stagnation pressure was found to increase jet plume visibility and the length of supersonic core increased with increasing NPR.

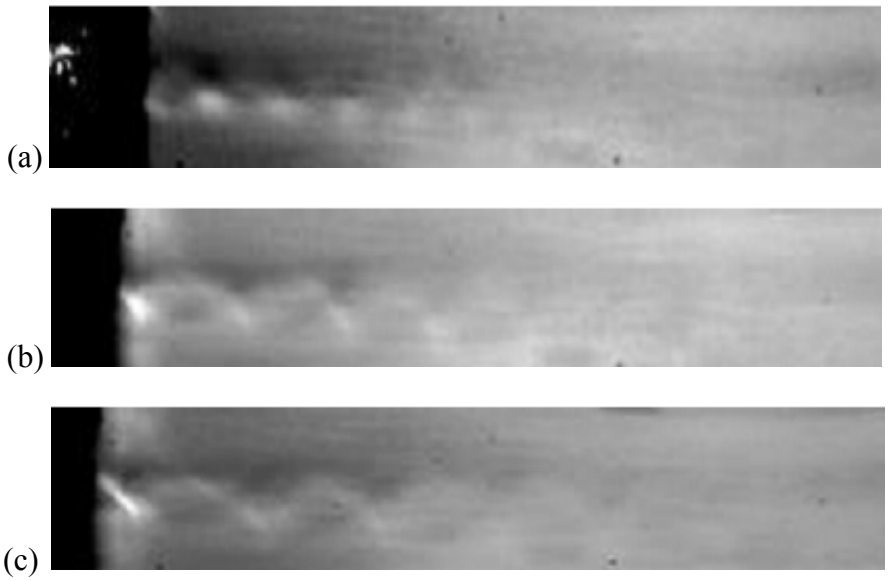

Figure 2.14 Schlieren Images of Underexpanded 100 µm jet at (a) 60 psia, (b) 80 psia and (c) 100 psia[15].

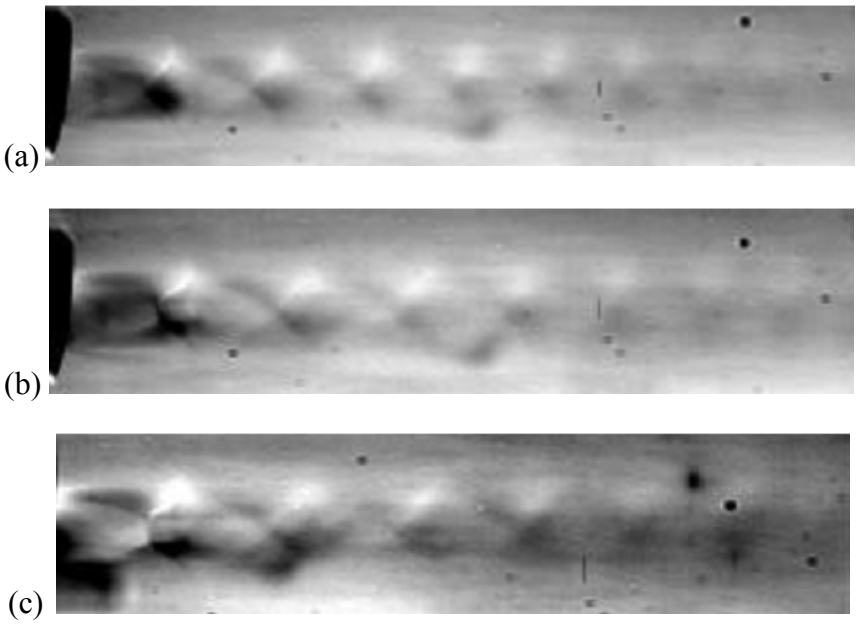

Figure 2.15 Schlieren Images of Underexpanded 200 µm jet at (a) 80 psia, (b) 100 psia and (c) 120 psia[15].

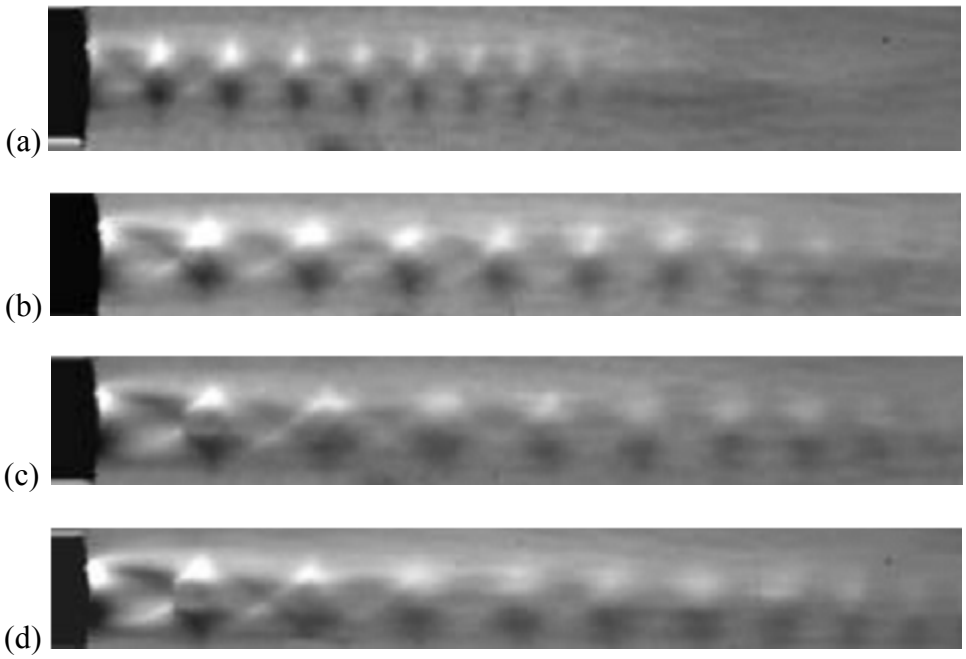

Figure 2.16 Schlieren Images of Underexpanded 400 µm jet at (a) 60 psia, (b) 80 psia (c) 100 psia and (d) 120 psia[15].

Mach wave radiation studied by Tam[16] in 2001 as a possible mechanism for noise radiation from large turbulent structures of high-speed jets can be directly correlated to the flow induction mechanism that aids the conversion of aerodynamic to mechanical power through turbulent mixing between supersonic and low subsonic flow. Large turbulent structure noise and fine-scale turbulence noise are two components evident in jet mixing noise[16]. Tam found that Mach wave radiation by large turbulent structures of high-speed jets was similar to the sound generated by a supersonic traveling wavy wall[16]. In addition, it was observed from the results that Mach wave radiates primarily in directions with a large inlet angle and the Mach waves were very energetic and fairly coherent extending over many jet diameters downstream[16]. The following chapter will provide a brief overview of the proposed concept for power extraction from very high speed jets.

3.0 TURBINE OVERVIEW

The proposed concept for the present study is a nozzle-turbine configuration that is able to operate over a wide range of rotational and tip speeds up to the transonic regime while using an extremely low cost turbine configuration. The nozzle-turbine configuration is concerned with converting the potential aerodynamic fluid power from gas flow (air in the proof of concept case) that is expanded at the exit of a convergent nozzle. The concept described in this chapter has marked resemblance to the working principle of a De Laval type turbine where a divergent nozzle was designed to further expand the high pressures of the working medium such that a conversion from pressure to total kinetic energy was realized and mechanical power extraction was achieved by gas velocity impingement on an impulse turbine. Because the primary cost driver of any turbine system is related to the manufacturing techniques used on the blades themselves, an extremely low-cost, stamped turbine blade system was chosen for this study. Several subscale commercial products could easily employ a low-cost turbine system provided the price point is favorable. Accordingly, this study explores the performance of such a turbine as a precursor study to further commercial development.

The engine model built for the abovementioned used compressed air for a proof of concept study. Air entered a pressure chamber and flowed through pressure lines to a convergent nozzle. At the exit of a fully opened nozzle, the flow was highly underexpanded as it exhausted into still air. Air could be further expanded by superheating the pressure chamber, pressure lines or at the nozzle exit to supercritical state. This process would provide higher working pressures for an engine and a higher NPR. The gas flow in pre-heated state could potentially increase the

nozzle exit total pressures and mass flow rates. The maximum kinetic energy available for power extraction would also be increased.

The engine is fully throttlable using a needle spike valve to control the area ratio at the nozzle exit. At the nozzle exit, the flow would be choked due to the converging geometry and allowed to expand over the diverging surface of the needle valve. Therefore, mass flow rate was varied as a function of the total exit area upon which flow was expanded. As a consequence of flow expansion through the nozzle, the local flow velocity was increased for a given mass flow rate and conversion of the kinetic energy of the gas flow to mechanical power was achieved with a 45^{o} planar bladed mini-turbine wheel. Further details of the nozzle geometry and individual engine components are found in Chapter 5.

The motivation for the present study was to determine the maximum amount of mechanical shaft power derived from the supersonic air flow through the nozzle while using a very easily manufactured, inexpensive flat blade turbine. The mechanical efficiency of the power conversion from air flow to turbine shaft power was also determined to realize the potential of utilizing a supersonic pressure jet to power turbines that could generate shaft and/or electric power. This proof of concept study could be further expanded to various applications that require shaft power or electric energy.

4.0 THEORETICAL CONSIDERATIONS

The underlying theory and assumptions for the analysis of quasi-one-dimensional flow in a nozzle of the De Laval type is presented in this chapter. Theoretical equations are combined with empirical relations to calculate important parameters such as nozzle mass flow rate, fluid power and aero-mechanical efficiency of power conversion from aerodynamic to mechanical shaft power.

The basic assumptions that have been considered in this present investigation include:

- Air as the working fluid or medium
- Air modeled after perfect gas behavior, with $\gamma = 1.4$.
- Isentropic gas expansion process throughout nozzle
- No viscous effects dominate in flow through nozzle
- Quasi-one-dimensional flow properties of air through nozzle

Figure 4.1 on the following page shows the ejector nozzle configuration used in the present study and the locations of the important gas parameters which would be pertinent to the determination of fluidic aerodynamic power at the exit of a sonic nozzle.

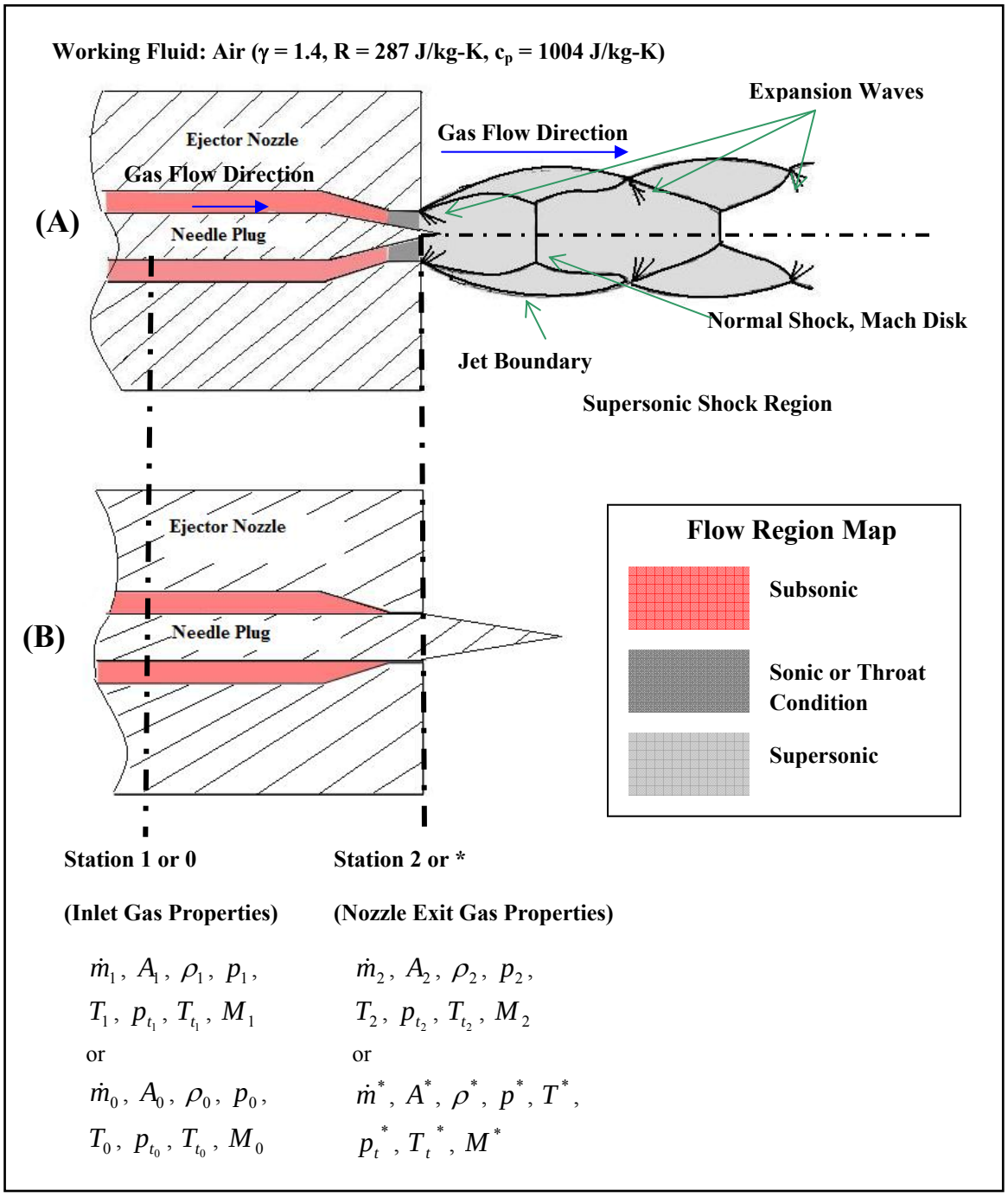

Figure 4.1 **Nozzle-Injector Configuration (A) Open Nozzle and (B) Closed Nozzle Showing Important Gas Parameters and Supersonic Shock Flow Region.**

4.1 Determination of Mass Flow Rate from Nozzle Exit Flow

As subsonically flowing gas enters a convergent nozzle, it is well known that flow is accelerated in the convergent section from subsonic speeds until it reaches sonic condition at the throat or minimum cross-sectional area of the nozzle. The flow is further accelerated to supersonic speeds in the divergent portion of the nozzle where the increasing area allows for gas expansion to take place. The behavior of gas flow in a convergent and divergent duct is given by the area-Mach relationship.

The area-Mach relation is given by[17]:

$$\left(M^2 - 1\right)\frac{du}{u} = \frac{dA}{A} \qquad \text{(Eq. 4.1)}$$

A is the duct area and u is the streamwise velocity

The state at which a sonic condition occurs at the throat of a nozzle is commonly referred to as the choked flow condition (M* = 1). Gas properties at the sonic condition are usually denoted with the superscript *. Therefore, at sonic point, the pressure is p^*, the gas density is ρ^* and the temperature is T^*. In addition, the nozzle minimum (or throat) area can be denoted by A^* and the local speed of sound at choked conditions is a^*. The flow throughout a convergent duct is assumed to be isentropic which implies that the stagnation pressure remains constant. An adiabatic duct flow can also be assumed which results in the stagnation temperature inside a convergent nozzle remaining constant as well.

Since the flow through the convergent nozzle in Figure 4.1 is isentropic, it is essential to review the following isentropic equations which relate total or stagnation to static gas

properties. The following isentropic relations for temperature, pressure and density are derived for an isentropic process at constant entropy[17]:

$$\frac{T_t}{T} = 1 + \left(\frac{\gamma - 1}{2}\right) M^2 \qquad \text{(Eq. 4.2)}$$

$$\frac{p_t}{p} = \left[1 + \left(\frac{\gamma - 1}{2}\right) M^2\right]^{\frac{\gamma}{\gamma - 1}} \qquad \text{(Eq. 4.3)}$$

$$\frac{\rho_t}{\rho} = \left[1 + \left(\frac{\gamma - 1}{2}\right) M^2\right]^{\frac{1}{\gamma - 1}} \qquad \text{(Eq. 4.4)}$$

With the condition that stagnation gas properties remain constant throughout a nozzle, the static gas properties can be replaced with that of sonic gas condition (where M* = 1) to yield the following relations:

$$\frac{T_t}{T^*} = \left(\frac{\gamma + 1}{2}\right) \qquad \text{(Eq. 4.5)}$$

$$\frac{p_t}{p^*} = \left(\frac{\gamma + 1}{2}\right)^{\frac{\gamma}{\gamma - 1}} \qquad \text{(Eq. 4.6)}$$

$$\frac{\rho_t}{\rho^*} = \left(\frac{\gamma + 1}{2}\right)^{\frac{1}{\gamma - 1}} \qquad \text{(Eq. 4.7)}$$

The stagnation temperature can be written in terms of local static temperatures and local Mach number, and may be related to sonic temperature by[17]:

$$T_t = T\left[1 + \left(\frac{\gamma - 1}{2}\right) M^2\right] = T^*\left[1 + \left(\frac{\gamma - 1}{2}\right)(1)^2\right] = T^*\left(\frac{\gamma + 1}{2}\right) \qquad \text{(Eq. 4.8)}$$

The ratio of local static temperature to sonic temperature is written as:

$$\frac{T}{T^*} = \frac{\left(\frac{\gamma+1}{2}\right)}{\left[1+\left(\frac{\gamma-1}{2}\right)M^2\right]} \qquad \text{(Eq. 4.9)}$$

Isentropic relations for a calorically perfect gas are derived from the Gibbs equation which relates pressure and temperature ratio for an isentropic process:

$$\frac{p_2}{p_1} = \left(\frac{T_2}{T_1}\right)^{\frac{\gamma}{\gamma-1}} \qquad \text{(Eq. 4.10)}$$

Similarly, using the perfect gas law to replace the temperature ratio by pressure and density ratios yields the following:

$$\frac{p_2}{p_1} = \left(\frac{\rho_2}{\rho_1}\right)^{\gamma} \qquad \text{(Eq. 4.11)}$$

Using the isentropic relations above and the relation between local static to sonic temperature ratio, an expression for $\frac{p}{p^*}$ and $\frac{\rho}{\rho^*}$ is derived and presented on the following page.

$$\frac{p}{p^*} = \left(\frac{\left(\frac{\gamma+1}{2}\right)}{\left[1+\left(\frac{\gamma-1}{2}\right)M^2\right]} \right)^{\frac{\gamma}{\gamma-1}} \qquad \text{(Eq. 4.12)}$$

and

$$\frac{\rho}{\rho^*} = \left(\frac{\left(\frac{\gamma+1}{2}\right)}{\left[1+\left(\frac{\gamma-1}{2}\right)M^2\right]} \right)^{\frac{1}{\gamma-1}} \qquad \text{(Eq. 4.13)}$$

The mass flow rate in any section of the nozzle and throat is determined using principle of continuity whereby mass flow rate remains constant throughout any section of the nozzle. By application of the continuity equation for a uniform flow, the mass flow rate can be written in terms of p_t and T_t [17].

Mass flow rate in the nozzle is given by:

$$\dot{m} = \rho AV = \frac{\gamma p}{a^2} AV = \frac{\gamma pAM}{a} = \sqrt{\frac{\gamma}{R}} \frac{p}{\sqrt{T}} AM \qquad \text{(Eq. 4.14-a)}$$

where $M = Va$ and $a = \sqrt{\gamma RT} = \sqrt{\frac{\gamma p}{\rho}}$

Substituting the static pressure and temperature of Eq. 4.14-a with the relations for stagnation pressure and temperature of Eq. 4.2 and Eq. 4.3, the following result is obtained for mass flow rate in terms of stagnation properties[17]:

$$\dot{m} = \sqrt{\frac{\gamma}{R}} \frac{p_t}{\sqrt{T_t}} AM \left(\frac{1}{1 + \frac{\gamma - 1}{2} M^2} \right)^{\frac{\gamma+1}{2(\gamma-1)}} \qquad \text{(Eq. 4.14-b)}$$

According to Eq. 4.14-b, the local mass flow rate can be determined by knowledge of the local flow area A, local Mach number M, local stagnation pressure p_t and stagnation temperature T_t, and the type of gas to define γ and R[17]. Adiabatic flow through a nozzle implies that stagnation temperature remains constant while isentropic flow through a nozzle demands that total pressure remains constant with no shaft work derived from the flow through a nozzle. By the law of conservation of mass, the mass flow rate between any two sections of a nozzle in steady flow must be equal. The mass flow rate at choked condition can be taken in ratio to the mass flow rate at any section of the nozzle using the definition of Eq. 4.14-b to express a non-dimensional area ratio. Sonic flow area is defined by A* and M* = 1, the non-dimensional area ratio is given by:

$$\frac{A}{A^*} = \frac{1}{M} \left(\frac{1 + \frac{\gamma - 1}{2} M^2}{\frac{\gamma + 1}{2}} \right)^{\frac{\gamma+1}{2(\gamma-1)}} = \frac{1}{M} \left(\frac{\gamma + 1}{2} \left[1 + \frac{\gamma - 1}{2} M^2 \right] \right)^{\frac{\gamma+1}{2(\gamma-1)}} \qquad \text{(Eq. 4.15)}$$

If the nozzle geometry is known, one can determine the inlet and exit Mach number of the nozzle flow based on the known area ratios between inlet and exit area to the throat area, respectively. According to Ref. 16, the ratio of mass flow rate to nozzle cross sectional area is

maximized at the minimum or throat section. Therefore, at sonic condition where M = 1, the mass flow rate is maximized. For a sonic nozzle, the flow is choked at the exit and the mass flow rate per cross sectional area is maximum. Due to viscous effects of the flow interaction with the nozzle wall boundary, a discharge coefficient is introduced to the mass flow rate equation to account for these effects. The discharge coefficient $C_{D,}$ is the ratio of actual mass flow rate to the ideal mass flow rate through the nozzle. Approximate values of 0.95 to 0.995 can be safely assumed for sonic nozzles and convergent orifices[17, pp. 277, Fig. 5.60]. The viscous effects result in a reduction of the overall flow area upon the nozzle exit. Therefore, the resulting flow exit area can be expressed in terms of effective nozzle area, $A_{eff} = C_D A$. This relation is substituted into Eq. 4.14b to yield:

$$\dot{m} = \sqrt{\frac{\gamma}{R}} \frac{p_t}{\sqrt{T_t}} A_{eff} M \left(\frac{1}{1 + \frac{\gamma - 1}{2} M^2} \right)^{\frac{\gamma+1}{2(\gamma-1)}} = \sqrt{\frac{\gamma}{R}} \frac{p_t}{\sqrt{T_t}} C_D A M \left(\frac{1}{1 + \frac{\gamma - 1}{2} M^2} \right)^{\frac{\gamma+1}{2(\gamma-1)}} \quad \text{(Eq. 4.16)}$$

Based on nozzle geometry, the area ratio is known at the inlet of a nozzle. The nozzle inlet Mach number can be determined by using Eq. 4.14. Solving Eq. 4.14 yields a subsonic and supersonic solution. Based on stagnation condition at the inlet of a nozzle, the subsonic solution is considered. With the knowledge of the stagnation pressure, one can determine the sonic pressure p^*, density is ρ^* and temperature T^* using Eq. 4.5, 4.6 and 4.7.

For a sonic nozzle, the exit is choked and the sonic conditions of the nozzle are at the exit. Nozzle exit gas properties correspond to the sonic properties of the gas. At the nozzle exit, Mach number $M_2 = M^* = 1$ and the total gas exit properties are derived with the help of Eq. 4.5, 4.6 and 4.7 and evaluated as follows:

$$\frac{T_{t_2}}{T_2} = \frac{T_{t_2}}{T^*} = \left(\frac{\gamma+1}{2}\right) \qquad \text{(Eq. 4.17)}$$

$$\frac{p_{t_2}}{p_2} = \frac{p_{t_2}}{p^*} = \left(\frac{\gamma+1}{2}\right)^{\frac{\gamma}{\gamma-1}} \qquad \text{(Eq. 4.18)}$$

$$\frac{\rho_{t_2}}{\rho_2} = \frac{\rho_{t_2}}{\rho^*} = \left(\frac{\gamma+1}{2}\right)^{\frac{1}{\gamma-1}} \qquad \text{(Eq. 4.19)}$$

4.2 Determination of Fluid Aerodynamic Power from Nozzle Exit Flow

The fluid aerodynamic power for the gas flow at the nozzle exit is determined by applying the energy equation to the mass flow rate of air $\dot{m}_2$ at the nozzle exit carrying total enthalpy h_{t_2}. The power of the air flow at the exit of a choked nozzle is given by:

$$\wp_2 = \dot{m}_2 h_{t_2} = \dot{m}_2 c_p T_{t_2} \qquad \text{(Eq. 4.20)}$$

This equation is valid for the determination of the power from the fluid flow at the location of nozzle exit. For an underexpanded nozzle, the shock structure that emerges from the nozzle exit consists of a combination of expansion and compression waves as explained in Chapter 2.

4.3 Determination of Aero-Mechanical Efficiency from Conversion of Aerodynamic to Mechanical Turbine Shaft Power

Mechanical efficiency of power conversion from pure air flow kinetic energy to mechanical shaft power is defined as the amount of mechanical shaft power generated by the amount of fluid power that is imparted by the flow velocity on a turbine wheel. Shaft power can be measured by placing a turbine wheel in the jet stream. Parameters such as torque generated and corresponding turbine wheel rotational speed are recorded.

The shaft power is given by the following equation:

$$\wp_{turbine} = \wp_{shaft} = Q_{turbine} \cdot \omega_{turbine} \qquad \text{(Eq. 4.21)}$$

If the fluid power is calculated based on the gas properties at the nozzle exit and the shaft power is measured, the aero-mechanical efficiency of the power conversion can be calculated for a gas flow that impinges on the blades of a turbine wheel to produce rotational motion. The equation below is used:

$$\eta_{aero-mech} = \frac{\wp_{shaft}}{\wp_2} = \frac{\wp_{turbine}}{\wp_{aero}} \qquad \text{(Eq. 4.22)}$$

The following chapter of this document will further detail the experimental setup and procedures that were performed to determine the aero-mechanical efficiency of the power conversion as derived above.

5.0 EXPERIMENTAL SETUP AND PROCEDURES

The purpose of this chapter is to present a detailed description of the experimental facilities, pressurized gas generation assembly, supersonic plug nozzle, mini-turbine, instrumentation, torque measurement assembly, focused shadowgraph flow visualization and data measurements for the experimentation performed for the current study.

The experiments were conducted at the Adaptive Aerostructures Laboratory of the University of Kansas. The Adaptive Aerostructures Laboratory houses various machining equipment and materials that were used to fabricate the main components of the experimental setup for this research. The compressed air supply system at the facility was used to supply pressurized air to the experimental assembly to simulate gas flow through a gas generator and exhausting into still air through a pre-fabricated ejector plug type nozzle. Instrumentation and experimental equipment for the shadowgraph visualization of the supersonic jet from the nozzle was also provided by the facility.

5.1 Pressurized Gas Generation Assembly

The pressurized gas generation system of Figure 5.1 was assembled using high pressure rated components purchased from Hi-Pressure Equipment. The components were assembled based on preliminary sizing and design considerations. The maximum rated pressure for each of the components is 150,000 psi. Attachments were built using aluminum stock material to support each of the components connected by high pressure tubing with an internal and outer diameter of 1/8” and 3/8”, respectively. The supporting attachments for each component of the gas generator were bolted down to a Rohacell-graphite sandwich panel. Detailed

dimensioned drawings of each high pressure component, attachment and gas generation assembly can be found in Appendix D. Manufacturer's data for the components acquired from Hi-Pressure equipment are also presented in Appendix A.

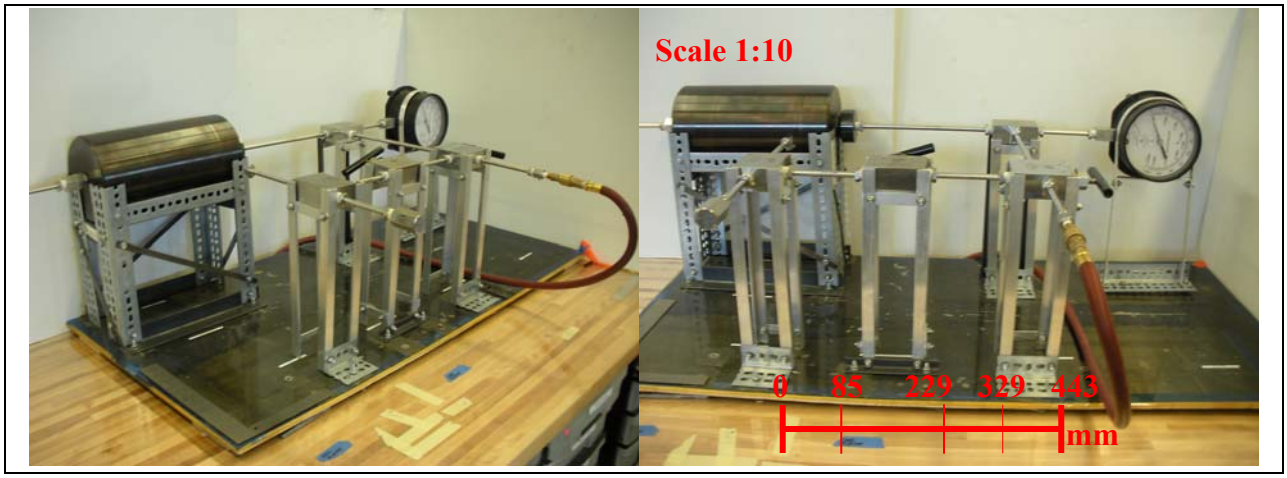

Figure 5.1 Two Views of the Pressurized Gas Generation Assembly.

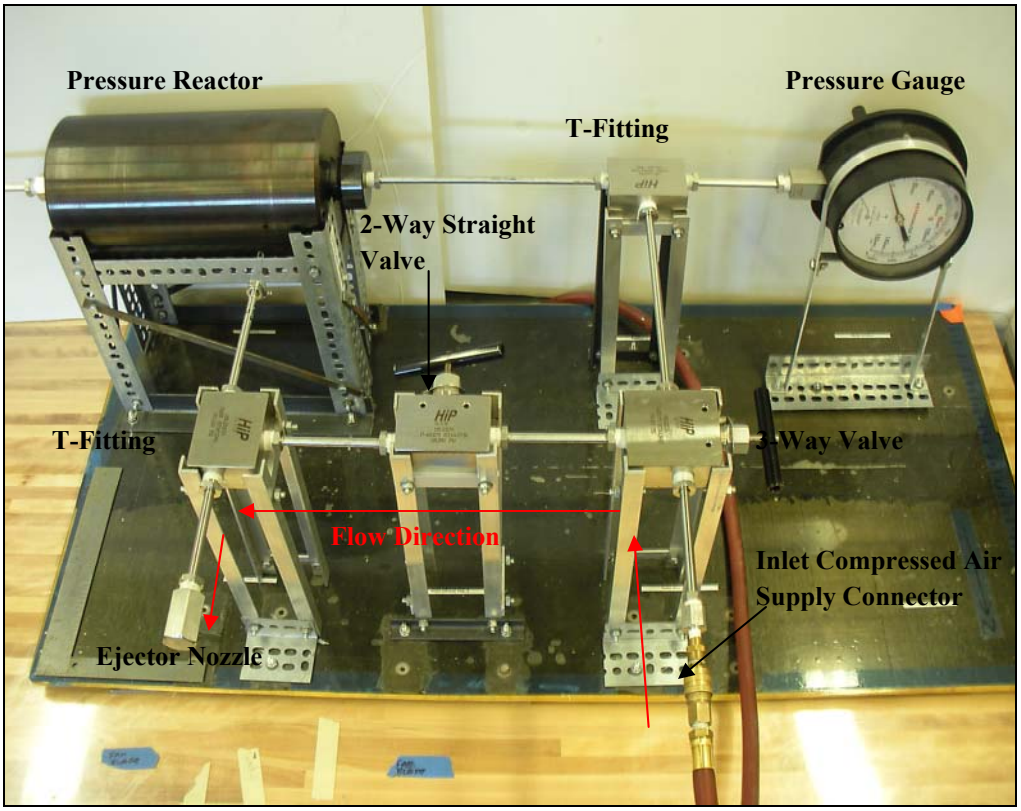

Figure 5.2 Top View of the Pressurized Gas Generation Assembly.

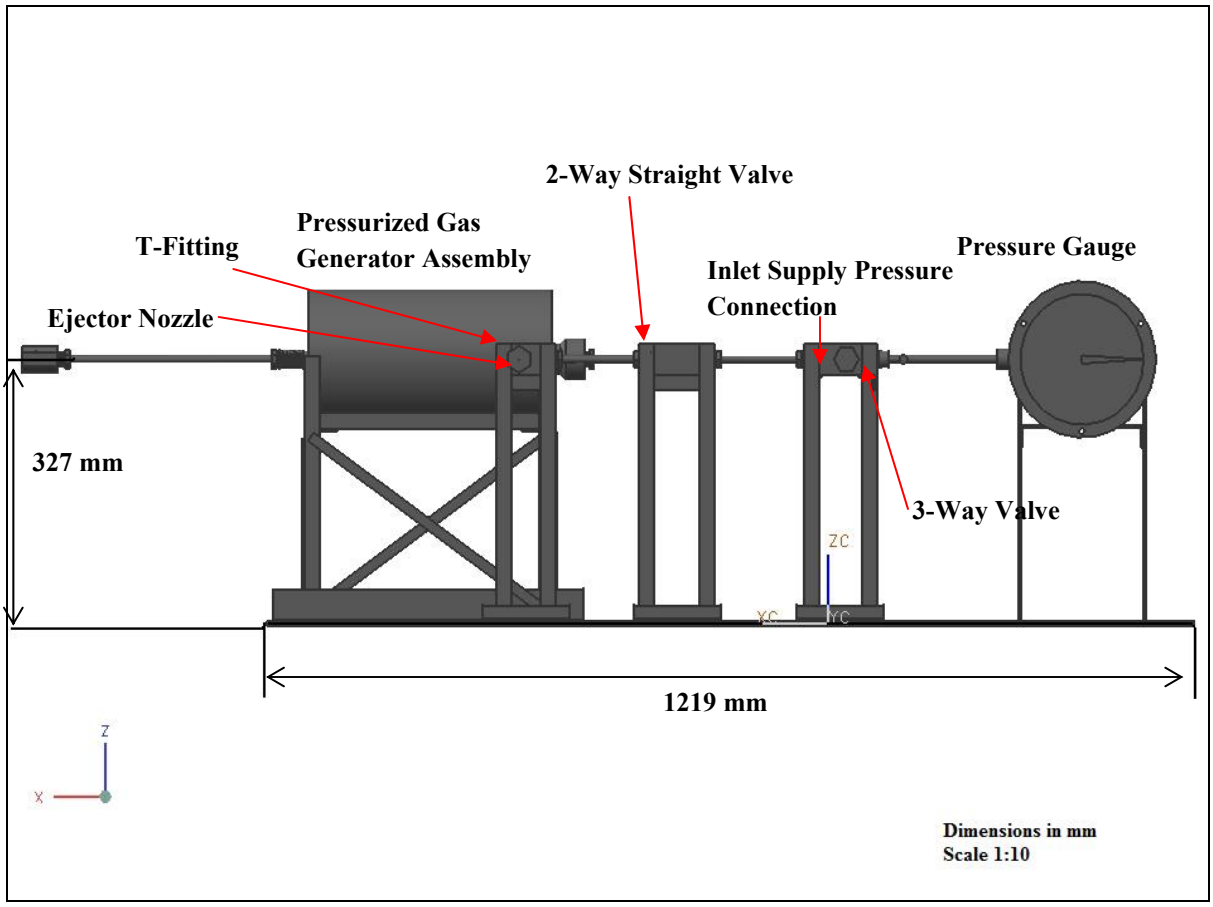

Figure 5.3 **CAD Figure of the Pressurized Gas Generation Assembly with Front View (Scale 1:10).**

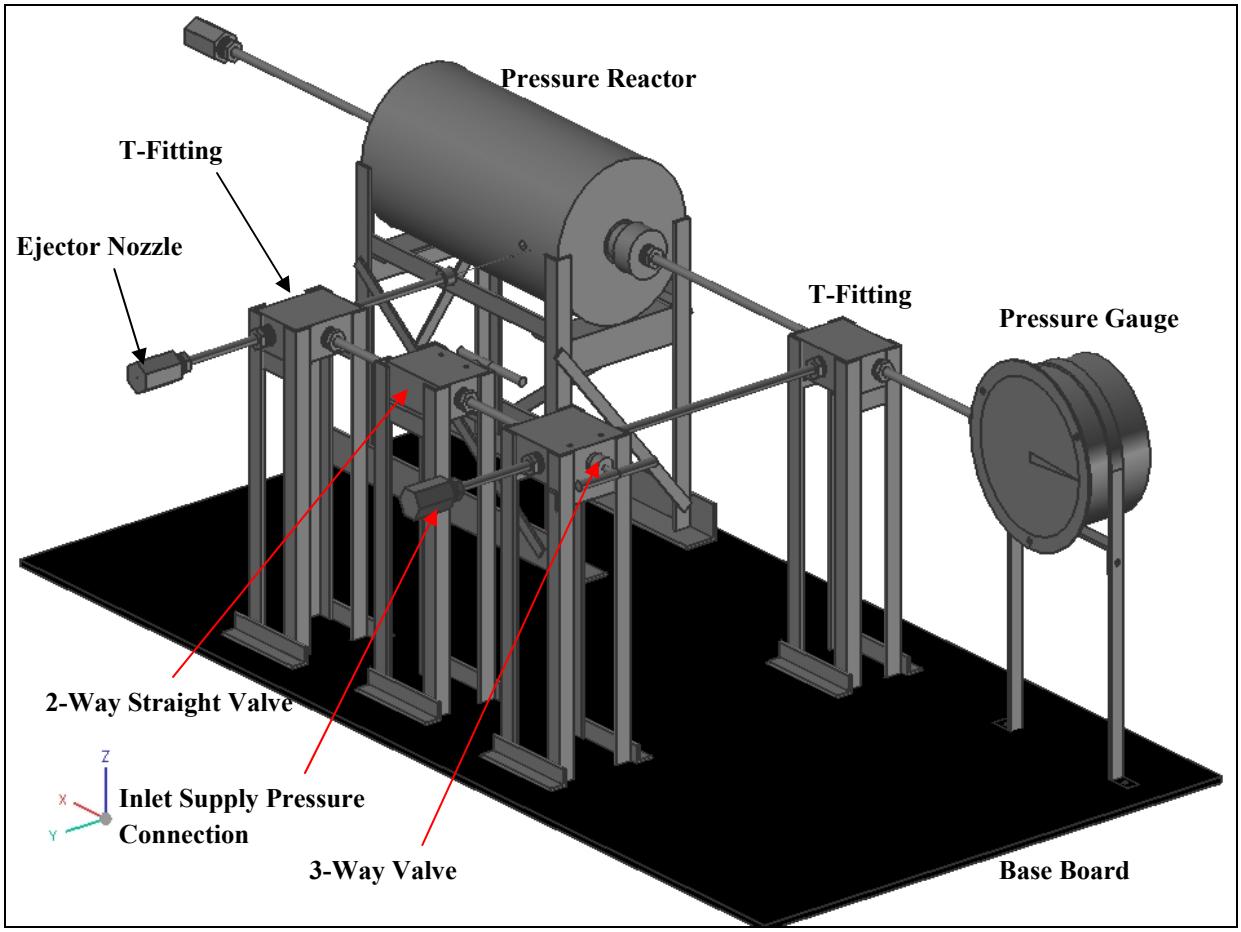

Figure 5.4 **CAD Figure of the Pressurized Gas Generation Assembly with Isometric View.**

5.1.1 Pressure Reactor Assembly Operation

The gas generation assembly consists of the following components (Refer to Figure 5.5 for location of each component):

- Pressurized Air Supply Inlet Connection Adapter (Part A)
- One 3-way valve (Part B)
- Two T-fitting connections (Part C & G)
- One pressure reactor (Part D)
- Pressure gauge (Part E)
- One 2-way valve (Part F)
- Ejector Nozzle (Part H)
- High pressure tubing with collars and glands for connection to major components
- Base Plate made from Rohacell foam core (Part I)
- Needle Plug Valve Turn Screw Mechanism (Part J)

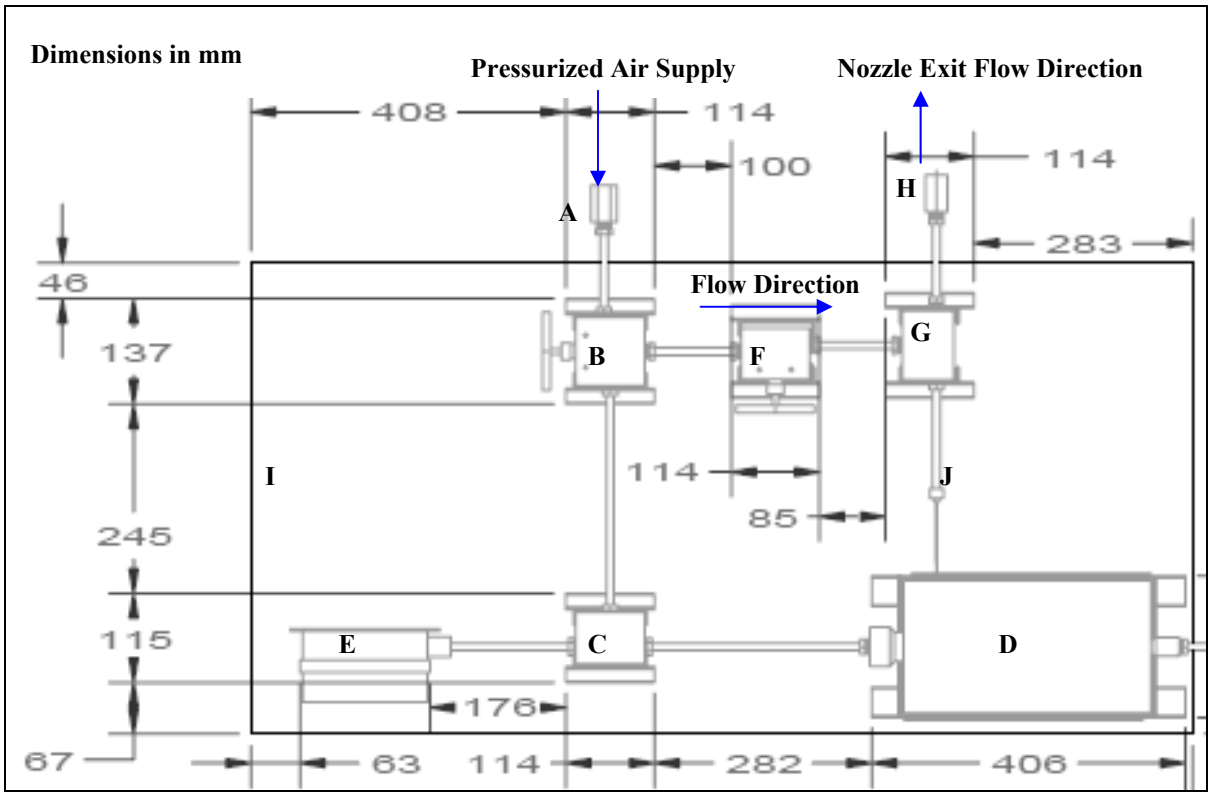

Figure 5.5 CAD Figure of the Pressurized Gas Generation Assembly Top View Showing Gas Flow Directions (Scale 1:10).

The pressurized gas generation assembly is shown in Figure 5.5 with directions labeled for the pressurized air flow that enters at A. The pressurized air is supplied from the compressed air outlets in the experimental facility. Air enters through the 3 way valve system of Part B and flows through the tubing connecting Parts B and F. The purpose of the 3 way valve is to allow air to enter the system and provide a method to shutoff air flow from the supply inlet to the pressure reactor at D and the valve at F.

At the T-fitting (Part C), the air is diverted to flow into the pressure reactor at D and through the tubing to the pressure gauge at E. In addition, pressurized air would be able to flow from the 2 way straight valve at F to the T-fitting component at G. The 2 way valve can be used as a means of throttling supply pressure to the ejector nozzle at H.

The purpose of the T-fitting (Part G) is to divert air through the tubing that is connected to Part H where the ejector nozzle is attached. Air exits at supersonic speeds through the nozzle into the ambient air during experimentation. The ejector nozzle is a plug type nozzle and the nozzle exit area can be varied using the screw-head mechanism at J.

5.2 Supersonic Nozzle and Needle Spike Valve

The supersonic ejector nozzle was designed and fabricated at the Adaptive Aerostructures Laboratory. The ejector nozzle inner geometry was designed to have a convergent cross section such that air entering the ejector nozzle inlet would increase in speed from subsonic to sonic as it approached the nozzle exit where the flow was choked. The nozzle flow is then expanded to supersonic speeds as it flows over the needle plug with a half angle of 1 degree.

The ejector nozzle was manufactured from an end cap that was purchased from Hi-Pressure Equipment. The 316 Stainless Steel end cap was pre-drilled three times in order to create the converging nozzle inner geometry. The end cap would be drilled from the threaded end to a short length before the nozzle exit twice using drill bits of 3.18 mm and 2.06 mm, respectively, followed by a drilling procedure from the closed end of the component. The end cap was placed on a turning lathe and a 0.711 mm drill bit was then used to drill the nozzle exit face to its specified diameter at the centerline.

The nozzle plug valve was fabricated from a stainless steel wire with a diameter of 0.711 mm and length of 0.508 m. The stock material was cut to length and the half angle of the needle plug valve was manufactured using a belt sander. First, the desired half angle was designed using a CAD program to determine the appropriate length for the ramp portion of

the needle valve. An angled guide was placed on the belt sander and stock material was then sanded down at an angle to create a sharp needle-like geometry at one end of the 0.711 mm diameter steel wire. The purpose of the needle-like plug valve was to provide an expansion surface for the nozzle flow to become supersonic as it passed the ejector nozzle exit. Also, it served as a means of varying the nozzle exit area when the rod was moved in and out of the nozzle. A screw-head fitting was then fabricated so that the nozzle exit area can be controlled. This allows the variation of nozzle exit area and static pressure. Figure 5.6 illustrates the ejector nozzle outer geometry with a needle plug valve protruding from the exit of the nozzle. A schematic diagram of the ejector nozzle side view is presented in Figure 5.7 to show the three drilled diameters on the ejector nozzle.

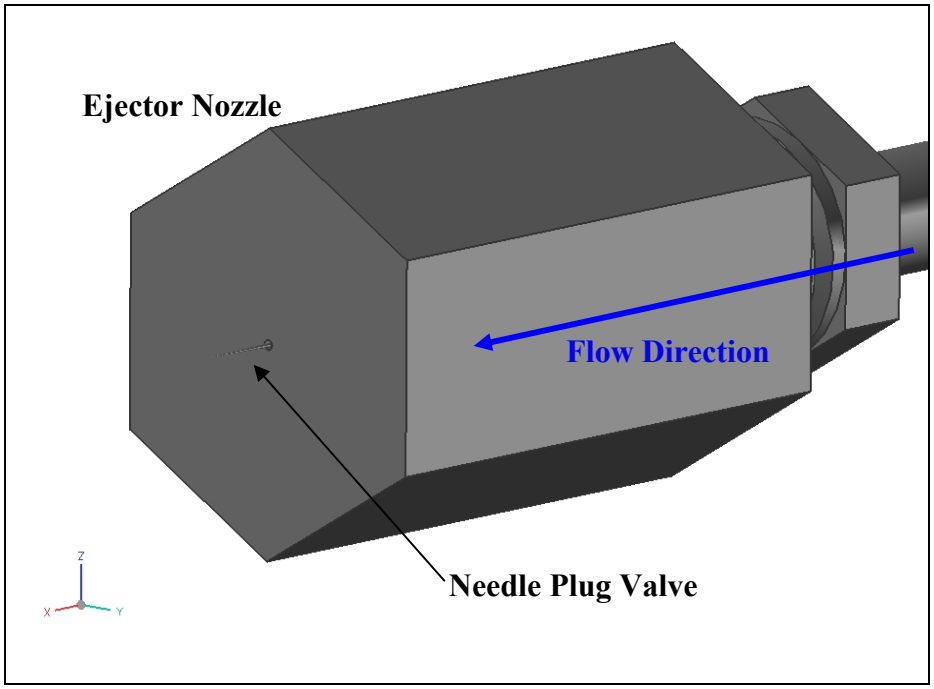

Figure 5.6 Isometric CAD Diagram of the Ejector Nozzle with a Needle Plug Protruding from the Nozzle Exit.

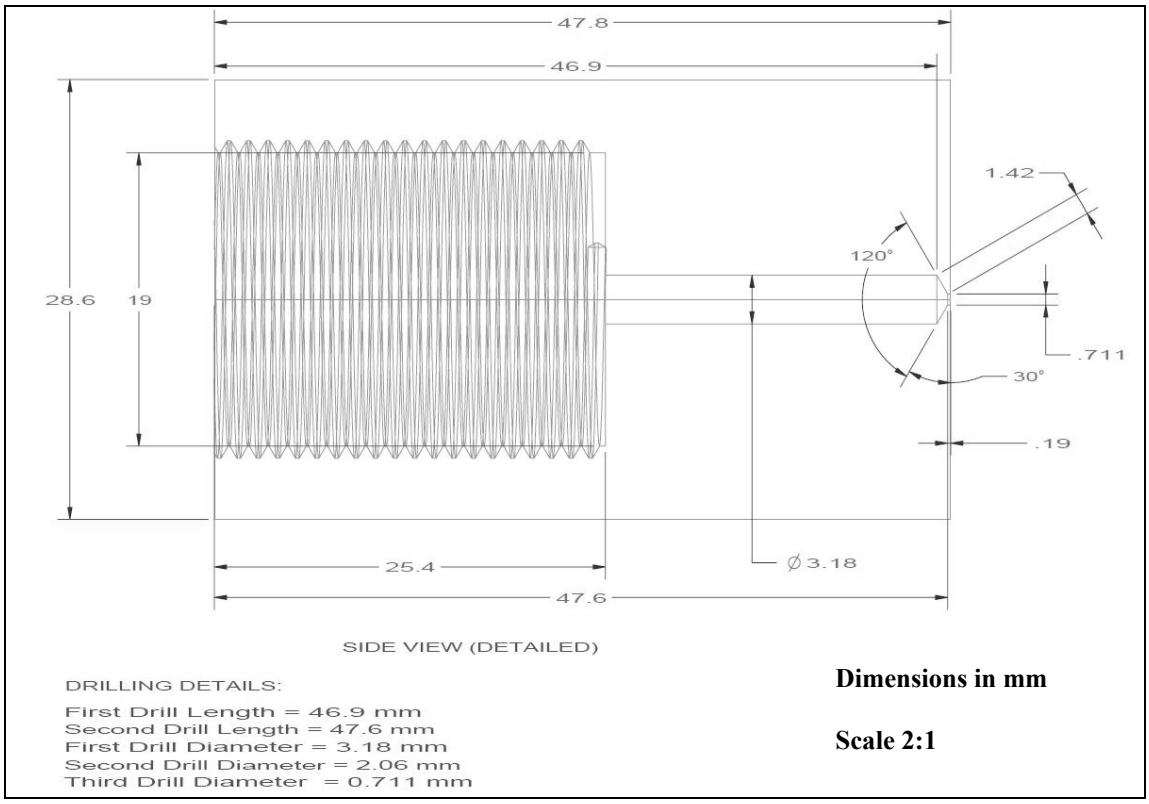

Figure 5.7 Schematic CAD Diagram of the Ejector Nozzle showing Dimensions in mm (Scale 2:1).

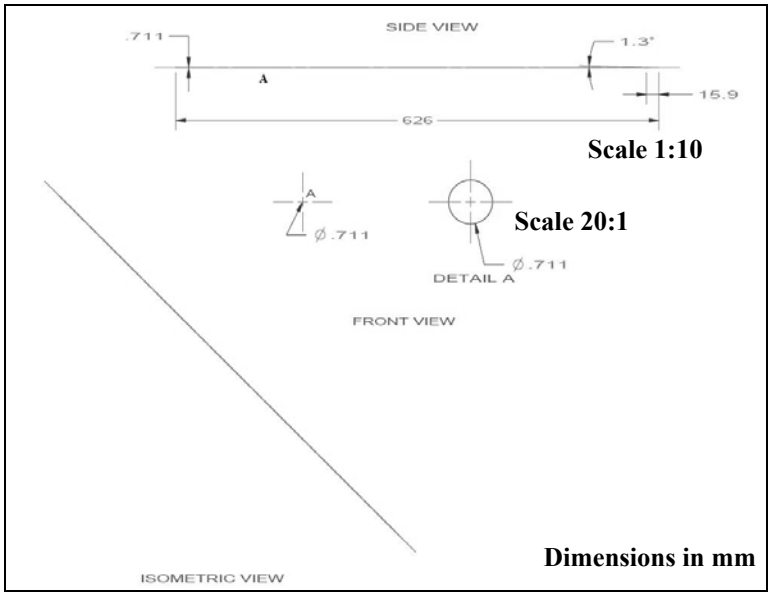

Figure 5.8 Schematic Diagram of the Needle Plug Valve Geometry.

5.3 Mini-Turbine

Figure 5.9 illustrates the mini-turbine used for the current study. The mini-turbine consists of a shroud that encases 12 planar blades stacked at an angle of 45 degrees. The outer diameter of the mini-turbine measures 25.7 mm. A connection for the turbine was fabricated using a bolt and nut assembly. The bolt size was selected based on the inner hub diameter for the turbine. Also, the bolt was pre-drilled with a 2 mm hole at one end for connection to the shaft of a Kyosho Le Mans DM 200 electric motor. The electric engine was used for measuring torque of the turbine during experimentation. The torque measurement assembly will be further detailed in Section 5.5 of this chapter.

Figure 5.9 Digital Photographs of the 45 degree Planar Blade Mini-Turbine.

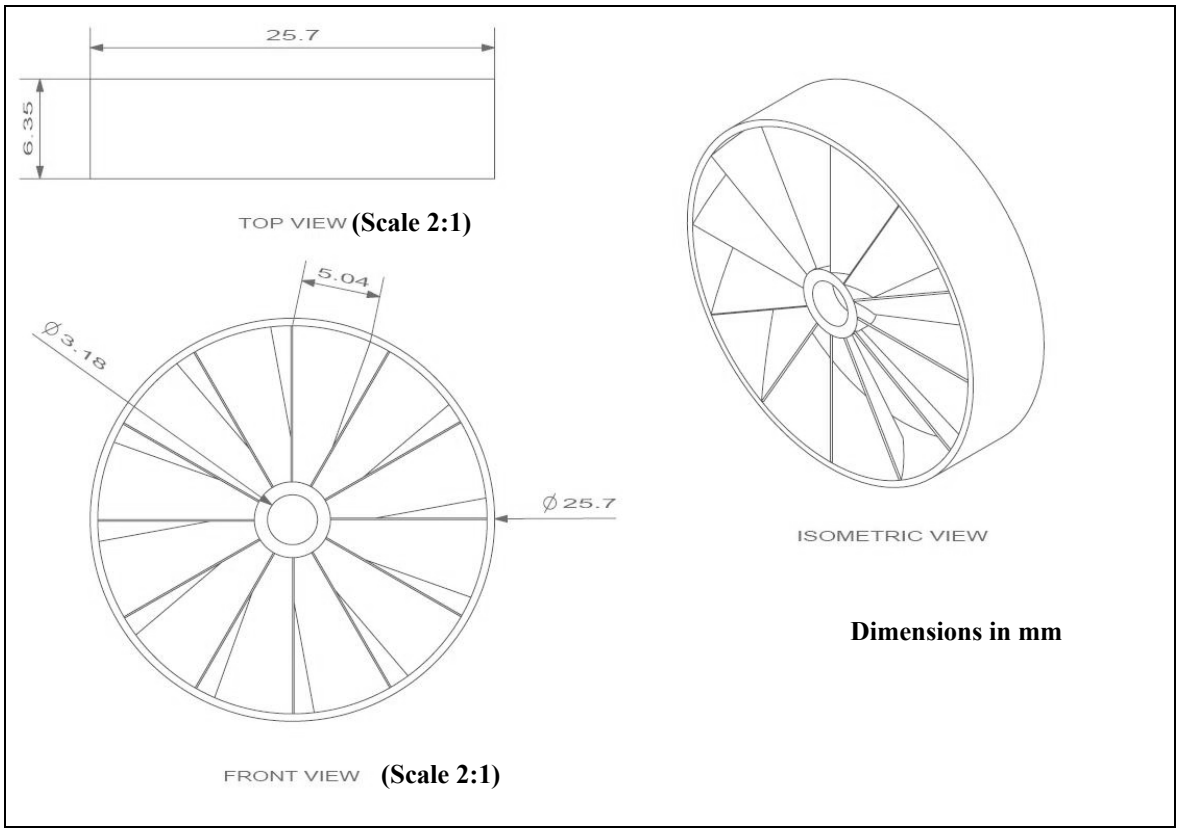

Figure 5.10 CAD Diagram of the Planar Blade Mini-Turbine.

Table 5.1 Salient Cascade Parameters for the Mini-Turbine Test Article.

Parameter	Value
Blade Camber Angle, φ	0^o
Blade Tip Chord, c_{tip}	0.749 mm
Blade Root Chord, c_{root}	0.200 mm
Blade Solidity at Pitchline Radius (R_m), $\sigma_{Rm} = c_{blade}/s_{blade}$	0.119
Blade Aspect Ratio, $AR_{blade} = b^2/S$	21.1
Blade Root Thickness-to-Chord Ratio, t/c_{root}	0.696
Blade Tip Thickness-to-Chord Ratio, t/c_{tip}	0.186

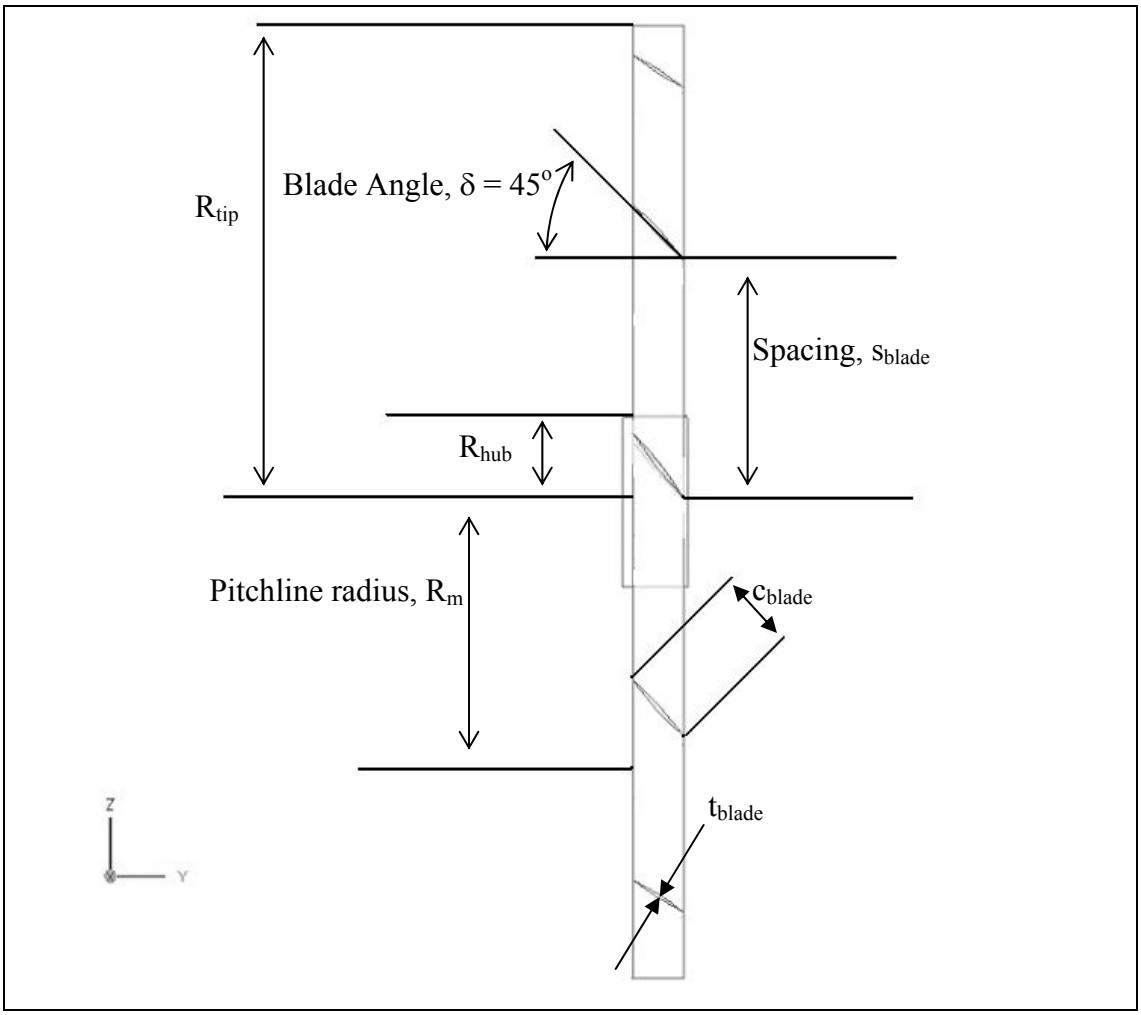

Figure 5.11 Schematic Diagram of a Mini-Turbine with 45° Planar Blades showing Definition of Salient Cascade Parameters.

5.4 Instrumentation

This section details the instrumentation that was used for the measurements taken for the current investigation.

5.4.1 Pressure Measurement

A portable digital pressure gauge was used to measure the inlet pressure supply to the pressurized gas generation assembly. The digital pressure gauge model DPG6000 was manufactured by Omega. The pressure gauge measured the total inlet pressure of the gas generator assembly in pound per square inch. The total pressure was considered as the inlet total pressure for the ejector nozzle and was measured at the beginning of each run. Table 5.2 shows the specifications for the pressure gauge used. Additional model specifications can be found in Appendix A.

Table 5.2 Omega Engineering DPG6000 Digital Pressure Gauge Specifications[19].

Manufacturer	**Omega**
Accuracy (linearity, hysteresis and repeatability)	±0.25% FS + 1 LSD
Pressure Cavity Volume	0.06 in^3
Thermal Zero Shift	±0.02% F.S./0.6 °C (±0.02% F.S./°F)
Thermal Sensitivity Shift	±0.02% F.S./°F
Durability	>10 million cycles
Voltage	3.6 V/cell, no-load
Capacity	5.2 Ah/cell
Case	Stainless Steel 15-5 PH

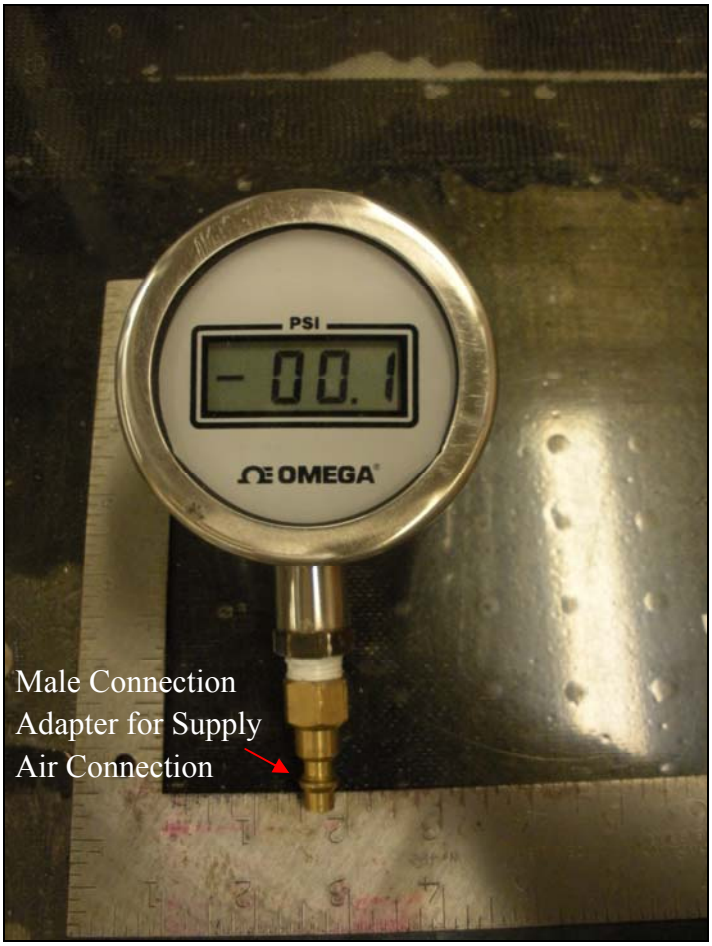

Figure 5.12 Photograph of the Omega DPG6000 Portable Digital Pressure Gauge.

5.4.2 Temperature Measurement

The static temperature of the gas at the nozzle exit was measured using a handheld non-contact infrared thermometer. The thermometer had a built-in laser pointer that aided in aiming the device at a desired location where the temperature was to be measured. The device was able to measure temperatures up to 600 ^{o}F without contact and the temperature readings on the digital display can be switched between ^{o}F and ^{o}C units. Also, the thermometer had a narrow field of view if pointed at the target as close as possible for an accurate temperature reading to be measured.

The device recorded the temperature at a specific location when the infra-red beam was pointed at the target. At the beginning of each experimental run, static temperature of the gas was measured in Fahrenheit by pointing the infra-red beam at the exit of the ejector nozzle. The temperature readings were displayed on a digital LCD display on the handheld device. This reading gave a fairly accurate determination of the static temperature of the nozzle exit gas for calculation of the aerodynamic fluid power of the nozzle gas flow. The product specifications are described in the following table and the device used can be seen in the figure below.

Table 5.3 Manufacturer's Specifications for the Non-Contact Infrared Thermometer[20].

Manufacturer	CEN-TECH Instruments
Range	0 to 600 °F or -20 to 320 °C
Accuracy	±2% of reading or ±4 °F/ 2 °C (whichever is greater)
Resolution	1 °F/ °C
Emissivity	0.95 fixed
Field of View	8:1 (at 8" distance measure 1" target)
Dimensions	8.3 x 3.5 x 1.5" (211 x 89 x 38mm)
Weight	6.4 oz. (200 g)

Figure 5.13 Handheld Non-Contact Infrared Thermometer (CEN-TECH 91778) used for Temperature Measurements.

5.4.3 Mini-Turbine Rotational Speed Measurement

The rotational speed of the mini-turbine was measured using an EXTECH 461893 digital non-contact photo tachometer. When the mini-turbine was exposed to the jet stream of the nozzle exit flow, the turbine would rotate at high RPM and these speeds were measured with the photo tachometer. The measurements were made by placement of the tachometer adjacent and directed in-plane to the outer surface of the mini-turbine shroud. The surface of the mini-turbine shroud was painted half black and the rest of the surface was polished to replace the use of a reflective tape which is required for RPM measurements of a rotating component.

For accurate measurements, the device had to be pointed directly to the polished surface for reflection. In addition, ambient light had a significant influence on the RPM

readings measured by the tachometer. The manufacturer suggested that the device be placed at least 2 to 6 inches (50 to 150 mm) from the target. The device measured accurate RPM readings (0.05%) which are updated every second and displays the readings on a LCD display. The photo tachometer could provide non-contact measurements from 5 to 99,999 RPM and has a built-in memory to store the last maximum or minimum value recorded.

Table 5.4 Manufacturer's Specifications for the Photo Tachometer[21].

Manufacturer	EXTECH Instruments
Range	5 to 99,999 rpm
Accuracy	±(0.05%rdg +1d)
Sampling Time	1sec > 60 rpm
Resolution	0.1 rpm (0.5 to 999.9 rpm); 1 rpm (>1000rpm)
Dimensions	6.7 x 2.8 x 1.5" (170 x 27 x 37 mm)
Weight	8.8 oz (250 g)

Figure 5.14 EXTECH 461893 Photo Tachometer Used for RPM Measurements.

5.4.4 Electric Motor

A brushed DC electric motor was used for torque measurement purposes. The electric motor requires a direct current supply to power up. The electric motor, Le Mans DM 200 model, used was manufactured by Kyosho Corporation. This specific motor is currently out of production and performance specifications were not available during this time.

A mini-turbine was attached to the electric motor shaft and the torque generated by the rotational motion of the turbine was transferred to the motor casing through the shaft. The mini-turbine and electric motor assembly was attached to a torque swing assembly which will be described in Section 5.5 of this chapter. The figure below shows the representative size of the electric motor used for the current study.

Figure 5.15 Kyosho Le Mans DM 200 Electric Motor.

5.4.5 DC Generator Supply

The electric motor used for torque measurement was powered by an EXTECH 0-30V 0-3A DC power supply. The device was provided by the Adaptive Aerostructures Laboratory of the University of Kansas. This power supply generator has an analog display of the adjustable voltage and current output ranges. The component also has independent 5V and 12V output terminals and provides constant voltage and current during operation. The table below provides the specifications for the DC generator.

Table 5.5 DC Power Supply Product Specifications[22].

Manufacturer	EXTECH Instruments
Voltage Output	DC 0 to 30 Volts
Current Output	DC 0 to 3 Amps
Ripple and Noise	<5 mV
Line Regulation	<0.05%+10 mV
Load Regulation	<0.05%+10 mV
Fixed Output Voltage	5V/0.5 A (cont.), 1A(max); 12 V/0.5 A (cont.), 1 A(max)
Power	110/220VAC 50/60Hz
Dimensions	6 x 5.6 x 9.5" (152 x 142 x 242) mm
Weight	11 lbs. (5 kg)

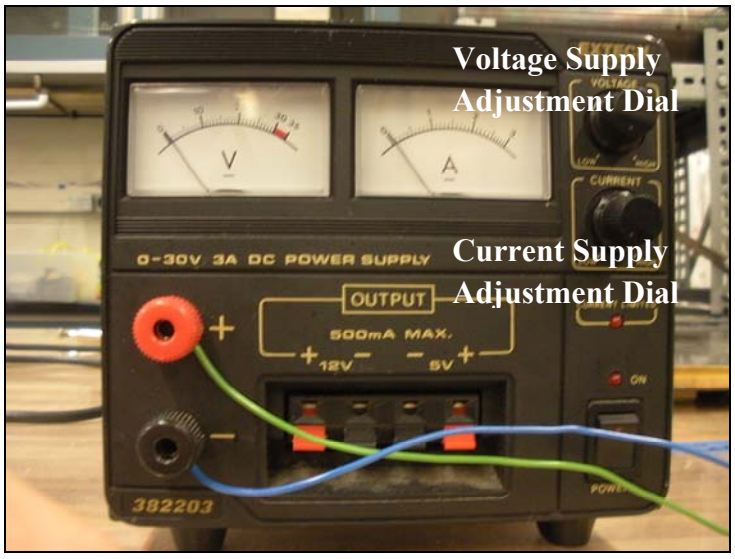

Figure 5.16 EXTECH 382203 Analog Output DC Power Supply with Adjustable Voltage and Current Output.

5.4.6 Digital Camera and Lens

The photographic equipment that was used for the supersonic jet flow visualization was captured by a Nikon Digital SLR Model D5000 camera. This camera was provided by Mr. Scott Cravens, graduate student of Aerospace Engineering at University of Kansas. The specifications of the Nikon Digital SLR camera are summarized in Table 5 and additional information can be found in Appendix A. An AF NIKKOR Micro Focusing Lens with a focal length of 60 mm and aperture of 1:2.8 was used with the camera to focus the object to be visualized in the current study. The NIKKOR lens was a macro zoom lens although labeled by the manufacturer as a micro lens. The setup for taking the digital images of the supersonic jet flow from the ejector nozzle exit included a sliding tripod, a 75 mm focal length convex lens and a light source. These items were setup for a shadowgraph type visualization of the supersonic nozzle flow. Further details of the flow visualization setup are described in Section 5.6.

Table 5.6 Nikon Digital SLR D5000 Model Specfications[23].

Manufacturer & Model	NIKON Digital SLR D5000
Type	Single-lens reflex digital camera
Lens Mount	Nikon F mount (with AF contacts)
Effective Picture Angle	Approx. 1.5 x lens focal length (Nikon DX format)
Effective Pixels	12.3 million
Total Pixels	12.9 million
Image Size (Pixels)	4,288 x 2,848 [Large], 3,216 x 2,136 [Medium], 2,144 x 1,424 [Small]
Frame Coverage	Approx. 95% horizontal and 95% vertical
Magnification	Approx. 0.78 x (50 mm f/1.4 lens at infinity; -1.0 m^{-1}
Eye Point	17.9 mm (-1.0 m^{-1})
Shutter	Electronically controlled vertical-travel focal-plane shutter
Shutter Speed	1/4,000 to 30 s in steps of 1/3 or 1/2 EV
Exposure Compensation	±5 EV in increments of 1/3 or 1/2 EV
Autofocus	Nikon Multi-CAM 1000 autofocus sensor module with TTL phase detection, 11 focus points (including 1 cross-type sensor) and AF-assist illuminator (range approx. 1 ft. 8 in.–9 ft. 10 in. / 0.5–3 m)
AF detection range	-1 to +19 EV (ISO 100 equivalent, 68°F/20°C)
Dimensions	Approx. 5.0 x 4.1 x 3.1 in. / 127 x 104 x 80 mm
Weight	1 lb. 4 oz. / 560 g without battery, memory card, or body cap

Figure 5.17 Nikon Digital SLR D5000 Camera used for Taking Still Photographs for Supersonic Jet Flow[23].

5.5 Torque Measurement Assembly

The torque measurement set up used for the experimentation in the current study was selected for its simple design and concept of measuring the torque generated by the rotating mini-turbine. The method of measuring torque in this set up was based on the angular deflection of a swing arm caused by torque of an object connected to the arm. The overall setup was made from stock wood material and dimensioned drawings of the assembly can be found in Appendix D.

The torque measurements were achieved using a swing arm technique where the torque generated by the object of study causes an angular deflection that was measured. A mini-turbine was attached to an electric motor shaft using a coupler since the inner hub diameter of the turbine was greater than the motor shaft. The torque from the rotational motion of the mini-turbine when exposed to a supersonic jet was transferred to the electric motor shaft. As a result, the motor casing reacted with a counter rotating torque to the motor shaft. The motor

casing was attached to a wooden block that has an angular dial at the top and a swing arm at the bottom as seen in Figures 5.18 through 5.21. The wooden block was free to rotate from 0 to +/-90 degrees based on the amount of torque being generated from the mini-turbine (See Figure 5.18). A mass, W, placed on the swing arm made from graphite could be moved up or down until a reasonable angular deflection was observed. When a reasonable angular deflection was observed, the distance from the center of the mini-turbine to the mass center was determined as the moment arm, d, for the counter rotating torque of the motor casing in reaction to the torque direction of the motor shaft. The torque measured from the turbine was approximated with the following equation:

$$Q_{turbine}\left(N \cdot m\right) = W \times d \cdot \sin\theta \qquad \text{(Eq. 5.1)}$$

If the rotational speed of the mini-turbine, ω, was measured, the mechanical shaft power of the mini-turbine is determined by:

$$\wp_{turbine} = Q_{turbine} \cdot \omega_{turbine} \qquad \text{(Eq. 5.2)}$$

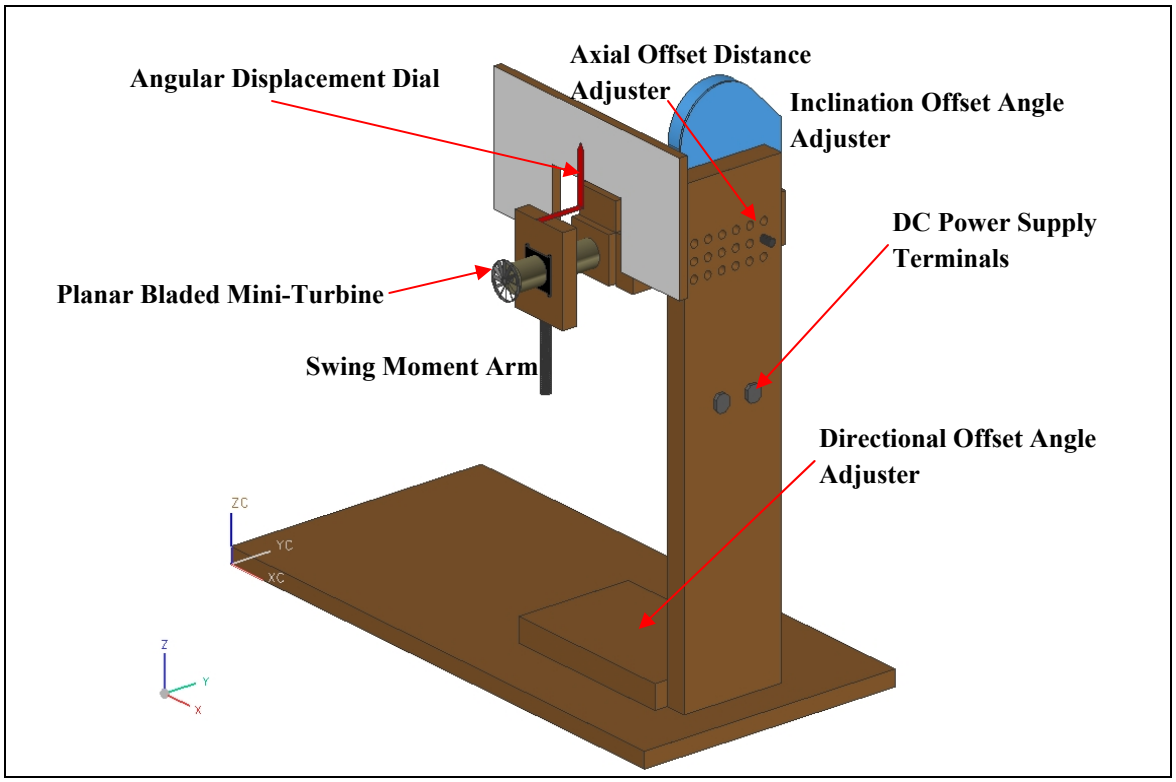

Figure 5.18 Isometric View of the Torque Measuring Equipment.

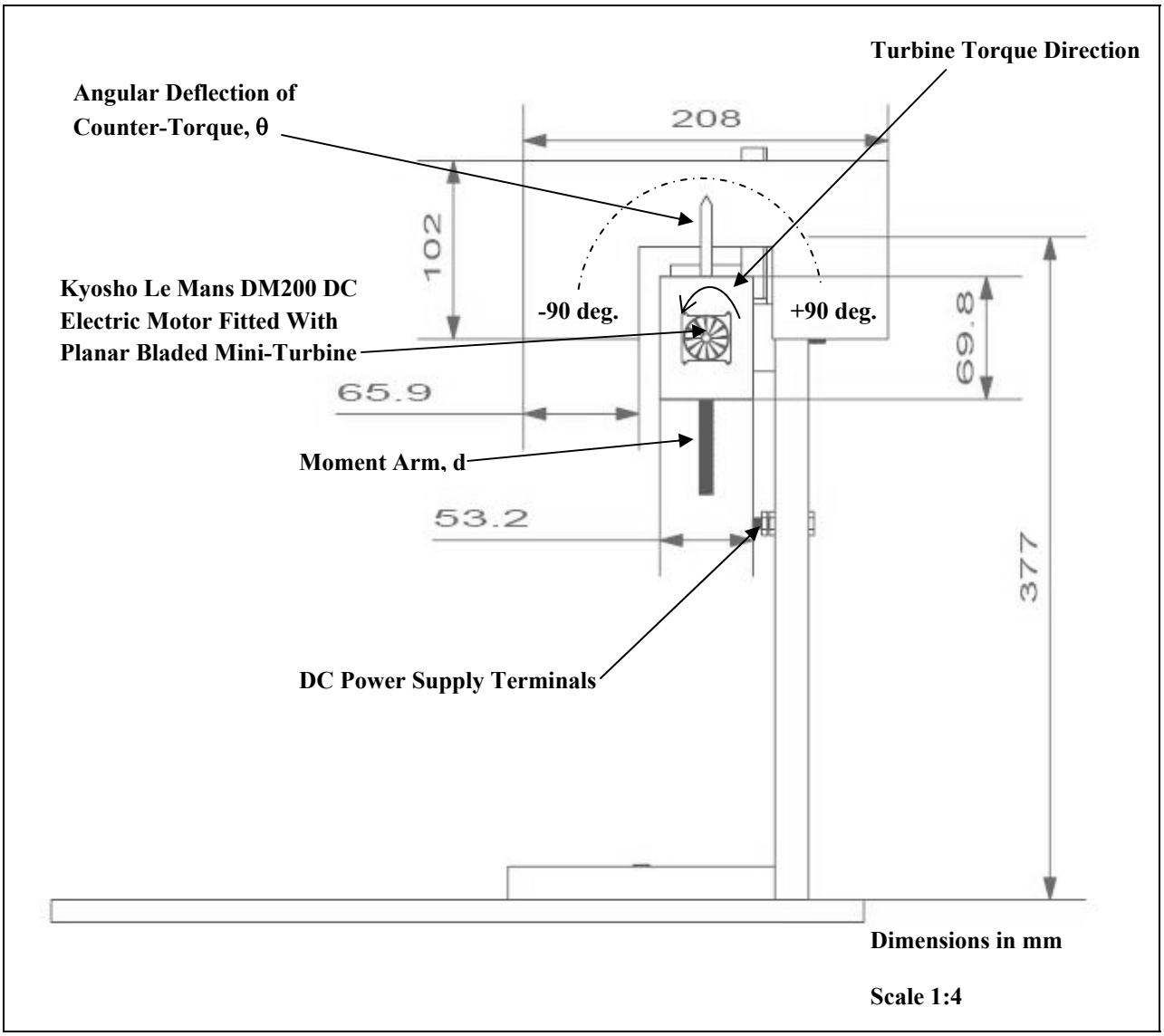

Figure 5.19 Labeled Diagram to Show the Angular Deflection Dial and Torque Measurement Assembly.

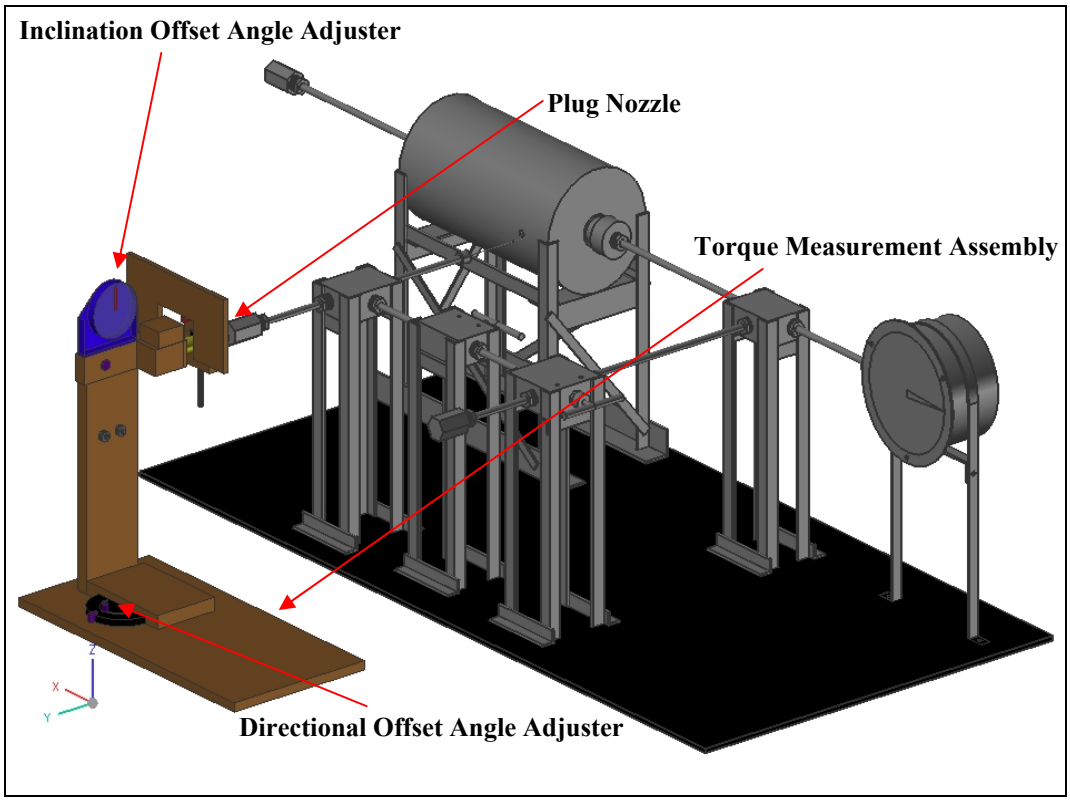

Figure 5.20 **Isometric View of the Torque Swing Assembly Located at the Nozzle Exit of the Pressurized Gas Generation Assembly.**

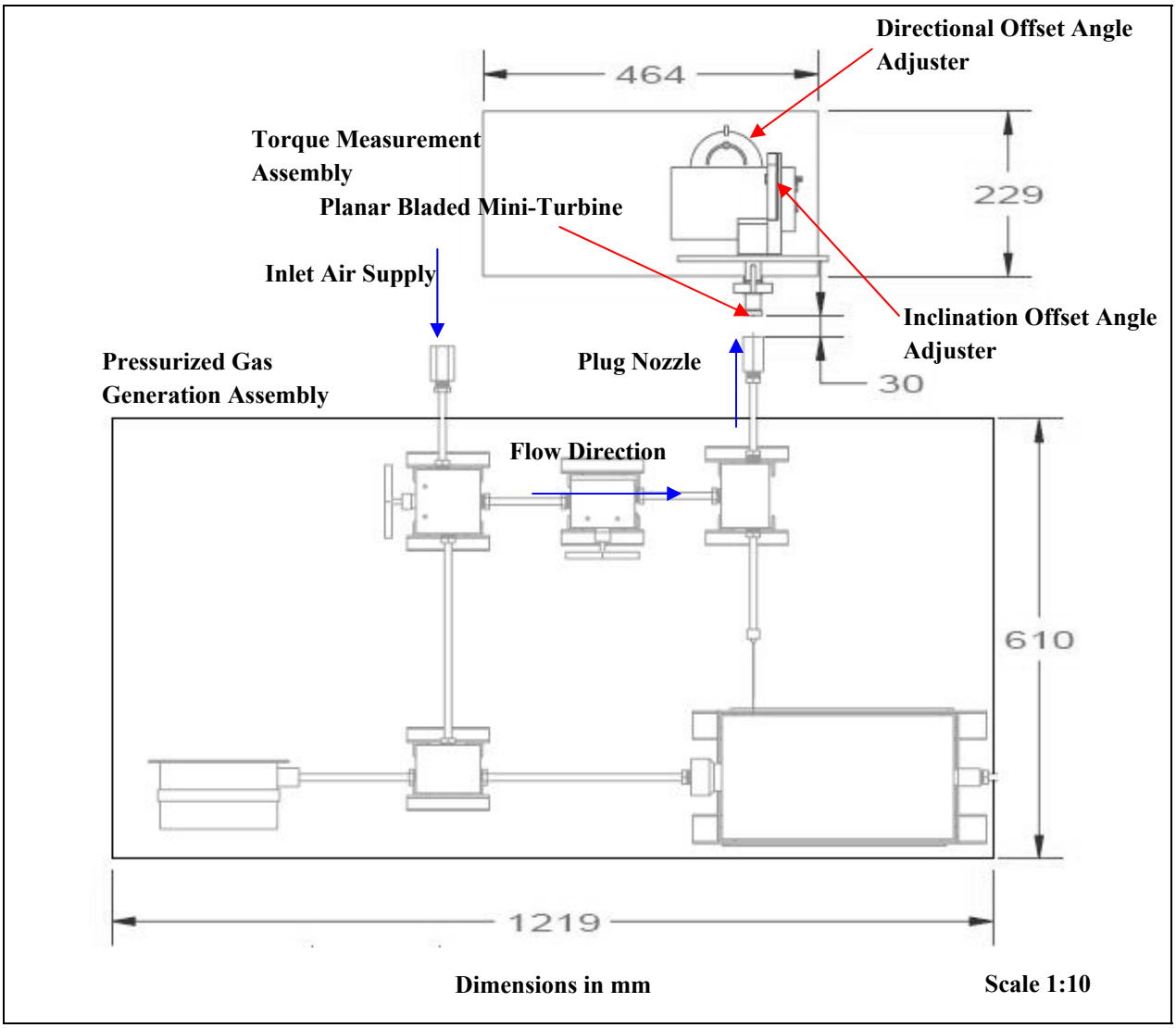

Figure 5.21 Top View CAD Diagram of the Torque Measurement Assembly and Gas Generator Assembly (Scale 1:10).

The torque measurement assembly was also used to hold the mini-turbine in place such that the position of the turbine could be varied with respect to the nozzle jet flow. The mini-turbine was varied in axial distance, radial distance, inclination angle and directional angle relative to the nozzle exit jet flow centerline for each of the experimental runs described in Section 5.7.1. The inclination angle and directional angle

could be varied with the help of the movable assembly and an angle finder attached to the adjustable parts of the assembly.

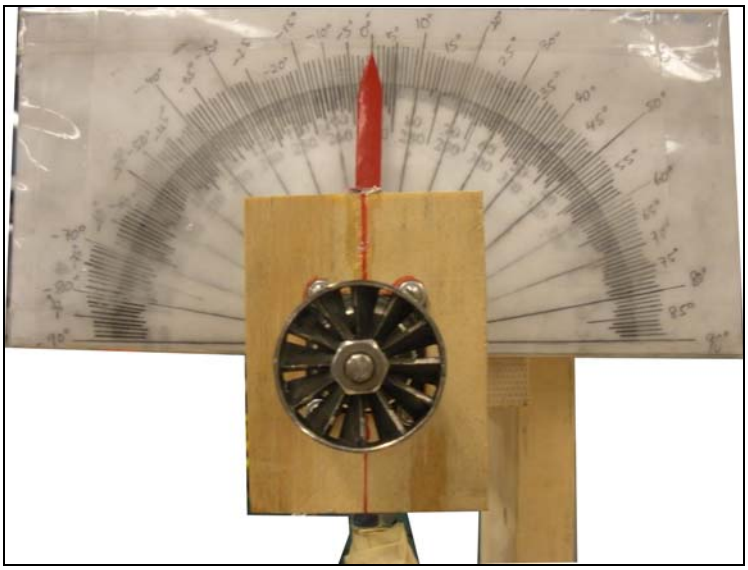

Figure 5.22 Digital Photograph of the Front View of the Torque Swing Assembly with Mini-Turbine Attached Showing Angular Scale.

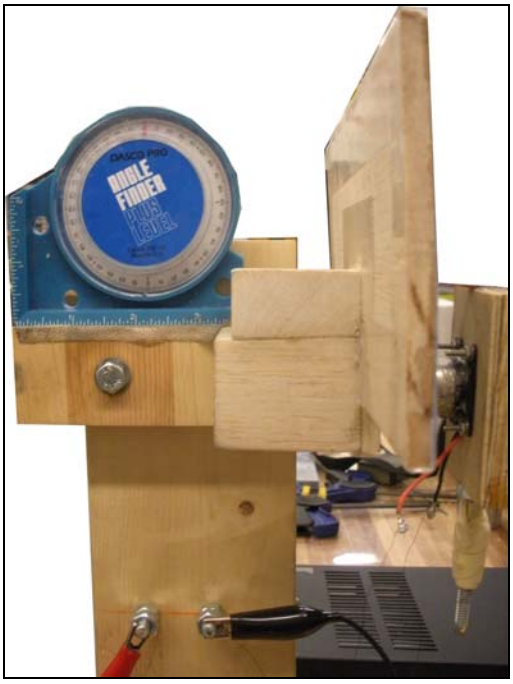

Figure 5.23 Vertical Offset Angle Adjustment Device Side View Taken with a Digital Camera.

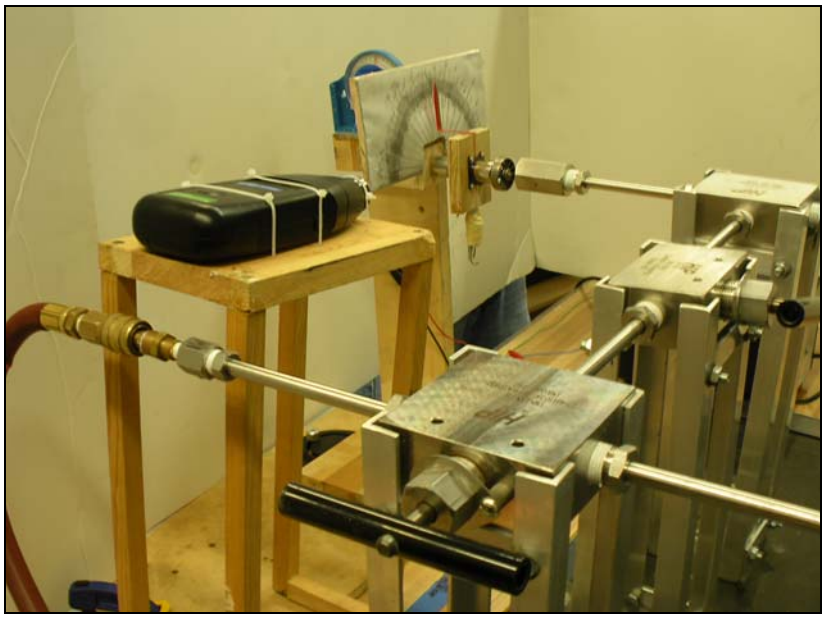

Figure 5.24 Off-axis View of the Ejector Nozzle, Torque Swing Assembly and Photo Tachometer.

5.6 Focusing Shadowgraph Flow Visualization

Figure 5.25 shows the setup for the shadowgraph visualization of the shock structure that was present in the supersonic jet exhausting into still air from the ejector nozzle. Figure 5.26 shows a photographic representation of the visualization setup. The Nikon digital SLR camera was fitted with a NIKKOR 60 mm macro focusing lens and placed behind a 75 mm focal length convex lens for the setup. The 75 mm focal length optical convex lens was used to magnify the miniature size of the image from the supersonic jet of micro dimensions. This lens was placed behind the jet stream during experimentation as shown in Figure 5.26.

A single light source was placed at a distance in front of the convex lens and aimed such that a parallel beam of light rays would pass through the flow field emanating from the ejector nozzle. The size of the image captured was limited to the overall diameter of the

convex lens. To capture the image focused by the camera, the macro lens had to be adjusted such that a clear image was visualized by the camera's focus. In addition, the convex lens used for magnification had to be adjusted on a slider beam to focus a clear magnified image that was approximately twice the size of the real image. A series of trial and error procedures had to be taken in order to visualize the supersonic jet and the shock structure that existed in the flow. A general outline of the steps taken in order to capture the supersonic jet visualized was as follows:

1. Pressurized air supply was connected to the inlet supply port of the gas generation assembly.

2. Pressurized air flowed to the ejector nozzle shown in Figure 5.26.

3. The pressurized gas exits the nozzle at supersonic speeds and the jet contains a visible shock structure.

4. The shock structure present in the supersonic jet could be visualized by the human eye using the 75 mm convex lens. This lens provided a magnified image of the shock structure.

5. The beam of light from the single light source was aimed directly at the ejector nozzle exit.

6. The observer focused on the supersonic jet using the convex lens and adjusted the focus of the image by sliding the lens holder forward and back over the slider beam.

7. By trial an error, the observer should be able to find and focus on the image of the supersonic jet. At this point, the convex lens position on the slider beam would be fixed.

8. The supersonic jet could be captured using the digital SLR camera. The camera was placed on a tripod stand behind the convex lens and the image was displayed on the LCD screen of the camera.

9. The macro lens of the camera was then adjusted such that a clear image would be present and focused on the LCD display. Still photographs and movies were then taken for the supersonic jet with flow exhausting into still air at three different nozzle area configurations.

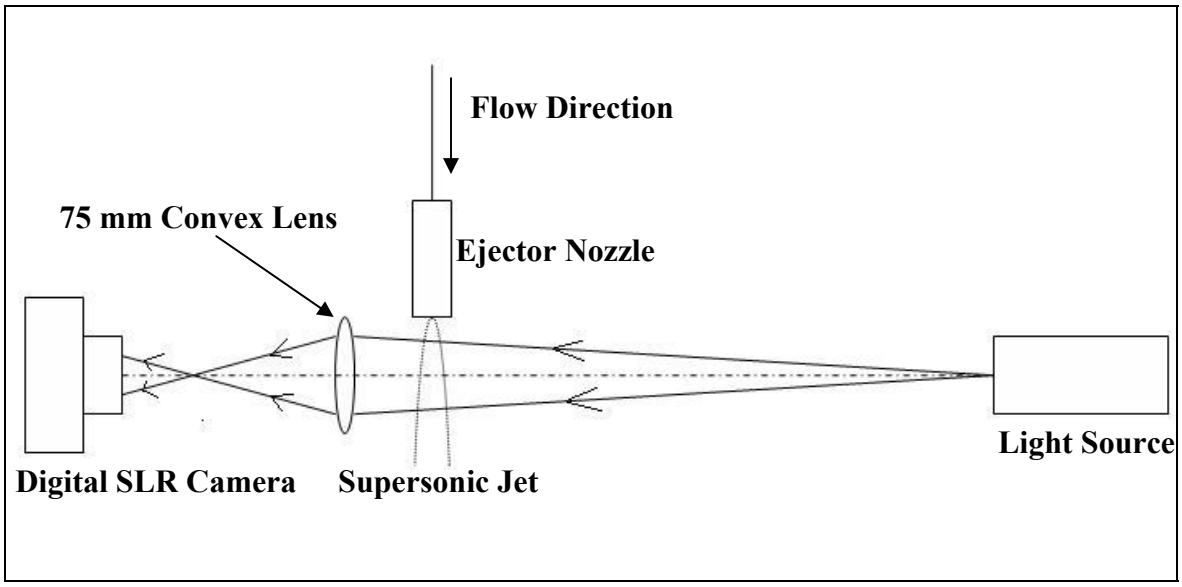

Figure 5.25 Schematic Diagram of the Shadowgraph Visualization Setup Used During Experimentation.

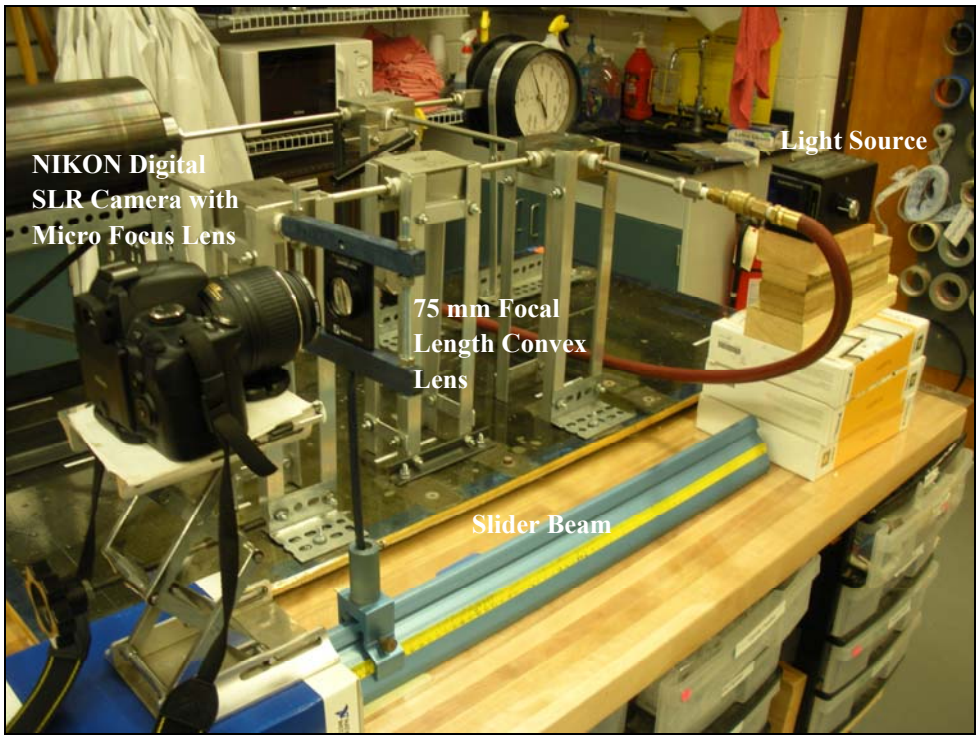

Figure 5.26 Digital Image of the Shadowgraph Visualization Setup for the Supersonic Jet from the Ejector Nozzle.

5.7 Data Measurements

5.7.1 Experimentation Run Configurations

In the current investigation, a total of 10 different turbine positions relative to the nozzle exit orifice were considered. For each of the run configurations, the mini-turbine was placed in front of the ejector nozzle in the supersonic jet stream at specified axial, lateral and vertical offset distances measured from the nozzle exit. Also, inclination angle offset and directional angle offset for the mini-turbine relative to the nozzle exit jet flow centerline axis were tested. The coordinate system and angle definitions for the various experimental configuration runs were defined in the following table. Figure 5.27 through 5.30 shows the defined coordinate system for the experimental configuration runs.

Table 5.7 Coordinate System and Angle Definitions for Experimental Configurations.

Coordinate/ Angle	Definition
x/D_e	Lateral distance offset of planar bladed mini-turbine centerline measured from ejector nozzle exit centerline in terms of nozzle exit diameter.
y/D_e	Axial distance offset of planar bladed mini-turbine face measured from ejector nozzle exit face in terms of nozzle exit diameter.
z/D_e	Vertical distance offset of planar bladed turbine centerline measured from ejector nozzle exit centerline in terms of nozzle exit diameter.
α	Inclination angle offset of planar bladed mini-turbine centerline measured from ejector nozzle exit centerline.
β	Directional angle offset of planar bladed mini-turbine centerline measured from ejector nozzle exit centerline.

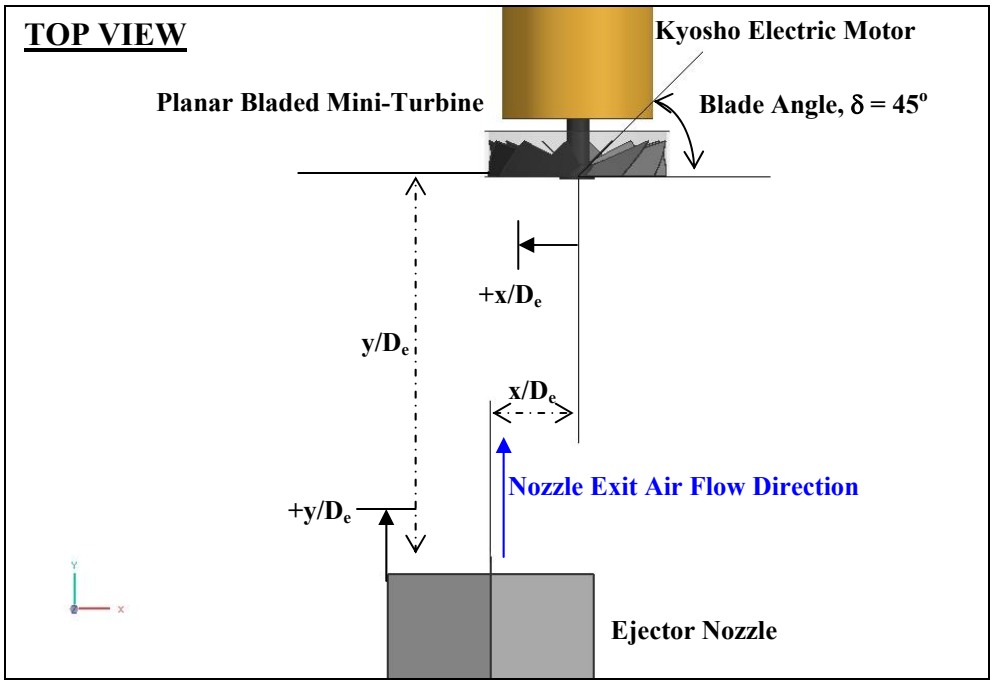

Figure 5.27 Top view of Experimental Setup Showing Coordinate System.

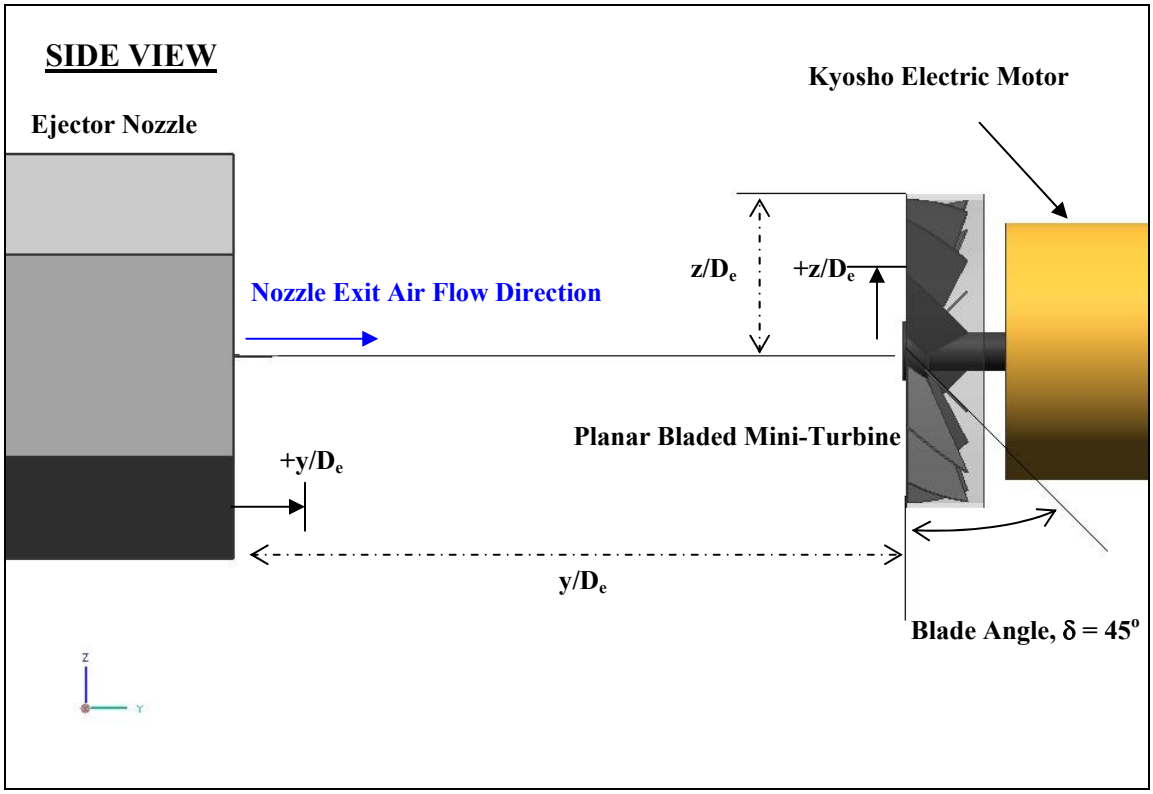

Figure 5.28 Side view of Experimental Setup Showing Coordinate System.

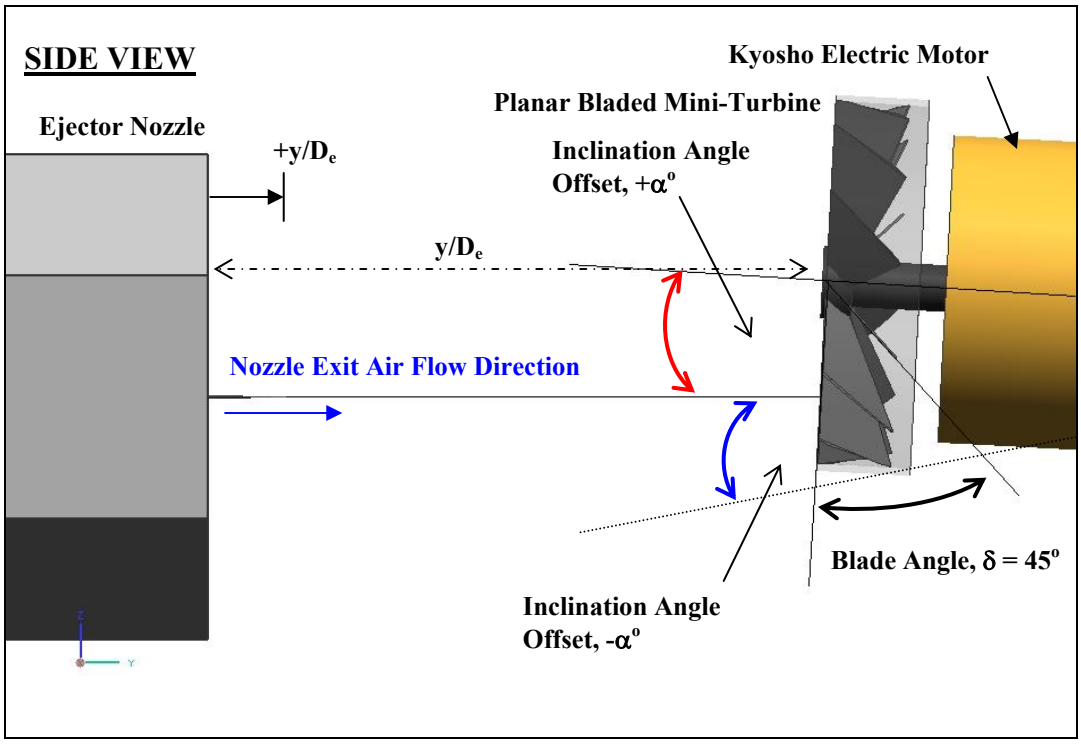

Figure 5.29 Side view of Experimental Setup Showing Coordinate System with Angular Offset.

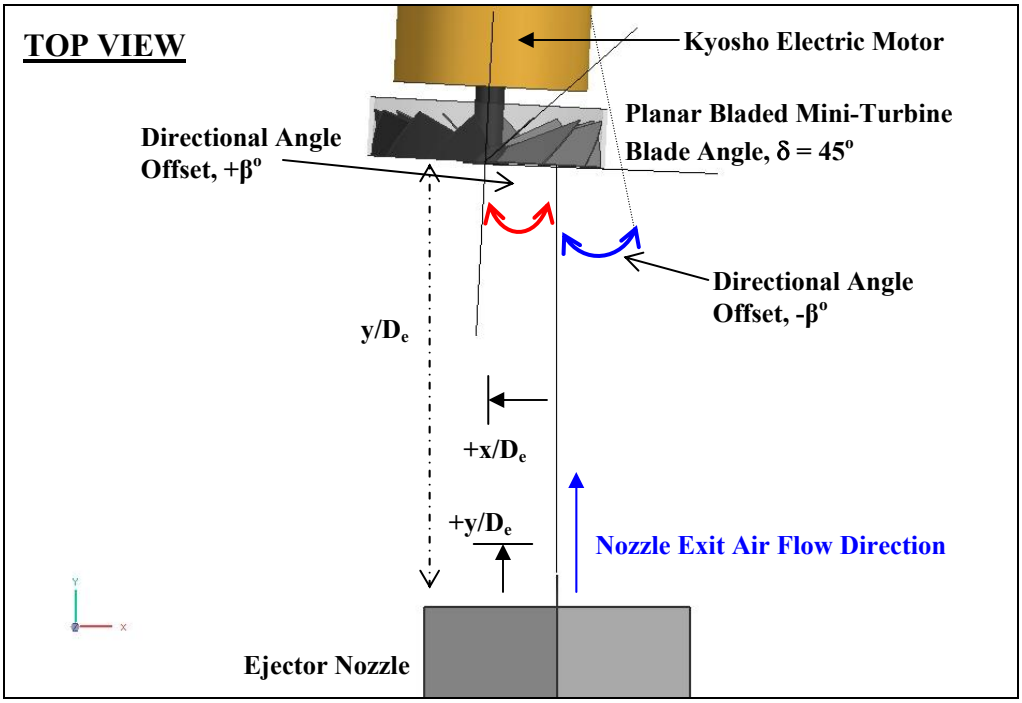

Figure 5.30 Top view of Experimental Setup Showing Coordinate System with Angular Offset.

Each experimental configuration run was set up and three axial distance offset, y, were selected for the current investigation and in terms of nozzle diameters were y/D_e = 11.2, 29.1 and 46.8, respectively (for D_e = 0.711 mm, See Appendix B for D_e = 0.616 mm and D_e = 0.503 mm). Table 5.8 through 5.10 below tabulates the various test configurations that were set up for the experimental runs. Figures 5.31 through 5.40 provide schematic diagrams representing the information summarized in the following tables.

Table 5.8 Coordinates, Offset Distances and Offset Angles Defined Matrix for Experimental Runs 1 through 10 with Planar Bladed Mini-Turbine Fixed at a distance of y/D_e = 11.2 from Ejector Nozzle Face (D_e = 0.711 mm).

Variables	Experimental Runs									
	1	2	3	4	5	6	7	8	9	10
x/D_e	18.0	9.02	0	0	0	0	0	0	0	0
y/D_e	11.2	11.2	11.2	11.2	11.2	11.2	11.2	11.2	11.2	11.2
z/D_e	0	0	0	0	0	0	0	0	0	0
α (deg)	0	0	-3	-1.5	3	1.5	0	0	0	0
β (deg)	0	0	0	0	0	0	2.5	1	-2.5	-1

Table 5.9 Coordinates, Offset Distances and Offset Angles Defined Matrix for Experimental Runs 1 through 10 with Planar Bladed Mini-Turbine Fixed at a distance of y/D_e = 29.1 from Ejector Nozzle Face (D_e = 0.711 mm).

Variables	Experimental Runs									
	1	2	3	4	5	6	7	8	9	10
x/D_e	18.0	9.02	0	0	0	0	0	0	0	0
y/D_e	29.1	29.1	29.1	29.1	29.1	29.1	29.1	29.1	29.1	29.1
z/D_e	0	0	0	0	0	0	0	0	0	0
α (deg)	0	0	-3	-1.5	3	1.5	0	0	0	0
β (deg)	0	0	0	0	0	0	2.5	1	-2.5	-1

Table 5.10 Coordinates, Offset Distances and Offset Angles Defined Matrix for Experimental Runs 1 through 10 with Planar Bladed Mini-Turbine Fixed at a distance of $y/D_e = 46.8$ from Ejector Nozzle Face ($D_e = 0.711$ mm).

Variables	Experimental Runs									
	1	2	3	4	5	6	7	8	9	10
x/D_e	18.0	9.02	0	0	0	0	0	0	0	0
y/D_e	46.8	46.8	46.8	46.8	46.8	46.8	46.8	46.8	46.8	46.8
z/D_e	0	0	0	0	0	0	0	0	0	0
α (deg)	0	0	-3	-1.5	3	1.5	0	0	0	0
β (deg)	0	0	0	0	0	0	2.5	1	-2.5	-1

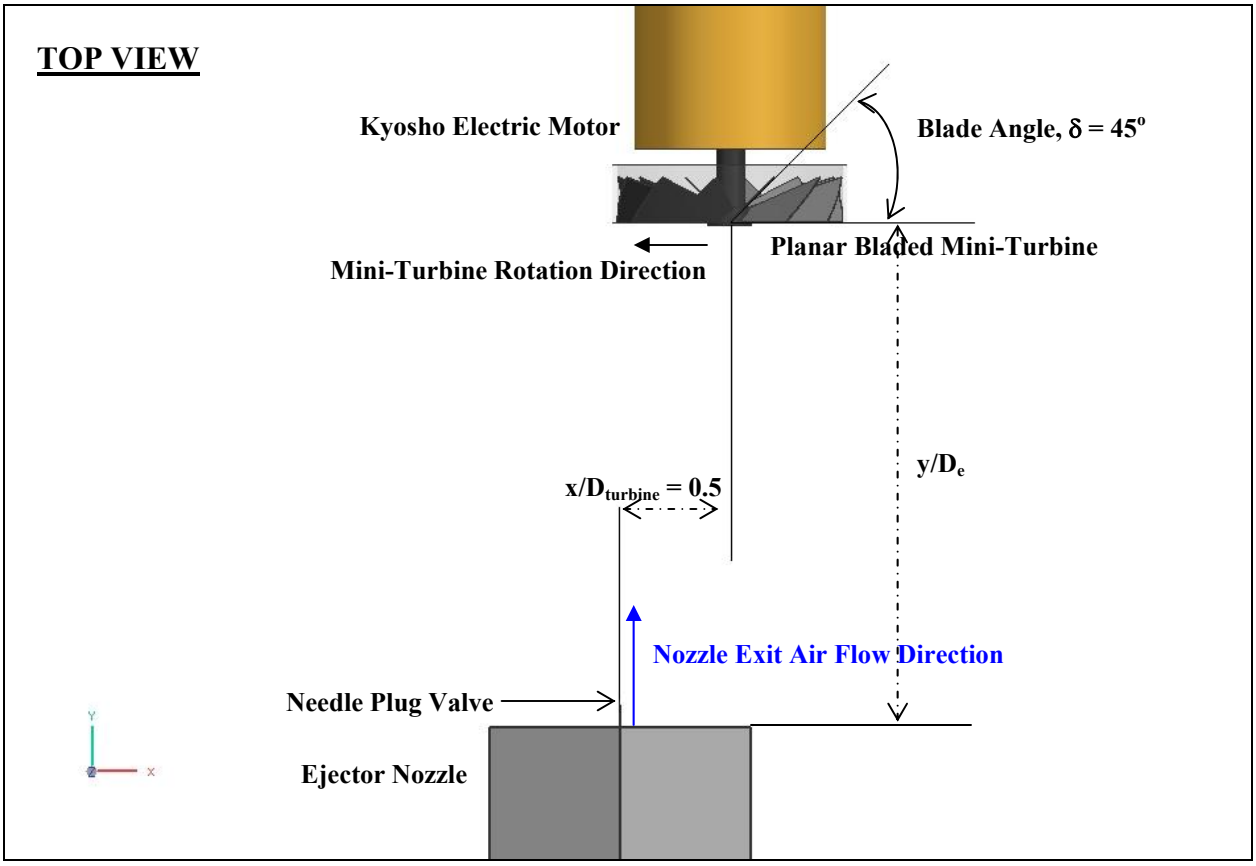

Figure 5.31 CAD Diagram to Show the Geometric Constraints of Run 1.

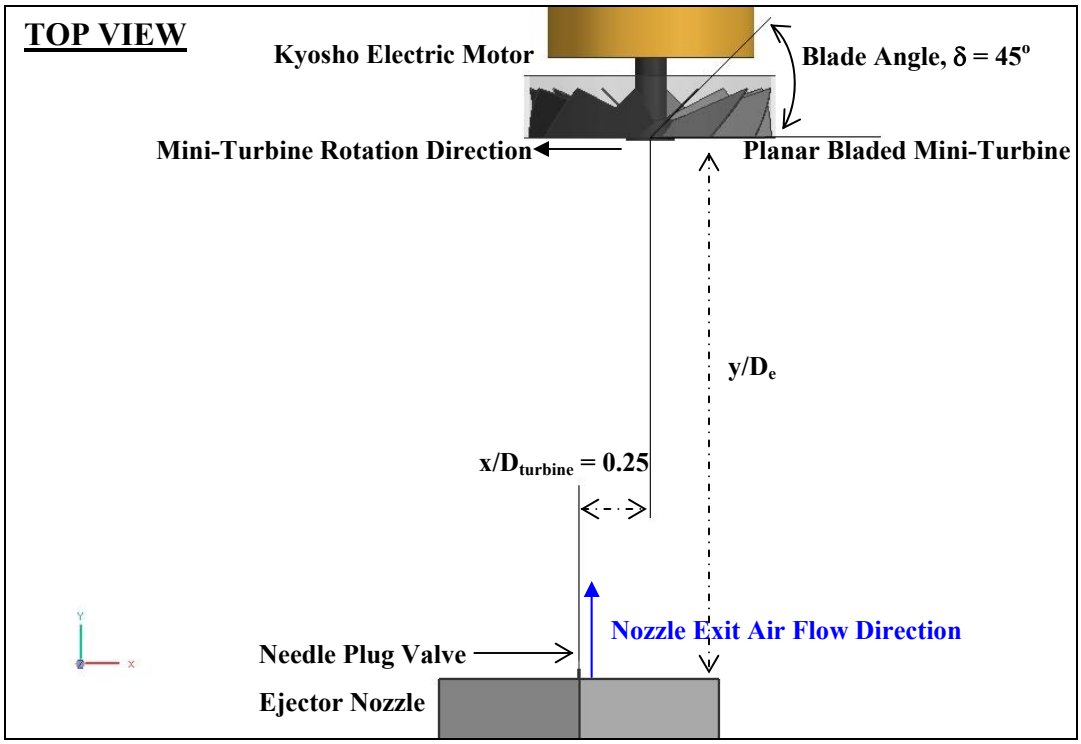

Figure 5.32 CAD Diagram to Show the Geometric Constraints of Run 2.

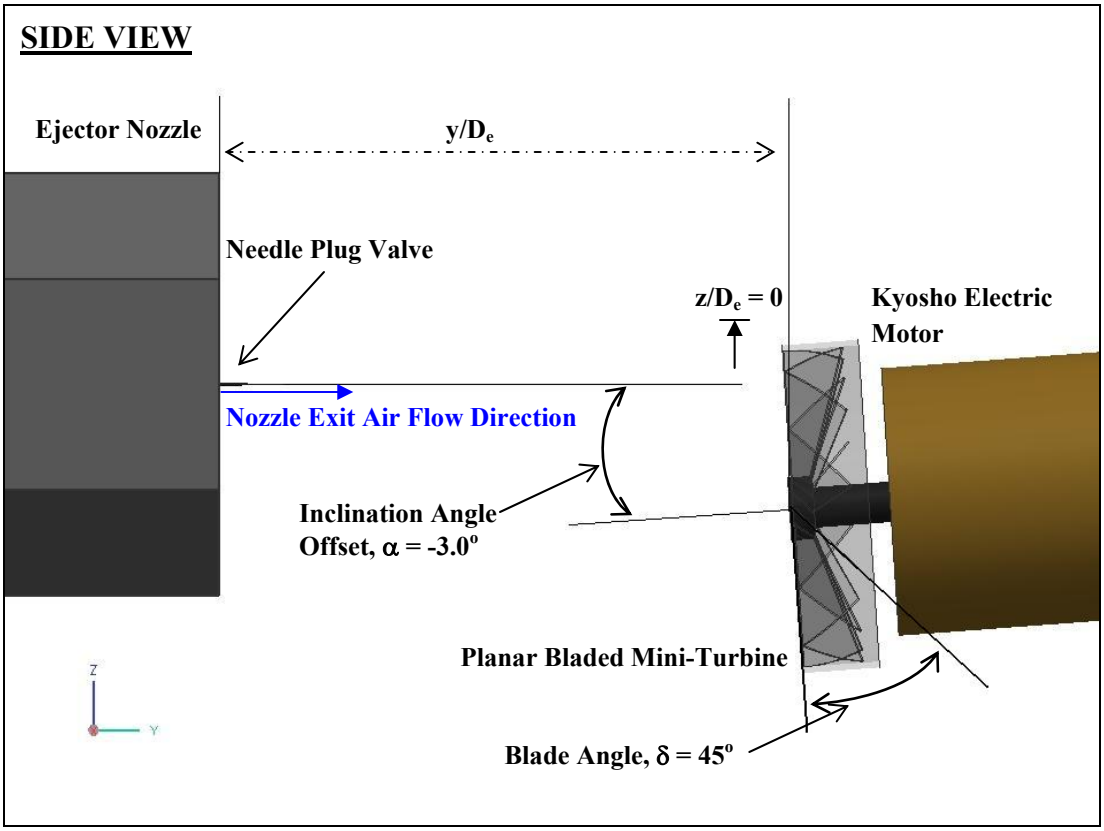

Figure 5.33 CAD Diagram to Show the Geometric Constraints of Run 3.

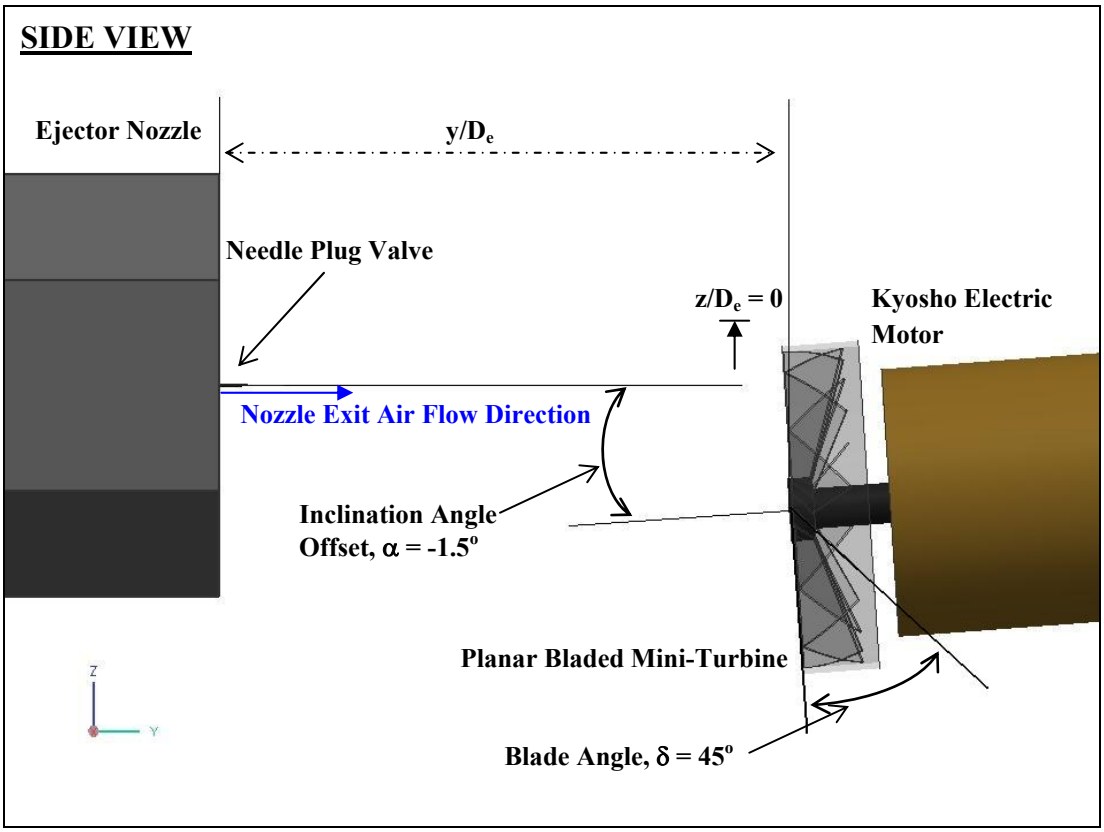

Figure 5.34 CAD Diagram to Show the Geometric Constraints of Run 4.

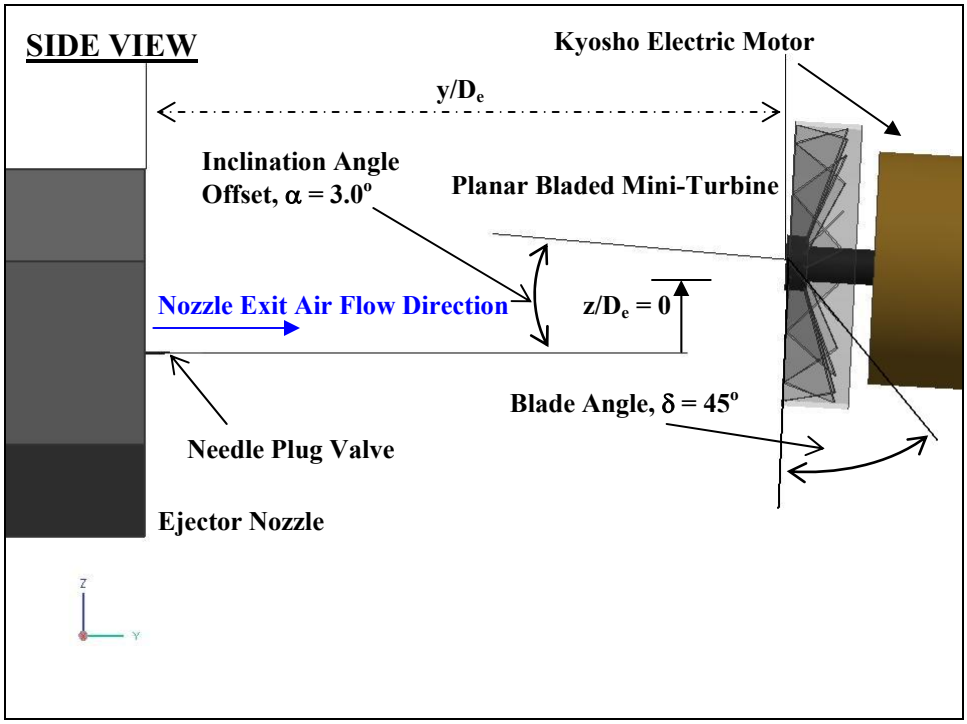

Figure 5.35 CAD Diagram to Show the Geometric Constraints of Run 5.

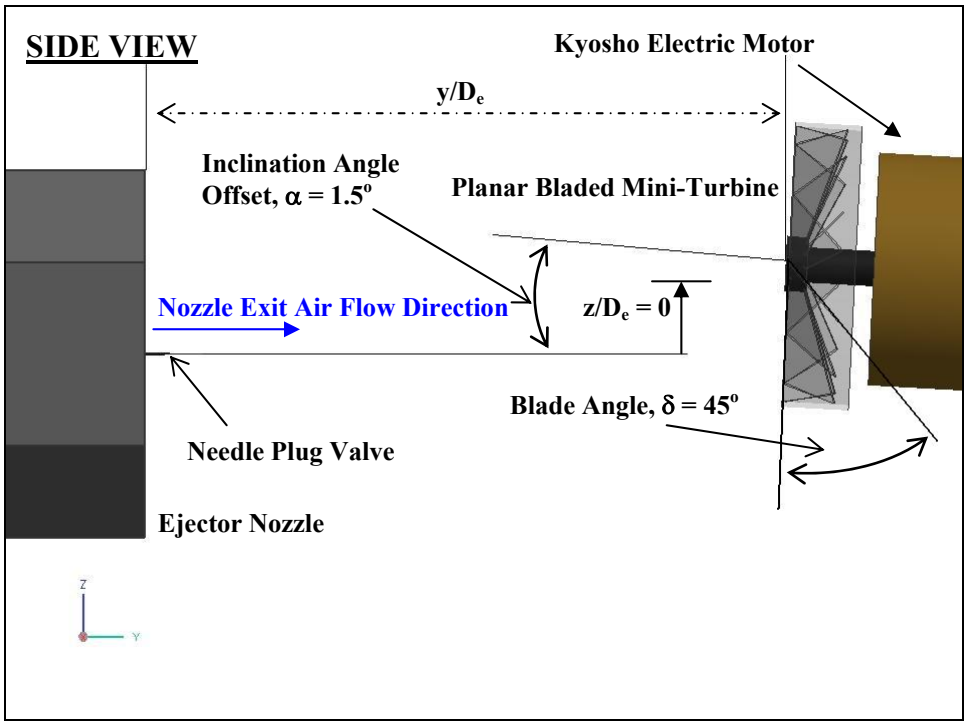

Figure 5.36 CAD Diagram to Show the Geometric Constraints of Run 6.

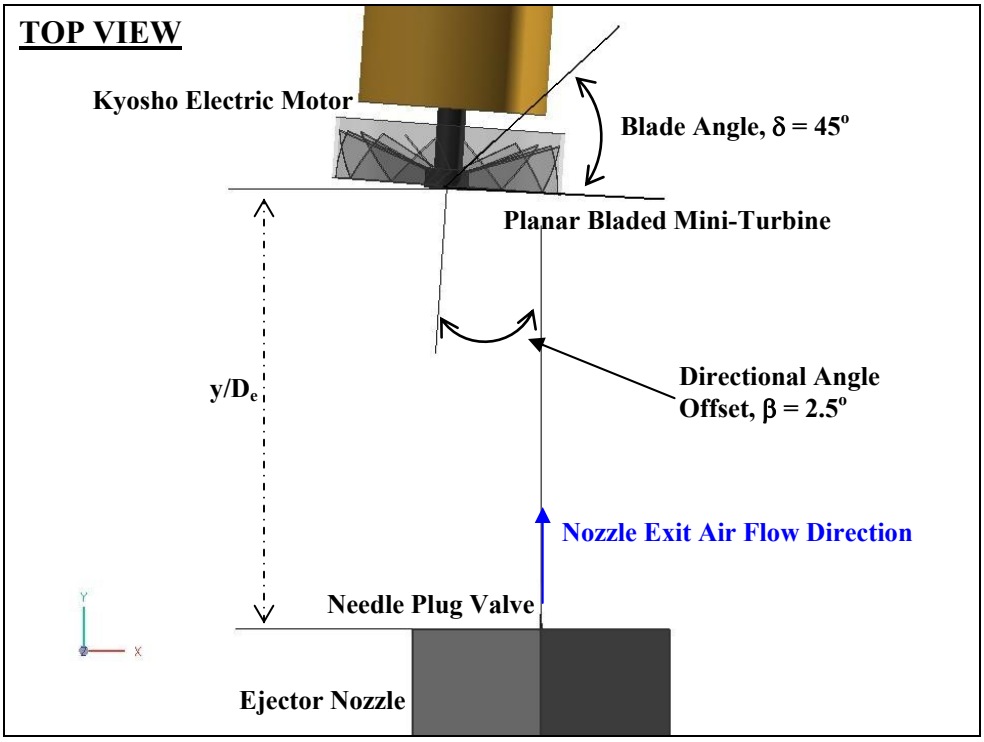

Figure 5.37 CAD Diagram to Show the Geometric Constraints of Run 7.

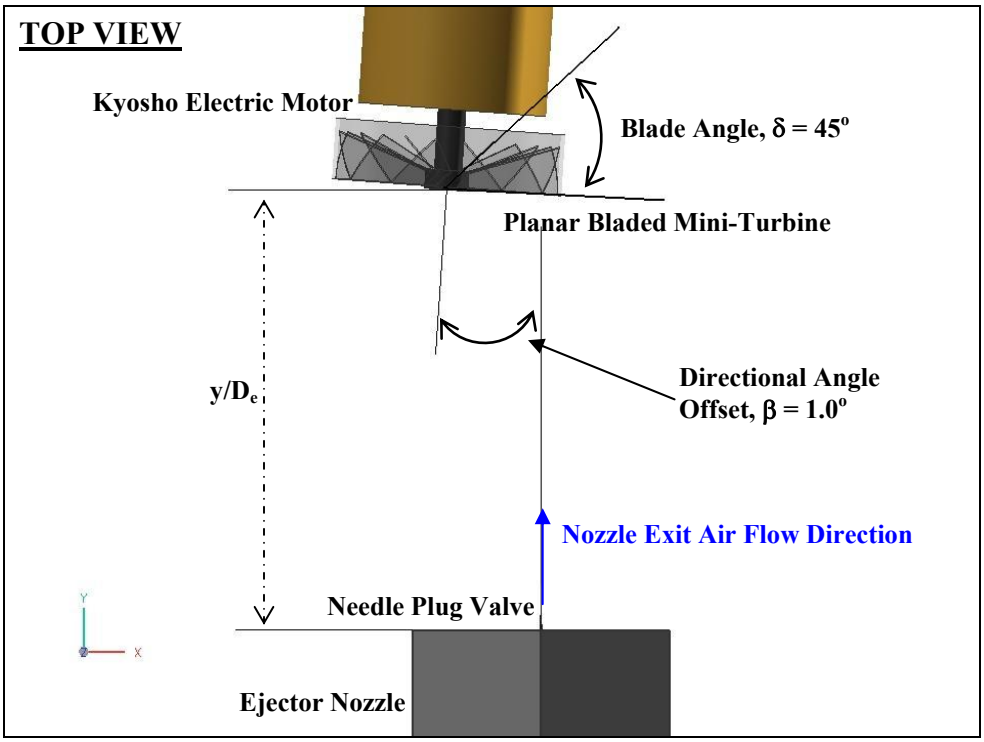

Figure 5.38 CAD Diagram to Show the Geometric Constraints of Run 8.

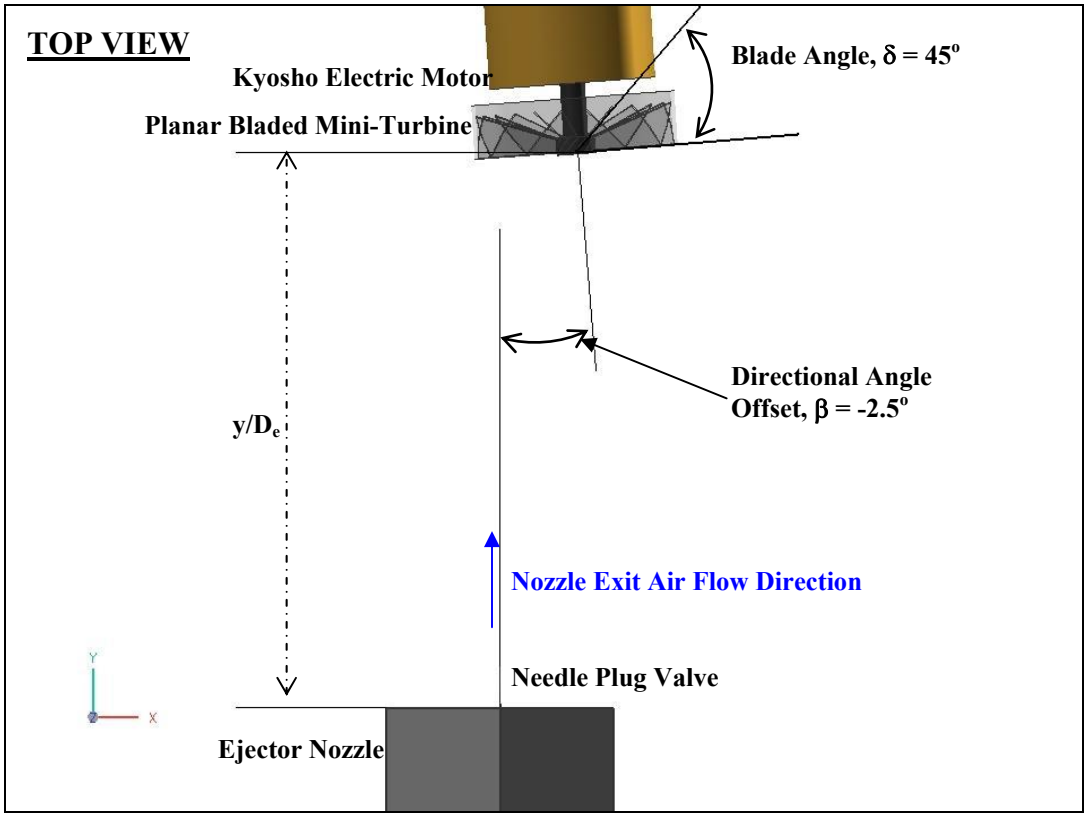

Figure 5.39 CAD Diagram to Show the Geometric Constraints of Run 9.

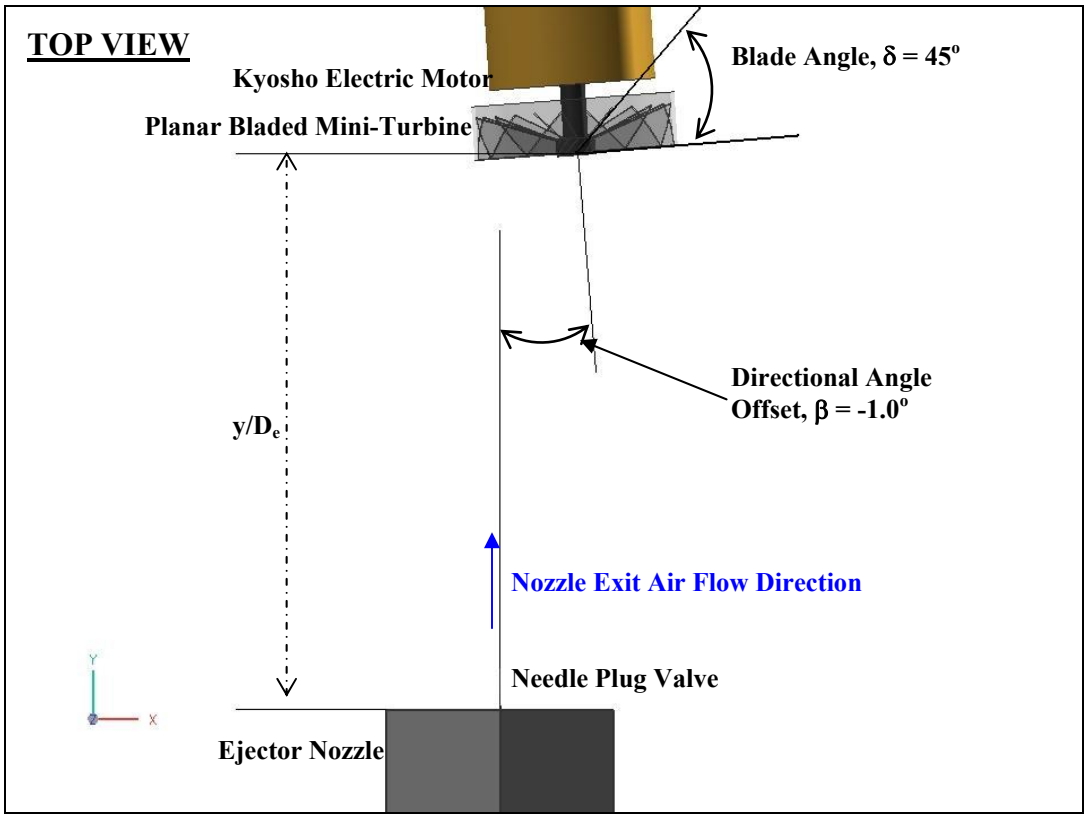

Figure 5.40 CAD Diagram to Show the Geometric Constraints of Run 10.

5.7.2 Ejector Nozzle Configurations

An additional study was performed for the current investigation to determine the effect of varying nozzle exit area on the amount of mechanical shaft power developed by the mini-turbine and the aero-mechanical efficiency of the power converted from fluid aerodynamic power to shaft power. Three nozzle area configurations were selected and the experimental configuration runs were performed for each of the nozzle exit areas selected.

The ejector nozzle exit area was varied using a screw-head mechanism which allowed the needle plug valve to travel inwards and outwards of the nozzle exit face. The

needle plug valve moves inside the ejector nozzle from a fully closed to fully opened position. This allowed for the variation of nozzle exit areas to perform a trade study of the effect of a fully opened nozzle exit area, 75% of the fully opened nozzle exit area and 50% of the fully opened nozzle exit area.

The nozzle exit areas performed in the current investigation were:

- $A_{nominal} = 0.397\ \mu m^2$, $D_e = 0.711$ mm
- $0.75*A_{nominal} = 0.298\ \mu m^2$, $D_e = 0.616$ mm
- $0.5*A_{nominal} = 0.199\ \mu m^2$, $D_e = 0.503$ mm

The experimental configuration test matrix defined for nozzle exit areas of $0.75*A_{nominal}$ and $0.5*A_{nominal}$ are given in Appendix B (Tables B91 through B96).

5.7.3 Experimental Procedures

The step-by-step procedures for operation of the pressurized gas generation assembly which provide nozzle exit air flow, instrumentation and testing procedures are presented as follows (See Figure below for reference):

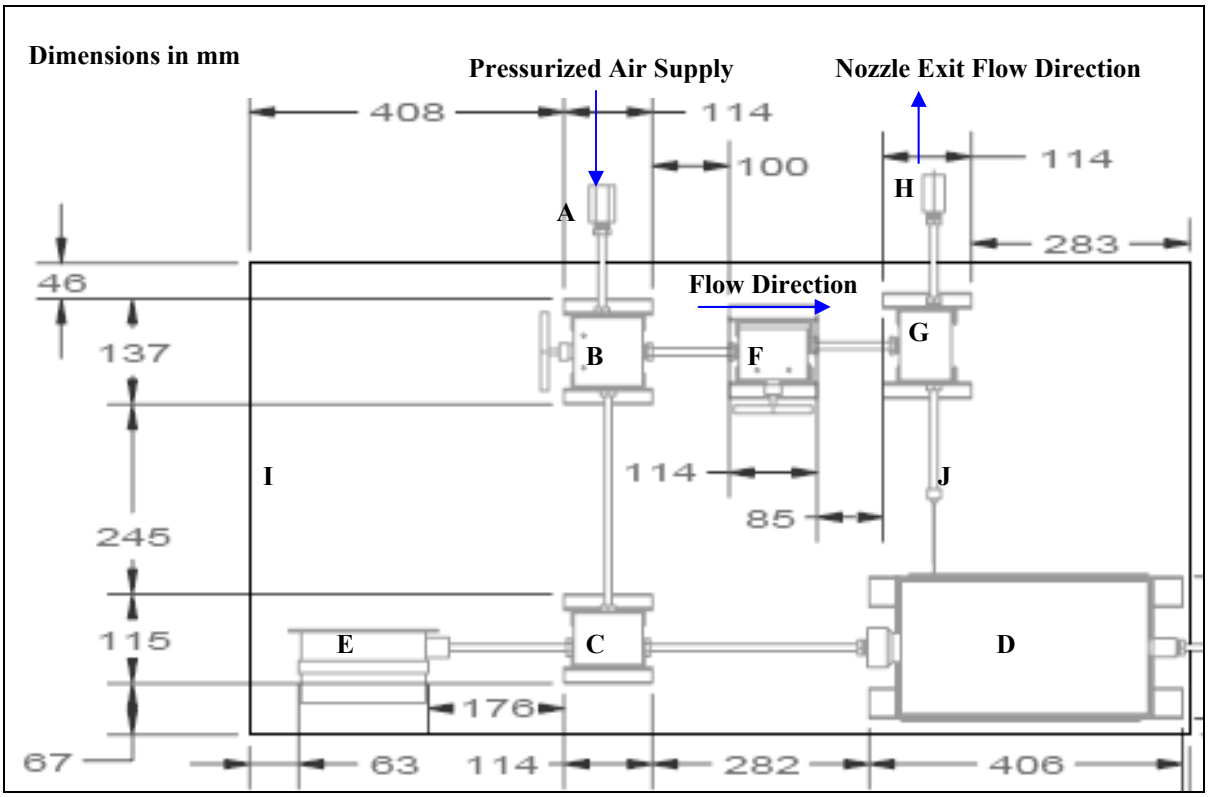

Figure 5.41 Pressurized Gas Generation Assembly.

Step 1: The compressed air supply outlet in the Adaptive Aerostructures Laboratory was located. The air supply valve was opened to its fully opened position.

Step 2: The air supply hose was unreeled and directed towards the pressurized gas generation assembly.

Step 3: The air supply hose was connected to the digital pressure gauge fitted with a male hose adapter so that the pressure of compressed air in the supply line was measured. Once the reading in the display was stable and recorded, the supply hose could be disconnected.

Step 4: The valves at B and F were in its fully closed position. The needle plug valve at the ejector nozzle exit should fully obstruct air from exhausting through the ejector nozzle.

Step 5: As shown in Figure 5.42, the female hose connection of the air supply hose was connected to the male connection adapter of the assembly at A.

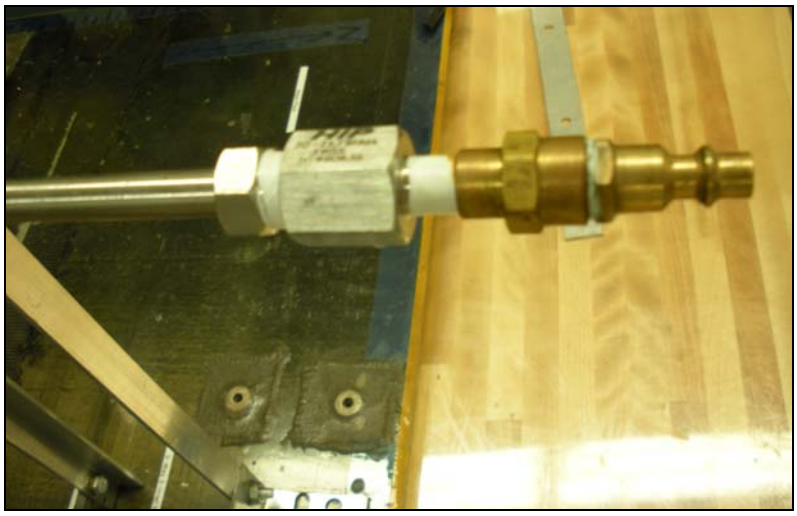

Figure 5.42 Male Connection Adapter for Pressurized Air Supply Connection.

Step 6: The three way valve at B was opened fully to allow maximum air supply to enter the assembly and flow from B to F.

Step 7: The two way straight valve at F was opened fully to let pressurized air to flow into the tee-fitting connection at G.

Step 8: From the fully closed position of the needle plug valve, the ejector nozzle exit would be opened to allow maximum air to flow out of the ejector nozzle using the turn screw mechanism at J.

Step 9: The nozzle flow exit static temperature was measured using the non-contact infrared thermometer. The guiding laser light on the device was directed at and as close as possible to the ejector nozzle exit at H. The static temperature was then measured.

Step 10: The torque measurement assembly was placed directly in the supersonic jet stream and positioned such that the mini-turbine centerline is aligned to the nozzle exit centerline.

Step 11: The torque measurement assembly was carefully positioned according to the coordinates and angle offset corresponding to Experimental Configuration Run 1.

Step 12: The non-contact photo-tachometer was placed at a distance of 150 mm from the mini-turbine. The field range of the tachometer was checked to ensure that it was directed to the outer surface of the turbine shroud.

Step 13: The DC power supply was connected to the bolt terminals using alligator clips for DC power supply current to the electric motor attached to the mini-turbine on the torque measurement assembly.

Step 14: The angle deflected by the angular displacement dial on the wooden block of the swing arm assembly was observed.

Step 15: The DC supply generator was powered up.

Step 16: The voltage supply dial was then turned to the middle position on the generator.

Step 17: The current supply dial of the power supply generator was then turned and the electric motor would operate as the amount of current supplied increased or decreased.

Step 18: The direction of rotation for the electric motor shaft was opposite to the direction of rotation for the mini-turbine when it was exposed to the supersonic jet flow at the ejector nozzle exit.

Step 19: As the current supply was increased to the electric motor, there was an observed point when the electric motor shaft torque was balanced with the torque of the mini-turbine. The mini-turbine did not have any rotational speed and the angular displacement dial would be deflected to give a deflection angle reading.

Step 20: With a 20g mass placed on the swing arm rod, the mass was positioned along the rod such that a reasonable angle deflection was observed. The location was marked as the moment arm for the counter rotating torque displacing the specified mass.

Step 21: Measurements for the current experimental configuration run were made when the current supply to the electric motor was slowly increased to produce one degree in angular deflection that was read off the angle scale on the torque measurement assembly.

Step 22: The rotational speed, RPM, of the mini-turbine was then recorded from the photo tachometer.

Step 23: The current supply was then increased again and another one degree of angular deflection was observed. The RPM of the mini-turbine was recorded at this point.

Step 24: The angle deflections of the angular displacement dial and mini-turbine rotational speed were recorded.

Step 25: Steps 21 through 24 were repeated to obtain a range of angular deflections as a variation of the mini-turbine rotational speed.

Step 26: Steps 21 and 24 were discontinued once the current supply to the electric motor had reached its maximum.

Step 27: The current supply to the electric motor was gradually decreased.

Step 28: Once the electric motor was switched off, the ejector nozzle exit could be returned to its fully closed position by turning the needle plug valve using the turn screw mechanism at J.

Step 29: The DC power supply generator was then switched off and the air supply hose connected to the pressurized gas generation assembly was disconnected.

Step 30: The valves at B and F were returned to its fully closed position.

Step 31: The procedures described in Steps 3 through 30 were then repeated for Experimental Configuration Runs 2 through 10.

Step 32: The axial distance of the torque measurement assembly from the ejector nozzle exit remained fixed.

Step 33: The nozzle exit area was then set to 75% of the fully opened nozzle exit area.

Step 34: Procedures in Steps 3 through 31 were repeated to determine the rotational speed variation of the mini-turbine in relation to the amount of torque generated (in terms of angular displacement of the swing arm) for each of the experimental runs.

Step 35: The nozzle exit area was then set to 50% of the fully opened nozzle exit area.

Step 36: Procedures in Steps 3 through 31 were repeated to determine the rotational speed variation of the mini-turbine in relation to the amount of torque generated (in terms of angular displacement of the swing arm) for each of the experimental runs.

Step 37: After data was measured and recorded for all of the experimental configurations specified, the torque measurement assembly was moved back by 12.7 mm.

Step 38: Steps 3 through 36 were repeated for Experimental Configuration Runs 1 through 10. The variation of angle deflections of the angular displacement dial with the mini-turbine rotational speed was determined for each run.

Step 39: After data was measured and recorded for Step 38, the torque measurement assembly was moved back by another 12.7 mm.

Step 40: Steps 3 through 36 were repeated for Experimental Configuration Runs 1 through 10. The variation of angle deflections of the angular displacement dial with the mini-turbine rotational speed was determined for each run.

Step 41: Once the data to be recorded was complete, a final check was performed to ensure that the DC power supply generator was switched off and the air supply hose connected to the pressurized gas generation assembly was disconnected.

Step 42: The compressed air supply hose was then returned to its original location in the laboratory.

Step 43: The valves at B and F were checked to ensure that they were turned back to its fully closed position. The needle plug valve should also be returned to the fully closed position.

5.7.4 Data Reduction

The data recorded from the experimental tests for the current study were tabulated and the raw data were presented in Appendix B. The deflection angle of the angular dial and the rotational speed of the mini-turbine were mapped for each experimental configuration run. The deflection angle was measured in degrees and the rotational speed was recorded in revolutions per minute. The recorded data for each experimental configuration run was tabulated in Microsoft Excel and an analysis was performed using the underlying theory described in Chapter 4 and Equations 5.1 and 5.2 to determine shaft torque of the mini-turbine presented in Section 5.5.

For one rotational speed of the mini-turbine recorded, the corresponding deflection angle measured was applied to Eq. 5.1 to determine the shaft torque. The shaft power developed by the rotational motion of the mini-turbine was calculated using Eq. 5.2:

$$Q_{turbine}\left(N \cdot m\right) = W \times d \cdot \sin\theta \qquad \text{(Eq. 5.1)}$$

$$\wp_{turbine} = Q_{turbine} \cdot \omega_{turbine} \qquad \text{(Eq. 5.2)}$$

For each experimental configuration, the inlet supply pressure was measured using the digital pressure gauge and the nozzle exit static temperature was measured using the handheld infrared thermometer. These parameters were defined as p_{t1} and T_2, respectively. The gas properties, mass flow rate and fluid aerodynamic power of the nozzle exit gas flow was determined using the equations previously described in Chapter 4. The reader is referred to Appendix C for detailed representative hand calculations of the fluid aerodynamic power for each of the experimental configuration runs. The following equations with assumption that air was modeled as a perfect gas and the process of gas expansion was isentropic were used:

$$\frac{T_t}{T^*} = \left(\frac{\gamma+1}{2}\right) \qquad \text{(Eq. 4.5)}$$

$$\frac{p_t}{p^*} = \left(\frac{\gamma+1}{2}\right)^{\frac{\gamma}{\gamma-1}} \qquad \text{(Eq. 4.6)}$$

$$\frac{\rho_t}{\rho^*} = \left(\frac{\gamma+1}{2}\right)^{\frac{1}{\gamma-1}} \qquad \text{(Eq. 4.7)}$$

$$\frac{A}{A^*} = \frac{1}{M}\left(\frac{1+\frac{\gamma-1}{2}M^2}{\frac{\gamma+1}{2}}\right)^{\frac{\gamma+1}{2(\gamma-1)}} = \frac{1}{M}\left(\frac{\gamma+1}{2}\left[1+\frac{\gamma-1}{2}M^2\right]\right)^{\frac{\gamma+1}{2(\gamma-1)}} \quad \text{(Eq. 4.15)}$$

$$\dot{m} = \sqrt{\frac{\gamma}{R}}\frac{p_t}{\sqrt{T_t}}C_D A M\left(\frac{1}{1+\frac{\gamma-1}{2}M^2}\right)^{\frac{\gamma+1}{2(\gamma-1)}} \quad \text{(Eq. 4.16)}$$

$$\frac{T_{t_2}}{T_2} = \frac{T_{t_2}}{T^*} = \left(\frac{\gamma+1}{2}\right) \quad \text{(Eq. 4.17)}$$

$$\frac{p_{t_2}}{p_2} = \frac{p_{t_2}}{p^*} = \left(\frac{\gamma+1}{2}\right)^{\frac{\gamma}{\gamma-1}} \quad \text{(Eq. 4.18)}$$

$$\frac{\rho_{t_2}}{\rho_2} = \frac{\rho_t}{\rho^*} = \left(\frac{\gamma+1}{2}\right)^{\frac{1}{\gamma-1}} \quad \text{(Eq. 4.19)}$$

The fluid aerodynamic power of the nozzle exit gas flow was determined as a function of the nozzle exit gas total temperature and mass flow rate. The measure of the efficiency of power conversion was the ratio of the mini-turbine shaft power extracted to fluid aerodynamic power available from the ejector nozzle exit gas flow. Equations 4.20 and 4.22 on the following page were used to determine the fluid power available and the mechanical efficiency of the power conversion for each of the data points collected.

$$\wp_2 = \dot{m}_2 h_{t_2} = \dot{m}_2 c_p T_{t_2} \qquad \text{(Eq. 4.20)}$$

$$\eta_{aero-mech} = \frac{\wp_{shaft}}{\wp_2} = \frac{\wp_{turbine}}{\wp_{aero}} \qquad \text{(Eq. 4.22)}$$

The results from the tabulated data and resulting calculations of Appendix B were then graphed using Excel. The shaft power extracted using the mini-turbine was graphed as a variation of increasing RPM of the mini-turbine. Also, the mechanical efficiency of the power conversion process from fluid aerodynamic power to measured mini-turbine shaft power was plotted against RPM of the mini-turbine. These graphs are presented in Sections 6.1 through 6.10 of Chapter 6.

6.0 EXPERIMENTAL RESULTS AND DISCUSSION

The purpose of this section is to present the experimental results that were performed to measure the shaft torque of the mini-turbine. The experimental equipment to measure mechanical shaft torque generated from the rotational motion of the impulse turbine was setup in 10 different configurations. In each of these configurations, geometrical parameters defining positions of the mini-turbine relative to the nozzle jet centerline axis were varied. Among these parameters were the lateral spatial distance or deviation, the inclination angle deviation and the directional or aiming angle of the turbine face centerline relative to the nozzle exit jet flow centerline. The experimental configurations were detailed in Section 5.7.1. The mechanical shaft power extracted and the aero-mechanical efficiency of power conversion by the mini-turbine were calculated for each experimental run. The results were then used for plots of mechanical turbine shaft power and aero-mechanical efficiency of power conversion against turbine rotational speed.

To study the effect of varying the axial spatial distance of the turbine face from the nozzle exit face on the absolute amount of torque generated on the impulse turbine by the nozzle flow, the torque measurement assembly with the impulse turbine attached was positioned at three different axial distances normalized to the nominal nozzle exit diameter (D_e = 0.711 mm). The non-dimensional parameters for axial spatial distance were:

- $y/D_e = 11.2$,
- $y/D_e = 29.1$,
- $y/D_e = 46.8$

Similarly, the effect of varying the axial spatial distance of the turbine face from the nozzle exit face on the amount of torque generated by the impulse turbine measured was studied for three nozzle exit areas, given as:

- **Case 1:** $A_{nominal} = 0.397\ \mu m^2$, $D_e = 0.711$ mm
- **Case 2:** $0.75*A_{nominal} = 0.298\ \mu m^2$, $D_e = 0.616$ mm
- **Case 3:** $0.5*A_{nominal} = 0.199\ \mu m^2$, $D_e = 0.503$ mm

The normalized axial spatial variations for the other two nozzle exit area cases were:

- **Case 2:** $0.75*A_{nominal} = 0.298\ \mu m^2$, $D_e = 0.616$ mm
  - $y/D_e = 12.9$,
  - $y/D_e = 33.4$,
  - $y/D_e = 54.1$
- **Case 3:** $0.5*A_{nominal} = 0.199 \mu m^2$, $D_e = 0.503$ mm
  - $y/D_e = 15.8$,
  - $y/D_e = 41.0$,
  - $y/D_e = 66.2$

The experimental plots determined for each of the experimental runs carried out in Case 1, Case 2 and Case 3 with axial spatial deviation, inclination and directional angular offset of the mini-turbine relative to the nozzle exit jet centerline are presented in the following sections of this chapter.

6.1 Experimental Results for Determined Mechanical Power Output and Conversion Efficiency

6.1.1 Experimental Results Determined for Run 1 at Various Nozzle Exit Areas and Nozzle Downstream Axial Distances

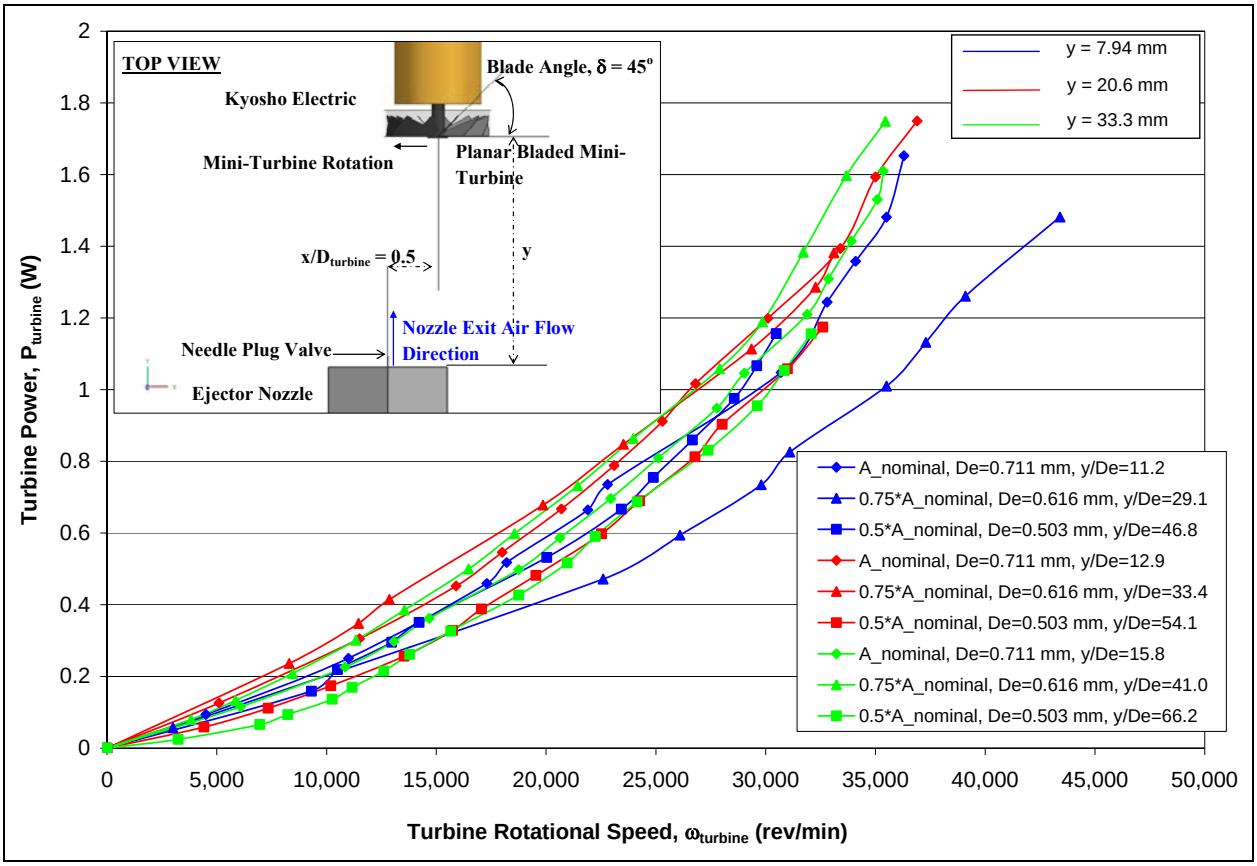

Figure 6.1 Mechanical Turbine Power Extracted at Various Nozzle Exit Area as a function of Turbine RPM (x=12.8 mm, y=(7.94 mm, 20.6 mm & 33.3 mm), z=0 mm, $\alpha=0^o$ & $\beta=0^o$).

Figure 6.1 shows the mini-turbine shaft power as a function of turbine rotational speed for experimental Run 1. The mini-turbine was positioned such that the nozzle jet flow centerline would be directed at the tip of the planar 45° bladed mini-turbine. The non-dimensional parameter for the position of the turbine centerline relative to the nozzle flow centerline described was $x/D_{turbine} = 0.5$. From the results shown in Figure 6.19, it was observed that the

range of maximum turbine mechanical shaft power obtained was approximately 1.75 W. Results also showed that the maximum shaft power extracted increased as the mini-turbine was placed further downstream of the nozzle exit face.

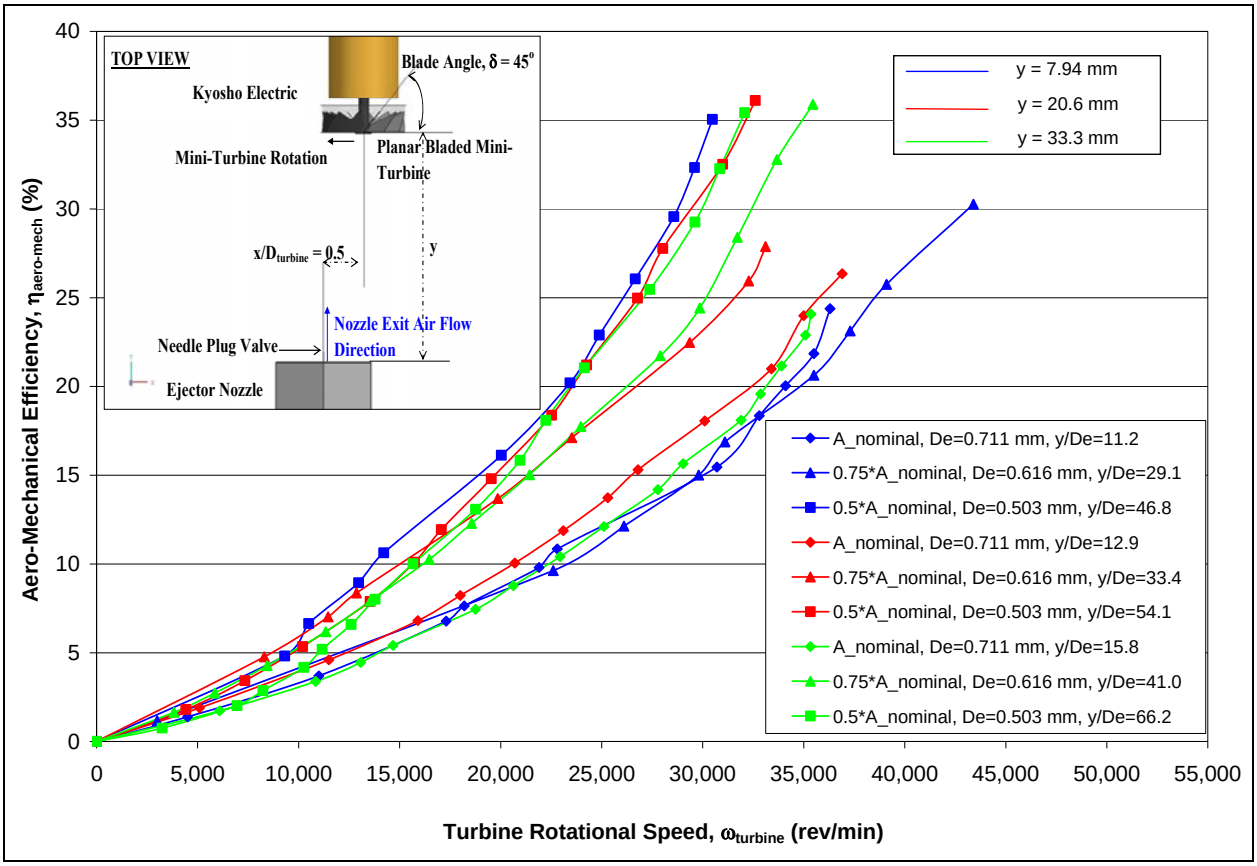

Figure 6.2 Aero-Mechanical Efficiency of Mechanical Power Extracted from Aerodynamic Power at Various Nozzle Exit Area as a function of Turbine RPM (x=12.8 mm, y=(12.8 mm, 20.6 mm & 33.3 mm), z=0 mm, $\alpha=0^o$ & $\beta=0^o$).

For experimental Run 1, the results shown in Figure 6.2 showed that the effect of decreasing nozzle exit area resulted in an increase in the maximum range of values for the aero-mechanical efficiency of power conversion obtained. The maximum range of values obtained for the efficiencies in power conversion during experimental Run 1 were approximately 35.0% to 36.1%. Also, it was observed from the plot of Figure 6.2 that the maximum efficiency values

increased when the mini-turbine was placed at axial locations downstream of the nozzle exit face.

The maximum aero-mechanical efficiency obtained for experimental Run 1 was obtained when the mini-turbine was placed at an axial location of $y/D_e = 41.0$ (**Case 3:** $0.5*A_{nominal} = 0.199\mu m^2$, $D_e = 0.503$ mm) with the nozzle exit flow centerline directed at $x/D_{turbine} = 0.5$ relative to the turbine centerline. The results showed that 36.1% of the fluidic aerodynamic power from the nozzle exit flow was extracted and converted into mechanical shaft power by the planar bladed mini-turbine.

6.1.2 *Experimental Results Determined for Run 2 at Various Nozzle Exit Areas and Nozzle Downstream Axial Distances*

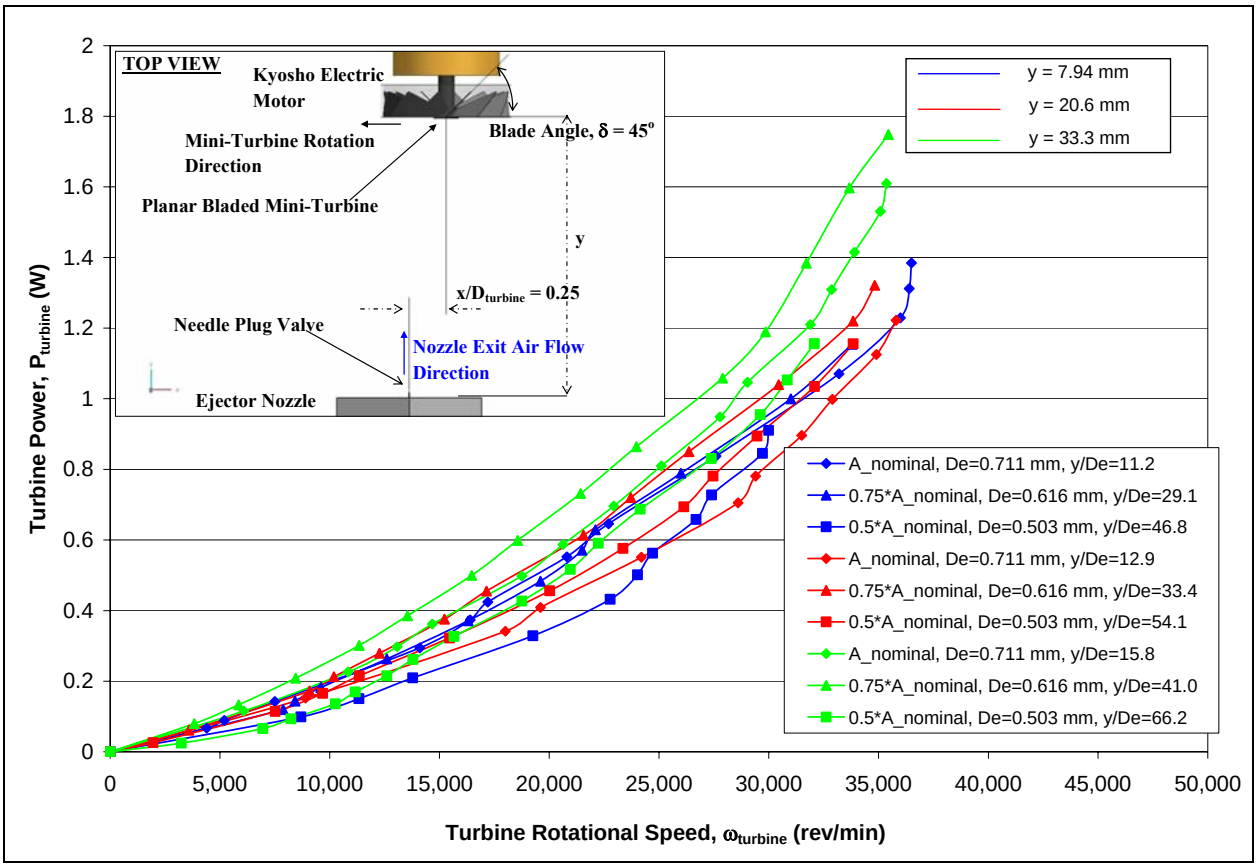

Figure 6.3 Mechanical Turbine Power Extracted at Various Nozzle Exit Area as a function of Turbine RPM (x=6.41 mm, y=(7.94 mm, 20.6 mm & 33.3 mm), z=0 mm, $\alpha=0^o$ & $\beta=0^o$).

Figure 6.3 shows the mini-turbine shaft power as a function of turbine rotational speed for experimental Run 2. The mini-turbine was positioned such that the nozzle jet flow centerline would be directed at the half radius location between the tip and centerline of the planar 45° bladed mini-turbine. The non-dimensional parameter for the position of the turbine centerline relative to the nozzle flow centerline described was $x/D_{turbine} = 0.25$. From the results shown in Figure 6.3, it was observed that the range of maximum turbine mechanical shaft power obtained

was from 1.61 W to 1.75 W. Results also showed that the maximum shaft power extracted increased as the mini-turbine was placed further downstream of the nozzle exit face.

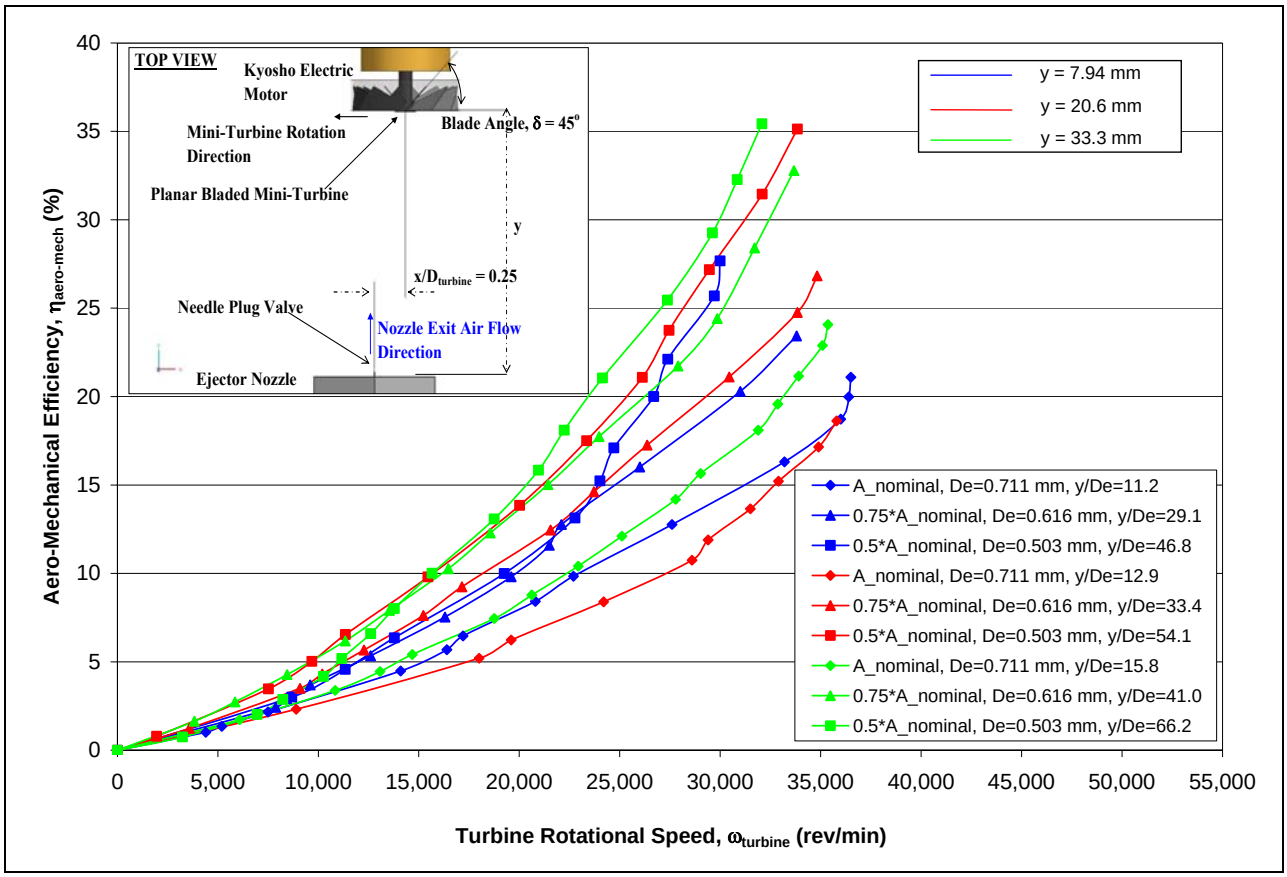

Figure 6.4 Aero-Mechanical Efficiency of Mechanical Power Extracted from Aerodynamic Power at Various Nozzle Exit Area as a function of Turbine RPM (x=6.41 mm, y=(7.94 mm, 20.6 mm & 33.3 mm), z=0 mm, $\alpha=0^o$ & $\beta=0^o$).

For experimental Run 2, the results shown in Figure 6.4 showed that the effect of decreasing nozzle exit area resulted in an increase in the maximum range of values for the aero-mechanical efficiency of power conversion obtained. The maximum range of values obtained for the efficiencies in power conversion during experimental Run 2 were approximately 35.1% to 35.9%. Also, it was observed from the plot of Figure 6.3 that the maximum efficiency values increased when the mini-turbine was placed at axial locations downstream of the nozzle exit face.

The maximum aero-mechanical efficiency obtained for experimental Run 2 was obtained when the mini-turbine was placed at an axial location of $y/D_e = 66.2$ (**Case 3:** $0.5*A_{nominal} = 0.199\mu m^2$, $D_e = 0.503$ mm) with the nozzle exit flow centerline directed at $x/D_{turbine} = 0.25$ relative to the turbine centerline. The results showed that 35.9% of the fluidic aerodynamic power from the nozzle exit flow was extracted and converted into mechanical shaft power by the planar bladed mini-turbine. The maximum values of aero-mechanical efficiencies obtained in Run 1 were higher than Run 2. This implied that a larger moment arm for the torque of the mini-turbine was utilized when the nozzle jet flow was directed at the tip radius of the mini-turbine in Run 1.

6.1.3 *Experimental Results Determined for Run 3 at Various Nozzle Exit Areas and Nozzle Downstream Axial Distances*

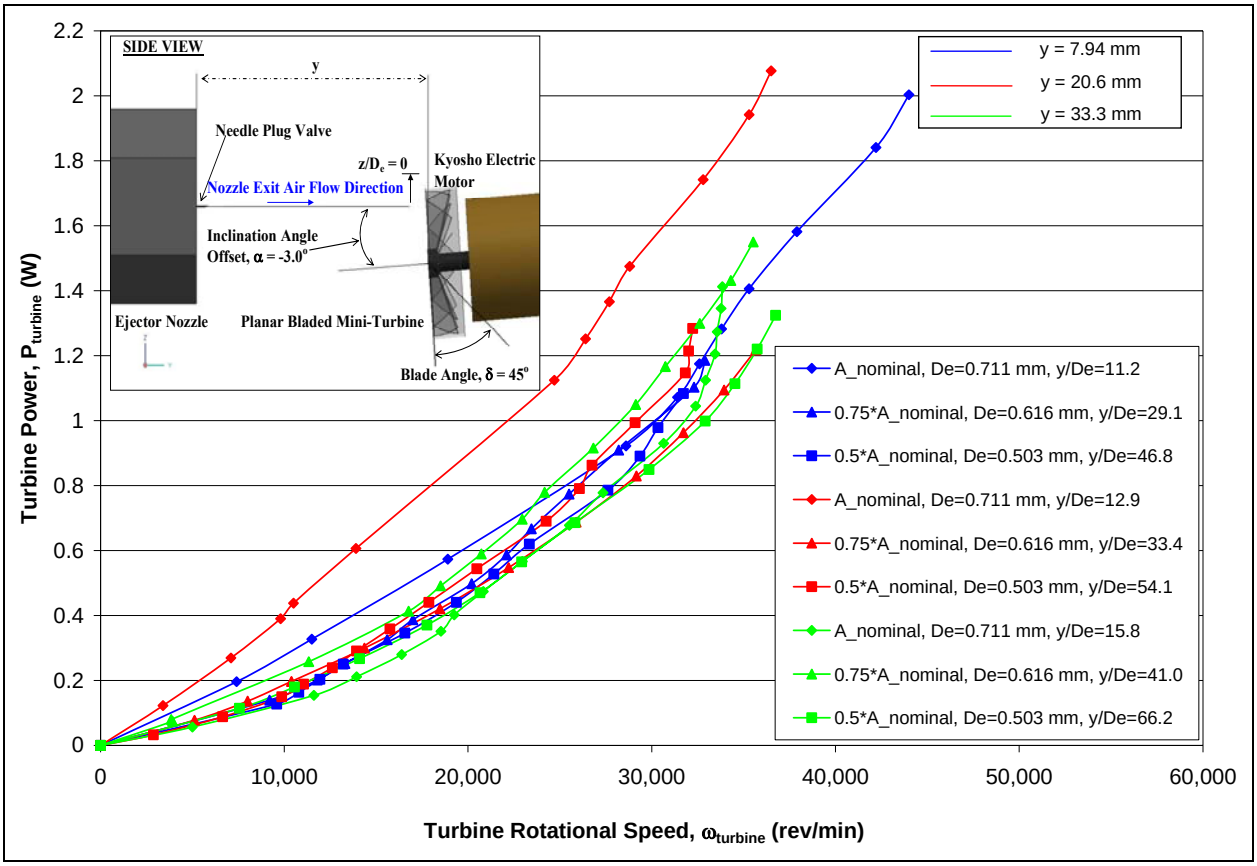

Figure 6.5 Mechanical Turbine Power Extracted at Various Nozzle Exit Area as a function of Turbine RPM (x=0 mm, y=(7.94 mm, 20.6 mm & 33.3 mm), z=0 mm, α=-3.0^o & β=0^o).

Figures 6.5 and 6.6 show a plot of shaft power and aero-mechanical efficiency as a function of turbine rotational speed (in RPM) for Run 3, respectively. The mini-turbine was positioned such that the nozzle jet flow centerline would be directed at an angle of α = -3.0 degrees measured from the centerline of the planar 45^o bladed mini-turbine. The non-dimensional parameter for the position of the turbine centerline relative to the nozzle flow centerline described was $x/D_{turbine}$ = 0. From the results shown in Figure 6.5, it was observed that the range of maximum turbine mechanical shaft power obtained was around 2 W. Results also

showed that the maximum shaft power extracted increased as the mini-turbine was placed further downstream of the nozzle exit face.

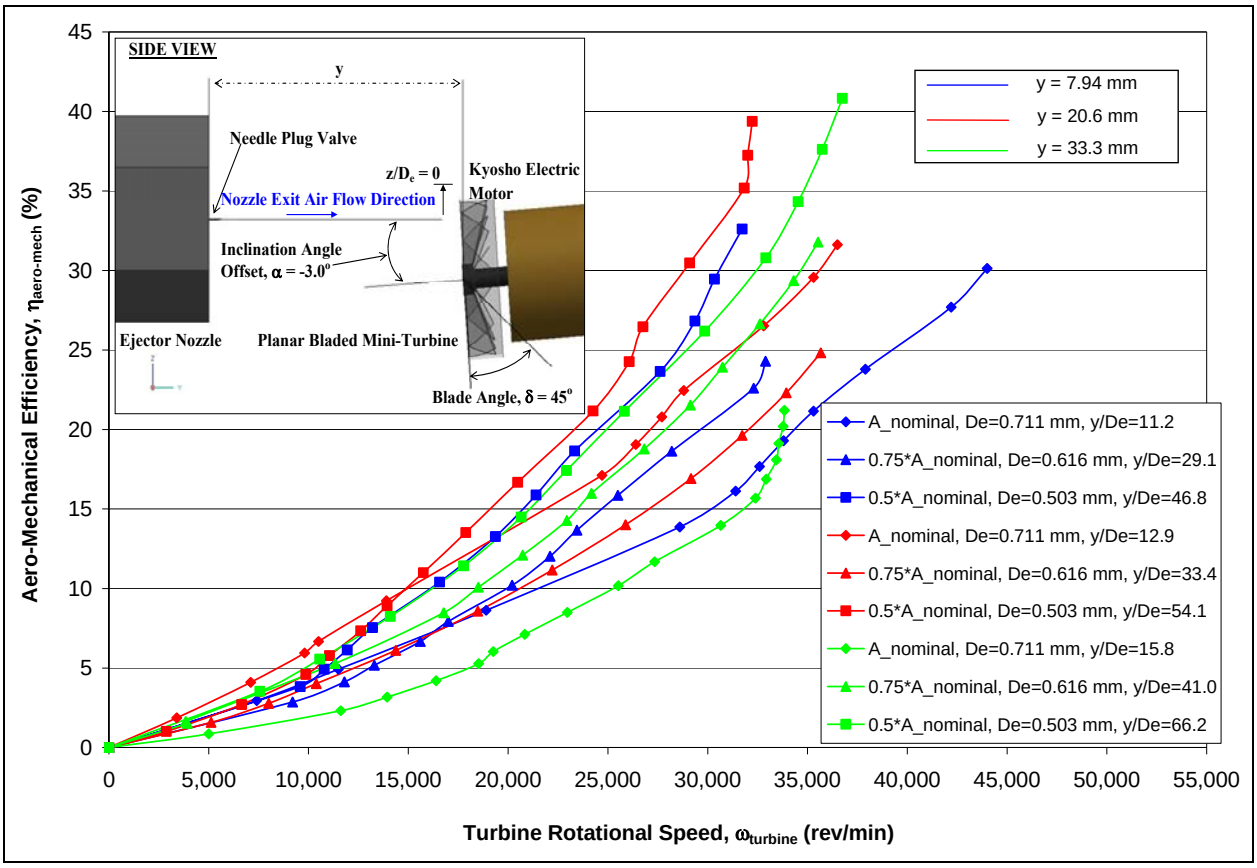

Figure 6.6 Aero-Mechanical Efficiency of Mechanical Power Extracted from Aerodynamic Power at Various Nozzle Exit Area as a function of Turbine RPM (x=0 mm, y=(7.94 mm, 20.6 mm & 33.3 mm), z=0 mm, α=-3.0^o & β=0^o).

For experimental Run 3, the results shown in Figure 6.6 showed that the effect of decreasing nozzle exit area resulted in an increase in the maximum range of values for the aero-mechanical efficiency of power conversion obtained. The maximum range of values obtained for the efficiencies in power conversion during experimental Run 3 were approximately 39.4% to 40.8%. Also, it was observed from the plot of Figure 6.6 that the maximum efficiency values increased when the mini-turbine was placed at axial locations downstream of the nozzle exit face.

The maximum aero-mechanical efficiency obtained for experimental Run 3 was obtained when the mini-turbine was placed at an axial location of $y/D_e = 66.2$ (**Case 3:** $0.5*A_{nominal} = 0.199\mu m^2$, $D_e = 0.503$ mm) with the nozzle exit flow centerline directed at an angle, $\alpha = -3.0^o$ relative to the turbine centerline. The results showed that approximately 40.8% of the fluidic aerodynamic power from the nozzle exit flow was extracted and converted into mechanical shaft power by the planar bladed mini-turbine.

6.1.4 *Experimental Results Determined for Run 4 at Various Nozzle Exit Areas and Nozzle Downstream Axial Distances*

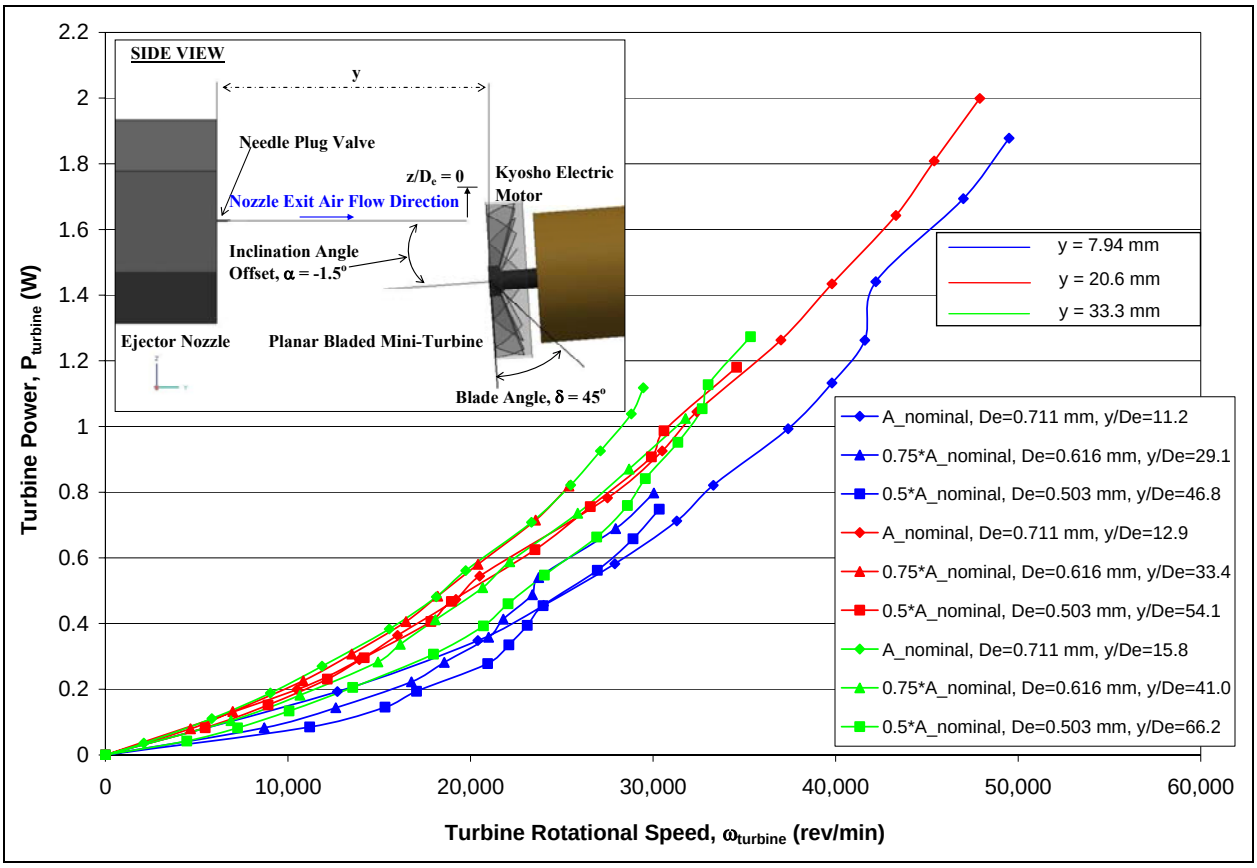

Figure 6.7 Mechanical Turbine Power Extracted at Various Nozzle Exit Area as a function of Turbine RPM (x=0 mm, y=(7.94 mm, 20.6 mm & 33.3 mm), z=0 mm, α=-1.5^o & β=0^o).

Figures 6.7 and 6.8 show a plot of shaft power and aero-mechanical efficiency as a function of turbine rotational speed (in RPM) for Run 3, respectively. The mini-turbine was positioned such that the nozzle jet flow centerline would be directed at an angle of α = -1.5 degrees measured from the centerline of the planar 45^o bladed mini-turbine. The non-dimensional parameter for the position of the turbine centerline relative to the nozzle flow centerline described was $x/D_{turbine} = 0$. From the results shown in Figure 6.7, it was observed that the range of maximum turbine mechanical shaft power obtained was 1.88 W to 1.99 W. Results

also showed that the maximum shaft power extracted increased as the mini-turbine was placed further downstream of the nozzle exit face.

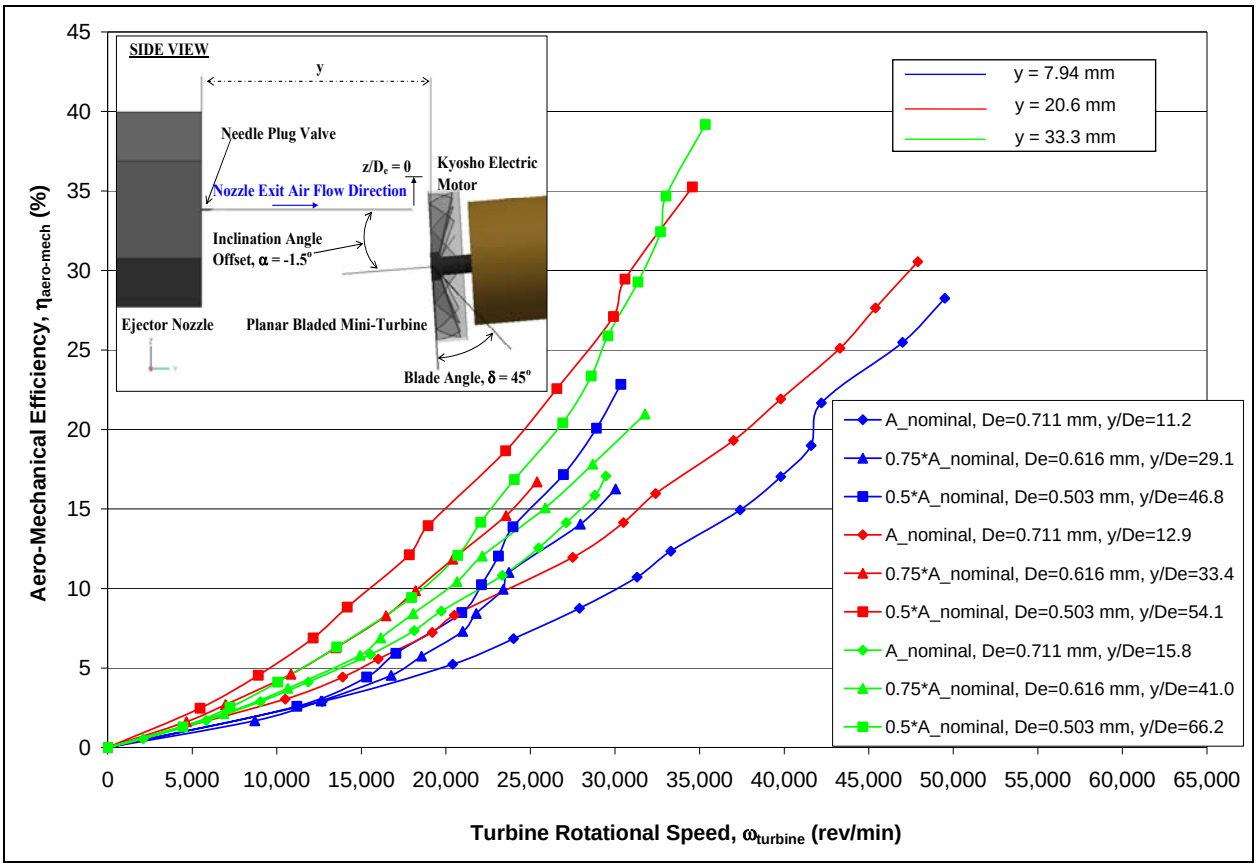

Figure 6.8 Aero-Mechanical Efficiency of Mechanical Power Extracted from Aerodynamic Power at Various Nozzle Exit Area as a function of Turbine RPM (x=0 mm, y=(7.94 mm, 20.6 mm & 33.3 mm), z=0 mm, α=-1.5^o & β=0^o).

For experimental Run 4, the results shown in Figure 6.8 showed that the effect of decreasing nozzle exit area resulted in an increase in the maximum range of values for the aero-mechanical efficiency of power conversion obtained. The maximum range of values obtained for the efficiencies in power conversion during experimental Run 4 were approximately 35.3% to 39.2%. Also, it was observed from the plot of Figure 6.8 that the maximum efficiency values increased when the mini-turbine was placed at axial locations downstream of the nozzle exit face.

The maximum aero-mechanical efficiency obtained for experimental Run 4 was obtained when the mini-turbine was placed at an axial location of $y/D_e = 66.2$ (**Case 3:** $0.5*A_{nominal} = 0.199\mu m^2$, $D_e = 0.503$ mm) with the nozzle exit flow centerline directed at an angle, $\alpha = -1.5^o$ relative to the turbine centerline. The results showed that approximately 39.2% of the fluidic aerodynamic power from the nozzle exit flow was extracted and converted into mechanical shaft power by the planar bladed mini-turbine. The maximum values of aero-mechanical efficiencies obtained in Run 3 were higher than Run 4 when the inclination angle was increased. This implied that there was a larger flow turning angle measured at the blade in Run 3 as compared to Run 4 resulting in higher values of aero-mechanical efficiencies in the power conversion from the fluidic power from the nozzle exit to the shaft power obtained at the turbine.

6.1.5 Experimental Results Determined for Run 5 at Various Nozzle Exit Areas and Nozzle Downstream Axial Distances

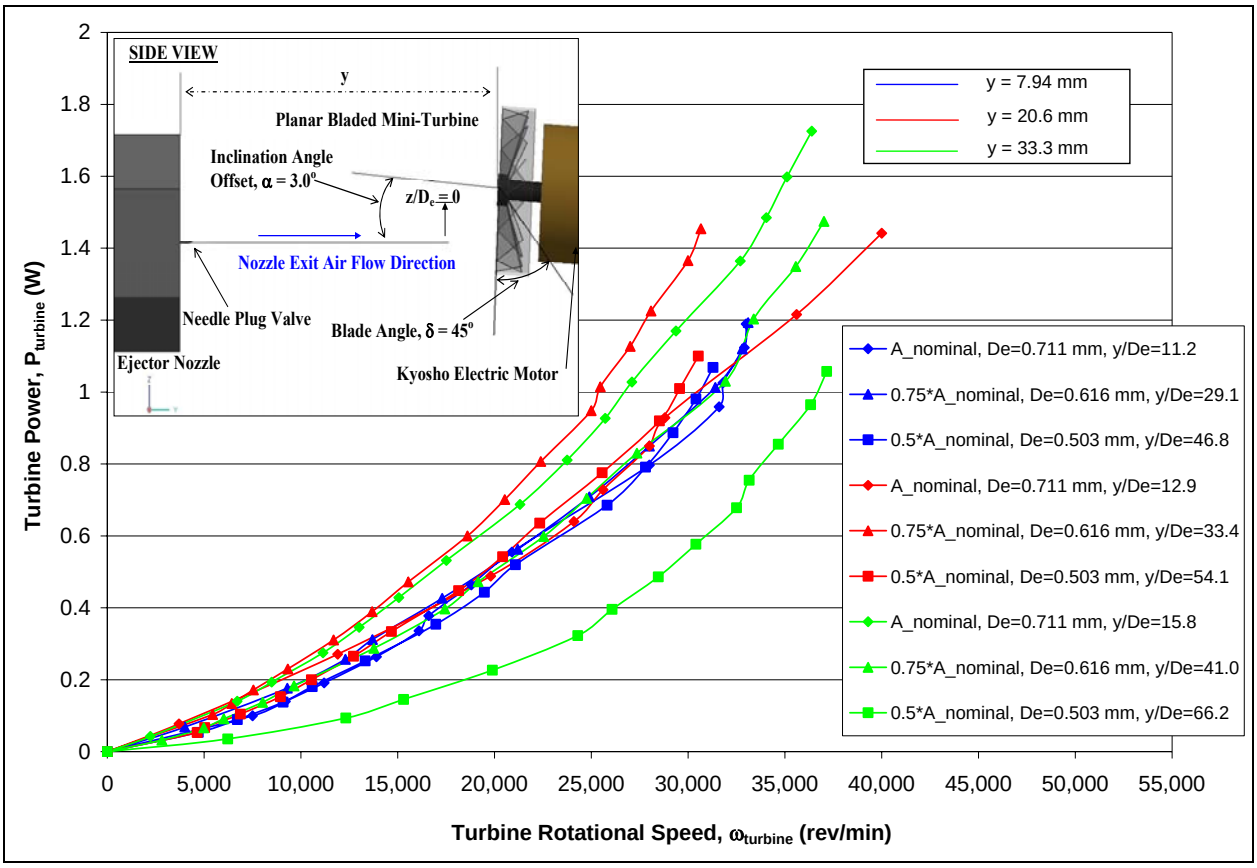

Figure 6.9 Mechanical Turbine Power Extracted at Various Nozzle Exit Area as a function of Turbine RPM (x=0 mm, y=(7.94 mm, 20.6 mm & 33.3 mm), z=0 mm, α=3.0^o & β=0^o).

Figure 6.9 shows the mini-turbine shaft power as a function of turbine rotational speed for experimental Run 5. The mini-turbine was positioned such that the nozzle jet flow centerline would be directed at an angle of α = 3.0 degrees measured from the centerline of the planar 45^o bladed mini-turbine. The non-dimensional parameter for the position of the turbine centerline relative to the nozzle flow centerline described was $x/D_{turbine}$ = 0. From the results shown in Figure 6.9, it was observed that the range of maximum turbine mechanical shaft power obtained

was from 1.44 W to 1.73 W. Results also showed that the maximum shaft power extracted increased as the mini-turbine was placed further downstream of the nozzle exit face.

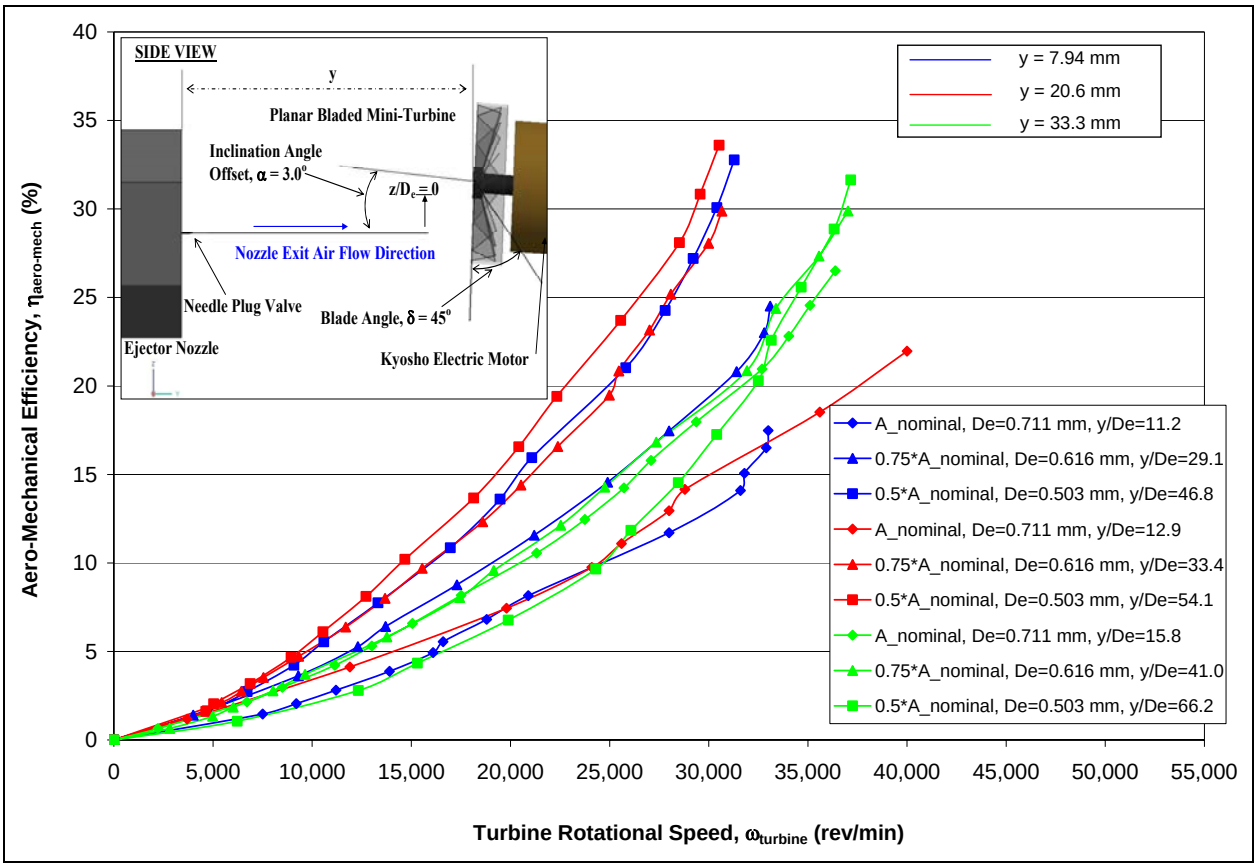

Figure 6.10 Aero-Mechanical Efficiency of Mechanical Power Extracted from Aerodynamic Power at Various Nozzle Exit Area as a function of Turbine RPM (x=0 mm, y=(7.94 mm, 20.6 mm & 33.3 mm), z=0 mm, α=3.0^o & β=0^o).

For experimental Run 5, the results shown in Figure 6.10 showed that the effect of decreasing nozzle exit area resulted in an increase in the maximum range of values for the aero-mechanical efficiency of power conversion obtained. The maximum range of values obtained for the efficiencies in power conversion during experimental Run 5 were approximately 31.6% to 33.6%. Also, it was observed from the plot of Figure 6.10 that the maximum efficiency values increased when the mini-turbine was placed at axial locations downstream of the nozzle exit face.

The maximum aero-mechanical efficiency obtained for experimental Run 5 was obtained when the mini-turbine was placed at an axial location of $y/D_e = 41.0$ (**Case 2:** $0.75*A_{nominal} = 0.298\ \mu m^2$, $D_e = 0.616$ mm) with the nozzle exit flow centerline directed at an angle, $\alpha = 3.0^o$ relative to the turbine centerline. The results showed that 33.6% of the fluidic aerodynamic power from the nozzle exit flow was extracted and converted into mechanical shaft power by the planar bladed mini-turbine.

6.1.6 *Experimental Results Determined for Run 6 at Various Nozzle Exit Areas and Nozzle Downstream Axial Distances*

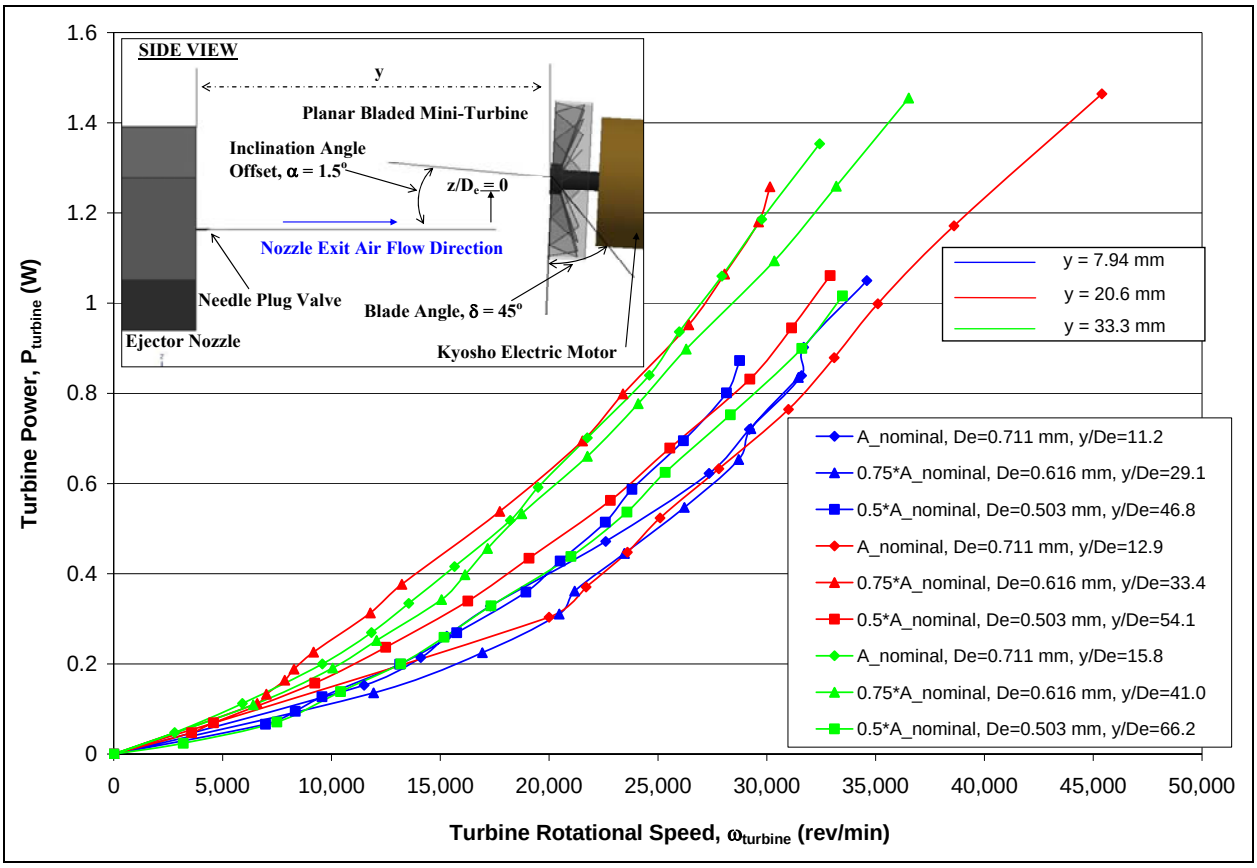

Figure 6.11 Mechanical Turbine Power Extracted at Various Nozzle Exit Area as a function of Turbine RPM (x=0 mm, y=(7.94 mm, 20.6 mm & 33.3 mm), z=0 mm, α=1.5° & β=0°).

Figure 6.11 shows the mini-turbine shaft power as a function of turbine rotational speed for experimental Run 6. The mini-turbine was positioned such that the nozzle jet flow centerline would be directed at an angle of α = 1.5 degrees measured from the centerline of the planar 45° bladed mini-turbine. The non-dimensional parameter for the position of the turbine centerline relative to the nozzle flow centerline described was $x/D_{turbine}$ = 0. From the results shown in Figure 6.11, it was observed that the range of maximum turbine mechanical shaft power obtained

was from 1.35 W to 1.46 W. Results also showed that the maximum shaft power extracted increased as the mini-turbine was placed further downstream of the nozzle exit face.

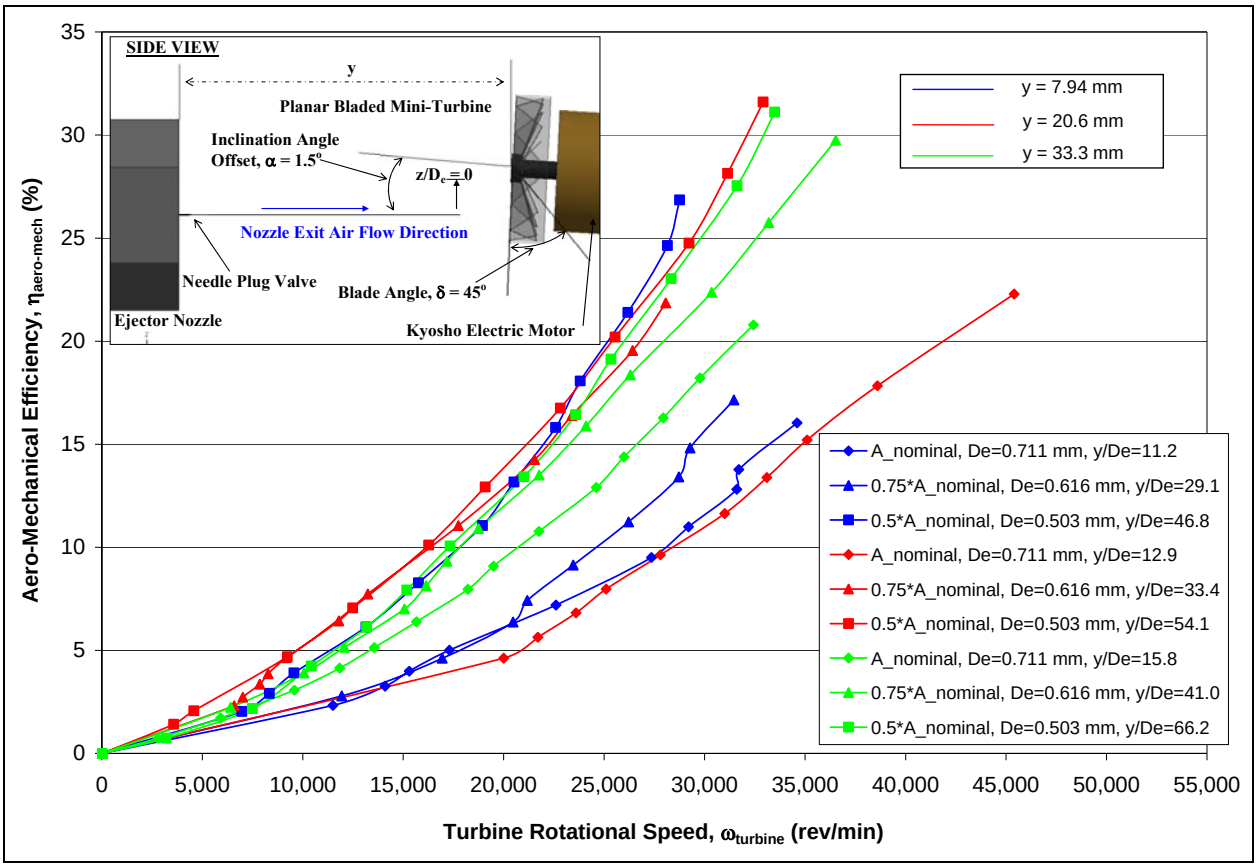

Figure 6.12 Aero-Mechanical Efficiency of Mechanical Power Extracted from Aerodynamic Power at Various Nozzle Exit Area as a function of Turbine RPM (x=0 mm, y=(7.94 mm, 20.6 mm & 33.3 mm), z=0 mm, $\alpha=1.5^{o}$ & $\beta=0^{o}$).

For experimental Run 6, the results shown in Figure 6.12 showed that the effect of decreasing nozzle exit area resulted in an increase in the maximum range of values for the aero-mechanical efficiency of power conversion obtained. The maximum range of values obtained for the efficiencies in power conversion during experimental Run 6 were approximately 29.7% to 31.6%. Also, it was observed from the plot of Figure 6.12 that the maximum efficiency values increased when the mini-turbine was placed at axial locations downstream of the nozzle exit face.

The maximum aero-mechanical efficiency obtained for experimental Run 6 was obtained when the mini-turbine was placed at an axial location of $y/D_e = 41.0$ (**Case 2:** $0.75*A_{nominal} = 0.298\ \mu m^2$, $D_e = 0.616$ mm) with the nozzle exit flow centerline directed at an angle, $\alpha = 1.5^o$ relative to the turbine centerline. The results showed that 31.6% of the fluidic aerodynamic power from the nozzle exit flow was extracted and converted into mechanical shaft power by the planar bladed mini-turbine. From comparison of the results obtained in experimental Runs 3 through 6, it was observed that the aero-mechanical efficiency was the highest in experimental Run 3 and the maximum values of aero-mechanical efficiency for power conversion decreased from Runs 3 through 6, and the aero-mechanical efficiency results observed in Runs 4 and 5 were similar. It was concluded that an increase in the inclination angle from -3^o to 3^o decreased the aero-mechanical efficiency of the planar bladed turbine to convert fluidic aerodynamic power available in the nozzle exit supersonic jet flow to turbine shaft power.

6.1.7 Experimental Results Determined for Run 7 at Various Nozzle Exit Areas and Nozzle Downstream Axial Distances

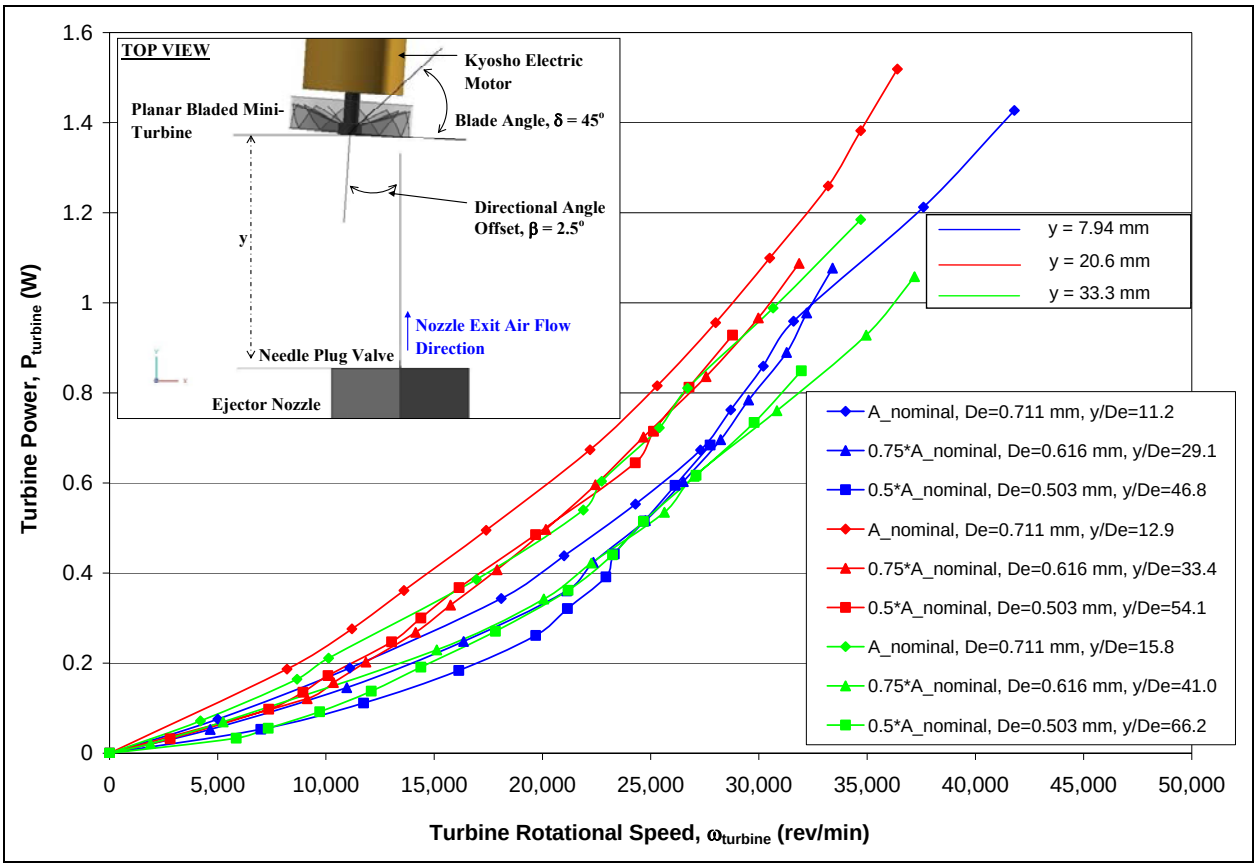

Figure 6.13 Mechanical Turbine Power Extracted at Various Nozzle Exit Area as a function of Turbine RPM (x=0 mm, y=(7.94 mm, 20.6 mm & 33.3 mm), z=0 mm, $\alpha=0^o$ & $\beta=2.5^o$).

Figure 6.13 shows the mini-turbine shaft power as a function of turbine rotational speed for experimental Run 7. The mini-turbine was positioned such that the nozzle jet flow centerline would be directed at a directional offset angle of $\beta = 2.5$ degrees measured from the centerline of the planar 45^o bladed mini-turbine. The non-dimensional parameter for the position of the turbine centerline relative to the nozzle flow centerline described was $x/D_{turbine} = 0$. From the results shown in Figure 6.13, it was observed that the range of maximum turbine mechanical shaft

power obtained was from 1.43 W to 1.52 W. Results also showed that the maximum shaft power extracted increased as the mini-turbine was placed further downstream of the nozzle exit face.

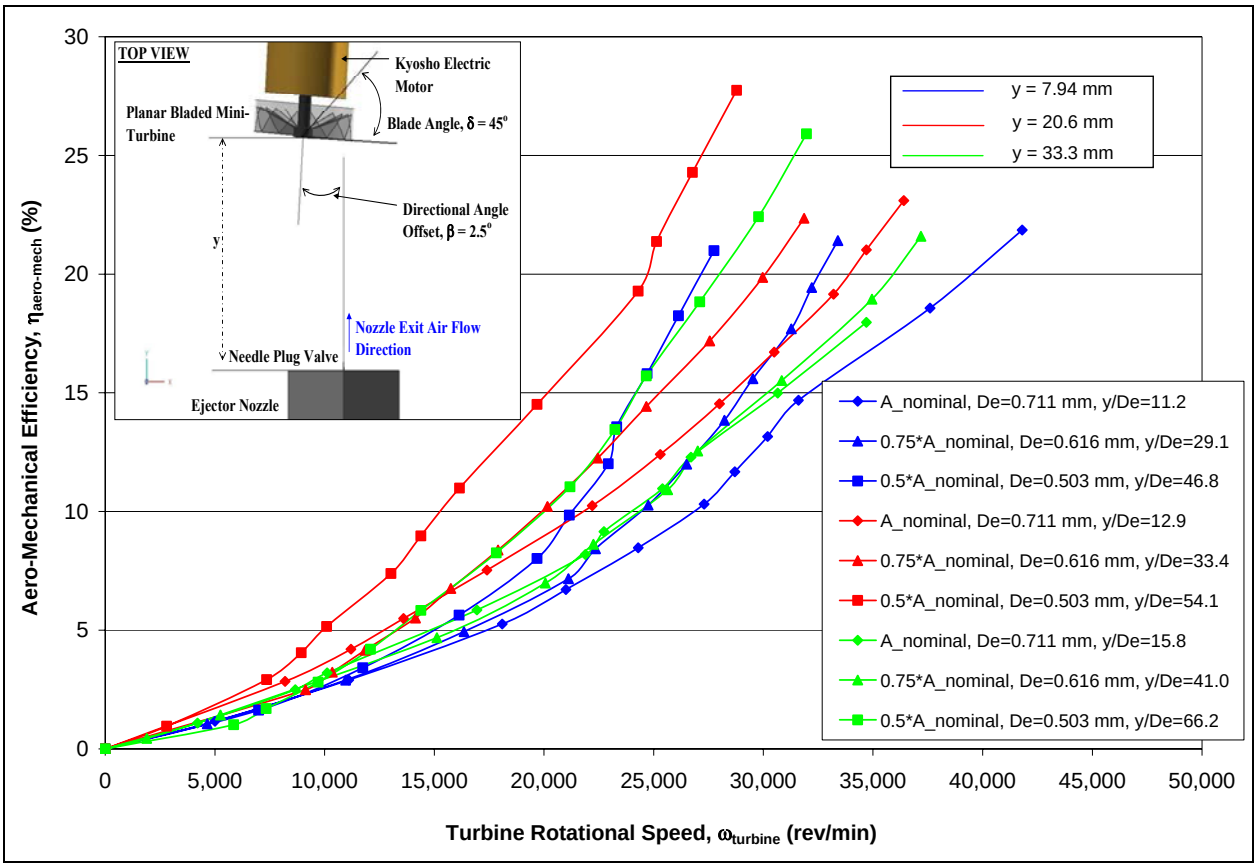

Figure 6.14 Aero-Mechanical Efficiency of Mechanical Power Extracted from Aerodynamic Power at Various Nozzle Exit Area as a function of Turbine RPM (x=0 mm, y=(7.94 mm, 20.6 mm & 33.3 mm), z=0 mm, $\alpha=0^o$ & $\beta=2.5^o$).

The results shown in Figure 6.14 showed that the effect of decreasing nozzle exit area resulted in an increase in the maximum range of values for the aero-mechanical efficiency of power conversion obtained. The maximum range of values obtained for the efficiencies in power conversion during experimental Run 7 were approximately 25.9% to 27.7%. Also, it was observed from the plot of Figure 6.14 that the maximum efficiency values increased when the mini-turbine was placed at axial locations downstream of the nozzle exit face.

The maximum aero-mechanical efficiency obtained for experimental Run 7 was obtained when the mini-turbine was placed at an axial location of y/D_e = 41.0 (**Case 2:** $0.75*A_{nominal}$ = 0.298 μm^2, D_e = 0.616 mm) with the nozzle exit flow centerline directed at an angle, β= 2.5^o relative to the turbine centerline. The results showed that 27.7% of the fluidic aerodynamic power from the nozzle exit flow was extracted and converted into mechanical shaft power by the planar bladed mini-turbine.

6.1.8 *Experimental Results Determined for Run 8 at Various Nozzle Exit Areas and Nozzle Downstream Axial Distances*

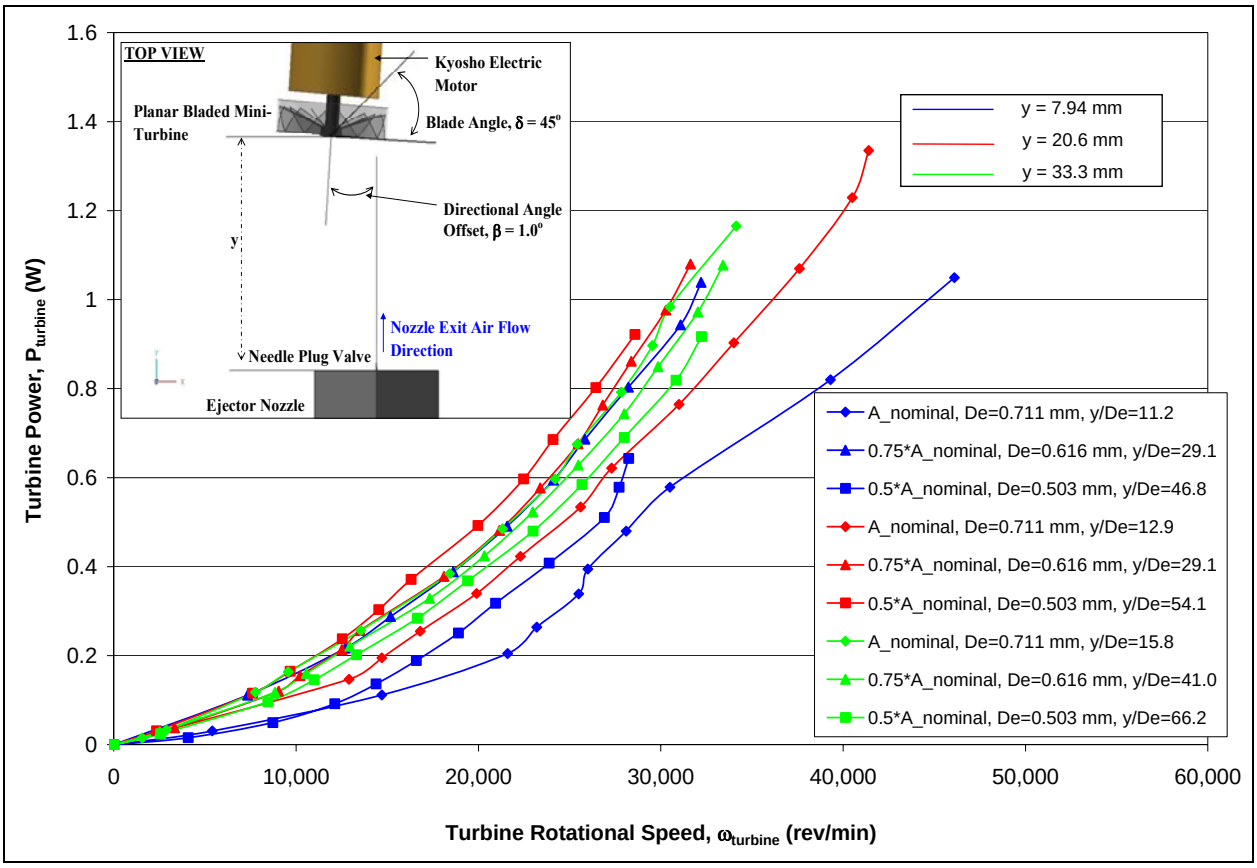

Figure 6.15 Mechanical Turbine Power Extracted at Various Nozzle Exit Area as a function of Turbine RPM (x=0 mm, y=(7.94 mm, 20.6 mm & 33.3 mm), z=0 mm, $\alpha=0^o$ & $\beta=1.0^o$).

Figure 6.15 shows the mini-turbine shaft power as a function of turbine rotational speed for experimental Run 8. The mini-turbine was positioned such that the nozzle jet flow centerline would be directed at a directional offset angle of β = 1.0 degree measured from the centerline of the planar 45^o bladed mini-turbine. The non-dimensional parameter for the position of the turbine centerline relative to the nozzle flow centerline described was $x/D_{turbine}$ = 0. From the results shown in Figure 6.15, it was observed that the range of maximum turbine mechanical shaft

power obtained was approximately 1.34 W. Results also showed that the maximum shaft power extracted increased as the mini-turbine was placed further downstream of the nozzle exit face.

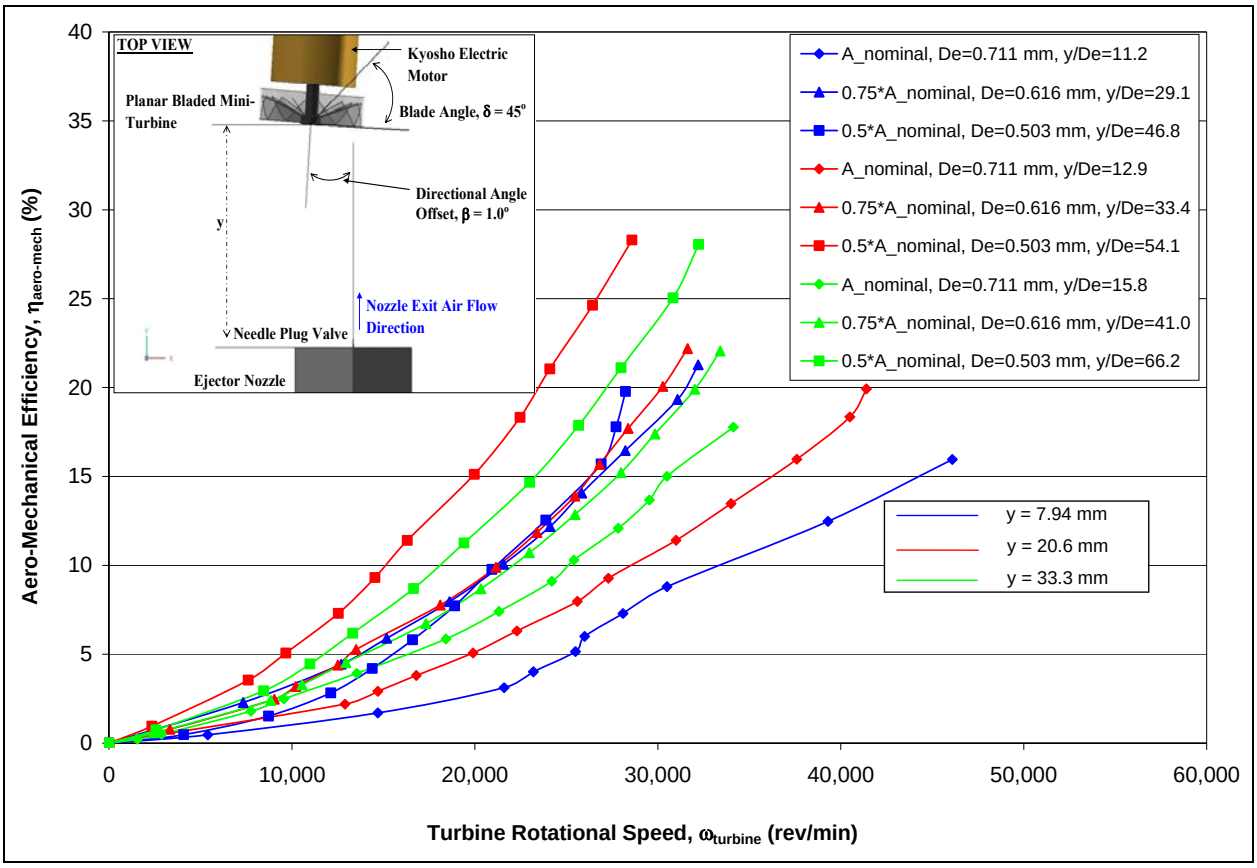

Figure 6.16 Aero-Mechanical Efficiency of Mechanical Power Extracted from Aerodynamic Power at Various Nozzle Exit Area as a function of Turbine RPM (x=0 mm, y=(7.94 mm, 20.6 mm & 33.3 mm), z=0 mm, $\alpha=0^o$ & $\beta=1.0^o$).

The results shown in Figure 6.16 showed that the effect of decreasing nozzle exit area resulted in an increase in the maximum range of values for the aero-mechanical efficiency of power conversion obtained. The maximum range of values obtained for the efficiencies in power conversion during experimental Run 8 were around 28.0%. Also, it was observed from the plot of Figure 6.16 that the maximum efficiency values increased when the mini-turbine was placed at axial locations downstream of the nozzle exit face.

The maximum aero-mechanical efficiency obtained for experimental Run 8 was obtained when the mini-turbine was placed at an axial location of $y/D_e = 41.0$ (**Case 2:** $0.75*A_{nominal} = 0.298\ \mu m^2$, $D_e = 0.616$ mm) with the nozzle exit flow centerline directed at an angle, $\beta = 1.0^o$ relative to the turbine centerline. The results showed that 28.3% of the fluidic aerodynamic power from the nozzle exit flow was extracted and converted into mechanical shaft power by the planar bladed mini-turbine. The maximum values of aero-mechanical efficiencies obtained in Run 8 were higher than Run 7 when the directional angle offset was decreased from 2.5^o to 1.0^o.

6.1.9 *Experimental Results Determined for Run 9 at Various Nozzle Exit Areas and Nozzle Downstream Axial Distances*

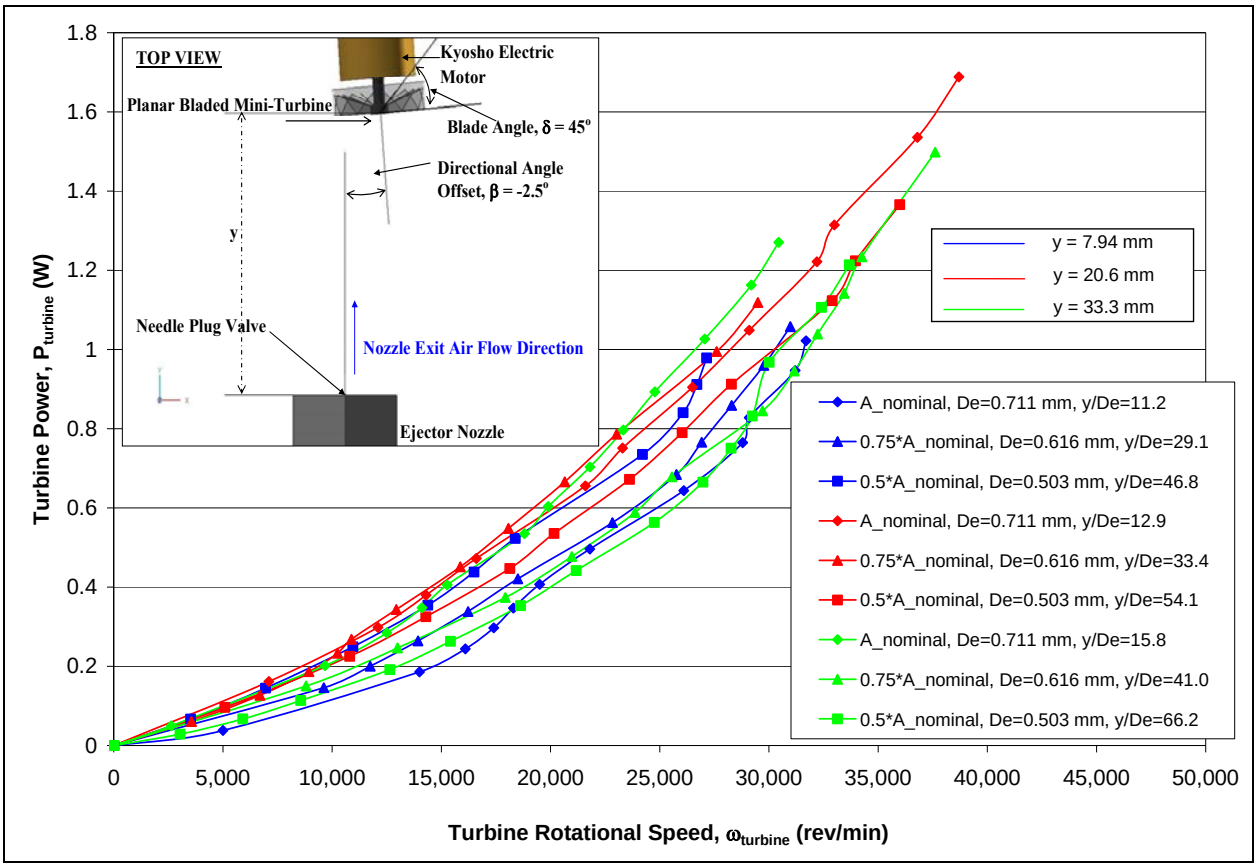

Figure 6.17 Mechanical Turbine Power Extracted at Various Nozzle Exit Area as a function of Turbine RPM (x=0 mm, y=(7.94 mm, 20.6 mm & 33.3 mm), z=0 mm, $\alpha=0^o$ & $\beta=-2.5^o$).

Figure 6.17 shows the mini-turbine shaft power as a function of turbine rotational speed for experimental Run 9. The mini-turbine was positioned such that the nozzle jet flow centerline would be directed at a directional offset angle of β = -2.5 degrees measured from the centerline of the planar 45° bladed mini-turbine. The non-dimensional parameter for the position of the turbine centerline relative to the nozzle flow centerline described was $x/D_{turbine} = 0$. From the results shown in Figure 6.17, it was observed that the range of maximum turbine mechanical shaft power obtained was approximately 1.50 W to 1.69 W. Results also showed that the

maximum shaft power extracted increased as the mini-turbine was placed further downstream of the nozzle exit face.

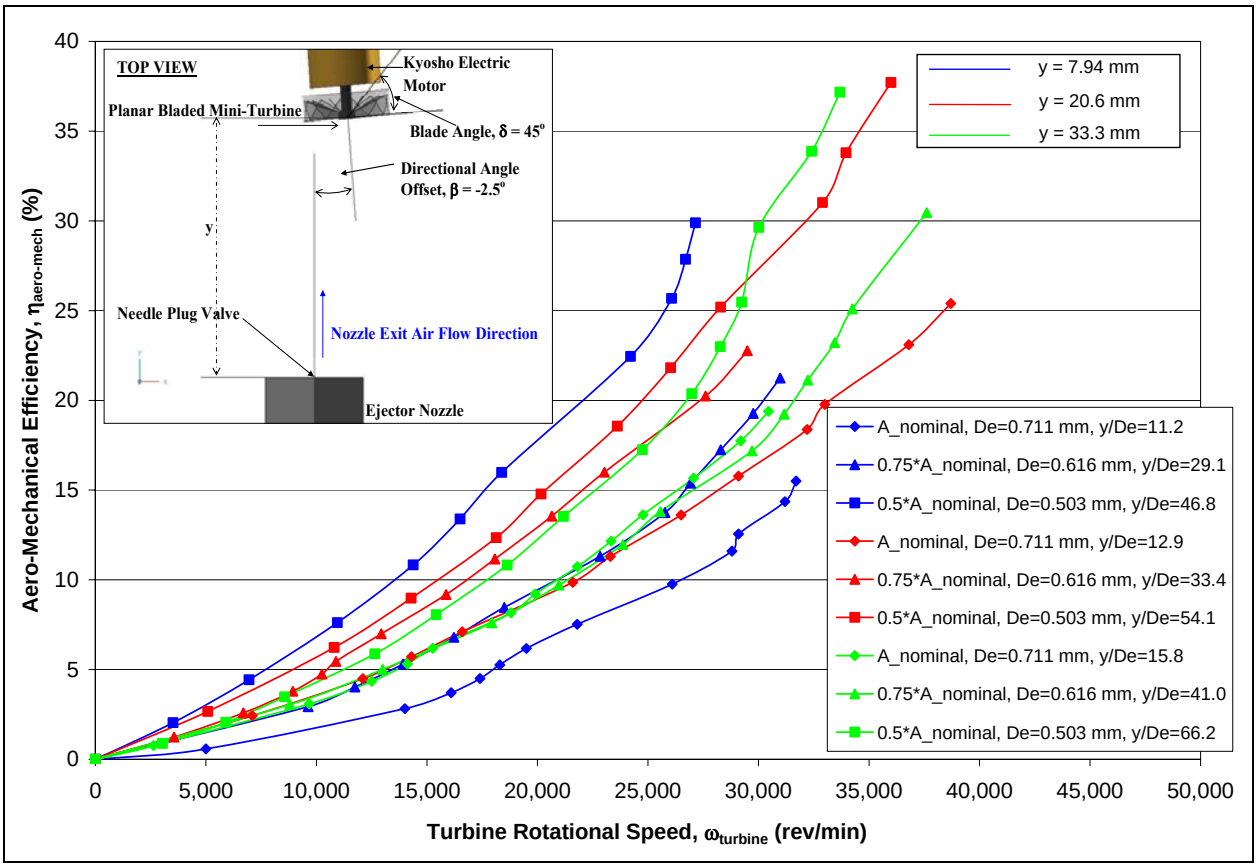

Figure 6.18 Aero-Mechanical Efficiency of Mechanical Power Extracted from Aerodynamic Power at Various Nozzle Exit Area as a function of Turbine RPM (x=0 mm, y=(7.94 mm, 20.6 mm & 33.3 mm), z=0 mm, $\alpha=0^{o}$ & $\beta=-2.5$).

The results shown in Figure 6.18 showed that the effect of decreasing nozzle exit area resulted in an increase in the maximum range of values for the aero-mechanical efficiency of power conversion obtained. The maximum range of values obtained for the efficiencies in power conversion during experimental Run 9 were approximately 29.9% to 37.7%. Also, it was observed from the plot of Figure 6.18 that the maximum efficiency values increased when the mini-turbine was placed at axial locations downstream of the nozzle exit face.

The maximum aero-mechanical efficiency obtained for experimental Run 9 was obtained when the mini-turbine was placed at an axial location of $y/D_e = 41.0$ (**Case 2:** $0.75*A_{nominal} = 0.298\ \mu m^2$, $D_e = 0.616$ mm) with the nozzle exit flow centerline directed at an angle, $\beta = -2.5^o$ relative to the turbine centerline. The results showed that 37.7% of the fluidic aerodynamic power from the nozzle exit flow was extracted and converted into mechanical shaft power by the planar bladed mini-turbine.

6.1.10 *Experimental Results Determined for Run 10 at Various Nozzle Exit Areas and Nozzle Downstream Axial Distances*

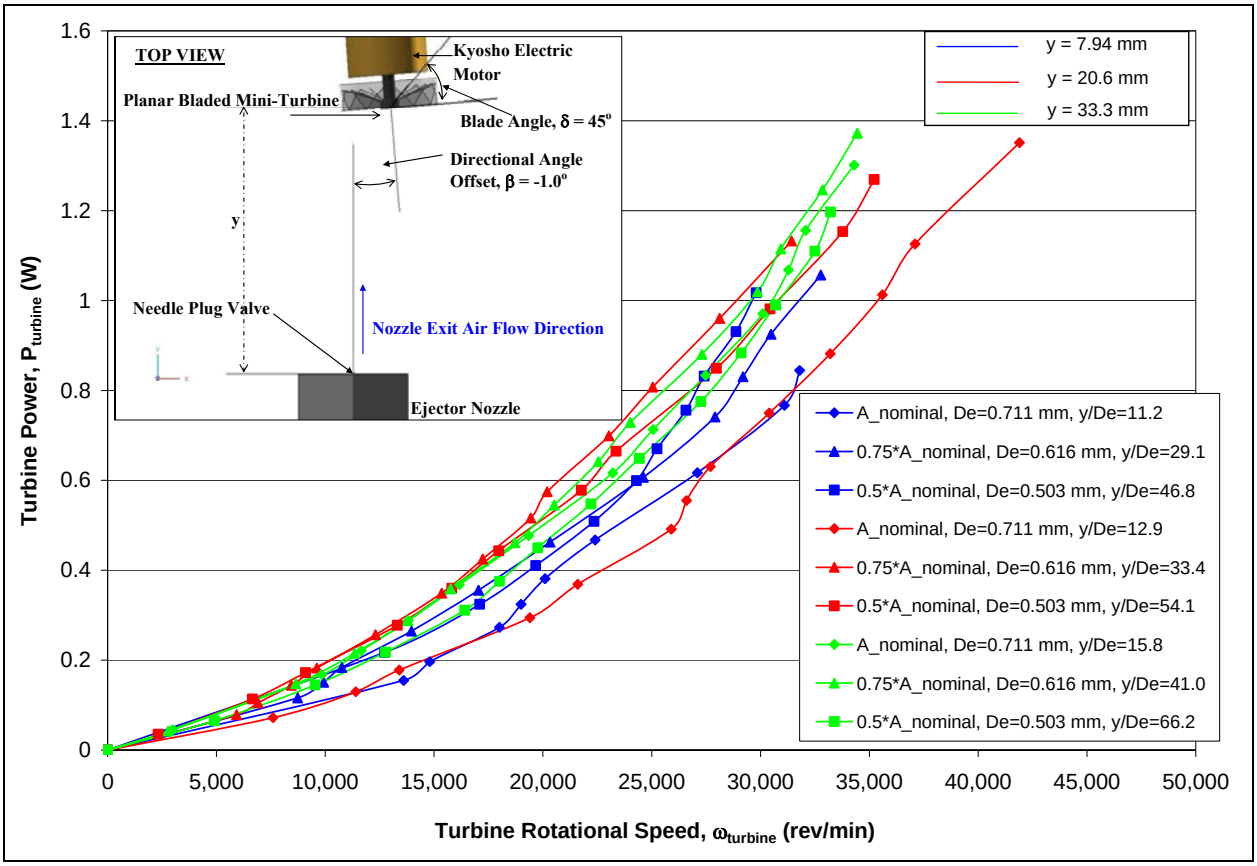

Figure 6.19 Mechanical Turbine Power Extracted at Various Nozzle Exit Area as a function of Turbine RPM (x=0 mm, y=(7.94 mm, 20.6 mm & 33.3 mm), z=0 mm, $\alpha=0^o$ & $\beta=-1.0^o$).

Figure 6.19 shows the mini-turbine shaft power as a function of turbine rotational speed for experimental Run 10. The mini-turbine was positioned such that the nozzle jet flow centerline would be directed at a directional offset angle of β = -1.0 degree measured from the centerline of the planar 45^o bladed mini-turbine. The non-dimensional parameter for the position of the turbine centerline relative to the nozzle flow centerline described was $x/D_{turbine} = 0$. From the results shown in Figure 6.19, it was observed that the maximum turbine mechanical shaft

power obtained was approximately 1.38 W. Results also showed that the maximum shaft power extracted increased as the mini-turbine was placed further downstream of the nozzle exit face.

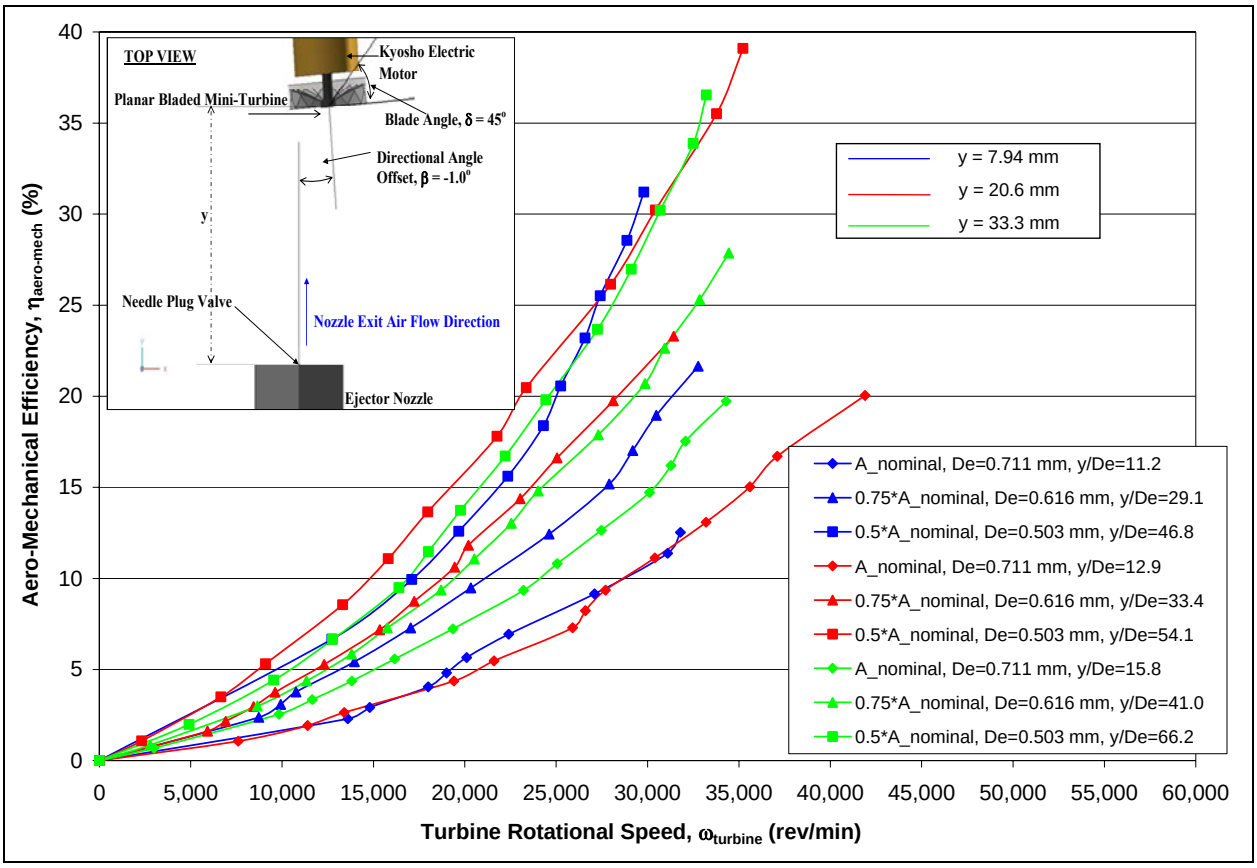

Figure 6.20 Aero-Mechanical Efficiency of Mechanical Power Extracted from Aerodynamic Power at Various Nozzle Exit Area as a function of Turbine RPM (x=0 mm, y=(7.94 mm, 20.6 mm & 33.3 mm), z=0 mm, $\alpha=0^{o}$ & $\beta=-1.0^{o}$).

From the results shown in Figure 6.20, the effect of decreasing nozzle exit area resulted in an increase in the maximum range of values for the aero-mechanical efficiency of power conversion obtained. The maximum range of values obtained for the efficiencies in power conversion during experimental Run 10 was approximately 36.5% to 39.1%. Also, it was observed from the plot of Figure 6.20 that the maximum efficiency values increased when the mini-turbine was placed at axial locations downstream of the nozzle exit face.

The maximum aero-mechanical efficiency obtained for experimental Run 10 was obtained when the mini-turbine was placed at an axial location of y/D_e = 41.0 (**Case 2:** $0.75*A_{nominal}$ = 0.298 μm^2, D_e = 0.616 mm) with the nozzle exit flow centerline directed at an angle, $\beta = -1.0^o$ relative to the turbine centerline. The results showed that 39.1% of the fluidic aerodynamic power from the nozzle exit flow was extracted and converted into mechanical shaft power by the planar bladed mini-turbine. Comparison of the results obtained for experimental runs 7 through 10 showed that the aero-mechanical efficiency of power conversion increased as the directional angle offset was decreased from 2.5 to -2.5 degrees. The maximum value of aero-mechanical efficiency was highest in Run 10 as compared to Runs 7, 8, and 9.

The general observations of the results obtained from each experimental runs were:

- Shaft Power of around 1-2W were obtained from the experiments
- Aero-mechanical efficiency of power conversion of around 25% to 40% was obtained.
- In order to obtain the shaft power and conversion efficiency range determined in the experiments, the mini-turbine operated at rotational speeds of up to 50,000 RPM.

The effects of positioning the mini-turbine at a greater distance away from the nozzle exit face and the change in turbine configuration relative to nozzle exit jet centerline did not cause any significant difference in shaft power and conversion efficiency values when a comparison of the results was made between each of the experimental runs performed in this study. This could be due to jet spreading being more significant downstream away from nozzle exit at a location that was not considered in the present research but would contribute to the understanding of

larger variations in the results between each of the experimental runs. The variation in shaft power and conversion efficiency results was not much different for each run when compared.

In addition, reducing nozzle exit area also showed no significant deviations of the data for the shaft power and conversion efficiency between each experimental run. The jet exiting from the ejector nozzle also caused very little deviation in the range of shaft power and conversion efficiencies measured for each configuration of the turbine relative to the ejector nozzle when the nozzle exit area was decreased for each experimental run. Chamber total pressure was kept constant and the effect of nozzle exit area variation was to control the amount of expansion at the exit. The back pressure ratio, p_e/p_{amb} decreased as the nozzle exit area was decreased.

As seen from the flow visualization pictures presented in the following section, the shock structure that existed in the flow was weaker and the region of supersonic flow decreased. This implied that the jet spread was wider at a shorter distance downstream of the nozzle exit when the nozzle exit area was decreased. If this was the case, the wider jet radius would fully encase the turbine radius or would impart more flow onto the turbine face than a flow from the larger nozzle exit area at the same axial position downstream of the nozzle exit.

6.2 Flow Visualization of Supersonic Nozzle Exit Flow

The flow visualization results carried out for the three different nozzle exit area cases are shown in the figures below. The shadowgraph image captured for the nozzle exit nominal area (Case 1) is presented in Figure 6.21 showing the diamond shock structure emanating from the nozzle exit. There were no Mach disks present in the supersonic flow region but the figure clearly shows the flow characteristics of an underexpanded nozzle. As observed in Figure 6.21, the supersonic flow region extends up to 9 nozzle diameters downstream of the nozzle exit.

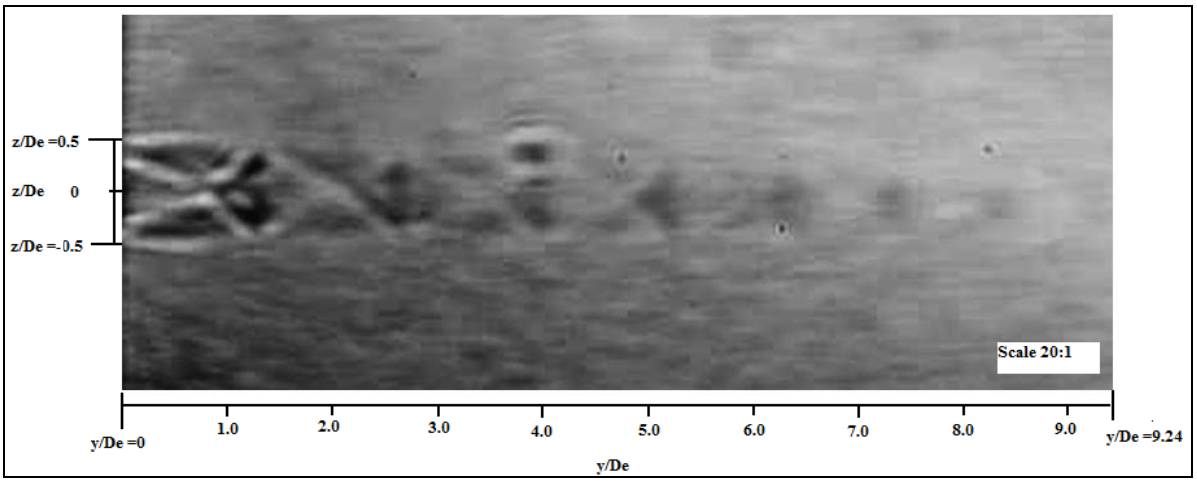

Figure 6.21 Shadowgraph Image of the Underexpanded Supersonic Microjet showing Shock Structure for Case 1: D_e = 711 μm, A_e = 0.397 μm^2, P_e/P_{amb} = 3.72 and NPR = 7.03 (Note: Nozzle plug is not protruding in nozzle exit flow).

Figure 6.22 shows the supersonic flow region captured using the shadowgraph technique for nozzle exit area (Case 2) extending up to 9.5 nozzle diameters downstream of the ejector nozzle exit. The nominal nozzle exit area was decreased by 25% by extension of the nozzle plug into the supersonic flow emanating from the nozzle exit. The supersonic shock structure observed in Figure 6.22 was less evident than in Figure 6.39. The spacing between each

shock cell increased from 1 to 1.5 nozzle diameters. It was also observed that the supersonic jet transitioned from supersonic to subsonic flow at approximately 8 nozzle diameters downstream of the nozzle exit. This suggested that Case 1 had a larger supersonic flow region as compared to Case 2.

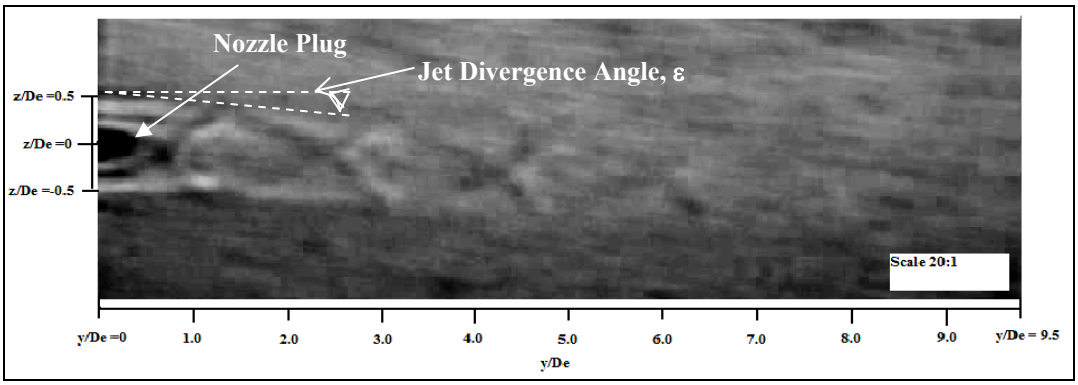

Figure 6.22 Shadowgraph Image of the Underexpanded Supersonic Microjet showing Shock Structure for Case 2: D_e = 616 μm , A_e = 0.298 μm^2, P_e/P_{amb} = 3.67 and NPR = 6.77.

Figure 6.23 presents the shadowgraph image captured for a nozzle exit area decreased by 50% of the nominal exit area shown in Figure 6.21. The nozzle plug was further extended into the nozzle exit flow as seen in the figure. There was evidence of supersonic shock structure for this nozzle exit area case. As observed in Figure 6.23, a shear layer was present between the nozzle exit primary flow and the still air surroundings. The supersonic shock structure was less evident than in the previous two cases suggesting a weaker shock structure was formed in the flow emanating from the nozzle exit. This was also supported by the amount of flow expansion observed in the shadowgraph image. There was also an observed jet divergence angle of $\varepsilon = 5.71^{o}$ (shown in Figure 6.22) as compared to the flow images of the nominal exit area case. The divergence angle measured was due to a fabrication defect in the needle plug resulting in a non-concentric circular cross-section for the manufactured

needle plug. By comparison of the maximum jet diameter in all three cases, it was observed that Case 1 showed more flow expansion than Case 2 and Case 3. Case 2 showed more flow expansion than Case 3 and the transition from supersonic to subsonic flow region in Case 3 occurred at approximately 7 nozzle diameters downstream of the nozzle exit.

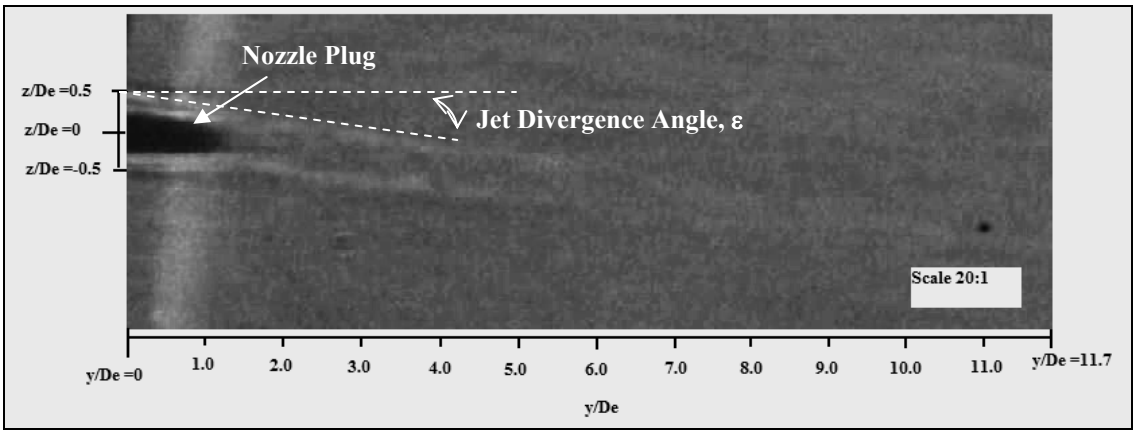

Figure 6.23 Shadowgraph Image of the Supersonic Microjet for Case 3: D_e = 503 μm, A_e = 0.199 μm^2, P_e/P_{amb} = 3.58 and NPR = 6.73.

The flow visualization images captured using the focused shadowgraph technique for the three nozzle exit area cases presented above clearly showed evidence of supersonic shock structure emanating from and extending several nozzle diameters downstream of the nozzle exit. All three cases showed underexpanded flow from a Mach 1.0 supersonic jet of 0.711 mm, 0.616 mm and 0.503 mm, respectively. The amount of underexpansion decreased from Case 1 through 3 and evidence in the shadowgraph images suggested that the amount of flow expansion at the nozzle exit decreased from Case 1 through 3. In addition, there was also an observed jet divergence angle of $\varepsilon = 7.12^o$ (shown in Figure 6.23) as compared to the flow images of the exit area Case 1 and 2. The divergence angle measured was also due to a fabrication defect in the needle plug resulting in a non-concentric circular cross-section observed on the nozzle plug.

A mixing shear layer between the supersonic flow region and the subsonic region of quiescent air was also observed in the three cases presented. There was no significant difference in the structure or behavior of the supersonic jets from the three nozzle diameters except that the location of shear layer transition varied between each case. Shear layer transition length decreased and jet spread increased as the nozzle exit area was decreased, respectively.

The results presented in this section were consistent with the findings of Scroggs and Settles[14] (1996) when they concluded from observations of supersonic microjets that the supersonic length grew at a slowly increasing rate as a supersonic flow transitioned from underexpanded to the overexpanded case. Scroggs and Settles also found that the perfectly-expanded condition for the nozzle flow was featureless and uniform since there was no pressure mismatch at the free shear layer boundary[14]. In underexpanded flow cases, the maximum diameter of a shock cell increased as exit pressure decreased and stagnation pressure increased[14].

In addition, Scroggs and Settles provided information on the supersonic length and location of shear layer transition. The research findings concluded that two modes of supersonic microjet transition were observed. The first mode was the classical shear layer instability that grew with increasing length along the free jet mixing layer[14]. This transitional zone was a radial growth with axial distance which was observed to be initially weak but increasing gradually in strength along the jet length[14]. The rate of growth was found at a minimum for perfectly expanded jets but increased for overexpanded or underexpanded conditions[14].

The second mode of transition was attributed to the dependence on exit pressure ratio (p_{amb}/p_e) and a result of acoustic-feedback-generated-instability[14]. Acoustic waves were captured and observed in Schlieren images. The research findings concluded that flow was disrupted downstream of the instability and turbulent mixing was stronger as the exit pressure ratio approached unity[14]. The location of the onset of subsonic mixing region moved further downstream from the nozzle exit as exit pressure ratio was decreased[14]. Figure 6.24 shows the three different regions in a supersonic jet and Figure 6.25 shows the correlated data for determination of supersonic length as a function of jet Mach number.

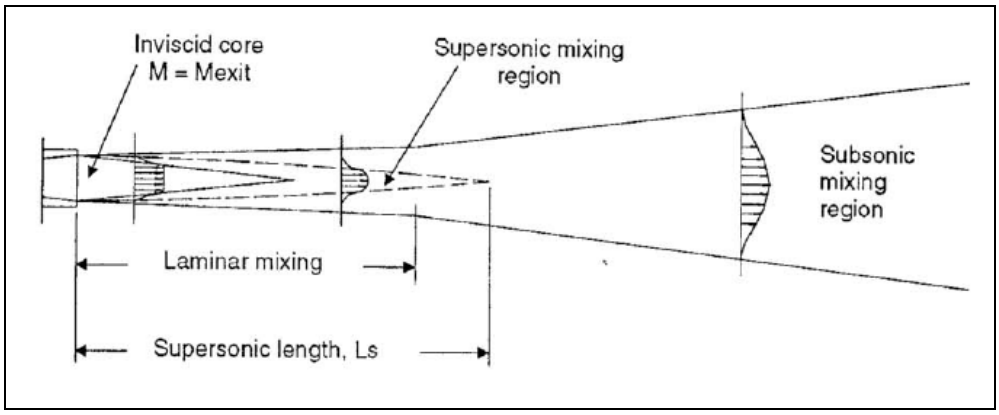

Figure 6.24 Three Regions of a Supersonic Microjet, Showing Approximate Velocity Profiles[14].

As seen from Figure 6.25 on the following page, a nozzle with a jet exit Mach number of 1.0 has a supersonic length of approximately 8 nozzle diameters downstream of the nozzle exit. The flow visualization pictures obtained from the shadowgraph technique for the three nozzle exit area cases in the present study also showed a supersonic core length that extended approximately 9.5 to 8 nozzle diameters downstream of the sonic nozzle exit with jet Mach number of 1.

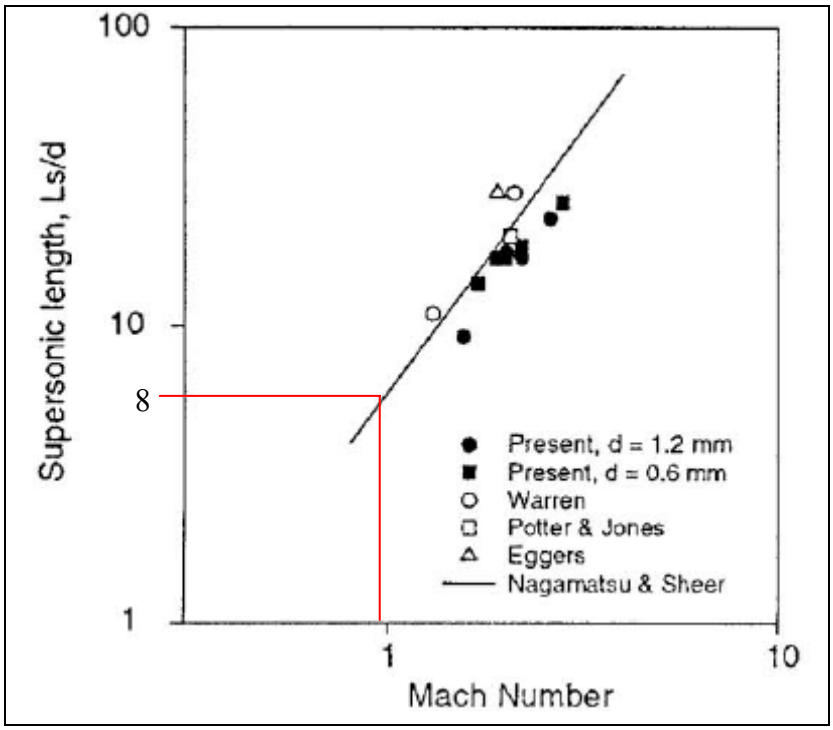

Figure 6.25 Microjet Non-Dimensional Supersonic Length, Other Investigator's Data and Correlation of Nagamatsu and Sheer[14].

The flow visualization pictures of nozzle exit area Cases 1 and 2 were consistent with the correlation of supersonic length and jet Mach number determined by Nagamatsu and Sheer[14] as described in Figure 6.25. The supersonic core length in the nozzle exit area Case 3 was not clearly captured and a conclusion cannot be made at this point on whether the findings were consistent with the supersonic length determined for Cases 1 and 2. According to the research of Scroggs and Settles[14], the results showed that turbulent mixing was stronger as the exit pressure ratio approached unity and the location of the onset of subsonic mixing region moved further downstream from the nozzle exit as exit pressure ratio was decreased[14].

The nozzle exit pressure ratio increased from nozzle exit area Case 1 through 3 for the present study and this implied that the location of the onset of subsonic mixing region measured downstream from the nozzle exit would be further downstream in Case 1 compared

to Cases 2 and Case 2 compared to Case 3, respectively. These findings could possibly explain the rate of jet spread and shear layer transition for each of the nozzle exit area cases resulting in larger values of shaft power extracted and aero-mechanical efficiency of power conversion when the planar bladed mini-turbine was placed further downstream of the nozzle exit face and when the nozzle exit area was decreased (nozzle exit pressure was decreased from Case 1 through 3) as determined in the current study.

7.0 CONCLUSIONS AND RECOMMENDATIONS

7.1 Conclusions of Present Study

An inexpensive method of power extraction from a supersonic jet using a mini-turbine assembly was developed. A gas generator was designed and built to provide pressurized air flow which exhausted into ambient air though a convergent nozzle with a plug needle valve and the kinetic energy related properties of very high pressure gas flow was investigated. A planar bladed mini-turbine assembly was placed in various positions relative to the nozzle exit jet centerline to determine the shaft power of the turbine when exposed to the nozzle exit flow.

Studies were also performed to determine the effect of the sonic nozzle area contraction ratio on the efficiency of mechanical work conversion from aerodynamic fluidic power. The flow emanating from the sonic nozzle exit was also visualized using the focused shadowgraph technique. Supersonic shock structures were visible in the nozzle exit gas flow and the effect of jet spreading of the flow impinging on the planar blades of the mini-turbine was also observed.

Reasonable values for the mechanical power output of the mini-turbine were obtained and reasonable percentages of power conversion from fluid aerodynamic power to mechanical shaft power were determined. The following conclusions were determined for the experiments carried out in this investigation:

i) Mechanical shaft power of approximately 1-2 W were measured and determined from the torque measurements carried out for the experiments.

ii) The aero-mechanical efficiency for the power conversion achieved from fluid aerodynamic power of the nozzle exit flow to the mechanical shaft power deduced from the measured data were in the reasonable range of 25% to 40%.

iii) The mini-turbine achieved the reasonable range of mechanical shaft power and aero-mechanical efficiencies with rotational speeds up to 50,000 RPM.

iv) The maximum values of mechanical shaft power and aero-mechanical efficiency increased when the nominal nozzle exit area was decreased by 25% and 50%, respectively.

v) The maximum values of mechanical shaft power and aero-mechanical efficiency increased when the mini-turbine was placed further away from the nozzle exit flow.

vi) The maximum values of mechanical shaft power and aero-mechanical efficiency varied as the mini-turbine was positioned in 10 different geometrical configurations relative to the nozzle exit flow.

vii) The flow visualization pictures provided evidence of visible diamond shock structures in the underexpanded flow emanating from the fully opened nozzle exit. There were supersonic shock cells and a supersonic core length observed for the flow in the near-field region.

viii) The observed supersonic core length was in the range of 8 to 9 nozzle exit diameters. The supersonic core length decreased as the nozzle exit area was decreased as observed in the flow visualization images captured.

ix) The maximum diameter of the supersonic jet from the nozzle exit decreased as the nozzle exit area was decreased by 25% and 50%, respectively. In addition, the shock cell spacing observed in the shadowgraph images increased with decreasing nozzle exit area.

7.2 Recommendations for Further Study

The current investigation was a proof of concept study that determined reasonable mechanical power output and aero-mechanical efficiencies. Further work needs to be done to justify the underlying assumptions in the current investigation and to fully understand the structure of the turbulent micro supersonic jet flow emanating from the exit of the mm-scale sonic plug nozzle. In addition, the current research can be expanded to design an efficient method of power extraction for implementation in future aerospace propulsion technologies.

The following recommendations are made for the improvement of the torque measurements in the present study:

i) Consider alternative methods of determining mini-turbine shaft torque accurately from the supersonic flow. These methods include the water-brake dynamometer, electrical dynamometer, electromagnetic brake dynamometer and hydraulic brake dynamometer.

ii) Consider using load cells to measure torque loads from the mini-turbine shaft so that data can be logged on a computer and analyzed.

iii) Consider the inclusion of pitot pressure probes and thermocouple sensors to measure pressure and temperature variation in the flow from nozzle exit to locations downstream of the nozzle exit. The pressure and temperature data measured can be used to map the velocity profile of the supersonic flow from the nozzle exit.

iv) Fabricate and test nozzles with larger exit areas to match Reynold's numbers in previous investigations of supersonic jet flow. In addition, consider the study of larger nozzle exit areas to determine whether data obtained is in good agreement with the results of the current study.

v) To reduce the frictional losses in the transfer of torque from the mini-turbine wheel to the motor shaft, it is recommended that an improved design for the coupling used in the current experiment to be fabricated.

The following recommendations are made for the supersonic flow visualization methods used for the current investigation:

i) Consider using various colored light sources and different focal length convex lens to obtain shadowgraph images of the supersonic jet with higher resolution and magnification.
ii) Increase the field of view of the current supersonic flow visualized to observe and capture the jet spreading and flow behavior further downstream of the nozzle exit. The correlation of empirical data and the observed experimental results can be complemented from such images.
iii) Consider using a Schlieren system to visualize the supersonic flow from the nozzle exit.
iv) Make improvements to the current Schlieren optical system of the University of Kansas, Department of Aerospace Engineering so that flow visualization images can be captured and observed for mini supersonic jets.
v) Consider making modifications to the current Schlieren optical system such that the nozzle tested in the current experiments are incorporated in the test section of the supersonic wind tunnel of the University of Kansas.

The following recommendations are made for further research for the investigation of the potential mechanical work extraction of mini-turbine assemblies from supersonic jets:

i) Investigate different nozzle configurations such as a convergent-divergent nozzle to determine the effect on flow expansion and aero-mechanical efficiency of power conversion.
ii) Investigate different nozzle exit shapes to determine the effect of rectangular, triangular or oval shaped nozzles on flow expansion and aero-mechanical efficiency of power conversion.
iii) Study the potential of mechanical work extraction from the fluid aerodynamic power available in supersonic flow from co-axial and stacked nozzles.
iv) Attach an electric generator to the mini-turbine shaft to determine the amount of electric power generated from the conversion of fluid aerodynamic power to mechanical shaft power.
v) Conduct additional studies to determine the amount of shaft power extracted and aero-mechanical efficiency achieved using the current setup by testing with different values of NPR. It is recommended to increase the nozzle supply pressure using a high pressure pumping system or by superheating of the gas flow at the nozzle exit.
vi) Investigate the potential mechanical work extraction from cold and heated supersonic jet flows using air and other types of gas combinations as the working fluid.
vii) Investigate the effect on aero-mechanical efficiency of power conversion when a mini-turbine with cambered airfoils is tested. Also, the study can be supplemented with experiments determining the effect of using shrouded and non-shrouded turbines, and the effect of utilizing turbine staging for power extraction from mm-scale supersonic jets.

8.0 REFERENCES

1. De Laval, C. G. P., "Steam-Turbine," Stockholm, Sweden, Application 1 May 1889, US Pat. No. 522,066, Issued 26 June 1894.

2. Stevens, T. and Hobart, H. M., *Steam Turbine Engineering*, The Macmillan Co., New York, 1906.

3. Lester, G. F., *Steam Turbines: Practice and Theory*, First Edition, The Technical Press, Brattleboro, VT, 1907.

4. Keding, M., Dudzinski, P., Tajmar, M., Willinger, R., and Käfer, K., "Development of a μ-Scale Turbine Expander for Energy Recovery," ASME Paper GT2009-59092, Proceedings of ASME Turbo Expo 2009: Power for Land, Sea and Air, GT2009, June 8-12, 2009, Orlando, Florida.

5. Krähenbühl, D., Zwyssig, C., Hörler, H. and Kolar, J. W., "Design Considerations and Experimental Results of a 60 W Compressed-Air-to-Electric-Power System," Journal of Micromechanics and Microengineering, Vol. 19, No. 9, August 2009. Institute of Physics Publications.

6. Krähenbühl, D., Zwyssig, C., Hörler, H. and Kolar, J. W., "Theoretical and Experimental Results of a Mesoscale Electric Power Generation System from Pressurized Gas Flow," Journal of Micromechanics and Microengineering, Vol. 19, No. 9, August 2009. Institute of Physics Publications.

7. Peirs, J., Reynaerts, D., and Verplaetsen, F., "Development of an Axial Microturbine for a Portable Gas Turbine Generator," Journal of Micromechanics and Microengineering, Vol. 13, Pg. 190-195, June 2003. Institute of Physics Publications.

8. Peirs, J., Reynaerts, D., and Verplaetsen, F., "A Micro Gas Turbine Unit for Electric Power Generation: Design and Testing of Turbine and Compressor," Conference Proceedings of Actuator 2004, 9th International Conference on New Actuators, 14-16 June 2004, Bremen, Germany.

9. Peirs, J., Reynaerts, D., Verplaetsen, F., Norman, F., and Lefever, S., "Development of A Micro Gas Turbine for Electric Power Generation," MME 2003, 14th Micromechanics Europe Workshop, 2–4 November 2003, Delft University of Technology, Netherlands.

10. Norman, M. L., Smarr, L., Winkler, K.–H. A., and Smith, M. D., "Structure and Dynamics of Supersonic Jets," Journal of Astronomy and Astrophysics, Vol. 113, Pg. 285-302, May 1982.

8.0 REFERENCES (CONT'D)

11. Adamson, T.C. JR., and Nicholls, J. A., "On the Structure of Jets from Highly Underexpanded Nozzles into Still Air," Journal of Aerospace Sciences, Vol. 26, Pg. 16-24, January 1959.

12. Otobe, Y., Kashimura, H., Matsuo, S., Setoguchi, T., and Kim, H.-D., "Influence of Nozzle Geometry on the Near-Field Structure of a Highly Underexpanded Sonic Jet," Journal of Fluids and Structure, Vol. 24, Pg. 281-293, July 2007.

13. Lee, K.-H., Setoguchi, T., Matsuo, S., and Kim, H.-D., "An Experimental Study of Underexpanded Sonic, Coaxial, Swirl Jets," Journal of Mechanical Engineering Science, Vol. 217 Part C, Pg. 93-103, January 2004.

14. Scroggs, S. D. and Settles, G. S., "An Experimental Study of Supersonic Microjets," Journal of Experiments in Fluids, Vol. 21, Pg. 401-409, April 1996.

15. Phalnikar, K. A., Alvi, F. S., and Shih, C., "Behavior of Free and Impinging Supersonic Microjets," AIAA Paper 2001-3047, 31st AIAA Fluid Dynamics Conference and Exhibit, Anaheim, CA, June 2001.

16. Tam, C. K. W., "Mach Wave Radiation from High-Speed Jets," AIAA Journal, Vol. 47, No. 10, Pg. 2440-2448, October 2009.

17. Farokhi, S., *Aircraft Propulsion*, First Edition, John Wiley & Sons, Inc., New Jersey, 2009.

18. Anon., "HiP: Ultra-High Pressure Equipment Products," High Pressure Equipment Company Product Catalog, Erie, Pennsylvania, 2008.

19. Anon., "Omega Engineering Inc.: All Stainless Steel Digital Pressure Gauge DPG6000" Omega Engineering Inc. Company Product Catalog, Stamford, Connecticut, 2009.

20. Anon., "CEN-TECH Instruments: InfraRed Thermometer 91778," CEN-TECH Instruments Product Specifications, accessed on 12/07/2009, http://www.harborfreight.com/cpi/ctaf/Category.taf?f=bylogo&logourl=Centech.gif&brand=Cen-Tech.

21. Anon., "EXTECH Instruments: Photo Tachometer 461893," EXTECH Instruments Company Product Catalog, Waltham, Massachusetts, 2009.

22. Anon., "EXTECH Instruments: Digital Single Output DC Power Supply 382203," EXTECH Instruments Company Product Catalog, Waltham, Massachusetts, 2009.

8.0 REFERENCES (CONT'D)

23. Anon., "Nikon Digital SLR Camera D5000 Specifications," Nikon Inc. Product Brochure SLR D5000, Melville, New York, 2009.

24. Love, E. S., Grigsby, C. E., Lee, L. P., and Woodling, M. J., "Experimental and Theoretical Studies of Axisymmetric Free Jets," NASA Technical Report, TR-6, 1959, Langley Research Center, Langley Field, Virginia, USA.

25. Anderson, J. D., *Modern Compressible Flow: With Historical Perspective*, Third Edition, McGraw-Hill, New York, 2003.

26. Gostintsev, Y. A., Zelentsov, V. V., Ilyuikhin, V. S., and Pokhil P.F., "Structure of Underexpanded Supersonic Swirling Jet," Journal of Fluid Dynamics, Vol. 4, No. 5, Pg. 105-107, September 1969.

27. Hebbar, K. S., Sridhara, K., and Paranjpe, P. A., "Performance of Conical Jet Nozzles in Terms of Discharge Coefficient," Journal of the Aeronautical Society of India, Vol. 22, No. 1, February 1970.

28. Kedia, K. S. and Kurian, J., "Supersonic Freejets from Shaped Nozzles," Conference Paper, 32nd National Conference on Fluid Mechanics & Fluid Power, 15-17 December 2005, Osmanabad, Maharashtra.

29. Miller, S. A. E., Veltin, J., Morris, P. J. and McLaughlin, D. K., "Assessment of Computational Fluid Dynamics for Supersonic Shock Containing Jets," AIAA Paper 2988, AIAA Journal, Vol. 47, No. 11, Pg. 2738-2746, November 2009, 14th AIAA/CEAS Aeroacoustics Conference, 5-7 May 2008, Vancouver BC, Canada.

30. Lovaraju, P., Clement, S. and Rathakrishnan, E., "Effect of Cross-wire and Tabs on Sonic Jet Structure," Journal of Shock Waves, Vol. 17, No. 1-2, Pg. 71-83, August 2007.

31. Katanoda, H., Miyazato, Y., Masuda, M., and Matsuo, K., "Pitot Pressure of Correctly Expanded and Underexpanded Free Jets from Axisymmetric Supersonic Nozzles," Journal of Shock Waves, Vol. 10, No. 2, Pg. 95-101, May 2000.

32. Krothapalli, A., Rajkuperan, E., Alvi, F. and Lourenco, L., "Flow Field and Noise Characteristics of a Supersonic Impinging Jet," Journal of Fluid Mechanics, Vol. 392, Pg. 155-181, 1999.

33. Zapryagaev, V. I. and Solotchin, A. V., "Three-dimensional Structure of Flow in a Supersonic Underexpanded Jet," Journal of Applied Mechanics and Technical Physics, Vol. 32, No. 4, Pg. 503-507, July 1991.

8.0 REFERENCES (CONT'D)

34. Papamoschou, D., "Structure of the Compressible Turbulent Shear Layer," AIAA Paper 1989-0126, 27th Aerospace Sciences Meeting, 9-12 January 1989, Reno, Nevada, USA.

35. Papamoschou, D. and Roshko, A., "The Compressible Turbulent Shear Layer: An Experimental Study," Journal of Fluid Mechanics, Vol. 197, Pg. 453-477, May 1988.

36. Papamoschou, D. and Roshko, A., "Observations of Supersonic Shear Layers," Sadhana Journal, Vol. 12, Pg. 1-14, February 1988.

37. Bogdanoff, D. W., "Compressibility Effects in Turbulent Shear Layers," AIAA Journal, Vol. 21, Pg 926-927, June 1983.

38. Chuech, S. G., Lai, M. C., and Faeth, G. M., "Structure of Turbulent Sonic Underexpanded Free Jets," AIAA Journal, Vol. 27, No. 5, Pg. 549-559, May 1989.

39. Iyogun, C. O. and Birouk, M., "Effect of Sudden Expansion on Entrainment and Spreading Rates of a Jet Issuing from Asymmetric Nozzles," Flow Turbulence Combustion Journal, Vol. 82, Pg. 287-315, September 2008.

40. Wishart, D. P. and Krothapalli, A., "On the Structure of a Heated Supersonic Jet," AIAA Paper 94-0666, 32nd Aerospace Sciences Meeting & Exhibit, 10-13 January 1994, Reno, Nevada, USA.

41. Crist, S., Sherman, P.M., and Glass, D. R., "Study of Highly Underexpanded Sonic Jet," AIAA Journal, Vol. 4, No. 1, Pg. 68-71, January 1966.

42. Crist, S., "Experimental Study of the Shock Structure of a Highly Underexpanded Jet Exhausting from a Sonic Nozzle," AIAA Student Journal, Vol. 3, No. 2, Pg. 43-48, April 1965.

43. Glass, D. R., "Effects on Acoustic Feedback on the Spread and Decay of Supersonic Jets," AIAA Journal, Vol. 6, No. 10, Pg. 1890-1897, October 1968.

44. Zaman, K. B. M. Q., "Spreading Characteristics of Compressible Jets from Nozzles of Various Geometries," Journal of Fluid Mechanics, Vol. 383, Pg. 197-228, October 1998.

45. Shadow, K. C., Gutmark, E., and Wilson, K. J., "Compressible Spreading Rates of Supersonic Coaxial Jets," Experiments in Fluids Journal, Pg. 161-167, December 1990.

46. Ramesh, R., Pradeep, S., Muruganandam, T. M., and Sujith, R. I., "Studies on Freejets from Nozzles for High-Speed Mixing Applications," Experiments in Fluids Journal, Vol. 29, Pg. 359-368, November 1999.

APPENDIX A: EXPERIMENTAL EQUIPMENT SPECIFICATIONS

This Appendix section tabulates the various components and experimental instrumentation used for the present study.

High Pressure Equipment

Series "R" Reactors
O-Ring Closure

The Series "R" O-ring Closure Reactors are easily assembled and disassembled with minimal torque required for complete engagement.

Material of construction for standard models is Type 4340 alloy steel (or equivalent) properly heat treated for use at elevated pressures. (Some models can be provided in stainless steel construction at reduced pressures — consult factory).

Sealing is accomplished by a highly reliable combination of O-ring and separate metal back-up ring. The wedge shaped back-up ring is designed to expand and contact as pressure increases or decreases. Consequently, the O-ring is continuously confined with no clearance for extrusion. Minimal initial torque is required to effect a positive seal.

Temperature on these vessels must be restricted to 250°F maximum, due to the BUNA-N (nitrile) O-ring.

(continued on page 10.9)

O-Ring Closure Reactors *(one piece cover)*

I.D.	O.D.	Pressure Rating psi	Material	Inside Depth 6"	10"	12"	16"	20"	24"
1"	3 1/8"	30,000	4340 Alloy Steel or equivalent	R1-6-30	R1-10-30	R1-12-30	R1-16-30		
	3 1/2"	40,000		R1-6-40	R1-10-40	R1-12-40	R1-16-40		
	4 1/4"	60,000		R1-6-60	R1-10-60	R1-12-60	R1-16-60		
	5 1/2"	100,000		R1-6-100	R1-10-100	R1-12-100	R1-16-100		
	6 3/4"	150,000		R1-6-150	R1-10-150	R1-12-150	R1-16-150		
1 1/2"	3 5/8"	20,000	4340 Alloy Steel or equivalent	R1.5-6-20	R1.5-10-20	R1.5-12-20	R1.5-16-20		
	4 1/8"	30,000		R1.5-6-30	R1.5-10-30	R1.5-12-30	R1.5-16-30		
	4 3/4"	40,000		R1.5-6-40	R1.5-10-40	R1.5-12-40	R1.5-16-40		
	6 1/2"	60,000		R1.5-6-60	R1.5-10-60	R1.5-12-60	R1.5-16-60		
	8"	100,000		R1.5-6-100	R1.5-10-100	R1.5-12-100	R1.5-16-100		
	10 1/2"	150,000		R1.5-6-150	R1.5-10-150	R1.5-12-150	R1.5-16-150		
2"	4 1/4"	20,000	4340 Alloy Steel or equivalent	R2-6-20	R2-10-20	R2-12-20	R2-16-20	R2-20-20	R2-24-20
	5"	30,000		R2-6-30	R2-10-30	R2-12-30	R2-16-30	R2-20-30	R2-24-30
	6 1/2"	40,000		R2-6-40	R2-10-40	R2-12-40	R2-16-40	R2-20-40	R2-24-40
	8 1/2"	60,000		R2-6-60	R2-10-60	R2-12-60	R2-16-60	R2-20-60	R2-24-60
	12"	100,000		R2-6-100	R2-10-100	R2-12-100	R2-16-100	R2-20-100	R2-24-100

Figure A-1 Information Adapted from Hi Pressure Equipment Company Product Catalog for High Pressure Reactors[18] (Highlighted information describes maximum pressure ratings and geometrical characteristics selected for experimental setup).

Ultra High Pressure Valves

150,000 psi service

High Pressure (coned and threaded) type connections for 3/8" O.D. by 1/16" I.D. tubing.

Non-rotating tip stems insure long life on valve seats. Heavy duty "rolled style" stem design is shown below.

Glands and collars for tubing are supplied with each valve unless otherwise requested (glands and collars are shown on page 5.A).

Materials include 17-4 PH for valve bodies with tool steel lower section stems. Valve packing is teflon.

Corresponding fittings (elbows, tees, crosses, etc.) are shown on page 5.4.

Replaceable Seat Valves are available for 3/8" O.D. tubing. These valves feature the same body style and dimensions as the two way valves (shown below).

To order add "R" to the corresponding two way valve catalog number (eg. 150-12XF6R).

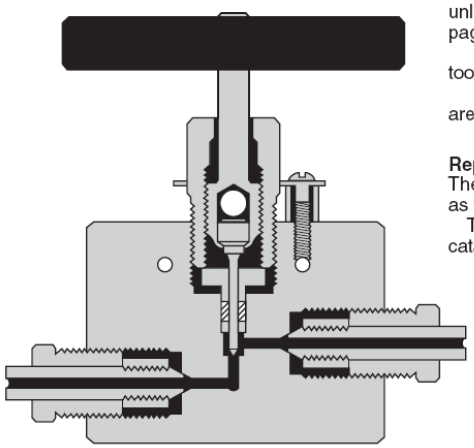

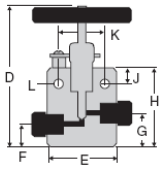

Two Way Straight

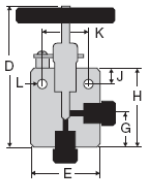

Two Way Angle

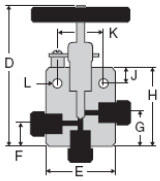

Three Way Two Inlets

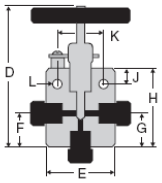

Three Way One Inlet

Manual Shutoff Valves

Body Pattern	Tubing	Catalog No.	psi	Connection	Orifice	D	E	F	G	H	J	K	L	Thickness
2-Way Straight	3/8" O.D.	150-11XF6	150,000	XF6	1/16"	5"	3 1/2"	7/8"	1 3/16"	2 5/8"	1/2"	1 5/8"	7/32"	1 1/2"
2-Way Angle	3/8" O.D.	150-12XF6	150,000	XF6	1/16"	5 7/8"	3 1/2"	—	2 1/16"	3 1/2"	1/2"	1 5/8"	7/32"	1 1/2"
3-Way/2 Inlets	3/8" O.D.	150-13XF6	150,000	XF6	1/16"	5 7/8"	3 1/2"	1 3/4"	2 1/16"	3 1/2"	1/2"	1 5/8"	7/32"	1 1/2"
3-Way/1 Inlet	3/8" O.D.	150-14XF6	150,000	XF6	1/16"	5 7/8"	3 1/2"	2 1/16"	2 1/16"	3 1/2"	1/2"	1 5/8"	7/32"	1 1/2"

Figure A-2 Information Adapted from Hi Pressure Equipment Company Product Catalog for High Pressure Valves[18] (Highlighted information describes maximum pressure ratings and geometrical characteristics selected for experimental setup).

High Pressure Equipment

Fittings/Check Valves

We have developed check valves, elbows, tees and crosses for both the 100,000 and 150,000 psi systems. *Material is high tensile 316 stainless steel. Standard tubing glands and collars are furnished unless otherwise specified.

* **Note:** Material for 150,000 psi check valve is 17-4 PH.

Ultra High Pressure Check Valves

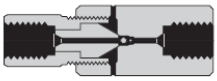

Catalog No.	psi	Connections	Length	Hex
100-41XF4	100,000	1/4" ULTRA PRESSURE	3 9/16"	1 1/2"
150-41XF6	150,000	3/8" ULTRA PRESSURE	4 1/2"	1 1/2"

Ultra High Pressure Elbows

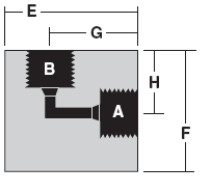

Catalog No.	Pressure Rating psi	Connections	A-B-C-D	E	F	G	H	Thickness
100-22XF4	100,000	1/4" O.D. TUBE	XF4	1 3/4"	1 3/4"	1 1/4"	1 1/4"	1"
150-22XF6	150,000	3/8" O.D. TUBE	XF6	2 5/8"	2 5/8"	1 3/4"	1 3/4"	1 1/2"

Ultra High Pressure Tees

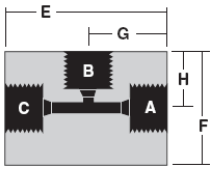

Catalog No.	Pressure Rating psi	Connections	A-B-C-D	E	F	G	H	Thickness
100-23XF4	100,000	1/4" O.D. TUBE	XF4	2 1/2"	1 3/4"	1 1/4"	1 1/4"	1"
150-23XF6	150,000	3/8" O.D. TUBE	XF6	3 1/2"	2 5/8"	1 3/4"	1 3/4"	1 1/2"

Ultra High Pressure Crosses

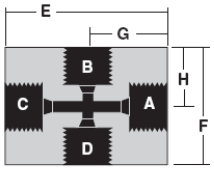

Catalog No.	Pressure Rating psi	Connections	A-B-C-D	E	F	G	H	Thickness
100-24XF4	100,000	1/4" O.D. TUBE	XF4	2 1/2"	2 1/2"	1 1/4"	1 1/4"	1"
150-24XF6	150,000	3/8" O.D. TUBE	XF6	3 1/2"	3 1/2"	1 3/4"	1 3/4"	1 1/2"

Figure A-3 Information Adapted from Hi Pressure Equipment Company Product Catalog for High Pressure Fittings[18] (Highlighted information describes maximum pressure ratings and geometrical characteristics selected for experimental setup).

Ultra High Pressure Tubing

Tubing is cold drawn, seamless, and is supplied in the 1/8 hard condition (not annealed). Tensile strength is approximately 40 percent higher than that of annealed tubing. All tubing is manufactured in strict accordance with High Pressure Equipment Company specifications to insure tolerances and bore quality. Tubing is stocked in lengths of 18 to 22 feet but may be ordered in shorter lengths with **no additional cutting charge.**

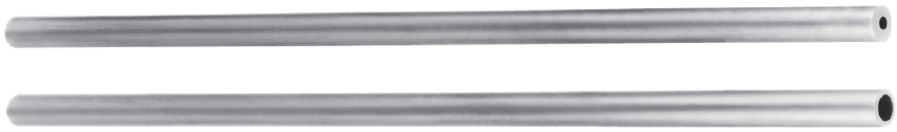

	Tubing Size	Working Pressure psi	Type of Connection Used	Material	Catalog Order Number
1/4"	1/4" O.D. x 1/16" I.D.	100,000	1/4" ULTRA HIGH PRESSURE (XF4)	316 SS	100-9X4-316
				304 SS	100-9X4-304
3/8"	3/8" O.D. x 1/16" I.D.	150,000	3/8" ULTRA HIGH PRESSURE (XF6)	304 SS	150-9X6

Figure A-4 Information Adapted from Hi Pressure Equipment Company Product Catalog for High Pressure Tubing[18] (Highlighted information describes maximum pressure ratings and geometrical characteristics selected for experimental setup).

Caps

Tubing end caps are offered for use in sealing off tubing ends either for temporary use or permanent use such as on small volume reservoirs. Standard material is high tensile 316 stainless steel. Standard tubing collars and glands are provided unless otherwise specified.

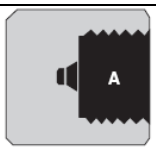

Catalog No.	Pressure Rating psi	Connections	A	Length	Hex Size
60-21HF2-C	60,000	1/8" O.D. TUBING	HF2	7/8"	3/4"
60-21HF4-C	60,000	1/4" O.D. TUBING	HF4	7/8"	3/4"
60-21HF6-C	60,000	3/8" O.D. TUBING	HF6	1 1/4"	1"
60-21HF9-C	60,000	9/16" O.D. TUBING	HF9	1 1/2"	1 3/8"
40-21HF9-C	40,000	9/16" O.D. TUBING	HF9	1 1/2"	1 3/8"
30-21HF16-C	30,000	1" O.D. TUBING	HF16	3"	1 3/4"

Figure A-5 Information Adapted from Hi Pressure Equipment Company Product Catalog for High Pressure End Caps[18] (Highlighted information describes maximum pressure ratings and geometrical characteristics selected for experimental setup).

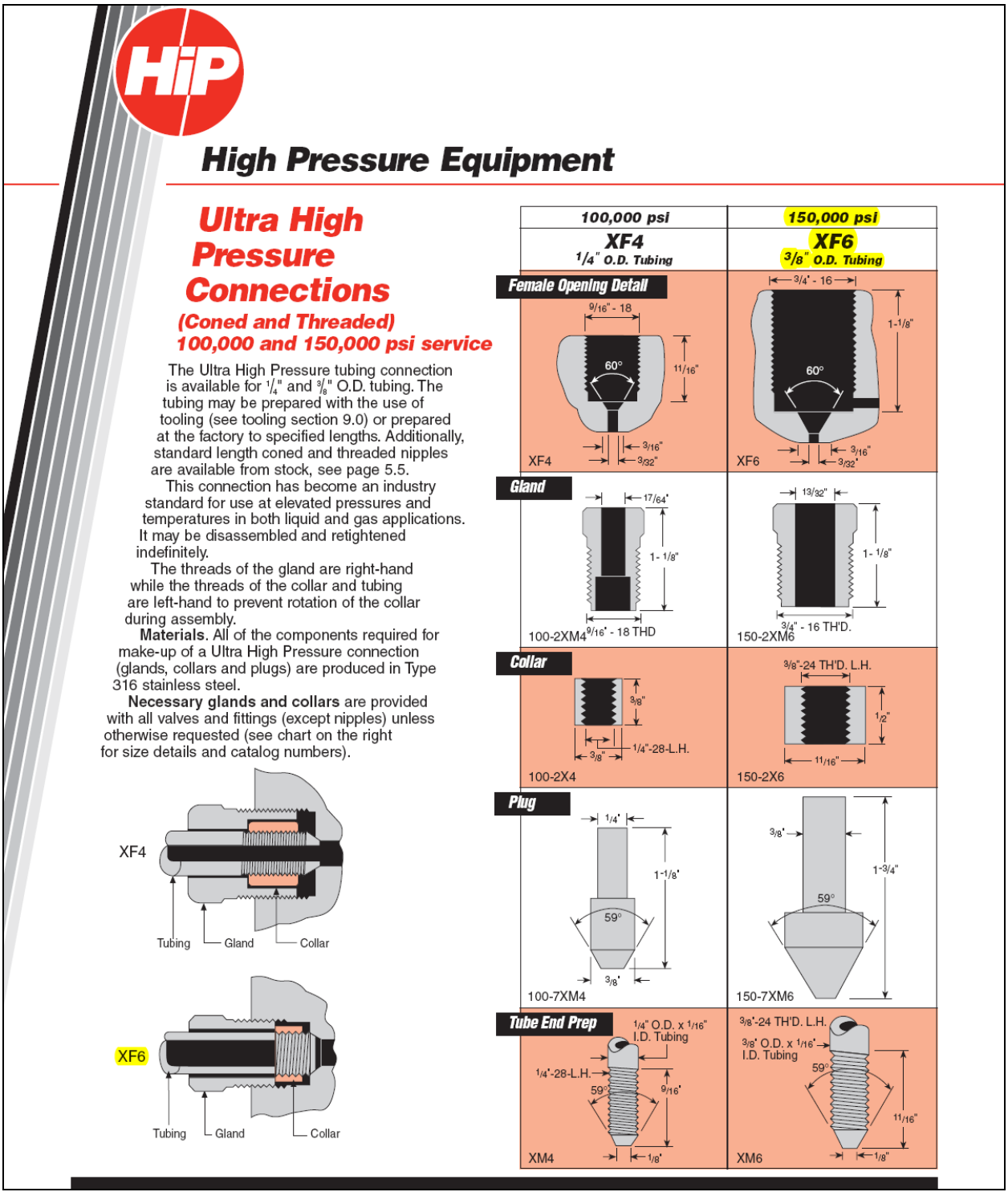

Figure A-6 Information Adapted from Hi Pressure Equipment Company Product Catalog for High Pressure Fittings[18] (Highlighted information describes maximum pressure ratings and geometrical characteristics selected for experimental setup).

Pressure Gauges

Standard pressure gauges as shown are available from stock for immediate delivery. Gauge models 4PG5 through 6PG50 are standard with a High Pressure ¼" O.D. tubing connection (HF4), while models 6PG75, 6PG100 and 6PG150 have a Ultra High Pressure ⅜" O.D. tubing connection (XF6). These coned and threaded connections are machined directly into the bottom inlet of the gauges. Adapters for other size connections are available from stock.

These gauges have a solid front separating the dial face from the pressure tube in order to provide maximum safety. Bourdon tube and socket are 316 S.S. on all gauges. Both styles include a safety blowout back. 5,000 psi to 30,000 psi gauges have laminated safety glass, while the 50,000 psi to 150,000 psi style have a removable polycarbonate plastic front window.

Gauges may be used intermittently to 100 percent of dial reading.

Accuracy on 5,000 psi and 10,000 psi models is ½% of full scale reading. Accuracy on 20,000 psi through 30,000 psi models is 1% of full scale reading. Accuracy on 50,000 psi through 150,000 psi models is ½% of full scale reading.

PANEL MOUNTING: 4PG5, 4PG10, 6PG20, 6PG30

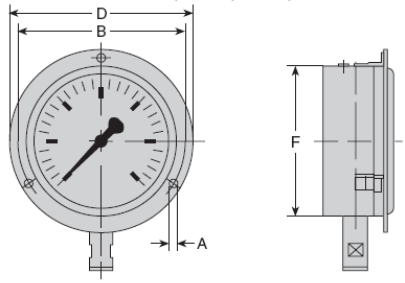

SURFACE MOUNTING: 6PG50, 6PG75, 6PG100

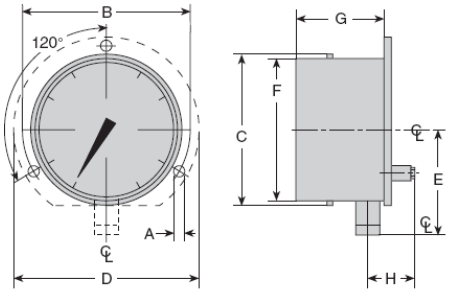

Standard Gauges In Stock

Gauge Size						Materials	
Catalog No.	Range psi	Dial Size	Graduations			Mounting	Case
4PG5	0-5,000	4"	500	100	50	Panel	316 S.S.
4PG10	0-10,000	4"	1,000	500	100		
6PG20	0-20,000	6"	2,000	1,000	200		
6PG30	0-30,000	6"	3,000	1,000	200		
6PG50	0-50,000	6"	5,000	2,500	500	* Surface	Heavy Duty Alum.
6PG75	0-75,000	6"	10,000	2,500	500		
6PG100	0-100,000	6"	10,000	5,000	1,000		
6PG150	0-150,000	6"	20,000	10,000	1,000		

* Panel mount kit available. Contact factory.

Dimensions

Dial Size	A	B	C	D	E	F	G	H
4" 4PG5, 4PG10	3/16"	4 35/64"	—	5 3/16"	—	3 7/8"	—	—
6" 6PG20, 6PG30	7/32"	7"	—	7 11/16"	—	6 1/4" – 6 5/16"	—	—
6" 6PG50, 6PG75, 6PG100, 6PG150	9/32"	7"	6 5/8"	7 5/8"	4 3/8"	6 3/8"	3 5/8"	1 3/4"

Figure A-7 Information Adapted from Hi Pressure Equipment Company Product Catalog for High Pressure Gauges[18] (Highlighted information describes maximum pressure ratings and geometrical characteristics selected for experimental setup).

ALL STAINLESS STEEL DIGITAL GAUGE
BATTERY POWERED

NEW

Shown smaller than actual size

DPG6000L
$500
psig Ranges

MADE IN USA · 1 YEAR WARRANTY

DPG6000L Series
15 to 2,000 psi

- Self-Powered by 2 "C" Size Lithium Batteries, Included
- Large, Easy to Read LCD Display
- All Stainless Steel

The latest in solid state design, the DPG6000L incorporates a semiconductor strain gage pressure transducer as the sensing element, conditioned by hybrid circuitry. The unit requires very little power, resulting in battery life of over two years with continuous operation. A low battery indicator is standard on all units.

The DPG6000L directly replaces many larger mechanical gauges while giving improved accuracy, readability, and durability. The digital circuitry averages and displays pulsating pressures which would quickly ruin a mechanical gauge. The DPG6000L has found wide acceptance in applications ranging from process measurements to use as a portable pressure standard.

Dimensions in mm (inches)

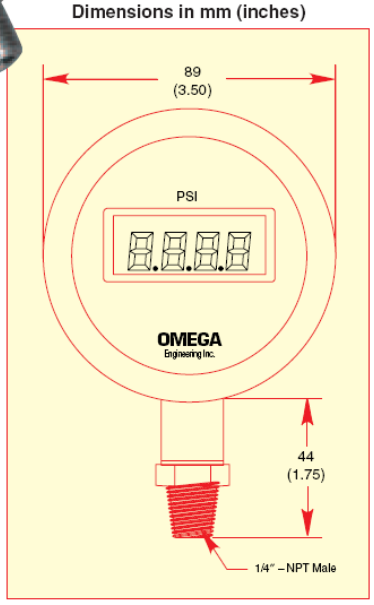

SPECIFICATIONS

Accuracy (linearity, hysteresis, and repeatability):
15: ±0.6% FS +1 LSD
30: ±0.3% FS +1 LSD
All other ranges: ±0.25% FS + 1 LSD
Overpressure: 2x full scale without damage
Burst Pressure: 10x full scale minimum
Pressure Cavity Volume: 0.06 in^3
Media Temperature: -18 to 82°C (0 to 180°F)
Storage Temperature: -40 to 71°C (-40 to 160°F)
Compensated Temperature: -1 to 71°C (30 to 130°F)
Thermal Zero Shift: ±0.02% F.S./0.6°C (±0.02% F.S./°F)
Thermal Sensitivity Shift: ±0.02% F.S./°F
Durability: >10 million cycles
Batteries: Lithium Thionyl Chloride, 2 cells, user replaceable, C-size included
Battery Life: 2 years normal operation
Voltage: 3.6 V/cell, no-load
Capacity: 5.2 Ah/cell
Type: LCD, seven segments, 13 mm (0.5") height digits
Overload: Displays "1---" when nominal pressure range is exceeded
Low Battery Detection: Displays "LOBAT" when approximately 80% of the capacity is depleted
Case: Stainless Steel 15-5 PH
Wetted Parts: 15-5 PH SS

☐ ***MOST POPULAR MODELS HIGHLIGHTED!***

To Order *(Specify Model Number)*

RANGE (psi)	MODEL NO.	PRICE	DESCRIPTION
0 to 15.0	DPG6000L-15G	$630	Lower fitting, psig range
0 to 30.0	DPG6000L-30G	630	Lower fitting, psig range
0 to 60.0	DPG6000L-60G	630	Lower fitting, psig range
0 to 100.0	DPG6000L-100G	500	Lower fitting, psig range
0 to 500	DPG6000L-500G	500	Lower fitting, psig range
0 to 1000	DPG6000L-1KG	500	Lower fitting, psig range
0 to 1999	DPG6000L-2KG	500	Lower fitting, psig range

*To order absolute pressure, replace the last "**G**" in the model number with an "**A**" and add **$65** to the price.*

Ordering Example: DPG6000L-100G** is a 100 psig, all stainless steel gage, **$500.

Figure A-8 Information Adapted from Omega Engineering Inc. Product Catalog for Digital Pressure Gauges[19] (Highlighted information describes specific model selected for experimental setup).

EXTECH INSTRUMENTS
A FLIR COMPANY

Experience the Extech Advantage

PRODUCT DATASHEET

Photo Tachometer

Non-Contact rpm and speed measurements

From 2 to 6 inches (50 to 150mm) measurement distance from target

Features:

- Large 5 digit LCD display is easy to read
- Built-in memory recalls last MAX/MIN value stored
- Autoranging with 0.05% accuracy
- Non-contact measurements from 5 to 99,999rpm
- Use reflective marker on object to be measured and point the integral light beam or accurate readings updated every second
- 2 to 6 inches (50 to 150mm) measurement distance (depending on ambient light)
- Complete with 23" reflective tape, four AA batteries and case

Non-contact measurement on machinery where access is limited

Specifications	
Range (rpm)	5 to 99,999
Accuracy	±(0.05%rdg +1d)
Sampling Time	1sec > 60rpm
Resolution	0.1rpm (0.5 to 999.9rpm);1rpm (>1000rpm)
Dimensions	6.7 x 2.8 x 1.5" (170 x 27 x 37mm)
Weight	8.8oz (250g)

Specifications	
Range (rpm)	5 to 99,999
Accuracy	±(0.05%rdg +1d)
Sampling Time	1sec > 60rpm
Resolution	0.1rpm (0.5 to 999.9rpm);1rpm (>1000rpm)
Dimensions	6.7 x 2.8 x 1.5" (170 x 27 x 37mm)
Weight	8.8oz (250g)

Figure A-9 Information Adapted from Extech Instruments Product Catalog for Digital Non-Contact Photo Tachometer selected for experimental setup[21].

Nikon Digital SLR Camera D5000 Specifications

Type	
Type	Single-lens reflex digital camera
Lens mount	Nikon F mount (with AF contacts)
Effective picture angle	Approx. 1.5 x lens focal length (Nikon DX format)
Effective pixels	
Effective pixels	12.3 million
Image sensor	
Image sensor	23.6 x 15.8 mm CMOS sensor
Total pixels	12.9 million
Dust-reduction system	Image Sensor Cleaning, Image Dust Off reference data (optional Capture NX 2 required)
Storage	
Image size (pixels)	4,288 x 2,848 [L], 3,216 x 2,136 [M], 2,144 x 1,424 [S]
File format	• NEF (RAW) • JPEG: JPEG-Baseline compliant with fine (approx. 1:4), normal (approx. 1:8), or basic (approx. 1:16) compression • NEF (RAW) + JPEG: Single photograph recorded in both NEF (RAW) and JPEG formats
Picture Control System	Can be selected from Standard, Neutral, Vivid, Monochrome, Portrait, Landscape; storage for up to nine custom Picture Controls
Media	SD memory cards, SDHC compliant
File system	DCF (Design Rule for Camera File System) 2.0, DPOF (Digital Print Order Format), Exif 2.21 (Exchangeable Image File Format for Digital Still Cameras), PictBridge
Viewfinder	
Viewfinder	Eye-level pentamirror single-lens reflex viewfinder
Frame coverage	Approx. 95% horizontal and 95% vertical
Magnification	Approx. 0.78 x (50 mm f/1.4 lens at infinity; -1.0 m^{-1})
Eyepoint	17.9 mm (-1.0 m^{-1})
Diopter adjustment	-1.7 to + 0.7 m^{-1}
Focusing screen	Type B BriteView Clear Matte screen Mark V with focus frame (framing grid can be displayed)
Reflex mirror	Quick-return type
Lens aperture	Instant return, electronically controlled
Lens	
Compatible lenses	• AF-S and AF-I NIKKOR: All functions supported • Type G or D AF NIKKOR not equipped with an autofocus motor: All functions supported except autofocus • Non-Type G or D AF NIKKOR not equipped with an autofocus motor: All functions supported except 3D color matrix metering II and autofocus • IX-NIKKOR and AF-NIKKOR for F3AF: Not supported • Type D PC NIKKOR: All functions supported except some shooting modes • AI-P NIKKOR: All functions supported except 3D color matrix metering II • Non-CPU: Autofocus not supported. Can be used in exposure mode M, but exposure meter does not function • Lens with maximum aperture of f/5.6 or faster: Electronic rangefinder can be used
Shutter	
Type	Electronically controlled vertical-travel focal-plane shutter
Speed	1/4,000 to 30 s in steps of 1/3 or 1/2 EV, Bulb, Time (with optional ML-L3 Remote Control)
Flash sync speed	X = 1/200 s; synchronizes with shutter at 1/200 s or slower
Release	
Release mode	[S] Single-frame, continuous, self-timer, quick-response, 2s delayed remote, [Q] quiet
Frame advance rate	Continuous high speed: up to 4 fps (manual focus, manual or shutter-priority auto exposure, 1/250 s or faster shutter speed; other settings at default values and memory remaining in memory buffer)
Self-timer	Can be selected from 2, 5, 10, and 20 s duration
Exposure	
Metering	TTL exposure metering using 420-pixel RGB sensor
Metering method	• Matrix: 3D color matrix metering II (type G and D lenses); color matrix metering II (other CPU lenses) • Center-weighted: Weight of 75% given to 8-mm circle in center of frame • Spot: Meters 3.5-mm circle (about 2.5% of frame) centered on selected focus point
Range (ISO 100 equivalent, f/1.4 lens, 68°F/20°C)	• Matrix or center-weighted metering: 0–20 EV • Spot metering: 2–20 EV
Exposure meter coupling	CPU
Exposure modes	Auto modes (auto, auto [flash off]), Advanced Scene Modes (Portrait, Landscape, Child, Sports, Close up, Night portrait, Night landscape, Party/indoor, Beach/snow, Sunset, Dusk/dawn, Pet portrait, Candlelight, Blossom, Autumn colors, Food, Silhouette, High key, and Low key), programmed auto with flexible program (P), shutter-priority auto (S), aperture-priority auto (A), manual (M)
Exposure compensation	±5 EV in increments of 1/3 or 1/2 EV
Auto exposure bracketing	3 frames in steps of 1/3 or 1/2 EV
Auto exposure lock	Luminosity locked at detected value with AE-L/AF-L button
ISO sensitivity (Recommended Exposure Index)	ISO 200 to 3200 in steps of 1/3 EV. Can also be set to approx. 0.3, 0.7, or 1 EV (ISO 100 equivalent) below ISO 200, or to approx. 0.3, 0.7, or 1 EV (ISO 6400 equivalent) over ISO 3200. ISO sensitivity auto control available
Active D-Lighting	Can be selected from Auto, Extra high, High, Normal, Low, or Off
Active D-Lighting bracketing	2 frames
Focus	
Autofocus	Nikon Multi-CAM 1000 autofocus sensor module with TTL phase detection, 11 focus points (including 1 cross-type sensor) and AF-assist illuminator (range approx. 1 ft. 8 in.–9 ft. 10 in. / 0.5–3 m)
AF detection range	-1 to +19 EV (ISO 100 equivalent, 68°F/20°C)
Lens servo	• Autofocus: Instant single-servo AF (AF-S); continuous-servo AF (AF-C); auto AF-S/AF-C selection (AF-A); predictive focus tracking automatically activated according to subject status (AF-A) • Manual (M): Electronic rangefinder supported
Focus point	Can be selected from 11 focus points
AF-area modes	Single-point AF, dynamic-area AF, auto-area AF, 3D-tracking (11 points) AF
Focus lock	Focus can be locked by pressing shutter-release button halfway (Single-servo AF) or by pressing AE-L/AF-L button

Figure A-10 Information Adapted from Nikon Product Catalog for Digital SLR Camera selected for experimental setup[23].

APPENDIX B: RAW DATA

This Appendix section tabulates the experimental data collected and analyzed for the determination of mechanical shaft power and the aero-mechanical efficiency of power conversion.

Table B-1 Sample Data Recorded and Analyzed to Determine Turbine Shaft Power and Aero-Mechanical Efficiency for Run 1 ($A_e = A_{nominal}$ (0.397 μm^2), x=12.8 mm, y=7.94 mm, z=0 mm, α=0^o & β=0^o).

x (mm)	12.8	R (mm)	12.83
y (mm)	7.94	P_{in} (kPa)	712.23
z (mm)	0	T_{amb} (^{o}K)	22.7
α (deg)	0	T_2 (^{o}K)	273.13
β (deg)	0	P_{amb} (kPa)	105.7

Θ (deg)	RPM	W (g)	d (mm)	$Q_{turbine}$ (N-m)	$P_{turbine}$ (W)	P_{aero} (W)	$\eta_{aero-mech}$ (%)
5	0	20	63.5	0.00109	0.0000	6.78	0.00
5.5	4,500	20	63.5	0.00120	0.0939	6.78	1.38
6	11,000	20	63.5	0.00130	0.2504	6.78	3.69
7	17,300	20	63.5	0.00152	0.4594	6.78	6.78
7.5	18,200	20	63.5	0.00163	0.5179	6.78	7.64
8	21,900	20	63.5	0.00174	0.6647	6.78	9.80
8.5	22,800	20	63.5	0.00185	0.7352	6.78	10.84
9	30,700	20	63.5	0.00196	1.0482	6.78	15.46
10	32,800	20	63.5	0.00217	1.2444	6.78	18.35
10.5	34,100	20	63.5	0.00228	1.3584	6.78	20.04
11	35,500	20	63.5	0.00239	1.4815	6.78	21.85
12	36,300	20	63.5	0.00261	1.6526	6.78	24.38

Table B-2 Sample Data Recorded and Analyzed to Determine Turbine Shaft Power and Aero-Mechanical Efficiency for Run 2 ($A_e = A_{nominal}$ (0.397 μm^2), x=6.41 mm, y=7.94 mm, z=0 mm, α=0^o & β=0^o).

x (mm)	6.41	R (mm)	12.83
y (mm)	7.94	P_{in} (kPa)	693.61
z (mm)	0	T_{amb} (^{o}C)	22.7
α (deg)	0	T_2 (^{o}K)	293.69
β (deg)	0	P_{amb} (kPa)	105.7

Θ (deg)	RPM	W (g)	d (mm)	$Q_{turbine}$ (N-m)	$P_{turbine}$ (W)	P_{aero} (W)	$\eta_{aero-mech}$ (%)
2	0	20	63.5	0.000435	0.0000	6.61	0.00
4	4,400	20	63.5	0.000869	0.0668	6.61	1.01
4.5	5,200	20	63.5	0.000978	0.0888	6.61	1.34
5	7,500	20	63.5	0.001087	0.1423	6.61	2.15
5.5	14,100	20	63.5	0.001196	0.2942	6.61	4.45
6	16,400	20	63.5	0.001304	0.3733	6.61	5.65
6.5	17,200	20	63.5	0.001413	0.4242	6.61	6.42
7	20,800	20	63.5	0.001522	0.5524	6.61	8.36
7.5	22,700	20	63.5	0.001630	0.6459	6.61	9.77
8	27,600	20	63.5	0.001739	0.8377	6.61	12.68
8.5	33,200	20	63.5	0.001848	1.0706	6.61	16.20
9	36,000	20	63.5	0.001956	1.2292	6.61	18.60
9.5	36,400	20	63.5	0.002065	1.3119	6.61	19.85
10	36,500	20	63.5	0.002174	1.3848	6.61	20.95

Table B-3 Sample Data Recorded and Analyzed to Determine Turbine Shaft Power and Aero-Mechanical Efficiency for Run 3 ($A_e = A_{nominal}$ (0.397 μm^2), x=0 mm, y=7.94 mm, z=0 mm, α=-3.0° & β=0°).

x (mm)	0	R (mm)	12.83
y (mm)	7.94	P_{in} (kPa)	697.75
z (mm)	0	T_{amb} (°C)	22.7
α (deg)	-3	T_2 (°K)	293.69
β (deg)	0	P_{amb} (kPa)	105.7

Θ (deg)	RPM	W (g)	d (mm)	$Q_{turbine}$ (N-m)	$P_{turbine}$ (W)	P_{aero} (W)	$\eta_{aero-mech}$ (%)
6	0	20	63.5	0.00130	0.0000	6.65	0.00
7	7,400	20	63.5	0.00152	0.1965	6.65	2.96
7.5	11,500	20	63.5	0.00163	0.3272	6.65	4.92
8	18,900	20	63.5	0.00174	0.5736	6.65	8.63
8.5	28,600	20	63.5	0.00185	0.9223	6.65	13.87
9	31,400	20	63.5	0.00196	1.0721	6.65	16.13
9.5	32,600	20	63.5	0.00207	1.1750	6.65	17.67
10	33,800	20	63.5	0.00217	1.2823	6.65	19.29
10.5	35,300	20	63.5	0.00228	1.4062	6.65	21.15
11	37,900	20	63.5	0.00239	1.5817	6.65	23.79
11.5	42,200	20	63.5	0.00250	1.8412	6.65	27.69
12	44,000	20	63.5	0.00261	2.0031	6.65	30.13

Table B-4 Sample Data Recorded and Analyzed to Determine Turbine Shaft Power and Aero-Mechanical Efficiency for Run 4 ($A_e = A_{nominal}$ (0.397 μm^2), x=0 mm, y=7.94 mm, z=0 mm, α=-1.5° & β=0°).

x (mm)	0	R (mm)	12.83
y (mm)	7.94	P_{in} (kPa)	697.75
z (mm)	0	T_{amb} (°C)	22.7
α (deg)	-1.5	T_2 (°K)	293.69
β (deg)	0	P_{amb} (kPa)	105.7

Θ (deg)	RPM	W (g)	d (mm)	$Q_{turbine}$ (N-m)	$P_{turbine}$ (W)	P_{aero} (W)	$\eta_{aero-mech}$ (%)
3	0	20	63.5	0.000652	0.000	6.65	0.00
4	12,700	20	63.5	0.000869	0.193	6.65	2.90
4.5	20,400	20	63.5	0.000978	0.348	6.65	5.24
5	24,000	20	63.5	0.001087	0.455	6.65	6.85
5.5	27,900	20	63.5	0.001196	0.582	6.65	8.76
6	31,300	20	63.5	0.001304	0.712	6.65	10.72
6.5	33,300	20	63.5	0.001413	0.821	6.65	12.35
7	37,400	20	63.5	0.001522	0.993	6.65	14.94
7.5	39,800	20	63.5	0.001630	1.132	6.65	17.03
8	41,600	20	63.5	0.001739	1.263	6.65	18.99
9	42,200	20	63.5	0.001956	1.441	6.65	21.67
9.5	47,000	20	63.5	0.002065	1.694	6.65	25.48
10	49,500	20	63.5	0.002174	1.878	6.65	28.25

Table B-5 Sample Data Recorded and Analyzed to Determine Turbine Shaft Power and Aero-Mechanical Efficiency for Run 5 ($A_e = A_{nominal}$ (0.397 μm^2), x=0 mm, y=7.94 mm, z=0 mm, α=3.0° & β=0°).

x (mm)	0	R (mm)	12.83
y (mm)	7.94	P_{in} (kPa)	714.30
z (mm)	0	T_{amb} (°C)	22.7
α (deg)	3	T_2 (°K)	293.69
β (deg)	0	P_{amb} (kPa)	105.7

Θ (deg)	RPM	W (g)	d (mm)	$Q_{turbine}$ (N-m)	$P_{turbine}$ (W)	P_{aero} (W)	$\eta_{aero-mech}$ (%)
3	0	20	63.5	0.000652	0.000	6.81	0.00
3.5	7,500	20	63.5	0.000761	0.100	6.81	1.46
4	9,200	20	63.5	0.000869	0.140	6.81	2.05
4.5	11,200	20	63.5	0.000978	0.191	6.81	2.81
5	13,900	20	63.5	0.001087	0.264	6.81	3.87
5.5	16,100	20	63.5	0.001196	0.336	6.81	4.94
6	16,600	20	63.5	0.001304	0.378	6.81	5.55
6.5	18,800	20	63.5	0.001413	0.464	6.81	6.81
7	20,900	20	63.5	0.001522	0.555	6.81	8.16
7.5	28,000	20	63.5	0.001630	0.797	6.81	11.71
8	31,600	20	63.5	0.001739	0.959	6.81	14.09
8.5	31,800	20	63.5	0.001848	1.025	6.81	15.07
9	32,900	20	63.5	0.001956	1.123	6.81	16.51
9.5	33,000	20	63.5	0.002065	1.189	6.81	17.48

Table B-6 Sample Data Recorded and Analyzed to Determine Turbine Shaft Power and Aero-Mechanical Efficiency for Run 6 ($A_e = A_{nominal}$ (0.397 μm^2), x=0 mm, y=7.94 mm, z=0 mm, α=1.5° & β=0°).

x (mm)	0	R (mm)	12.83
y (mm)	7.94	P_{in} (kPa)	687.41
z (mm)	0	T_{amb} (°C)	22.7
α (deg)	1.5	T_2 (°K)	293.69
β (deg)	0	P_{amb} (kPa)	105.7

Θ (deg)	RPM	W (g)	d (mm)	$Q_{turbine}$ (N-m)	$P_{turbine}$ (W)	P_{aero} (W)	$\eta_{aero-mech}$ (%)
3	0	20	63.5	0.000652	0.000	6.55	0.00
3.5	11,500	20	63.5	0.000761	0.153	6.55	2.33
4	14,100	20	63.5	0.000869	0.214	6.55	3.27
4.5	15,300	20	63.5	0.000978	0.261	6.55	3.99
5	17,300	20	63.5	0.001087	0.328	6.55	5.01
5.5	22,600	20	63.5	0.001196	0.472	6.55	7.20
6	27,350	20	63.5	0.001304	0.623	6.55	9.51
6.5	29,200	20	63.5	0.001413	0.720	6.55	10.99
7	31,600	20	63.5	0.001522	0.839	6.55	12.81
7.5	31,700	20	63.5	0.001630	0.902	6.55	13.77
8	34,600	20	63.5	0.001739	1.050	6.55	16.03

Table B-7 Sample Data Recorded and Analyzed to Determine Turbine Shaft Power and Aero-Mechanical Efficiency for Run 7 ($A_e = A_{nominal}$ (0.397 μm^2), x=0 mm, y=7.94 mm, z=0 mm, α=0^o & β=2.5^o).

x (mm)	0		R (mm)	12.83			
y (mm)	7.94		P_{in} (kPa)	685.34			
z (mm)	0		T_{amb} (^{o}C)	22.7			
α (deg)	0		T_2 (^{o}K)	293.69			
β (deg)	2.5		P_{amb} (kPa)	105.7			

Θ (deg)	RPM	W (g)	d (mm)	$Q_{turbine}$ (N-m)	$P_{turbine}$ (W)	P_{aero} (W)	$\eta_{aero-mech}$ (%)
3.5	0	20	63.5	0.000761	0.000	6.53	0.00
4	5,000	20	63.5	0.000869	0.076	6.53	1.16
4.5	11,100	20	63.5	0.000978	0.190	6.53	2.90
5	18,100	20	63.5	0.001087	0.343	6.53	5.26
5.5	21,000	20	63.5	0.001196	0.438	6.53	6.71
6	24,300	20	63.5	0.001304	0.553	6.53	8.47
6.5	27,300	20	63.5	0.001413	0.673	6.53	10.31
7	28,700	20	63.5	0.001522	0.762	6.53	11.67
7.5	30,200	20	63.5	0.001630	0.859	6.53	13.16
8	31,600	20	63.5	0.001739	0.959	6.53	14.69
8.5	37,600	20	63.5	0.001848	1.213	6.53	18.57
9	41,800	20	63.5	0.001956	1.427	6.53	21.86

Table B-8 Sample Data Recorded and Analyzed to Determine Turbine Shaft Power and Aero-Mechanical Efficiency for Run 8 ($A_e = A_{nominal}$ (0.397 μm^2), x=0 mm, y=7.94 mm, z=0 mm, α=0^o & β=1.0^o).

x (mm)	0		R (mm)	12.83			
y (mm)	7.94		P_{in} (kPa)	690.17			
z (mm)	0		T_{amb} (^{o}C)	22.7			
α (deg)	0		T_2 (^{o}K)	293.69			
β (deg)	1		P_{amb} (kPa)	105.7			

Θ (deg)	RPM	W (g)	d (mm)	$Q_{turbine}$ (N-m)	$P_{turbine}$ (W)	P_{aero} (W)	$\eta_{aero-mech}$ (%)
0	0	20	63.5	0.000000	0.000	6.58	0.00
1.5	5,400	20	63.5	0.000326	0.031	6.58	0.47
2	14,700	20	63.5	0.000435	0.112	6.58	1.70
2.5	21,600	20	63.5	0.000543	0.205	6.58	3.12
3	23,200	20	63.5	0.000652	0.264	6.58	4.02
3.5	25,500	20	63.5	0.000761	0.339	6.58	5.15
4	26,000	20	63.5	0.000869	0.395	6.58	6.00
4.5	28,100	20	63.5	0.000978	0.480	6.58	7.30
5	30,500	20	63.5	0.001087	0.579	6.58	8.80
5.5	39,300	20	63.5	0.001196	0.820	6.58	12.47
6	46,100	20	63.5	0.001304	1.049	6.58	15.96

Table B-9 Sample Data Recorded and Analyzed to Determine Turbine Shaft Power and Aero-Mechanical Efficiency for Run 9 ($A_e = A_{nominal}$ (0.397 μm^2), x=0 mm, y=7.94 mm, z=0 mm, α=0° & β=-2.5°).

x (mm)	0	R (mm)	12.83
y (mm)	7.94	P_{in} (kPa)	692.23
z (mm)	0	T_{amb} (°C)	22.7
α (deg)	0	T_2 (°K)	293.69
β (deg)	-2.5	P_{amb} (kPa)	105.7

Θ (deg)	RPM	W (g)	d (mm)	$Q_{turbine}$ (N-m)	$P_{turbine}$ (W)	P_{aero} (W)	$\eta_{aero-mech}$ (%)
0	0	20	63.5	0.000000	0.000	6.60	0.00
2	5,000	20	63.5	0.000435	0.038	6.60	0.58
3.5	14,000	20	63.5	0.000761	0.186	6.60	2.82
4	16,100	20	63.5	0.000869	0.244	6.60	3.70
4.5	17,400	20	63.5	0.000978	0.297	6.60	4.50
5	18,300	20	63.5	0.001087	0.347	6.60	5.26
5.5	19,500	20	63.5	0.001196	0.407	6.60	6.17
6	21,800	20	63.5	0.001304	0.496	6.60	7.52
6.5	26,100	20	63.5	0.001413	0.644	6.60	9.76
7	28,800	20	63.5	0.001522	0.765	6.60	11.60
7.5	29,100	20	63.5	0.001630	0.828	6.60	12.55
8	31,200	20	63.5	0.001739	0.947	6.60	14.36
8.5	31,700	20	63.5	0.001848	1.022	6.60	15.50

Table B-10 Sample Data Recorded and Analyzed to Determine Turbine Shaft Power and Aero-Mechanical Efficiency for Run 10 ($A_e = A_{nominal}$ (0.397 μm^2), x=0 mm, y=7.94 mm, z=0 mm, α=0° & β=-1.0°).

x (mm)	0	R (mm)	12.83
y (mm)	7.94	P_{in} (kPa)	706.02
z (mm)	0	T_{amb} (°C)	22.7
α (deg)	0	T_2 (°K)	294.80
β (deg)	-1	P_{amb} (kPa)	105.7

Θ (deg)	RPM	W (g)	d (mm)	$Q_{turbine}$ (N-m)	$P_{turbine}$ (W)	P_{aero} (W)	$\eta_{aero-mech}$ (%)
0	0	20	63.5	0.000000	0.000	6.74	0.00
3	13,600	20	63.5	0.000652	0.155	6.74	2.30
3.5	14,800	20	63.5	0.000761	0.197	6.74	2.92
4	18,000	20	63.5	0.000869	0.273	6.74	4.05
4.5	19,000	20	63.5	0.000978	0.324	6.74	4.81
5	20,100	20	63.5	0.001087	0.381	6.74	5.66
5.5	22,400	20	63.5	0.001196	0.467	6.74	6.94
6	27,100	20	63.5	0.001304	0.617	6.74	9.15
6.5	31,100	20	63.5	0.001413	0.767	6.74	11.38
7	31,800	20	63.5	0.001522	0.845	6.74	12.53

Table B-11 Sample Data Recorded and Analyzed to Determine Turbine Shaft Power and Aero-Mechanical Efficiency for Run 1 ($A_e = 0.75A_{nominal}$ (0.298 μm^2), x=12.8 mm, y=7.94 mm, z=0 mm, $\alpha=0^o$ & $\beta=0^o$).

x (mm)	12.8		R (mm)	12.83			
y (mm)	7.94		P_{in} (kPa)	686.03			
z (mm)	0		T_{amb} (^oC)	22.7			
α (deg)	0		T_2 (^oK)	293.13			
β (deg)	0		P_{amb} (kPa)	105.7			

Θ (deg)	RPM	W (g)	d (mm)	$Q_{turbine}$ (N-m)	$P_{turbine}$ (W)	P_{aero} (W)	$\eta_{aero-mech}$ (%)
4	0	20	63.5	0.00087	0.0000	4.90	0.00
5	3,000	20	63.5	0.00109	0.0569	4.90	1.16
5.5	22,600	20	63.5	0.00120	0.4716	4.90	9.63
6	26,100	20	63.5	0.00130	0.5941	4.90	12.13
6.5	29,800	20	63.5	0.00141	0.7349	4.90	15.01
7	31,100	20	63.5	0.00152	0.8259	4.90	16.87
7.5	35,500	20	63.5	0.00163	1.0101	4.90	20.63
8	37,300	20	63.5	0.00174	1.1321	4.90	23.12
8.5	39,100	20	63.5	0.00185	1.2609	4.90	25.75
9	43,400	20	63.5	0.00196	1.4819	4.90	30.26

Table B-12 Sample Data Recorded and Analyzed to Determine Turbine Shaft Power and Aero-Mechanical Efficiency for Run 2 ($A_e = 0.75A_{nominal}$ (0.298 μm^2), x=6.41 mm, y=7.94 mm, z=0 mm, $\alpha=0^o$ & $\beta=0^o$).

x (mm)	6.41		R (mm)	12.83			
y (mm)	7.94		P_{in} (kPa)	690.85			
z (mm)	0		T_{amb} (^oC)	22.7			
α (deg)	0		T_2 (^oK)	293.69			
β (deg)	0		P_{amb} (kPa)	105.7			

Θ (deg)	RPM	W (g)	d (mm)	$Q_{turbine}$ (N-m)	$P_{turbine}$ (W)	P_{aero} (W)	$\eta_{aero-mech}$ (%)
3	0	20	63.5	0.00065	0.0000	4.94	0.00
4	7,880	20	63.5	0.00087	0.1196	4.94	2.42
4.5	8,420	20	63.5	0.00098	0.1437	4.94	2.91
5	9,600	20	63.5	0.00109	0.1821	4.94	3.69
5.5	12,600	20	63.5	0.00120	0.2629	4.94	5.33
6	16,300	20	63.5	0.00130	0.3710	4.94	7.52
6.5	19,600	20	63.5	0.00141	0.4833	4.94	9.79
7	21,500	20	63.5	0.00152	0.5710	4.94	11.57
7.5	22,100	20	63.5	0.00163	0.6288	4.94	12.74
8	26,000	20	63.5	0.00174	0.7891	4.94	15.99
8.5	31,000	20	63.5	0.00185	0.9997	4.94	20.25
9	33,800	20	63.5	0.00196	1.1541	4.94	23.38

Table B-13 Sample Data Recorded and Analyzed to Determine Turbine Shaft Power and Aero-Mechanical Efficiency for Run 3 ($A_e = 0.75A_{nominal}$ (0.298 μm^2), x=0 mm, y=7.94 mm, z=0 mm, α=-3.0° & β=0°).

x (mm)	0	R (mm)	12.83
y (mm)	7.94	P_{in} (kPa)	681.89
z (mm)	0	T_{amb} (°C)	22.7
α (deg)	-3	T_2 (°K)	294.80
β (deg)	0	P_{amb} (kPa)	105.7

Θ (deg)	RPM	W (g)	d (mm)	$Q_{turbine}$ (N-m)	$P_{turbine}$ (W)	P_{aero} (W)	$\eta_{aero-mech}$ (%)
3	0	20	63.5	0.00065	0.0000	4.88	0.00
4	9,200	20	63.5	0.00087	0.1396	4.88	2.86
4.5	11,800	20	63.5	0.00098	0.2015	4.88	4.13
5	13,300	20	63.5	0.00109	0.2523	4.88	5.17
5.5	15,600	20	63.5	0.00120	0.3255	4.88	6.67
6	17,000	20	63.5	0.00130	0.3870	4.88	7.93
6.5	20,200	20	63.5	0.00141	0.4981	4.88	10.21
7	22,100	20	63.5	0.00152	0.5869	4.88	12.03
7.5	23,450	20	63.5	0.00163	0.6672	4.88	13.67
8	25,500	20	63.5	0.00174	0.7739	4.88	15.86
8.5	28,200	20	63.5	0.00185	0.9094	4.88	18.63
9	32,300	20	63.5	0.00196	1.1029	4.88	22.60
9.5	32,900	20	63.5	0.00207	1.1858	4.88	24.29

Table B-14 Sample Data Recorded and Analyzed to Determine Turbine Shaft Power and Aero-Mechanical Efficiency for Run 4 ($A_e = A_{nominal}$ (0.397 μm^2), x=0 mm, y=7.94 mm, z=0 mm, α=-1.5° & β=0°).

x (mm)	0	R (mm)	12.83
y (mm)	7.94	P_{in} (kPa)	686.03
z (mm)	0	T_{amb} (°C)	22.7
α (deg)	-1.5	T_2 (°K)	294.24
β (deg)	0	P_{amb} (kPa)	105.7

Θ (deg)	RPM	W (g)	d (mm)	$Q_{turbine}$ (N-m)	$P_{turbine}$ (W)	P_{aero} (W)	$\eta_{aero-mech}$ (%)
1	0	20	63.5	0.000217	0.000	4.91	0.00
2.5	8,700	20	63.5	0.000543	0.083	4.91	1.68
3	12,620	20	63.5	0.000652	0.144	4.91	2.93
3.5	16,763	20	63.5	0.000761	0.223	4.91	4.54
4	18,563	20	63.5	0.000869	0.282	4.91	5.74
4.5	20,993	20	63.5	0.000978	0.358	4.91	7.31
5	21,797	20	63.5	0.001087	0.413	4.91	8.43
5.5	23,389	20	63.5	0.001196	0.488	4.91	9.95
6	23,727	20	63.5	0.001304	0.540	4.91	11.01
6.5	27,949	20	63.5	0.001413	0.689	4.91	14.05
7	30,040	20	63.5	0.001522	0.798	4.91	16.26

Table B-15 Sample Data Recorded and Analyzed to Determine Turbine Shaft Power and Aero-Mechanical Efficiency for Run 5 ($A_e = 0.75A_{nominal}$ (0.298 μm^2), x=0 mm, y=7.94 mm, z=0 mm, α=3.0° & β=0°).

x (mm)	0	R (mm)	12.83	
y (mm)	7.94	P_{in} (kPa)	681.20	
z (mm)	0	T_{amb} (°C)	22.7	
α (deg)	3	T_2 (°K)	293.69	
β (deg)	0	P_{amb} (kPa)	105.7	

Θ (deg)	RPM	W (g)	d (mm)	$Q_{turbine}$ (N-m)	$P_{turbine}$ (W)	P_{aero} (W)	$\eta_{aero-mech}$ (%)
4	0	20	63.5	0.000869	0.000	4.87	0.00
4.5	4,000	20	63.5	0.000978	0.068	4.87	1.40
5	9,300	20	63.5	0.001087	0.176	4.87	3.63
5.5	12,300	20	63.5	0.001196	0.257	4.87	5.27
6	13,700	20	63.5	0.001304	0.312	4.87	6.41
6.5	17,300	20	63.5	0.001413	0.427	4.87	8.77
7	21,200	20	63.5	0.001522	0.563	4.87	11.57
7.5	24,900	20	63.5	0.001630	0.708	4.87	14.56
8	28,000	20	63.5	0.001739	0.850	4.87	17.46
8.5	31,400	20	63.5	0.001848	1.013	4.87	20.81
9	32,800	20	63.5	0.001956	1.120	4.87	23.01
9.5	33,100	20	63.5	0.002065	1.193	4.87	24.51

Table B-16 Sample Data Recorded and Analyzed to Determine Turbine Shaft Power and Aero-Mechanical Efficiency for Run 6 ($A_e = 0.75A_{nominal}$ (0.298 μm^2), x=0 mm, y=7.94 mm, z=0 mm, α=1.5° & β=0°).

x (mm)	0	R (mm)	12.83	
y (mm)	7.94	P_{in} (kPa)	681.20	
z (mm)	0	T_{amb} (°C)	22.7	
α (deg)	1.5	T_2 (°K)	294.24	
β (deg)	0	P_{amb} (kPa)	105.7	

Θ (deg)	RPM	W (g)	d (mm)	$Q_{turbine}$ (N-m)	$P_{turbine}$ (W)	P_{aero} (W)	$\eta_{aero-mech}$ (%)
2.5	0	20	63.5	0.000543	0.000	4.87	0.00
3	11,937	20	63.5	0.000652	0.136	4.87	2.79
3.5	16,937	20	63.5	0.000761	0.225	4.87	4.62
4	20,467	20	63.5	0.000869	0.311	4.87	6.38
4.5	21,178	20	63.5	0.000978	0.362	4.87	7.42
5	23,461	20	63.5	0.001087	0.445	4.87	9.14
5.5	26,215	20	63.5	0.001196	0.547	4.87	11.23
6	28,711	20	63.5	0.001304	0.654	4.87	13.42
6.5	29,273	20	63.5	0.001413	0.722	4.87	14.82
7	31,456	20	63.5	0.001522	0.835	4.87	17.15

Table B-17 Sample Data Recorded and Analyzed to Determine Turbine Shaft Power and Aero-Mechanical Efficiency for Run 7 ($A_e = 0.75A_{nominal}$ (0.298 μm^2), x=0 mm, y=7.94 mm, z=0 mm, $\alpha=0^o$ & $\beta=2.5^o$).

x (mm)	0	R (mm)	12.83
y (mm)	7.94	P_{in} (kPa)	703.27
z (mm)	0	T_{amb} (^{o}C)	22.7
α (deg)	0	T_2 (^{o}K)	294.24
β (deg)	2.5	P_{amb} (kPa)	105.7

Θ (deg)	RPM	W (g)	d (mm)	$Q_{turbine}$ (N-m)	$P_{turbine}$ (W)	P_{aero} (W)	$\eta_{aero-mech}$ (%)
2.5	0	20	63.5	0.00054	0.000	5.03	0.00
3	4,650	20	63.5	0.00065	0.053	5.03	1.05
3.5	10,962	20	63.5	0.00076	0.146	5.03	2.89
4	16,354	20	63.5	0.00087	0.248	5.03	4.93
4.5	21,118	20	63.5	0.00098	0.361	5.03	7.17
5	22,350	20	63.5	0.00109	0.424	5.03	8.43
5.5	24,752	20	63.5	0.00120	0.516	5.03	10.27
6	26,504	20	63.5	0.00130	0.603	5.03	12.00
6.5	28,232	20	63.5	0.00141	0.696	5.03	13.84
7	29,524	20	63.5	0.00152	0.784	5.03	15.59
7.5	31,278	20	63.5	0.00163	0.890	5.03	17.70
8	32,205	20	63.5	0.00174	0.977	5.03	19.44
8.5	33,400	20	63.5	0.00185	1.077	5.03	21.42

Table B-18 Sample Data Recorded and Analyzed to Determine Turbine Shaft Power and Aero-Mechanical Efficiency for Run 8 ($A_e = 0.75A_{nominal}$ (0.298 μm^2), x=0 mm, y=7.94 mm, z=0 mm, $\alpha=0^o$ & $\beta=1.0^o$).

x (mm)	0	R (mm)	12.83
y (mm)	7.94	P_{in} (kPa)	682.58
z (mm)	0	T_{amb} (^{o}C)	22.7
α (deg)	0	T_2 (^{o}K)	294.24
β (deg)	1	P_{amb} (kPa)	105.7

Θ (deg)	RPM	W (g)	d (mm)	$Q_{turbine}$ (N-m)	$P_{turbine}$ (W)	P_{aero} (W)	$\eta_{aero-mech}$ (%)
3.5	0	20	63.5	0.000761	0.000	4.88	0.00
4	7,339	20	63.5	0.000869	0.111	4.88	2.28
4.5	12,695	20	63.5	0.000978	0.217	4.88	4.44
5	15,179	20	63.5	0.001087	0.288	4.88	5.90
5.5	18,618	20	63.5	0.001196	0.388	4.88	7.96
6	21,566	20	63.5	0.001304	0.491	4.88	10.06
6.5	24,110	20	63.5	0.001413	0.595	4.88	12.18
7	25,838	20	63.5	0.001522	0.686	4.88	14.06
7.5	28,226	20	63.5	0.001630	0.803	4.88	16.45
8	31,081	20	63.5	0.001739	0.943	4.88	19.33
8.5	32,210	20	63.5	0.001848	1.039	4.88	21.28

Table B-19 Sample Data Recorded and Analyzed to Determine Turbine Shaft Power and Aero-Mechanical Efficiency for Run 9 ($A_e = 0.75A_{nominal}$ (0.298 μm^2), x=0 mm, y=7.94 mm, z=0 mm, $\alpha=0^o$ & $\beta=-2.5^o$).

x (mm)	0		R (mm)	12.83	
y (mm)	7.94		P_{in} (kPa)	696.37	
z (mm)	0		T_{amb} (^oC)	22.7	
α (deg)	0		T_2 (^oK)	294.24	
β (deg)	-2.5		P_{amb} (kPa)	105.7	

Θ (deg)	RPM	W (g)	d (mm)	$Q_{turbine}$ (N-m)	$P_{turbine}$ (W)	P_{aero} (W)	$\eta_{aero-mech}$ (%)
3.5	0	20	63.5	0.000761	0.000	4.98	0.00
4	9,622	20	63.5	0.000869	0.146	4.98	2.93
4.5	11,742	20	63.5	0.000978	0.200	4.98	4.03
5	13,928	20	63.5	0.001087	0.264	4.98	5.31
5.5	16,224	20	63.5	0.001196	0.339	4.98	6.80
6	18,501	20	63.5	0.001304	0.421	4.98	8.46
6.5	22,837	20	63.5	0.001413	0.563	4.98	11.31
7	25,769	20	63.5	0.001522	0.684	4.98	13.74
7.5	26,924	20	63.5	0.001630	0.766	4.98	15.38
8	28,294	20	63.5	0.001739	0.859	4.98	17.25
8.5	29,768	20	63.5	0.001848	0.960	4.98	19.28
9	30,983	20	63.5	0.001956	1.058	4.98	21.24

Table B-20 Sample Data Recorded and Analyzed to Determine Turbine Shaft Power and Aero-Mechanical Efficiency for Run 10 ($A_e = 0.75A_{nominal}$ (0.298 μm^2), x=0 mm, y=7.94 mm, z=0 mm, $\alpha=0^o$ & $\beta=-1.0^o$).

x (mm)	0		R (mm)	12.83	
y (mm)	7.94		P_{in} (kPa)	682.58	
z (mm)	0		T_{amb} (^oC)	22.7	
α (deg)	0		T_2 (^oK)	294.24	
β (deg)	-1		P_{amb} (kPa)	105.7	

Θ (deg)	RPM	W (g)	d (mm)	$Q_{turbine}$ (N-m)	$P_{turbine}$ (W)	P_{aero} (W)	$\eta_{aero-mech}$ (%)
3	0	20	63.5	0.00065	0.000	4.88	0.00
3.5	8,729	20	63.5	0.00076	0.116	4.88	2.37
4	9,924	20	63.5	0.00087	0.151	4.88	3.09
4.5	10,761	20	63.5	0.00098	0.184	4.88	3.76
5	13,958	20	63.5	0.00109	0.265	4.88	5.42
5.5	17,037	20	63.5	0.00120	0.355	4.88	7.28
6	20,326	20	63.5	0.00130	0.463	4.88	9.48
6.5	24,615	20	63.5	0.00141	0.607	4.88	12.44
7	27,904	20	63.5	0.00152	0.741	4.88	15.18
7.5	29,193	20	63.5	0.00163	0.831	4.88	17.02
8	30,482	20	63.5	0.00174	0.925	4.88	18.95
8.5	32,771	20	63.5	0.00185	1.057	4.88	21.65

Table B-21 Sample Data Recorded and Analyzed to Determine Turbine Shaft Power and Aero-Mechanical Efficiency for Run 1 ($A_e = 0.5A_{nominal}$ (0.199 μm^2), x=12.8 mm, y=7.94 mm, z=0 mm, $\alpha=0^o$ & $\beta=0^o$).

x (mm)	12.8		R (mm)	12.83			
y (mm)	7.94		P_{in} (kPa)	692.23			
z (mm)	0		T_{amb} (^oC)	22.7			
α (deg)	0		T_2 (^oK)	294.24			
β (deg)	0		P_{amb} (kPa)	105.7			

Θ (deg)	RPM	W (g)	d (mm)	$Q_{turbine}$ (N-m)	$P_{turbine}$ (W)	P_{aero} (W)	$\eta_{aero-mech}$ (%)
4	0	20	63.5	0.00087	0.0000	3.30	0.00
4.5	9,314	20	63.5	0.00098	0.1590	3.30	4.82
5.5	10,499	20	63.5	0.00120	0.2191	3.30	6.64
6	12,965	20	63.5	0.00130	0.2951	3.30	8.94
6.5	14,215	20	63.5	0.00141	0.3505	3.30	10.62
7	20,033	20	63.5	0.00152	0.5320	3.30	16.12
7.5	23,429	20	63.5	0.00163	0.6666	3.30	20.20
8	24,885	20	63.5	0.00174	0.7553	3.30	22.89
8.5	26,661	20	63.5	0.00185	0.8598	3.30	26.06
9	28,571	20	63.5	0.00196	0.9755	3.30	29.57
9.5	29,597	20	63.5	0.00207	1.0667	3.30	32.33
10	30,480	20	63.5	0.00217	1.1564	3.30	35.05

Table B-22 Sample Data Recorded and Analyzed to Determine Turbine Shaft Power and Aero-Mechanical Efficiency for Run 2 ($A_e = 0.5A_{nominal}$ (0.199 μm^2), x=6.41 mm, y=7.94 mm, z=0 mm, $\alpha=0^o$ & $\beta=0^o$).

x (mm)	6.41		R (mm)	12.83			
y (mm)	7.94		P_{in} (kPa)	696.37			
z (mm)	0		T_{amb} (^oC)	22.7			
α (deg)	0		T_2 (^oK)	294.24			
β (deg)	0		P_{amb} (kPa)	105.7			

Θ (deg)	RPM	W (g)	d (mm)	$Q_{turbine}$ (N-m)	$P_{turbine}$ (W)	P_{aero} (W)	$\eta_{aero-mech}$ (%)
2	0	20	63.5	0.00043	0.0000	3.32	0.00
3	8,684	20	63.5	0.00065	0.0988	3.32	2.98
3.5	11,336	20	63.5	0.00076	0.1505	3.32	4.54
4	13,781	20	63.5	0.00087	0.2091	3.32	6.30
4.5	19,258	20	63.5	0.00098	0.3288	3.32	9.91
5	22,774	20	63.5	0.00109	0.4320	3.32	13.02
5.5	24,017	20	63.5	0.00120	0.5011	3.32	15.10
6	24,708	20	63.5	0.00130	0.5624	3.32	16.95
6.5	26,691	20	63.5	0.00141	0.6582	3.32	19.83
7	27,393	20	63.5	0.00152	0.7275	3.32	21.92
7.5	29,713	20	63.5	0.00163	0.8454	3.32	25.47
8	29,995	20	63.5	0.00174	0.9104	3.32	27.43

Table B-23 Sample Data Recorded and Analyzed to Determine Turbine Shaft Power and Aero-Mechanical Efficiency for Run 3 ($A_e = 0.5A_{nominal}$ (0.199 μm^2), x=0 mm, y=7.94 mm, z=0 mm, α=-3.0° & β=0°).

x (mm)	0	R (mm)	12.83
y (mm)	7.94	P_{in} (kPa)	696.37
z (mm)	0	T_{amb} (°C)	22.7
α (deg)	-3	T_2 (°K)	294.80
β (deg)	0	P_{amb} (kPa)	105.7

Θ (deg)	RPM	W (g)	d (mm)	$Q_{turbine}$ (N-m)	$P_{turbine}$ (W)	P_{aero} (W)	$\eta_{aero-mech}$ (%)
3	0	20	63.5	0.00065	0.0000	3.32	0.00
3.5	9,589	20	63.5	0.00076	0.1273	3.32	3.83
4	10,787	20	63.5	0.00087	0.1637	3.32	4.93
4.5	11,940	20	63.5	0.00098	0.2038	3.32	6.14
5	13,211	20	63.5	0.00109	0.2506	3.32	7.54
5.5	16,563	20	63.5	0.00120	0.3456	3.32	10.40
6	19,364	20	63.5	0.00130	0.4408	3.32	13.27
6.5	21,404	20	63.5	0.00141	0.5278	3.32	15.89
7	23,336	20	63.5	0.00152	0.6197	3.32	18.65
7.5	27,617	20	63.5	0.00163	0.7858	3.32	23.65
8	29,359	20	63.5	0.00174	0.8911	3.32	26.82
8.5	30,340	20	63.5	0.00185	0.9784	3.32	29.45
9	31,726	20	63.5	0.00196	1.0833	3.32	32.61

Table B-24 Sample Data Recorded and Analyzed to Determine Turbine Shaft Power and Aero-Mechanical Efficiency for Run 4 ($A_e = 0.5A_{nominal}$ (0.199 μm^2), x=0 mm, y=7.94 mm, z=0 mm, α=-1.5° & β=0°).

x (mm)	0	R (mm)	12.83
y (mm)	7.94	P_{in} (kPa)	687.41
z (mm)	0	T_{amb} (°C)	22.7
α (deg)	-1.5	T_2 (°K)	294.24
β (deg)	0	P_{amb} (kPa)	105.7

Θ (deg)	RPM	W (g)	d (mm)	$Q_{turbine}$ (N-m)	$P_{turbine}$ (W)	P_{aero} (W)	$\eta_{aero-mech}$ (%)
1.5	0	20	63.5	0.000326	0.000	3.28	0.00
2	11,190	20	63.5	0.000435	0.085	3.28	2.59
2.5	15,320	20	63.5	0.000543	0.145	3.28	4.43
3	17,045	20	63.5	0.000652	0.194	3.28	5.92
3.5	20,940	20	63.5	0.000761	0.278	3.28	8.49
4	22,105	20	63.5	0.000869	0.335	3.28	10.24
4.5	23,109	20	63.5	0.000978	0.395	3.28	12.04
5	23,973	20	63.5	0.001087	0.455	3.28	13.88
5.5	26,947	20	63.5	0.001196	0.562	3.28	17.16
6	28,901	20	63.5	0.001304	0.658	3.28	20.08
6.5	30,340	20	63.5	0.001413	0.748	3.28	22.84

Table B-25 Sample Data Recorded and Analyzed to Determine Turbine Shaft Power and Aero-Mechanical Efficiency for Run 5 ($A_e = 0.5A_{nominal}$ (0.199 μm^2), x=0 mm, y=7.94 mm, z=0 mm, α=3.0° & β=0°).

x (mm)	0	R (mm)	12.83
y (mm)	7.94	P_{in} (kPa)	683.96
z (mm)	0	T_{amb} (°C)	22.7
α (deg)	3	T_2 (°K)	294.24
β (deg)	0	P_{amb} (kPa)	105.7

Θ (deg)	RPM	W (g)	d (mm)	$Q_{turbine}$ (N-m)	$P_{turbine}$ (W)	P_{aero} (W)	$\eta_{aero-mech}$ (%)
2.5	0	20	63.5	0.000543	0.000	3.26	0.00
3	4,697	20	63.5	0.000652	0.053	3.26	1.64
3.5	6,720	20	63.5	0.000761	0.089	3.26	2.74
4	9,078	20	63.5	0.000869	0.138	3.26	4.23
4.5	10,587	20	63.5	0.000978	0.181	3.26	5.54
5	13,318	20	63.5	0.001087	0.253	3.26	7.75
5.5	16,967	20	63.5	0.001196	0.354	3.26	10.86
6	19,476	20	63.5	0.001304	0.443	3.26	13.60
6.5	21,080	20	63.5	0.001413	0.520	3.26	15.95
7	25,814	20	63.5	0.001522	0.686	3.26	21.03
7.5	27,803	20	63.5	0.001630	0.791	3.26	24.27
8	29,220	20	63.5	0.001739	0.887	3.26	27.20
8.5	30,406	20	63.5	0.001848	0.981	3.26	30.08
9	31,284	20	63.5	0.001956	1.068	3.26	32.77

Table B-26 Sample Data Recorded and Analyzed to Determine Turbine Shaft Power and Aero-Mechanical Efficiency for Run 6 ($A_e = 0.5A_{nominal}$ (0.199 μm^2), x=0 mm, y=7.94 mm, z=0 mm, α=1.5° & β=0°).

x (mm)	0	R (mm)	12.83
y (mm)	7.94	P_{in} (kPa)	681.20
z (mm)	0	T_{amb} (°C)	22.7
α (deg)	1.5	T_2 (°K)	294.80
β (deg)	0	P_{amb} (kPa)	105.7

Θ (deg)	RPM	W (g)	d (mm)	$Q_{turbine}$ (N-m)	$P_{turbine}$ (W)	P_{aero} (W)	$\eta_{aero-mech}$ (%)
2	0	20	63.5	0.000435	0.000	3.25	0.00
2.5	6,971	20	63.5	0.000543	0.066	3.25	2.03
3	8,337	20	63.5	0.000652	0.095	3.25	2.92
3.5	9,564	20	63.5	0.000761	0.127	3.25	3.91
4	13,143	20	63.5	0.000869	0.199	3.25	6.14
4.5	15,754	20	63.5	0.000978	0.269	3.25	8.28
5	18,938	20	63.5	0.001087	0.359	3.25	11.05
5.5	20,512	20	63.5	0.001196	0.428	3.25	13.17
6	22,586	20	63.5	0.001304	0.514	3.25	15.82
6.5	23,811	20	63.5	0.001413	0.587	3.25	18.07
7	26,177	20	63.5	0.001522	0.695	3.25	21.39
7.5	28,147	20	63.5	0.001630	0.801	3.25	24.64
8	28,751	20	63.5	0.001739	0.873	3.25	26.85

Table B-27 Sample Data Recorded and Analyzed to Determine Turbine Shaft Power and Aero-Mechanical Efficiency for Run 7 ($A_e = 0.5A_{nominal}$ (0.199 μm^2), x=0 mm, y=7.94 mm, z=0 mm, $\alpha=0^o$ & $\beta=2.5^o$).

x (mm)	0		R (mm)	12.83
y (mm)	7.94		P_{in} (kPa)	683.96
z (mm)	0		T_{amb} (^oC)	22.7
α (deg)	0		T_2 (^oK)	294.24
β (deg)	2.5		P_{amb} (kPa)	105.7

Θ (deg)	RPM	W (g)	d (mm)	$Q_{turbine}$ (N-m)	$P_{turbine}$ (W)	P_{aero} (W)	$\eta_{aero-mech}$ (%)
1.5	0	20	63.5	0.00033	0.000	3.26	0.00
2	6,996	20	63.5	0.00043	0.053	3.26	1.63
2.5	11,737	20	63.5	0.00054	0.111	3.26	3.41
3	16,135	20	63.5	0.00065	0.184	3.26	5.63
3.5	19,688	20	63.5	0.00076	0.261	3.26	8.02
4	21,154	20	63.5	0.00087	0.321	3.26	9.85
4.5	22,933	20	63.5	0.00098	0.392	3.26	12.01
5	23,321	20	63.5	0.00109	0.442	3.26	13.57
5.5	24,703	20	63.5	0.00120	0.515	3.26	15.81
6	26,130	20	63.5	0.00130	0.595	3.26	18.25
6.5	27,748	20	63.5	0.00141	0.684	3.26	20.99
7	29,167	20	63.5	0.00152	0.775	3.26	23.76
7.5	29,855	20	63.5	0.00163	0.849	3.26	26.06

Table B-28 Sample Data Recorded and Analyzed to Determine Turbine Shaft Power and Aero-Mechanical Efficiency for Run 8 ($A_e = 0.5A_{nominal}$ (0.199 μm^2), x=0 mm, y=7.94 mm, z=0 mm, $\alpha=0^o$ & $\beta=1.0^o$).

x (mm)	0		R (mm)	12.83
y (mm)	7.94		P_{in} (kPa)	681.20
z (mm)	0		T_{amb} (^oC)	22.7
α (deg)	0		T_2 (^oK)	294.80
β (deg)	1		P_{amb} (kPa)	105.7

Θ (deg)	RPM	W (g)	d (mm)	$Q_{turbine}$ (N-m)	$P_{turbine}$ (W)	P_{aero} (W)	$\eta_{aero-mech}$ (%)
0.5	0	20	63.5	0.00011	0.000	3.25	0.00
1	4,086	20	63.5	0.00022	0.016	3.25	0.48
1.5	8,726	20	63.5	0.00033	0.050	3.25	1.53
2	12,123	20	63.5	0.00043	0.092	3.25	2.83
2.5	14,389	20	63.5	0.00054	0.136	3.25	4.20
3	16,596	20	63.5	0.00065	0.189	3.25	5.81
3.5	18,900	20	63.5	0.00076	0.251	3.25	7.72
4	20,937	20	63.5	0.00087	0.318	3.25	9.78
4.5	23,884	20	63.5	0.00098	0.408	3.25	12.55
5	26,908	20	63.5	0.00109	0.510	3.25	15.71
5.5	27,719	20	63.5	0.00120	0.578	3.25	17.80
6	28,238	20	63.5	0.00130	0.643	3.25	19.78

Table B-29 Sample Data Recorded and Analyzed to Determine Turbine Shaft Power and Aero-Mechanical Efficiency for Run 9 ($A_e = 0.5A_{nominal}$ (0.199 μm^2), x=0 mm, y=7.94 mm, z=0 mm, $\alpha=0^o$ & $\beta=-2.5^o$).

x (mm)	0	R (mm)	12.83
y (mm)	7.94	P_{in} (kPa)	686.72
z (mm)	0	T_{amb} (^oC)	22.7
α (deg)	0	T_2 (^oK)	294.24
β (deg)	-2.5	P_{amb} (kPa)	105.7

Θ (deg)	RPM	W (g)	d (mm)	$Q_{turbine}$ (N-m)	$P_{turbine}$ (W)	P_{aero} (W)	$\eta_{aero-mech}$ (%)
3.5	0	20	63.5	0.000761	0.000	3.27	0.00
5	3,516	20	63.5	0.001087	0.067	3.27	2.04
5.5	6,951	20	63.5	0.001196	0.145	3.27	4.43
6	10,950	20	63.5	0.001304	0.249	3.27	7.62
6.5	14,381	20	63.5	0.001413	0.355	3.27	10.83
7	16,501	20	63.5	0.001522	0.438	3.27	13.39
7.5	18,384	20	63.5	0.001630	0.523	3.27	15.98
8	24,214	20	63.5	0.001739	0.735	3.27	22.45
8.5	26,068	20	63.5	0.001848	0.841	3.27	25.68
9	26,702	20	63.5	0.001956	0.912	3.27	27.85
9.5	27,148	20	63.5	0.002065	0.978	3.27	29.89

Table B-30 Sample Data Recorded and Analyzed to Determine Turbine Shaft Power and Aero-Mechanical Efficiency for Run 10 ($A_e = 0.5A_{nominal}$ (0.199 μm^2), x=0 mm, y=7.94 mm, z=0 mm, $\alpha=0^o$ & $\beta=-1.0^o$).

x (mm)	0	R (mm)	12.83
y (mm)	7.94	P_{in} (kPa)	683.96
z (mm)	0	T_{amb} (^oC)	22.7
α (deg)	0	T_2 (^oK)	294.24
β (deg)	-1	P_{amb} (kPa)	105.7

Θ (deg)	RPM	W (g)	d (mm)	$Q_{turbine}$ (N-m)	$P_{turbine}$ (W)	P_{aero} (W)	$\eta_{aero-mech}$ (%)
3.5	0	20	63.5	0.00076	0.000	3.26	0.00
4.5	12,733	20	63.5	0.00098	0.217	3.26	6.67
5	17,094	20	63.5	0.00109	0.324	3.26	9.95
5.5	19,668	20	63.5	0.00120	0.410	3.26	12.59
6	22,353	20	63.5	0.00130	0.509	3.26	15.61
6.5	24,301	20	63.5	0.00141	0.599	3.26	18.38
7	25,242	20	63.5	0.00152	0.670	3.26	20.56
7.5	26,575	20	63.5	0.00163	0.756	3.26	23.20
8	27,410	20	63.5	0.00174	0.832	3.26	25.52
8.5	28,870	20	63.5	0.00185	0.931	3.26	28.56
9	29,799	20	63.5	0.00196	1.017	3.26	31.21

Table B-31 Sample Data Recorded and Analyzed to Determine Turbine Shaft Power and Aero-Mechanical Efficiency for Run 1 ($A_e = A_{nominal}$ (0.397 μm^2), x=12.8 mm, y=20.6 mm, z=0 mm, α=0° & β=0°).

x (mm)	12.8	R (mm)	12.83
y (mm)	20.6	P_{in} (kPa)	697.06
z (mm)	0	T_{amb} (°C)	22.3
α (deg)	0	T_2 (°K)	293.69
β (deg)	0	P_{amb} (kPa)	104.6

Θ (deg)	RPM	W (g)	d (mm)	$Q_{turbine}$ (N-m)	$P_{turbine}$ (W)	P_{aero} (W)	$\eta_{aero-mech}$ (%)
6	0	20	63.5	0.00130	0.0000	6.64	0.00
6.5	5,100	20	63.5	0.00141	0.1258	6.64	1.89
7	11,500	20	63.5	0.00152	0.3054	6.64	4.60
7.5	15,900	20	63.5	0.00163	0.4524	6.64	6.81
8	18,000	20	63.5	0.00174	0.5463	6.64	8.23
8.5	20,700	20	63.5	0.00185	0.6675	6.64	10.05
9	23,100	20	63.5	0.00196	0.7887	6.64	11.88
9.5	25,300	20	63.5	0.00207	0.9118	6.64	13.73
10	26,800	20	63.5	0.00217	1.0167	6.64	15.31
10.5	30,100	20	63.5	0.00228	1.1990	6.64	18.05
11	33,400	20	63.5	0.00239	1.3939	6.64	20.99
12	35,000	20	63.5	0.00261	1.5934	6.64	23.99
12.5	36,900	20	63.5	0.00272	1.7499	6.64	26.35

Table B-32 Sample Data Recorded and Analyzed to Determine Turbine Shaft Power and Aero-Mechanical Efficiency for Run 2 ($A_e = A_{nominal}$ (0.397 μm^2), x=6.41 mm, y=20.6 mm, z=0 mm, α=0° & β=0°).

x (mm)	6.41	R (mm)	12.83
y (mm)	20.6	P_{in} (kPa)	687.41
z (mm)	0	T_{amb} (°C)	22.3
α (deg)	0	T_2 (°K)	293.69
β (deg)	0	P_{amb} (kPa)	104.6

Θ (deg)	RPM	W (g)	d (mm)	$Q_{turbine}$ (N-m)	$P_{turbine}$ (W)	P_{aero} (W)	$\eta_{aero-mech}$ (%)
4	0	20	63.5	0.00087	0.0000	6.55	0.00
4.5	8,900	20	63.5	0.00098	0.1519	6.55	2.32
5	18,000	20	63.5	0.00109	0.3414	6.55	5.21
5.5	19,600	20	63.5	0.00120	0.4090	6.55	6.24
6	24,200	20	63.5	0.00130	0.5509	6.55	8.41
6.5	28,600	20	63.5	0.00141	0.7053	6.55	10.77
7	29,400	20	63.5	0.00152	0.7808	6.55	11.92
7.5	31,500	20	63.5	0.00163	0.8963	6.55	13.68
8	32,900	20	63.5	0.00174	0.9985	6.55	15.25
8.5	34,900	20	63.5	0.00185	1.1254	6.55	17.18
9	35,800	20	63.5	0.00196	1.2224	6.55	18.66

Table B-33 Sample Data Recorded and Analyzed to Determine Turbine Shaft Power and Aero-Mechanical Efficiency for Run 3 ($A_e = A_{nominal}$ (0.397 μm^2), x=0 mm, y=20.6 mm, z=0 mm, α=-3.0° & β=0°).

x (mm)	0	R (mm)	12.83
y (mm)	20.6	P_{in} (kPa)	689.48
z (mm)	0	T_{amb} (°C)	22.3
α (deg)	-3	T_2 (°K)	293.69
β (deg)	0	P_{amb} (kPa)	104.6

Θ (deg)	RPM	W (g)	d (mm)	$Q_{turbine}$ (N-m)	$P_{turbine}$ (W)	P_{aero} (W)	$\eta_{aero-mech}$ (%)
8	0	20	63.5	0.00174	0.0000	6.57	0.00
9.5	3,400	20	63.5	0.00207	0.1225	6.57	1.87
10	7,100	20	63.5	0.00217	0.2694	6.57	4.10
10.5	9,800	20	63.5	0.00228	0.3904	6.57	5.94
11	10,500	20	63.5	0.00239	0.4382	6.57	6.67
11.5	13,900	20	63.5	0.00250	0.6064	6.57	9.23
12	24,700	20	63.5	0.00261	1.1245	6.57	17.12
12.5	26,400	20	63.5	0.00272	1.2520	6.57	19.06
13	27,700	20	63.5	0.00283	1.3662	6.57	20.80
13.5	28,800	20	63.5	0.00293	1.4750	6.57	22.45
14	32,800	20	63.5	0.00304	1.7421	6.57	26.52
14.5	35,300	20	63.5	0.00315	1.9419	6.57	29.56
15	36,500	20	63.5	0.00326	2.0771	6.57	31.62

Table B-34 Sample Data Recorded and Analyzed to Determine Turbine Shaft Power and Aero-Mechanical Efficiency for Run 4 ($A_e = A_{nominal}$ (0.397 μm^2), x=0 mm, y=20.6 mm, z=0 mm, α=-1.5° & β=0°).

x (mm)	0	R (mm)	12.83
y (mm)	20.6	P_{in} (kPa)	686.72
z (mm)	0	T_{amb} (°C)	22.3
α (deg)	-1.5	T_2 (°K)	293.69
β (deg)	0	P_{amb} (kPa)	104.6

Θ (deg)	RPM	W (g)	d (mm)	$Q_{turbine}$ (N-m)	$P_{turbine}$ (W)	P_{aero} (W)	$\eta_{aero-mech}$ (%)
4.5	0	20	63.5	0.00098	0.000	6.54	0.00
5	10,500	20	63.5	0.00109	0.199	6.54	3.04
5.5	13,900	20	63.5	0.00120	0.290	6.54	4.43
6	16,000	20	63.5	0.00130	0.364	6.54	5.57
6.5	19,200	20	63.5	0.00141	0.473	6.54	7.24
7	20,500	20	63.5	0.00152	0.544	6.54	8.32
7.5	27,500	20	63.5	0.00163	0.782	6.54	11.96
8	30,500	20	63.5	0.00174	0.926	6.54	14.15
8.5	32,400	20	63.5	0.00185	1.045	6.54	15.97
9	37,000	20	63.5	0.00196	1.263	6.54	19.31
9.5	39,800	20	63.5	0.00207	1.434	6.54	21.92
10	43,300	20	63.5	0.00217	1.643	6.54	25.11
10.5	45,400	20	63.5	0.00228	1.809	6.54	27.64
11	47,900	20	63.5	0.00239	1.999	6.54	30.55

Table B-35 Sample Data Recorded and Analyzed to Determine Turbine Shaft Power and Aero-Mechanical Efficiency for Run 5 ($A_e = A_{nominal}$ (0.397 μm^2), x=0 mm, y=20.6 mm, z=0 mm, α=3.0^o & β=0^o).

x (mm)	0	R (mm)	12.83	
y (mm)	20.6	P_{in} (kPa)	688.79	
z (mm)	0	T_{amb} (^{o}C)	22.3	
α (deg)	3	T_2 (^{o}K)	293.69	
β (deg)	0	P_{amb} (kPa)	104.6	

Θ (deg)	RPM	W (g)	d (mm)	$Q_{turbine}$ (N-m)	$P_{turbine}$ (W)	P_{aero} (W)	$\eta_{aero-mech}$ (%)
5	0	20	63.5	0.00109	0.000	6.56	0.00
5.5	3,700	20	63.5	0.00120	0.077	6.56	1.18
6	11,900	20	63.5	0.00130	0.271	6.56	4.13
6.5	19,800	20	63.5	0.00141	0.488	6.56	7.44
7	24,100	20	63.5	0.00152	0.640	6.56	9.75
7.5	25,600	20	63.5	0.00163	0.728	6.56	11.10
8	28,000	20	63.5	0.00174	0.850	6.56	12.95
8.5	28,800	20	63.5	0.00185	0.929	6.56	14.15
9	35,600	20	63.5	0.00196	1.216	6.56	18.52
9.5	40,000	20	63.5	0.00207	1.442	6.56	21.97

Table B-36 Sample Data Recorded and Analyzed to Determine Turbine Shaft Power and Aero-Mechanical Efficiency for Run 6 ($A_e = A_{nominal}$ (0.397 μm^2), x=0 mm, y=20.6 mm, z=0 mm, α=1.5^o & β=0^o).

x (mm)	0	R (mm)	12.83	
y (mm)	20.6	P_{in} (kPa)	689.48	
z (mm)	0	T_{amb} (^{o}C)	22.3	
α (deg)	1.5	T_2 (^{o}K)	293.69	
β (deg)	0	P_{amb} (kPa)	104.6	

Θ (deg)	RPM	W (g)	d (mm)	$Q_{turbine}$ (N-m)	$P_{turbine}$ (W)	P_{aero} (W)	$\eta_{aero-mech}$ (%)
3.5	0	20	63.5	0.00076	0.000	6.57	0.00
4	20,000	20	63.5	0.00087	0.304	6.57	4.62
4.5	21,700	20	63.5	0.00098	0.370	6.57	5.64
5	23,600	20	63.5	0.00109	0.448	6.57	6.81
5.5	25,100	20	63.5	0.00120	0.524	6.57	7.97
6	27,800	20	63.5	0.00130	0.633	6.57	9.63
6.5	31,000	20	63.5	0.00141	0.764	6.57	11.64
7	33,100	20	63.5	0.00152	0.879	6.57	13.38
7.5	35,100	20	63.5	0.00163	0.999	6.57	15.20
8	38,600	20	63.5	0.00174	1.172	6.57	17.83
8.5	45,400	20	63.5	0.00185	1.464	6.57	22.29
11	47,900	20	63.5	0.00239	1.999	6.57	30.43

Table B-37 Sample Data Recorded and Analyzed to Determine Turbine Shaft Power and Aero-Mechanical Efficiency for Run 7 ($A_e = A_{nominal}$ (0.397 μm^2), x=0 mm, y=20.6 mm, z=0 mm, α=0° & β=2.5°).

x (mm)	0	R (mm)	12.83
y (mm)	20.6	P_{in} (kPa)	690.17
z (mm)	0	T_{amb} (°C)	22.3
α (deg)	0	T_2 (°K)	293.69
β (deg)	2.5	P_{amb} (kPa)	104.6

Θ (deg)	RPM	W (g)	d (mm)	$Q_{turbine}$ (N-m)	$P_{turbine}$ (W)	P_{aero} (W)	$\eta_{aero-mech}$ (%)
5.5	0	20	63.5	0.00120	0.000	6.58	0.00
6	8,200	20	63.5	0.00130	0.187	6.58	2.84
6.5	11,200	20	63.5	0.00141	0.276	6.58	4.20
7	13,600	20	63.5	0.00152	0.361	6.58	5.49
7.5	17,400	20	63.5	0.00163	0.495	6.58	7.53
8	22,200	20	63.5	0.00174	0.674	6.58	10.25
8.5	25,300	20	63.5	0.00185	0.816	6.58	12.41
9	28,000	20	63.5	0.00196	0.956	6.58	14.54
9.5	30,500	20	63.5	0.00207	1.099	6.58	16.72
10	33,200	20	63.5	0.00217	1.260	6.58	19.15
10.5	34,700	20	63.5	0.00228	1.382	6.58	21.02
11	36,400	20	63.5	0.00239	1.519	6.58	23.10
11.5	43,300	20	63.5	0.00250	1.889	6.58	28.73
12	45,000	20	63.5	0.00261	2.049	6.58	31.15
12.5	46,100	20	63.5	0.00272	2.186	6.58	33.25

Table B-38 Sample Data Recorded and Analyzed to Determine Turbine Shaft Power and Aero-Mechanical Efficiency for Run 8 ($A_e = A_{nominal}$ (0.397 μm^2), x=0 mm, y=20.6 mm, z=0 mm, α=0° & β=1.0°).

x (mm)	0	R (mm)	12.83
y (mm)	20.6	P_{in} (kPa)	703.27
z (mm)	0	T_{amb} (°C)	22.3
α (deg)	0	T_2 (°K)	293.69
β (deg)	1	P_{amb} (kPa)	104.6

Θ (deg)	RPM	W (g)	d (mm)	$Q_{turbine}$ (N-m)	$P_{turbine}$ (W)	P_{aero} (W)	$\eta_{aero-mech}$ (%)
2	0	20	63.5	0.00043	0.000	6.70	0.00
3	12,900	20	63.5	0.00065	0.147	6.70	2.19
3.5	14,700	20	63.5	0.00076	0.195	6.70	2.91
4	16,800	20	63.5	0.00087	0.255	6.70	3.80
4.5	19,900	20	63.5	0.00098	0.340	6.70	5.07
5	22,300	20	63.5	0.00109	0.423	6.70	6.31
5.5	25,600	20	63.5	0.00120	0.534	6.70	7.97
6	27,300	20	63.5	0.00130	0.621	6.70	9.27
6.5	31,000	20	63.5	0.00141	0.764	6.70	11.41
7	34,000	20	63.5	0.00152	0.903	6.70	13.48
7.5	37,600	20	63.5	0.00163	1.070	6.70	15.97
8	40,500	20	63.5	0.00174	1.229	6.70	18.34
8.5	41,400	20	63.5	0.00185	1.335	6.70	19.92

Table B-39 Sample Data Recorded and Analyzed to Determine Turbine Shaft Power and Aero-Mechanical Efficiency for Run 9 ($A_e = A_{nominal}$ (0.397 μm^2), x=0 mm, y=20.6 mm, z=0 mm, α=0^o & β=-2.5^o).

x (mm)	0	R (mm)	12.83
y (mm)	20.6	P_{in} (kPa)	697.75
z (mm)	0	T_{amb} (^{o}C)	22.3
α (deg)	0	T_2 (^{o}K)	293.69
β (deg)	-2.5	P_{amb} (kPa)	104.6

Θ (deg)	RPM	W (g)	d (mm)	$Q_{turbine}$ (N-m)	$P_{turbine}$ (W)	P_{aero} (W)	$\eta_{aero-mech}$ (%)
5	0	20	63.5	0.00109	0.000	6.65	0.00
6	7,100	20	63.5	0.00130	0.162	6.65	2.43
6.5	12,100	20	63.5	0.00141	0.298	6.65	4.49
7	14,300	20	63.5	0.00152	0.380	6.65	5.71
7.5	16,600	20	63.5	0.00163	0.472	6.65	7.10
8	21,600	20	63.5	0.00174	0.656	6.65	9.86
8.5	23,300	20	63.5	0.00185	0.751	6.65	11.30
9	26,500	20	63.5	0.00196	0.905	6.65	13.61
9.5	29,100	20	63.5	0.00207	1.049	6.65	15.78
10	32,200	20	63.5	0.00217	1.222	6.65	18.38
10.5	33,000	20	63.5	0.00228	1.315	6.65	19.77
11	36,800	20	63.5	0.00239	1.536	6.65	23.10
11.5	38,700	20	63.5	0.00250	1.688	6.65	25.40
12	41,900	20	63.5	0.00261	1.908	6.65	28.69
12.5	43,300	20	63.5	0.00272	2.053	6.65	30.89
13	46,100	20	63.5	0.00283	2.274	6.65	34.20

Table B-40 Sample Data Recorded and Analyzed to Determine Turbine Shaft Power and Aero-Mechanical Efficiency for Run 10 ($A_e = A_{nominal}$ (0.397 μm^2), x=0 mm, y=20.6 mm, z=0 mm, α=0^o & β=-1.0^o).

x (mm)	0	R (mm)	12.83
y (mm)	20.6	P_{in} (kPa)	706.02
z (mm)	0	T_{amb} (^{o}C)	22.3
α (deg)	0	T_2 (^{o}K)	294.80
β (deg)	-1	P_{amb} (kPa)	104.6

Θ (deg)	RPM	W (g)	d (mm)	$Q_{turbine}$ (N-m)	$P_{turbine}$ (W)	P_{aero} (W)	$\eta_{aero-mech}$ (%)
1.5	0	20	63.5	0.00033	0.000	6.74	0.00
2.5	7,600	20	63.5	0.00054	0.072	6.74	1.07
3	11,400	20	63.5	0.00065	0.130	6.74	1.93
3.5	13,400	20	63.5	0.00076	0.178	6.74	2.64
4	19,400	20	63.5	0.00087	0.294	6.74	4.37
4.5	21,600	20	63.5	0.00098	0.369	6.74	5.47
5	25,900	20	63.5	0.00109	0.491	6.74	7.29
5.5	26,600	20	63.5	0.00120	0.555	6.74	8.24
6	27,700	20	63.5	0.00130	0.631	6.74	9.36
6.5	30,400	20	63.5	0.00141	0.750	6.74	11.12
7	33,200	20	63.5	0.00152	0.882	6.74	13.08
7.5	35,600	20	63.5	0.00163	1.013	6.74	15.03
8	37,100	20	63.5	0.00174	1.126	6.74	16.71
8.5	41,900	20	63.5	0.00185	1.351	6.74	20.05

Table B-41 Sample Data Recorded and Analyzed to Determine Turbine Shaft Power and Aero-Mechanical Efficiency for Run 1 ($A_e = 0.75A_{nominal}$ (0.298 μm^2), x=12.8 mm, y=20.6 mm, z=0 mm, $\alpha=0^o$ & $\beta=0^o$).

x (mm)	12.8		R (mm)	12.83			
y (mm)	20.6		P_{in} (kPa)	693.61			
z (mm)	0		T_{amb} (^oC)	22.3			
α (deg)	0		T_2 (^oK)	293.69			
β (deg)	0		P_{amb} (kPa)	104.6			

Θ (deg)	RPM	W (g)	d (mm)	$Q_{turbine}$ (N-m)	$P_{turbine}$ (W)	P_{aero} (W)	$\eta_{aero-mech}$ (%)
7	0	20	63.5	0.00152	0.0000	4.96	0.00
7.5	8,300	20	63.5	0.00163	0.2362	4.96	4.77
8	11,460	20	63.5	0.00174	0.3478	4.96	7.02
8.5	12,862	20	63.5	0.00185	0.4148	4.96	8.37
9	19,858	20	63.5	0.00196	0.6780	4.96	13.68
9.5	23,524	20	63.5	0.00207	0.8478	4.96	17.11
10	29,351	20	63.5	0.00217	1.1135	4.96	22.47
10.5	32,273	20	63.5	0.00228	1.2856	4.96	25.94
11	33,104	20	63.5	0.00239	1.3815	4.96	27.88

Table B-42 Sample Data Recorded and Analyzed to Determine Turbine Shaft Power and Aero-Mechanical Efficiency for Run 2 ($A_e = 0.75A_{nominal}$ (0.298 μm^2), x=6.41 mm, y=20.6 mm, z=0 mm, $\alpha=0^o$ & $\beta=0^o$).

x (mm)	6.41		R (mm)	12.83			
y (mm)	20.6		P_{in} (kPa)	694.99			
z (mm)	0		T_{amb} (^oC)	22.3			
α (deg)	0		T_2 (^oK)	294.24			
β (deg)	0		P_{amb} (kPa)	104.6			

Θ (deg)	RPM	W (g)	d (mm)	$Q_{turbine}$ (N-m)	$P_{turbine}$ (W)	P_{aero} (W)	$\eta_{aero-mech}$ (%)
4	0	20	63.5	0.00087	0.0000	4.97	0.00
4.5	3,582	20	63.5	0.00098	0.0612	4.97	1.23
5	9,085	20	63.5	0.00109	0.1723	4.97	3.47
5.5	10,193	20	63.5	0.00120	0.2127	4.97	4.28
6	12,270	20	63.5	0.00130	0.2793	4.97	5.62
6.5	15,227	20	63.5	0.00141	0.3755	4.97	7.56
7	17,146	20	63.5	0.00152	0.4553	4.97	9.16
7.5	21,559	20	63.5	0.00163	0.6134	4.97	12.34
8	23,716	20	63.5	0.00174	0.7198	4.97	14.48
8.5	26,362	20	63.5	0.00185	0.8501	4.97	17.11
9	30,449	20	63.5	0.00196	1.0397	4.97	20.92
9.5	33,842	20	63.5	0.00207	1.2197	4.97	24.54
10	34,828	20	63.5	0.00217	1.3213	4.97	26.59

Table B-43 Sample Data Recorded and Analyzed to Determine Turbine Shaft Power and Aero-Mechanical Efficiency for Run 3 ($A_e = 0.75A_{nominal}$ (0.298 μm^2), x=0 mm, y=20.6 mm, z=0 mm, α=-3.0^o & β=0^o).

x (mm)	0	R (mm)	12.83	
y (mm)	20.6	P_{in} (kPa)	686.72	
z (mm)	0	T_{amb} (^{o}C)	22.3	
α (deg)	-3	T_2 (^{o}K)	293.69	
β (deg)	0	P_{amb} (kPa)	104.6	

Θ (deg)	RPM	W (g)	d (mm)	$Q_{turbine}$ (N-m)	$P_{turbine}$ (W)	P_{aero} (W)	$\eta_{aero-mech}$ (%)
3.5	0	20	63.5	0.000761	0.0000	4.91	0.00
4	5,116	20	63.5	0.000869	0.0776	4.91	1.58
4.5	8,004	20	63.5	0.000978	0.1366	4.91	2.79
5	10,391	20	63.5	0.001087	0.1971	4.91	4.02
5.5	14,367	20	63.5	0.001196	0.2998	4.91	6.11
6	18,479	20	63.5	0.001304	0.4206	4.91	8.57
6.5	22,208	20	63.5	0.001413	0.5476	4.91	11.16
7	25,884	20	63.5	0.001522	0.6874	4.91	14.01
7.5	29,167	20	63.5	0.001630	0.8299	4.91	16.92
8	31,725	20	63.5	0.001739	0.9629	4.91	19.63
8.5	33,936	20	63.5	0.001848	1.0944	4.91	22.31
9	35,665	20	63.5	0.001956	1.2178	4.91	24.82

Table B-44 Sample Data Recorded and Analyzed to Determine Turbine Shaft Power and Aero-Mechanical Efficiency for Run 4 ($A_e = A_{nominal}$ (0.397 μm^2), x=0 mm, y=20.6 mm, z=0 mm, α=-1.5^o & β=0^o).

x (mm)	0	R (mm)	12.83	
y (mm)	20.6	P_{in} (kPa)	686.03	
z (mm)	0	T_{amb} (^{o}C)	22.3	
α (deg)	-1.5	T_2 (^{o}K)	293.69	
β (deg)	0	P_{amb} (kPa)	104.6	

Θ (deg)	RPM	W (g)	d (mm)	$Q_{turbine}$ (N-m)	$P_{turbine}$ (W)	P_{aero} (W)	$\eta_{aero-mech}$ (%)
4	0	20	63.5	0.00087	0.000	4.90	0.00
4.5	4,656	20	63.5	0.00098	0.079	4.90	1.62
5	6,972	20	63.5	0.00109	0.132	4.90	2.70
5.5	10,838	20	63.5	0.00120	0.226	4.90	4.61
6	13,492	20	63.5	0.00130	0.307	4.90	6.27
6.5	16,465	20	63.5	0.00141	0.406	4.90	8.28
7	18,204	20	63.5	0.00152	0.483	4.90	9.86
7.5	20,410	20	63.5	0.00163	0.581	4.90	11.85
8	23,559	20	63.5	0.00174	0.715	4.90	14.59
8.5	25,391	20	63.5	0.00185	0.819	4.90	16.71

Table B-45 Sample Data Recorded and Analyzed to Determine Turbine Shaft Power and Aero-Mechanical Efficiency for Run 5 ($A_e = 0.75A_{nominal}$ (0.298 μm^2), x=0 mm, y=20.6 mm, z=0 mm, α=3.0° & β=0°).

x (mm)	0	R (mm)	12.83
y (mm)	20.6	P_{in} (kPa)	681.20
z (mm)	0	T_{amb} (°C)	22.3
α (deg)	3	T_2 (°K)	293.69
β (deg)	0	P_{amb} (kPa)	104.6

Θ (deg)	RPM	W (g)	d (mm)	$Q_{turbine}$ (N-m)	$P_{turbine}$ (W)	P_{aero} (W)	$\eta_{aero-mech}$ (%)
4.5	0	20	63.5	0.00098	0.000	4.87	0.00
5	5,438	20	63.5	0.00109	0.103	4.87	2.12
5.5	6,428	20	63.5	0.00120	0.134	4.87	2.76
6	7,544	20	63.5	0.00130	0.172	4.87	3.53
6.5	9,325	20	63.5	0.00141	0.230	4.87	4.73
7	11,688	20	63.5	0.00152	0.310	4.87	6.38
7.5	13,680	20	63.5	0.00163	0.389	4.87	8.00
8	15,551	20	63.5	0.00174	0.472	4.87	9.70
8.5	18,602	20	63.5	0.00185	0.600	4.87	12.33
9	20,531	20	63.5	0.00196	0.701	4.87	14.40
9.5	22,390	20	63.5	0.00207	0.807	4.87	16.58
10	24,993	20	63.5	0.00217	0.948	4.87	19.48
10.5	25,464	20	63.5	0.00228	1.014	4.87	20.84
11	27,011	20	63.5	0.00239	1.127	4.87	23.16
11.5	28,086	20	63.5	0.00250	1.225	4.87	25.18
12	29,995	20	63.5	0.00261	1.366	4.87	28.06
12.5	30,660	20	63.5	0.00272	1.454	4.87	29.88

Table B-46 Sample Data Recorded and Analyzed to Determine Turbine Shaft Power and Aero-Mechanical Efficiency for Run 6 ($A_e = 0.75A_{nominal}$ (0.298 μm^2), x=0 mm, y=20.6 mm, z=0 mm, α=1.5° & β=0°).

x (mm)	0	R (mm)	12.83
y (mm)	20.6	P_{in} (kPa)	681.89
z (mm)	0	T_{amb} (°C)	22.3
α (deg)	1.5	T_2 (°K)	293.69
β (deg)	0	P_{amb} (kPa)	104.6

Θ (deg)	RPM	W (g)	d (mm)	$Q_{turbine}$ (N-m)	$P_{turbine}$ (W)	P_{aero} (W)	$\eta_{aero-mech}$ (%)
4	0	20	63.5	0.00087	0.000	4.87	0.00
4.5	6,589	20	63.5	0.00098	0.112	4.87	2.31
5	7,013	20	63.5	0.00109	0.133	4.87	2.73
5.5	7,856	20	63.5	0.00120	0.164	4.87	3.36
6	8,280	20	63.5	0.00130	0.188	4.87	3.87
6.5	9,176	20	63.5	0.00141	0.226	4.87	4.64
7	11,791	20	63.5	0.00152	0.313	4.87	6.43

Table B-46 Sample Data Recorded and Analyzed to Determine Turbine Shaft Power and Aero-Mechanical Efficiency for Run 6 ($A_e = 0.75A_{nominal}$ (0.298 μm^2), x=0 mm, y=20.6 mm, z=0 mm, $\alpha=1.5^o$ & $\beta=0^o$) (Cont'd).

Θ (deg)	RPM	W (g)	d (mm)	$Q_{turbine}$ (N-m)	$P_{turbine}$ (W)	P_{aero} (W)	$\eta_{aero-mech}$ (%)
7.5	13,235	20	63.5	0.00163	0.377	4.87	7.73
8	17,739	20	63.5	0.00174	0.538	4.87	11.05
8.5	21,536	20	63.5	0.00185	0.694	4.87	14.26
9	23,394	20	63.5	0.00196	0.799	4.87	16.40
9.5	26,417	20	63.5	0.00207	0.952	4.87	19.54
10	28,063	20	63.5	0.00217	1.065	4.87	21.86
10.5	29,624	20	63.5	0.00228	1.180	4.87	24.22
11	30,149	20	63.5	0.00239	1.258	4.87	25.83

Table B-47 Sample Data Recorded and Analyzed to Determine Turbine Shaft Power and Aero-Mechanical Efficiency for Run 7 ($A_e = 0.75A_{nominal}$ (0.298 μm^2), x=0 mm, y=20.6 mm, z=0 mm, $\alpha=0^o$ & $\beta=2.5^o$).

x (mm)	0	R (mm)	12.83
y (mm)	20.6	P_{in} (kPa)	680.51
z (mm)	0	T_{amb} (^oC)	22.3
α (deg)	0	T_2 (^oK)	294.24
β (deg)	2.5	P_{amb} (kPa)	104.6

Θ (deg)	RPM	W (g)	d (mm)	$Q_{turbine}$ (N-m)	$P_{turbine}$ (W)	P_{aero} (W)	$\eta_{aero-mech}$ (%)
3	0	20	63.5	0.000652	0.000	4.87	0.00
3.5	9,131	20	63.5	0.000761	0.121	4.87	2.49
4	10,349	20	63.5	0.000869	0.157	4.87	3.23
4.5	11,844	20	63.5	0.000978	0.202	4.87	4.16
5	14,144	20	63.5	0.001087	0.268	4.87	5.51
5.5	15,755	20	63.5	0.001196	0.329	4.87	6.76
6	17,907	20	63.5	0.001304	0.408	4.87	8.38
6.5	20,157	20	63.5	0.001413	0.497	4.87	10.21
7	22,453	20	63.5	0.001522	0.596	4.87	12.25
7.5	24,669	20	63.5	0.001630	0.702	4.87	14.42
8	27,557	20	63.5	0.001739	0.836	4.87	17.19
8.5	29,973	20	63.5	0.001848	0.967	4.87	19.86
9	31,857	20	63.5	0.001956	1.088	4.87	22.35

Table B-48 Sample Data Recorded and Analyzed to Determine Turbine Shaft Power and Aero-Mechanical Efficiency for Run 8 ($A_e = 0.75A_{nominal}$ (0.298 μm^2), x=0 mm, y=20.6 mm, z=0 mm, α=0° & β=1.0°).

x (mm)	0	R (mm)	12.83
y (mm)	20.6	P_{in} (kPa)	681.20
z (mm)	0	T_{amb} (°C)	22.3
α (deg)	0	T_2 (°K)	293.69
β (deg)	1	P_{amb} (kPa)	104.6

Θ (deg)	RPM	W (g)	d (mm)	$Q_{turbine}$ (N-m)	$P_{turbine}$ (W)	P_{aero} (W)	$\eta_{aero-mech}$ (%)
2.5	0	20	63.5	0.00054	0.000	4.87	0.00
3	3,331	20	63.5	0.00065	0.038	4.87	0.78
3.5	9,041	20	63.5	0.00076	0.120	4.87	2.47
4	10,215	20	63.5	0.00087	0.155	4.87	3.19
4.5	12,511	20	63.5	0.00098	0.214	4.87	4.39
5	13,508	20	63.5	0.00109	0.256	4.87	5.27
5.5	18,115	20	63.5	0.00120	0.378	4.87	7.77
6	21,154	20	63.5	0.00130	0.482	4.87	9.89
6.5	23,389	20	63.5	0.00141	0.577	4.87	11.85
7	25,464	20	63.5	0.00152	0.676	4.87	13.90
7.5	26,815	20	63.5	0.00163	0.763	4.87	15.68
8	28,381	20	63.5	0.00174	0.861	4.87	17.70
8.5	30,279	20	63.5	0.00185	0.976	4.87	20.06
9	31,628	20	63.5	0.00196	1.080	4.87	22.19

Table B-49 Sample Data Recorded and Analyzed to Determine Turbine Shaft Power and Aero-Mechanical Efficiency for Run 9 ($A_e = 0.75A_{nominal}$ (0.298 μm^2), x=0 mm, y=20.6 mm, z=0 mm, α=0° & β=-2.5°).

x (mm)	0	R (mm)	12.83
y (mm)	20.6	P_{in} (kPa)	688.10
z (mm)	0	T_{amb} (°C)	22.3
α (deg)	0	T_2 (°K)	293.69
β (deg)	-2.5	P_{amb} (kPa)	104.6

Θ (deg)	RPM	W (g)	d (mm)	$Q_{turbine}$ (N-m)	$P_{turbine}$ (W)	P_{aero} (W)	$\eta_{aero-mech}$ (%)
4	0	20	63.5	0.00087	0.000	4.92	0.00
4.5	3,558	20	63.5	0.00098	0.061	4.92	1.24
5	6,694	20	63.5	0.00109	0.127	4.92	2.58
5.5	8,935	20	63.5	0.00120	0.186	4.92	3.79
6	10,248	20	63.5	0.00130	0.233	4.92	4.75
6.5	10,883	20	63.5	0.00141	0.268	4.92	5.46
7	12,937	20	63.5	0.00152	0.344	4.92	6.99
7.5	15,866	20	63.5	0.00163	0.451	4.92	9.18
8	18,069	20	63.5	0.00174	0.548	4.92	11.16
8.5	20,651	20	63.5	0.00185	0.666	4.92	13.55
9	23,029	20	63.5	0.00196	0.786	4.92	16.00
9.5	27,606	20	63.5	0.00207	0.995	4.92	20.24
10	29,495	20	63.5	0.00217	1.119	4.92	22.76

Table B-50 Sample Data Recorded and Analyzed to Determine Turbine Shaft Power and Aero-Mechanical Efficiency for Run 10 ($A_e = 0.75A_{nominal}$ (0.298 μm^2), x=0 mm, y=20.6 mm, z=0 mm, $\alpha=0^o$ & $\beta=-1.0^o$).

x (mm)	0	R (mm)	12.83
y (mm)	20.6	P_{in} (kPa)	680.51
z (mm)	0	T_{amb} (^oC)	22.3
α (deg)	0	T_2 (^oK)	293.69
β (deg)	-1	P_{amb} (kPa)	104.6

Θ (deg)	RPM	W (g)	d (mm)	$Q_{turbine}$ (N-m)	$P_{turbine}$ (W)	P_{aero} (W)	$\eta_{aero-mech}$ (%)
3	0	20	63.5	0.00065	0.000	4.86	0.00
3.5	5,921	20	63.5	0.00076	0.079	4.86	1.62
4	6,915	20	63.5	0.00087	0.105	4.86	2.16
4.5	8,440	20	63.5	0.00098	0.144	4.86	2.96
5	9,618	20	63.5	0.00109	0.182	4.86	3.75
5.5	12,305	20	63.5	0.00120	0.257	4.86	5.28
6	15,347	20	63.5	0.00130	0.349	4.86	7.19
6.5	17,235	20	63.5	0.00141	0.425	4.86	8.74
7	19,444	20	63.5	0.00152	0.516	4.86	10.62
7.5	20,198	20	63.5	0.00163	0.575	4.86	11.82
8	23,030	20	63.5	0.00174	0.699	4.86	14.38
8.5	25,049	20	63.5	0.00185	0.808	4.86	16.62
9	28,124	20	63.5	0.00196	0.960	4.86	19.75
9.5	31,425	20	63.5	0.00207	1.133	4.86	23.30

Table B-51 Sample Data Recorded and Analyzed to Determine Turbine Shaft Power and Aero-Mechanical Efficiency for Run 1 ($A_e = 0.5A_{nominal}$ (0.199 μm^2), x=12.8 mm, y=20.6 mm, z=0 mm, $\alpha=0^o$ & $\beta=0^o$).

x (mm)	12.8	R (mm)	12.83
y (mm)	20.6	P_{in} (kPa)	684.65
z (mm)	0	T_{amb} (^oC)	22.3
α (deg)	0	T_2 (^oK)	292.57
β (deg)	0	P_{amb} (kPa)	104.6

Θ (deg)	RPM	W (g)	d (mm)	$Q_{turbine}$ (N-m)	$P_{turbine}$ (W)	P_{aero} (W)	$\eta_{aero-mech}$ (%)
3	0	20	63.5	0.00065	0.000	3.25	0.00
3.5	4,418	20	63.5	0.00076	0.059	3.25	1.80
4	7,341	20	63.5	0.00087	0.111	3.25	3.42
4.5	10,197	20	63.5	0.00098	0.174	3.25	5.35
5	13,536	20	63.5	0.00109	0.257	3.25	7.89
5.5	15,736	20	63.5	0.00120	0.328	3.25	10.09
6	17,060	20	63.5	0.00130	0.388	3.25	11.93
6.5	19,535	20	63.5	0.00141	0.482	3.25	14.80
7	22,524	20	63.5	0.00152	0.598	3.25	18.38

Table B-51 Sample Data Recorded and Analyzed to Determine Turbine Shaft Power and Aero-Mechanical Efficiency for Run 1 ($A_e = 0.5A_{nominal}$ (0.199 μm^2), x=12.8 mm, y=20.6 mm, z=0 mm, $\alpha=0^o$ & $\beta=0^o$) (Cont'd).

Θ (deg)	RPM	W (g)	d (mm)	$Q_{turbine}$ (N-m)	$P_{turbine}$ (W)	P_{aero} (W)	$\eta_{aero-mech}$ (%)
7.5	24,255	20	63.5	0.00163	0.690	3.25	21.21
8	26,778	20	63.5	0.00174	0.813	3.25	24.98
8.5	28,021	20	63.5	0.00185	0.904	3.25	27.77
9	30,991	20	63.5	0.00196	1.058	3.25	32.52
9.5	32,601	20	63.5	0.00207	1.175	3.25	36.11
10	33,238	20	63.5	0.00217	1.261	3.25	38.75
10.5	33,622	20	63.5	0.00228	1.339	3.25	41.16
11	34,112	20	63.5	0.00239	1.424	3.25	43.75

Table B-52 Sample Data Recorded and Analyzed to Determine Turbine Shaft Power and Aero-Mechanical Efficiency for Run 2 ($A_e = 0.5A_{nominal}$ (0.199 μm^2), x=6.41 mm, y=20.6 mm, z=0 mm, $\alpha=0^o$ & $\beta=0^o$).

x (mm)	6.41	R (mm)	12.83
y (mm)	20.6	P_{in} (kPa)	676.38
z (mm)	0	T_{amb} (^oC)	22.3
α (deg)	0	T_2 (^oK)	292.57
β (deg)	0	P_{amb} (kPa)	104.6

Θ (deg)	RPM	W (g)	d (mm)	$Q_{turbine}$ (N-m)	$P_{turbine}$ (W)	P_{aero} (W)	$\eta_{aero-mech}$ (%)
3	0	20	63.5	0.00065	0.0000	3.21	0.00
3.5	1,953	20	63.5	0.00076	0.0259	3.21	0.81
4	7,518	20	63.5	0.00087	0.1141	3.21	3.55
4.5	9,681	20	63.5	0.00098	0.1653	3.21	5.14
5	11,347	20	63.5	0.00109	0.2152	3.21	6.70
5.5	15,458	20	63.5	0.00120	0.3225	3.21	10.03
6	20,022	20	63.5	0.00130	0.4558	3.21	14.18
6.5	23,354	20	63.5	0.00141	0.5759	3.21	17.91
7	26,130	20	63.5	0.00152	0.6939	3.21	21.59
7.5	27,456	20	63.5	0.00163	0.7812	3.21	24.30
8	29,463	20	63.5	0.00174	0.8942	3.21	27.82
8.5	32,087	20	63.5	0.00185	1.0347	3.21	32.19
9	33,847	20	63.5	0.00196	1.1557	3.21	35.95

Table B-53 Sample Data Recorded and Analyzed to Determine Turbine Shaft Power and Aero-Mechanical Efficiency for Run 3 ($A_e = 0.5A_{nominal}$ (0.199 μm^2), x=0 mm, y=20.6 mm, z=0 mm, α=-3.0° & β=0°).

x (mm)	0	R (mm)	12.83
y (mm)	20.6	P_{in} (kPa)	686.03
z (mm)	0	T_{amb} (°C)	22.3
α (deg)	-3	T_2 (°K)	292.57
β (deg)	0	P_{amb} (kPa)	104.6

Θ (deg)	RPM	W (g)	d (mm)	$Q_{turbine}$ (N-m)	$P_{turbine}$ (W)	P_{aero} (W)	$\eta_{aero-mech}$ (%)
2.5	0	20	63.5	0.000543	0.0000	3.26	0.00
3	2,878	20	63.5	0.000652	0.0328	3.26	1.00
3.5	6,651	20	63.5	0.000761	0.0883	3.26	2.71
4	9,867	20	63.5	0.000869	0.1497	3.26	4.59
4.5	11,055	20	63.5	0.000978	0.1887	3.26	5.79
5	12,620	20	63.5	0.001087	0.2394	3.26	7.34
5.5	13,933	20	63.5	0.001196	0.2907	3.26	8.92
6	15,752	20	63.5	0.001304	0.3586	3.26	11.00
6.5	17,877	20	63.5	0.001413	0.4408	3.26	13.52
7	20,480	20	63.5	0.001522	0.5439	3.26	16.68
7.5	24,256	20	63.5	0.001630	0.6902	3.26	21.17
8	26,063	20	63.5	0.001739	0.7910	3.26	24.26
8.5	26,755	20	63.5	0.001848	0.8628	3.26	26.46
9	29,100	20	63.5	0.001956	0.9936	3.26	30.47
9.5	31,831	20	63.5	0.002065	1.1472	3.26	35.19
10	32,008	20	63.5	0.002174	1.2143	3.26	37.24
10.5	32,228	20	63.5	0.002282	1.2838	3.26	39.37

Table B-54 Sample Data Recorded and Analyzed to Determine Turbine Shaft Power and Aero-Mechanical Efficiency for Run 4 ($A_e = 0.5A_{nominal}$ (0.199 μm^2), x=0 mm, y=20.6 mm, z=0 mm, α=-1.5° & β=0°).

x (mm)	0	R (mm)	12.83
y (mm)	20.6	P_{in} (kPa)	704.64
z (mm)	0	T_{amb} (°C)	22.3
α (deg)	-1.5	T_2 (°K)	292.57
β (deg)	0	P_{amb} (kPa)	104.6

Θ (deg)	RPM	W (g)	d (mm)	$Q_{turbine}$ (N-m)	$P_{turbine}$ (W)	P_{aero} (W)	$\eta_{aero-mech}$ (%)
3.5	0	20	63.5	0.00076	0.000	3.35	0.00
4	5,460	20	63.5	0.00087	0.083	3.35	2.47
4.5	8,906	20	63.5	0.00098	0.152	3.35	4.54
5	12,155	20	63.5	0.00109	0.231	3.35	6.88
5.5	14,173	20	63.5	0.00120	0.296	3.35	8.83
6	17,837	20	63.5	0.00130	0.406	3.35	12.12
6.5	18,949	20	63.5	0.00141	0.467	3.35	13.95
7	23,531	20	63.5	0.00152	0.625	3.35	18.66
7.5	26,564	20	63.5	0.00163	0.756	3.35	22.57
8	29,909	20	63.5	0.00174	0.908	3.35	27.10
8.5	30,597	20	63.5	0.00185	0.987	3.35	29.46
9	34,575	20	63.5	0.00196	1.181	3.35	35.25

Table B-55 Sample Data Recorded and Analyzed to Determine Turbine Shaft Power and Aero-Mechanical Efficiency for Run 5 ($A_e = 0.5A_{nominal}$ (0.199 μm^2), x=0 mm, y=20.6 mm, z=0 mm, α=3.0° & β=0°).

x (mm)	0	R (mm)	12.83
y (mm)	20.6	P_{in} (kPa)	687.41
z (mm)	0	T_{amb} (°C)	22.3
α (deg)	3	T_2 (°K)	293.69
β (deg)	0	P_{amb} (kPa)	104.6

Θ (deg)	RPM	W (g)	d (mm)	$Q_{turbine}$ (N-m)	$P_{turbine}$ (W)	P_{aero} (W)	$\eta_{aero-mech}$ (%)
2.5	0	20	63.5	0.00054	0.000	3.27	0.00
3	4,639	20	63.5	0.00065	0.053	3.27	1.61
3.5	5,034	20	63.5	0.00076	0.067	3.27	2.04
4	6,873	20	63.5	0.00087	0.104	3.27	3.19
4.5	8,938	20	63.5	0.00098	0.153	3.27	4.66
5	10,544	20	63.5	0.00109	0.200	3.27	6.11
5.5	12,717	20	63.5	0.00120	0.265	3.27	8.11
6	14,675	20	63.5	0.00130	0.334	3.27	10.21
6.5	18,146	20	63.5	0.00141	0.447	3.27	13.67
7	20,418	20	63.5	0.00152	0.542	3.27	16.57
7.5	22,337	20	63.5	0.00163	0.636	3.27	19.42
8	25,562	20	63.5	0.00174	0.776	3.27	23.70
8.5	28,523	20	63.5	0.00185	0.920	3.27	28.10
9	29,565	20	63.5	0.00196	1.009	3.27	30.84
9.5	30,523	20	63.5	0.00207	1.100	3.27	33.61

Table B-56 Sample Data Recorded and Analyzed to Determine Turbine Shaft Power and Aero-Mechanical Efficiency for Run 6 ($A_e = 0.5A_{nominal}$ (0.199 μm^2), x=0 mm, y=20.6 mm, z=0 mm, α=1.5° & β=0°).

x (mm)	0	R (mm)	12.83
y (mm)	20.6	P_{in} (kPa)	704.64
z (mm)	0	T_{amb} (°C)	22.3
α (deg)	1.5	T_2 (°K)	294.24
β (deg)	0	P_{amb} (kPa)	104.6

Θ (deg)	RPM	W (g)	d (mm)	$Q_{turbine}$ (N-m)	$P_{turbine}$ (W)	P_{aero} (W)	$\eta_{aero-mech}$ (%)
3	0	20	63.5	0.00065	0.000	3.36	0.00
3.5	3,577	20	63.5	0.00076	0.047	3.36	1.41
4	4,580	20	63.5	0.00087	0.070	3.36	2.07
4.5	9,233	20	63.5	0.00098	0.158	3.36	4.69
5	12,490	20	63.5	0.00109	0.237	3.36	7.05
5.5	16,269	20	63.5	0.00120	0.339	3.36	10.11
6	19,081	20	63.5	0.00130	0.434	3.36	12.93
6.5	22,819	20	63.5	0.00141	0.563	3.36	16.75
7	25,546	20	63.5	0.00152	0.678	3.36	20.20
7.5	29,222	20	63.5	0.00163	0.831	3.36	24.76
8	31,143	20	63.5	0.00174	0.945	3.36	28.14
8.5	32,912	20	63.5	0.00185	1.061	3.36	31.60

Table B-57 Sample Data Recorded and Analyzed to Determine Turbine Shaft Power and Aero-Mechanical Efficiency for Run 7 ($A_e = 0.5A_{nominal}$ (0.199 μm^2), x=0 mm, y=20.6 mm, z=0 mm, $\alpha=0^o$ & $\beta=2.5^o$).

x (mm)	0	R (mm)	12.83
y (mm)	20.6	P_{in} (kPa)	702.58
z (mm)	0	T_{amb} (^oC)	22.3
α (deg)	0	T_2 (^oK)	293.69
β (deg)	2.5	P_{amb} (kPa)	104.6

Θ (deg)	RPM	W (g)	d (mm)	$Q_{turbine}$ (N-m)	$P_{turbine}$ (W)	P_{aero} (W)	$\eta_{aero-mech}$ (%)
2.5	0	20	63.5	0.000543	0.000	3.35	0.00
3	2,801	20	63.5	0.000652	0.032	3.35	0.95
3.5	7,356	20	63.5	0.000761	0.098	3.35	2.92
4	8,936	20	63.5	0.000869	0.136	3.35	4.05
4.5	10,093	20	63.5	0.000978	0.172	3.35	5.15
5	13,030	20	63.5	0.001087	0.247	3.35	7.39
5.5	14,387	20	63.5	0.001196	0.300	3.35	8.97
6	16,148	20	63.5	0.001304	0.368	3.35	10.99
6.5	19,682	20	63.5	0.001413	0.485	3.35	14.51
7	24,291	20	63.5	0.001522	0.645	3.35	19.28
7.5	25,130	20	63.5	0.001630	0.715	3.35	21.37
8	26,773	20	63.5	0.001739	0.813	3.35	24.29
8.5	28,783	20	63.5	0.001848	0.928	3.35	27.74
9	31,669	20	63.5	0.001956	1.081	3.35	32.32

Table B-58 Sample Data Recorded and Analyzed to Determine Turbine Shaft Power and Aero-Mechanical Efficiency for Run 8 ($A_e = 0.5A_{nominal}$ (0.199 μm^2), x=0 mm, y=20.6 mm, z=0 mm, $\alpha=0^o$ & $\beta=1.0^o$).

x (mm)	0	R (mm)	12.83
y (mm)	20.6	P_{in} (kPa)	683.96
z (mm)	0	T_{amb} (^oC)	22.3
α (deg)	0	T_2 (^oK)	293.69
β (deg)	1	P_{amb} (kPa)	104.6

Θ (deg)	RPM	W (g)	d (mm)	$Q_{turbine}$ (N-m)	$P_{turbine}$ (W)	P_{aero} (W)	$\eta_{aero-mech}$ (%)
3	0	20	63.5	0.00065	0.000	3.26	0.00
3.5	2,346	20	63.5	0.00076	0.031	3.26	0.96
4	7,612	20	63.5	0.00087	0.116	3.26	3.55
4.5	9,670	20	63.5	0.00098	0.165	3.26	5.07
5	12,535	20	63.5	0.00109	0.238	3.26	7.30
5.5	14,537	20	63.5	0.00120	0.303	3.26	9.31
6	16,305	20	63.5	0.00130	0.371	3.26	11.40
6.5	19,968	20	63.5	0.00141	0.492	3.26	15.12
7	22,475	20	63.5	0.00152	0.597	3.26	18.33
7.5	24,095	20	63.5	0.00163	0.686	3.26	21.05
8	26,434	20	63.5	0.00174	0.802	3.26	24.63
8.5	28,583	20	63.5	0.00185	0.922	3.26	28.30

Table B-59 Sample Data Recorded and Analyzed to Determine Turbine Shaft Power and Aero-Mechanical Efficiency for Run 9 ($A_e = 0.5A_{nominal}$ (0.199 μm^2), x=0 mm, y=20.6 mm, z=0 mm, $\alpha=0^o$ & $\beta=-2.5^o$).

x (mm)	0	R (mm)	12.83
y (mm)	20.6	P_{in} (kPa)	760.49
z (mm)	0	T_{amb} (^oC)	22.3
α (deg)	0	T_2 (^oK)	293.69
β (deg)	-2.5	P_{amb} (kPa)	104.6

Θ (deg)	RPM	W (g)	d (mm)	$Q_{turbine}$ (N-m)	$P_{turbine}$ (W)	P_{aero} (W)	$\eta_{aero-mech}$ (%)
4.5	0	20	63.5	0.00098	0.000	3.62	0.00
5	5,087	20	63.5	0.00109	0.096	3.62	2.66
5.5	10,804	20	63.5	0.00120	0.225	3.62	6.23
6	14,289	20	63.5	0.00130	0.325	3.62	8.98
6.5	18,135	20	63.5	0.00141	0.447	3.62	12.35
7	20,165	20	63.5	0.00152	0.536	3.62	14.79
7.5	23,621	20	63.5	0.00163	0.672	3.62	18.56
8	26,029	20	63.5	0.00174	0.790	3.62	21.82
8.5	28,288	20	63.5	0.00185	0.912	3.62	25.19
9	32,898	20	63.5	0.00196	1.123	3.62	31.02
9.5	33,960	20	63.5	0.00207	1.224	3.62	33.80
10	35,996	20	63.5	0.00217	1.366	3.62	37.71

Table B-60 Sample Data Recorded and Analyzed to Determine Turbine Shaft Power and Aero-Mechanical Efficiency for Run 10 ($A_e = 0.5A_{nominal}$ (0.199 μm^2), x=0 mm, y=20.6 mm, z=0 mm, $\alpha=0^o$ & $\beta=-1.0^o$).

x (mm)	0	R (mm)	12.83
y (mm)	20.6	P_{in} (kPa)	681.89
z (mm)	0	T_{amb} (^oC)	22.3
α (deg)	0	T_2 (^oK)	293.69
β (deg)	-1	P_{amb} (kPa)	104.6

Θ (deg)	RPM	W (g)	d (mm)	$Q_{turbine}$ (N-m)	$P_{turbine}$ (W)	P_{aero} (W)	$\eta_{aero-mech}$ (%)
3.5	0	20	63.5	0.00076	0.000	3.25	0.00
4	2,321	20	63.5	0.00087	0.035	3.25	1.08
4.5	6,651	20	63.5	0.00098	0.114	3.25	3.50
5	9,094	20	63.5	0.00109	0.173	3.25	5.31
5.5	13,313	20	63.5	0.00120	0.278	3.25	8.56
6	15,814	20	63.5	0.00130	0.360	3.25	11.09
6.5	17,973	20	63.5	0.00141	0.443	3.25	13.65
7	21,766	20	63.5	0.00152	0.578	3.25	17.80
7.5	23,364	20	63.5	0.00163	0.665	3.25	20.47
8	27,977	20	63.5	0.00174	0.849	3.25	26.15
8.5	30,431	20	63.5	0.00185	0.981	3.25	30.22
9	33,777	20	63.5	0.00196	1.153	3.25	35.52
9.5	35,220	20	63.5	0.00207	1.269	3.25	39.09

Table B-61 Sample Data Recorded and Analyzed to Determine Turbine Shaft Power and Aero-Mechanical Efficiency for Run 1 ($A_e = A_{nominal}$ (0.397 μm^2), x=12.8 mm, y=33.3 mm, z=0 mm, α=0° & β=0°).

x (mm)	12.8	R (mm)	12.83
y (mm)	33.3	P_{in} (kPa)	697.06
z (mm)	0	T_{amb} (°C)	23.1
α (deg)	0	T_2 (°K)	293.69
β (deg)	0	P_{amb} (kPa)	105.5

Θ (deg)	RPM	W (g)	d (mm)	$Q_{turbine}$ (N-m)	$P_{turbine}$ (W)	P_{aero} (W)	$\eta_{aero-mech}$ (%)
3	0	20	63.5	0.00065	0.000	6.64	0.00
5	4,452	20	63.5	0.00109	0.084	6.64	1.27
5.5	8,625	20	63.5	0.00120	0.180	6.64	2.71
6	11,148	20	63.5	0.00130	0.254	6.64	3.82
6.5	12,769	20	63.5	0.00141	0.315	6.64	4.74
7	15,402	20	63.5	0.00152	0.409	6.64	6.16
7.5	20,975	20	63.5	0.00163	0.597	6.64	8.99
8	26,271	20	63.5	0.00174	0.797	6.64	12.01
8.5	28,843	20	63.5	0.00185	0.930	6.64	14.00
9	30,301	20	63.5	0.00196	1.035	6.64	15.58
9.5	31,759	20	63.5	0.00207	1.145	6.64	17.23
10	33,217	20	63.5	0.00217	1.260	6.64	18.97
10.5	34,675	20	63.5	0.00228	1.381	6.64	20.80
11	36,133	20	63.5	0.00239	1.508	6.64	22.70

Table B-62 Sample Data Recorded and Analyzed to Determine Turbine Shaft Power and Aero-Mechanical Efficiency for Run 2 ($A_e = A_{nominal}$ (0.397 μm^2), x=6.41 mm, y=33.3 mm, z=0 mm, α=0° & β=0°).

x (mm)	6.41	R (mm)	12.83
y (mm)	33.3	P_{in} (kPa)	701.89
z (mm)	0	T_{amb} (°C)	23.1
α (deg)	0	T_2 (°K)	293.69
β (deg)	0	P_{amb} (kPa)	105.5

Θ (deg)	RPM	W (g)	d (mm)	$Q_{turbine}$ (N-m)	$P_{turbine}$ (W)	P_{aero} (W)	$\eta_{aero-mech}$ (%)
4.5	0	20	63.5	0.00098	0.0000	6.69	0.00
5	6,088	20	63.5	0.00109	0.1155	6.69	1.73
5.5	10,840	20	63.5	0.00120	0.2262	6.69	3.38
6	13,073	20	63.5	0.00130	0.2976	6.69	4.45
6.5	14,675	20	63.5	0.00141	0.3619	6.69	5.41
7	18,753	20	63.5	0.00152	0.4980	6.69	7.45
7.5	20,627	20	63.5	0.00163	0.5869	6.69	8.78
8	22,940	20	63.5	0.00174	0.6962	6.69	10.41
8.5	25,109	20	63.5	0.00185	0.8097	6.69	12.11
9	27,781	20	63.5	0.00196	0.9486	6.69	14.18

Table B-62 Sample Data Recorded and Analyzed to Determine Turbine Shaft Power and Aero-c Mechanical Efficiency for Run 2 ($A_e = A_{nominal}$ (0.397 μm^2), x=6.41 mm, y=33.3 mm, z=0 mm, α=0^o & β=0^o) (Cont'd).

Θ (deg)	RPM	W (g)	d (mm)	$Q_{turbine}$ (N-m)	$P_{turbine}$ (W)	P_{aero} (W)	$\eta_{aero-mech}$ (%)
9.5	29,031	20	63.5	0.00207	1.0463	6.69	15.65
10	31,895	20	63.5	0.00217	1.2100	6.69	18.09
10.5	32,862	20	63.5	0.00228	1.3091	6.69	19.57
11	33,904	20	63.5	0.00239	1.4149	6.69	21.16
11.5	35,087	20	63.5	0.00250	1.5308	6.69	22.89
12	35,361	20	63.5	0.00261	1.6098	6.69	24.07

Table B-63 Sample Data Recorded and Analyzed to Determine Turbine Shaft Power and Aero-Mechanical Efficiency for Run 3 ($A_e = A_{nominal}$ (0.397 μm^2), x=0 mm, y=33.3 mm, z=0 mm, α=-3.0^o & β=0^o).

x (mm)	0	R (mm)	12.83
y (mm)	33.3	P_{in} (kPa)	699.13
z (mm)	0	T_{amb} (^{o}C)	23.1
α (deg)	-3	T_2 (^{o}K)	293.69
β (deg)	0	P_{amb} (kPa)	105.5

Θ (deg)	RPM	W (g)	d (mm)	$Q_{turbine}$ (N-m)	$P_{turbine}$ (W)	P_{aero} (W)	$\eta_{aero-mech}$ (%)
2.5	0	20	63.5	0.000543	0.0000	6.66	0.00
3	5,000	20	63.5	0.000652	0.0569	6.66	0.85
3.5	11,614	20	63.5	0.000761	0.1542	6.66	2.32
4	13,939	20	63.5	0.000869	0.2115	6.66	3.18
4.5	16,390	20	63.5	0.000978	0.2798	6.66	4.20
5	18,523	20	63.5	0.001087	0.3514	6.66	5.27
5.5	19,254	20	63.5	0.001196	0.4018	6.66	6.03
6	20,835	20	63.5	0.001304	0.4743	6.66	7.12
6.5	22,965	20	63.5	0.001413	0.5663	6.66	8.50
7	25,518	20	63.5	0.001522	0.6777	6.66	10.17
7.5	27,344	20	63.5	0.001630	0.7780	6.66	11.68
8	30,652	20	63.5	0.001739	0.9303	6.66	13.97
8.5	32,394	20	63.5	0.001848	1.0446	6.66	15.68
9	32,931	20	63.5	0.001956	1.1244	6.66	16.88
9.5	33,445	20	63.5	0.002065	1.2054	6.66	18.10
10	33,561	20	63.5	0.002174	1.2733	6.66	19.11
10.5	33,777	20	63.5	0.002282	1.3455	6.66	20.20
11	33,845	20	63.5	0.002391	1.4124	6.66	21.20

Table B-64 Sample Data Recorded and Analyzed to Determine Turbine Shaft Power and Aero-Mechanical Efficiency for Run 4 ($A_e = A_{nominal}$ (0.397 μm^2), x=0 mm, y=33.3 mm, z=0 mm, α=-1.5° & β=0°).

x (mm)	0	R (mm)	12.83
y (mm)	33.3	P_{in} (kPa)	684.65
z (mm)	0	T_{amb} (°C)	23.1
α (deg)	-1.5	T_2 (°K)	295.91
β (deg)	0	P_{amb} (kPa)	105.7

Θ (deg)	RPM	W (g)	d (mm)	$Q_{turbine}$ (N-m)	$P_{turbine}$ (W)	P_{aero} (W)	$\eta_{aero-mech}$ (%)
4	0	20	63.5	0.00087	0.000	6.55	0.00
4.5	2,103	20	63.5	0.00098	0.036	6.55	0.55
5	5,828	20	63.5	0.00109	0.111	6.55	1.69
5.5	9,034	20	63.5	0.00120	0.189	6.55	2.88
6	11,863	20	63.5	0.00130	0.270	6.55	4.12
6.5	15,546	20	63.5	0.00141	0.383	6.55	5.85
7	18,122	20	63.5	0.00152	0.481	6.55	7.35
7.5	19,731	20	63.5	0.00163	0.561	6.55	8.57
8	23,337	20	63.5	0.00174	0.708	6.55	10.82
8.5	25,484	20	63.5	0.00185	0.822	6.55	12.55
9	27,115	20	63.5	0.00196	0.926	6.55	14.14
9.5	28,806	20	63.5	0.00207	1.038	6.55	15.86
10	29,463	20	63.5	0.00217	1.118	6.55	17.07

Table B-65 Sample Data Recorded and Analyzed to Determine Turbine Shaft Power and Aero-Mechanical Efficiency for Run 5 ($A_e = A_{nominal}$ (0.397 μm^2), x=0 mm, y=33.3 mm, z=0 mm, α=3.0° & β=0°).

x (mm)	0	R (mm)	12.83
y (mm)	33.3	P_{in} (kPa)	683.27
z (mm)	0	T_{amb} (°C)	23.1
α (deg)	3	T_2 (°K)	293.69
β (deg)	0	P_{amb} (kPa)	105.7

Θ (deg)	RPM	W (g)	d (mm)	$Q_{turbine}$ (N-m)	$P_{turbine}$ (W)	P_{aero} (W)	$\eta_{aero-mech}$ (%)
4.5	0	20	63.5	0.00098	0.000	6.51	0.00
5	2,220	20	63.5	0.00109	0.042	6.51	0.65
5.5	6,710	20	63.5	0.00120	0.140	6.51	2.15
6	8,493	20	63.5	0.00130	0.193	6.51	2.97
6.5	11,141	20	63.5	0.00141	0.275	6.51	4.22
7	13,009	20	63.5	0.00152	0.345	6.51	5.31
7.5	15,056	20	63.5	0.00163	0.428	6.51	6.58
8	17,515	20	63.5	0.00174	0.532	6.51	8.17
8.5	21,317	20	63.5	0.00185	0.687	6.51	10.56
9	23,751	20	63.5	0.00196	0.811	6.51	12.46
9.5	25,719	20	63.5	0.00207	0.927	6.51	14.24
10	27,093	20	63.5	0.00217	1.028	6.51	15.79
10.5	29,369	20	63.5	0.00228	1.170	6.51	17.97
11	32,692	20	63.5	0.00239	1.364	6.51	20.96
11.5	34,039	20	63.5	0.00250	1.485	6.51	22.81
12	35,106	20	63.5	0.00261	1.598	6.51	24.55
12.5	36,385	20	63.5	0.00272	1.725	6.51	26.50

Table B-66 Sample Data Recorded and Analyzed to Determine Turbine Shaft Power and Aero-Mechanical Efficiency for Run 6 ($A_e = A_{nominal}$ (0.397 μm^2), x=0 mm, y=33.3 mm, z=0 mm, α=1.5^o & β=0^o).

x (mm)	0	R (mm)	12.83
y (mm)	33.3	P_{in} (kPa)	683.96
z (mm)	0	T_{amb} (^{o}C)	23.1
α (deg)	1.5	T_2 (^{o}K)	293.13
β (deg)	0	P_{amb} (kPa)	105.7

Θ (deg)	RPM	W (g)	d (mm)	$Q_{turbine}$ (N-m)	$P_{turbine}$ (W)	P_{aero} (W)	$\eta_{aero-mech}$ (%)
4	0	20	63.5	0.00087	0.000	6.51	0.00
4.5	2,794	20	63.5	0.00098	0.048	6.51	0.73
5	5,913	20	63.5	0.00109	0.112	6.51	1.72
5.5	9,583	20	63.5	0.00120	0.200	6.51	3.07
6	11,837	20	63.5	0.00130	0.269	6.51	4.14
6.5	13,552	20	63.5	0.00141	0.334	6.51	5.13
7	15,657	20	63.5	0.00152	0.416	6.51	6.39
7.5	18,217	20	63.5	0.00163	0.518	6.51	7.96
8	19,494	20	63.5	0.00174	0.592	6.51	9.09
8.5	21,753	20	63.5	0.00185	0.701	6.51	10.77
9	24,605	20	63.5	0.00196	0.840	6.51	12.90
9.5	25,985	20	63.5	0.00207	0.937	6.51	14.38
10	27,938	20	63.5	0.00217	1.060	6.51	16.28
10.5	29,768	20	63.5	0.00228	1.186	6.51	18.21
11	32,428	20	63.5	0.00239	1.353	6.51	20.79
11.5	34,253	20	63.5	0.00250	1.494	6.51	22.95
12	35,066	20	63.5	0.00261	1.596	6.51	24.52
12.5	37,234	20	63.5	0.00272	1.766	6.51	27.12

Table B-67 Sample Data Recorded and Analyzed to Determine Turbine Shaft Power and Aero-Mechanical Efficiency for Run 7 ($A_e = A_{nominal}$ (0.397 μm^2), x=0 mm, y=33.3 mm, z=0 mm, α=0^o & β=2.5^o).

x (mm)	0	R (mm)	12.83
y (mm)	33.3	P_{in} (kPa)	689.48
z (mm)	0	T_{amb} (^{o}C)	23.1
α (deg)	0	T_2 (^{o}K)	295.91
β (deg)	2.5	P_{amb} (kPa)	105.7

Θ (deg)	RPM	W (g)	d (mm)	$Q_{turbine}$ (N-m)	$P_{turbine}$ (W)	P_{aero} (W)	$\eta_{aero-mech}$ (%)
4	0	20	63.5	0.000869	0.000	6.59	0.00
4.5	4,204	20	63.5	0.000978	0.072	6.59	1.09
5	8,663	20	63.5	0.001087	0.164	6.59	2.49
5.5	10,117	20	63.5	0.001196	0.211	6.59	3.20
6	16,947	20	63.5	0.001304	0.386	6.59	5.85
6.5	21,891	20	63.5	0.001413	0.540	6.59	8.19
7	22,734	20	63.5	0.001522	0.604	6.59	9.16
7.5	25,404	20	63.5	0.001630	0.723	6.59	10.96
8	26,701	20	63.5	0.001739	0.810	6.59	12.29
8.5	30,652	20	63.5	0.001848	0.988	6.59	14.99
9	34,701	20	63.5	0.001956	1.185	6.59	17.97

Table B-68 Sample Data Recorded and Analyzed to Determine Turbine Shaft Power and Aero-Mechanical Efficiency for Run 8 ($A_e = A_{nominal}$ (0.397 μm^2), x=0 mm, y=33.3 mm, z=0 mm, α=0^o & β=1.0^o).

x (mm)	0	R (mm)	12.83
y (mm)	33.3	P_{in} (kPa)	686.03
z (mm)	0	T_{amb} (^{o}C)	23.1
α (deg)	0	T_2 (^{o}K)	295.35
β (deg)	1	P_{amb} (kPa)	105.7

Θ (deg)	RPM	W (g)	d (mm)	$Q_{turbine}$ (N-m)	$P_{turbine}$ (W)	P_{aero} (W)	$\eta_{aero-mech}$ (%)
2	0	20	63.5	0.000435	0	6.55	0.00
2.5	1,557	20	63.5	0.000543	0.015	6.55	0.23
3	2,884	20	63.5	0.000652	0.033	6.55	0.50
4	7,762	20	63.5	0.000869	0.118	6.55	1.80
4.5	9,568	20	63.5	0.000978	0.163	6.55	2.49
5	13,543	20	63.5	0.001087	0.257	6.55	3.92
5.5	18,417	20	63.5	0.001196	0.384	6.55	5.86
6	21,319	20	63.5	0.001304	0.485	6.55	7.40
6.5	24,202	20	63.5	0.001413	0.597	6.55	9.10
7	25,413	20	63.5	0.001522	0.675	6.55	10.30
7.5	27,835	20	63.5	0.001630	0.792	6.55	12.08
8	29,544	20	63.5	0.001739	0.897	6.55	13.68
8.5	30,500	20	63.5	0.001848	0.984	6.55	15.00
9	34,132	20	63.5	0.001956	1.165	6.55	17.78

Table B-69 Sample Data Recorded and Analyzed to Determine Turbine Shaft Power and Aero-Mechanical Efficiency for Run 9 ($A_e = A_{nominal}$ (0.397 μm^2), x=0 mm, y=33.3 mm, z=0 mm, α=0^o & β=-2.5^o).

x (mm)	0	R (mm)	12.83
y (mm)	33.3	P_{in} (kPa)	686.03
z (mm)	0	T_{amb} (^{o}C)	23.1
α (deg)	0	T_2 (^{o}K)	295.35
β (deg)	-2.5	P_{amb} (kPa)	105.7

Θ (deg)	RPM	W (g)	d (mm)	$Q_{turbine}$ (N-m)	$P_{turbine}$ (W)	P_{aero} (W)	$\eta_{aero-mech}$ (%)
4.5	0	20	63.5	0.00098	0.000	6.55	0.00
5	2,632	20	63.5	0.00109	0.050	6.55	0.76
5.5	9,677	20	63.5	0.00120	0.202	6.55	3.08
6	12,498	20	63.5	0.00130	0.284	6.55	4.34
6.5	14,113	20	63.5	0.00141	0.348	6.55	5.31
7	15,267	20	63.5	0.00152	0.405	6.55	6.19
7.5	18,806	20	63.5	0.00163	0.535	6.55	8.16
8	19,896	20	63.5	0.00174	0.604	6.55	9.21
8.5	21,806	20	63.5	0.00185	0.703	6.55	10.73
9	23,336	20	63.5	0.00196	0.797	6.55	12.16
9.5	24,773	20	63.5	0.00207	0.893	6.55	13.62
10	27,061	20	63.5	0.00217	1.027	6.55	15.66
10.5	29,195	20	63.5	0.00228	1.163	6.55	17.74
11	30,452	20	63.5	0.00239	1.271	6.55	19.39

Table B-70 Sample Data Recorded and Analyzed to Determine Turbine Shaft Power and Aero-Mechanical Efficiency for Run 10 ($A_e = A_{nominal}$ (0.397 μm^2), x=0 mm, y=33.3 mm, z=0 mm, α=0° & β=-1.0°).

x (mm)	0	R (mm)	12.83
y (mm)	33.3	P_{in} (kPa)	690.17
z (mm)	0	T_{amb} (°C)	23.1
α (deg)	0	T_2 (°K)	295.35
β (deg)	-1	P_{amb} (kPa)	105.7

Θ (deg)	RPM	W (g)	d (mm)	$Q_{turbine}$ (N-m)	$P_{turbine}$ (W)	P_{aero} (W)	$\eta_{aero-mech}$ (%)
3.5	0	20	63.5	0.00076	0.000	6.59	0.00
4	2,995	20	63.5	0.00087	0.045	6.59	0.69
4.5	9,834	20	63.5	0.00098	0.168	6.59	2.55
5	11,651	20	63.5	0.00109	0.221	6.59	3.35
5.5	13,815	20	63.5	0.00120	0.288	6.59	4.37
6	16,162	20	63.5	0.00130	0.368	6.59	5.58
6.5	19,345	20	63.5	0.00141	0.477	6.59	7.23
7	23,214	20	63.5	0.00152	0.616	6.59	9.35
7.5	25,061	20	63.5	0.00163	0.713	6.59	10.81
8	27,475	20	63.5	0.00174	0.834	6.59	12.65
8.5	30,106	20	63.5	0.00185	0.971	6.59	14.72
9	31,283	20	63.5	0.00196	1.068	6.59	16.20
9.5	32,077	20	63.5	0.00207	1.156	6.59	17.53
10	34,302	20	63.5	0.00217	1.301	6.59	19.73
10.5	35,606	20	63.5	0.00228	1.418	6.59	21.51
11.5	36,498	20	63.5	0.00250	1.592	6.59	24.15
12	37,778	20	63.5	0.00261	1.720	6.59	26.08

Table B-71 Sample Data Recorded and Analyzed to Determine Turbine Shaft Power and Aero-Mechanical Efficiency for Run 1 ($A_e = 0.75A_{nominal}$ (0.298 μm^2), x=12.8 mm, y=33.3 mm, z=0 mm, α=0° & β=0°).

x (mm)	12.8	R (mm)	12.83
y (mm)	33.3	P_{in} (kPa)	699.82
z (mm)	0	T_{amb} (°C)	23.1
α (deg)	0	T_2 (°K)	293.69
β (deg)	0	P_{amb} (kPa)	105.7

Θ (deg)	RPM	W (g)	d (mm)	$Q_{turbine}$ (N-m)	$P_{turbine}$ (W)	P_{aero} (W)	$\eta_{aero-mech}$ (%)
3.5	0	20	63.5	0.00076	0.000	5.00	0.00
4	5,427	20	63.5	0.00087	0.082	5.00	1.65
4.5	7,978	20	63.5	0.00098	0.136	5.00	2.72
5	10,959	20	63.5	0.00109	0.208	5.00	4.16
5.5	12,521	20	63.5	0.00120	0.261	5.00	5.23
6	17,582	20	63.5	0.00130	0.400	5.00	8.01
6.5	21,088	20	63.5	0.00141	0.520	5.00	10.40

Table B-71 Sample Data Recorded and Analyzed to Determine Turbine Shaft Power and Aero-Mechanical Efficiency for Run 1 ($A_e = 0.75A_{nominal}$ (0.298 μm^2), x=12.8 mm, y=33.3 mm, z=0 mm, $\alpha=0^o$ & $\beta=0^o$) (Cont'd).

Θ (deg)	RPM	W (g)	d (mm)	$Q_{turbine}$ (N-m)	$P_{turbine}$ (W)	P_{aero} (W)	$\eta_{aero-mech}$ (%)
7	24,620	20	63.5	0.00152	0.654	5.00	13.08
7.5	25,196	20	63.5	0.00163	0.717	5.00	14.34
8	27,029	20	63.5	0.00174	0.820	5.00	16.41
8.5	30,388	20	63.5	0.00185	0.980	5.00	19.60
9	32,512	20	63.5	0.00196	1.110	5.00	22.20
9.5	34,287	20	63.5	0.00207	1.236	5.00	24.72

Table B-72 Sample Data Recorded and Analyzed to Determine Turbine Shaft Power and Aero-Mechanical Efficiency for Run 2 ($A_e = 0.75A_{nominal}$ (0.298 μm^2), x=6.41 mm, y=33.3 mm, z=0 mm, $\alpha=0^o$ & $\beta=0^o$).

x (mm)	6.41	R (mm)	12.83
y (mm)	33.3	P_{in} (kPa)	681.89
z (mm)	0	T_{amb} (^oC)	23.1
α (deg)	0	T_2 (^oK)	293.69
β (deg)	0	P_{amb} (kPa)	105.7

Θ (deg)	RPM	W (g)	d (mm)	$Q_{turbine}$ (N-m)	$P_{turbine}$ (W)	P_{aero} (W)	$\eta_{aero-mech}$ (%)
5	0	20	63.5	0.00109	0.0000	4.87	0.00
5.5	3,831	20	63.5	0.00120	0.0799	4.87	1.64
6	5,852	20	63.5	0.00130	0.1332	4.87	2.73
6.5	8,445	20	63.5	0.00141	0.2083	4.87	4.27
7	11,341	20	63.5	0.00152	0.3012	4.87	6.18
7.5	13,544	20	63.5	0.00163	0.3854	4.87	7.91
8	16,468	20	63.5	0.00174	0.4998	4.87	10.26
8.5	18,560	20	63.5	0.00185	0.5985	4.87	12.29
9	21,431	20	63.5	0.00196	0.7318	4.87	15.02
9.5	23,973	20	63.5	0.00207	0.8640	4.87	17.74
10	27,899	20	63.5	0.00217	1.0584	4.87	21.73
10.5	29,855	20	63.5	0.00228	1.1893	4.87	24.41
11.5	31,712	20	63.5	0.00250	1.3836	4.87	28.40
12.5	33,673	20	63.5	0.00272	1.5969	4.87	32.78
13	35,451	20	63.5	0.00283	1.7484	4.87	35.89

Table B-73 Sample Data Recorded and Analyzed to Determine Turbine Shaft Power and Aero-Mechanical Efficiency for Run 3 ($A_e = 0.75A_{nominal}$ (0.298 μm^2), x=0 mm, y=33.3 mm, z=0 mm, α=-3.0^o & β=0^o).

x (mm)	0	R (mm)	12.83
y (mm)	33.3	P_{in} (kPa)	682.58
z (mm)	0	T_{amb} (^{o}C)	23.1
α (deg)	-3	T_2 (^{o}K)	293.69
β (deg)	0	P_{amb} (kPa)	105.7

Θ (deg)	RPM	W (g)	d (mm)	$Q_{turbine}$ (N-m)	$P_{turbine}$ (W)	P_{aero} (W)	$\eta_{aero-mech}$ (%)
4.5	0	20	63.5	0.000978	0.0000	4.88	0.00
5	3,924	20	63.5	0.001087	0.0744	4.88	1.53
5.5	3,844	20	63.5	0.001196	0.0802	4.88	1.64
6	11,333	20	63.5	0.001304	0.2580	4.88	5.29
6.5	16,766	20	63.5	0.001413	0.4134	4.88	8.48
7	18,509	20	63.5	0.001522	0.4915	4.88	10.08
7.5	20,725	20	63.5	0.001630	0.5897	4.88	12.09
8	22,948	20	63.5	0.001739	0.6965	4.88	14.28
8.5	24,173	20	63.5	0.001848	0.7795	4.88	15.99
9	26,820	20	63.5	0.001956	0.9158	4.88	18.78
9.5	29,132	20	63.5	0.002065	1.0500	4.88	21.53
10	30,744	20	63.5	0.002174	1.1664	4.88	23.92
10.5	32,617	20	63.5	0.002282	1.2993	4.88	26.64
11	34,309	20	63.5	0.002391	1.4318	4.88	29.36
11.5	35,529	20	63.5	0.002500	1.5501	4.88	31.79

Table B-74 Sample Data Recorded and Analyzed to Determine Turbine Shaft Power and Aero-Mechanical Efficiency for Run 4 ($A_e = A_{nominal}$ (0.397 μm^2), x=0 mm, y=33.3 mm, z=0 mm, α=-1.5^o & β=0^o).

x (mm)	0	R (mm)	12.83
y (mm)	33.3	P_{in} (kPa)	681.20
z (mm)	0	T_{amb} (^{o}C)	23.1
α (deg)	-1.5	T_2 (^{o}K)	295.91
β (deg)	0	P_{amb} (kPa)	105.7

Θ (deg)	RPM	W (g)	d (mm)	$Q_{turbine}$ (N-m)	$P_{turbine}$ (W)	P_{aero} (W)	$\eta_{aero-mech}$ (%)
3.5	0	20	63.5	0.00076	0.000	4.88	0.00
4	6,874	20	63.5	0.00087	0.104	4.88	2.14
4.5	10,655	20	63.5	0.00098	0.182	4.88	3.72
5	14,927	20	63.5	0.00109	0.283	4.88	5.80
5.5	16,148	20	63.5	0.00120	0.337	4.88	6.90
6	18,073	20	63.5	0.00130	0.411	4.88	8.42
6.5	20,664	20	63.5	0.00141	0.510	4.88	10.43
7	22,145	20	63.5	0.00152	0.588	4.88	12.04
7.5	25,872	20	63.5	0.00163	0.736	4.88	15.07
8	28,681	20	63.5	0.00174	0.870	4.88	17.82
8.5	31,775	20	63.5	0.00185	1.025	4.88	20.98

Table B-75 Sample Data Recorded and Analyzed to Determine Turbine Shaft Power and Aero-Mechanical Efficiency for Run 5 ($A_e = 0.75A_{nominal}$ (0.298 μm^2), x=0 mm, y=33.3 mm, z=0 mm, α=3.0° & β=0°).

x (mm)	0	R (mm)	12.83
y (mm)	33.3	P_{in} (kPa)	688.10
z (mm)	0	T_{amb} (°C)	23.1
α (deg)	3	T_2 (°K)	295.91
β (deg)	0	P_{amb} (kPa)	105.7

Θ (deg)	RPM	W (g)	d (mm)	$Q_{turbine}$ (N-m)	$P_{turbine}$ (W)	P_{aero} (W)	$\eta_{aero-mech}$ (%)
2	0	20	63.5	0.00043	0.000	4.93	0.00
3	2,821	20	63.5	0.00065	0.032	4.93	0.65
3.5	4,980	20	63.5	0.00076	0.066	4.93	1.34
4	6,019	20	63.5	0.00087	0.091	4.93	1.85
4.5	8,022	20	63.5	0.00098	0.137	4.93	2.78
5	9,646	20	63.5	0.00109	0.183	4.93	3.71
5.5	13,765	20	63.5	0.00120	0.287	4.93	5.82
6	17,435	20	63.5	0.00130	0.397	4.93	8.04
6.5	19,156	20	63.5	0.00141	0.472	4.93	9.57
7	22,537	20	63.5	0.00152	0.599	4.93	12.13
7.5	24,757	20	63.5	0.00163	0.704	4.93	14.28
8	27,355	20	63.5	0.00174	0.830	4.93	16.83
8.5	31,929	20	63.5	0.00185	1.030	4.93	20.87
9.5	33,385	20	63.5	0.00207	1.203	4.93	24.38
10	35,564	20	63.5	0.00217	1.349	4.93	27.34
10.5	37,020	20	63.5	0.00228	1.475	4.93	29.89

Table B-76 Sample Data Recorded and Analyzed to Determine Turbine Shaft Power and Aero-Mechanical Efficiency for Run 6 ($A_e = 0.75A_{nominal}$ (0.298 μm^2), x=0 mm, y=33.3 mm, z=0 mm, α=1.5° & β=0°).

x (mm)	0	R (mm)	12.83
y (mm)	33.3	P_{in} (kPa)	683.27
z (mm)	0	T_{amb} (°C)	23.1
α (deg)	1.5	T_2 (°K)	294.80
β (deg)	0	P_{amb} (kPa)	105.7

Θ (deg)	RPM	W (g)	d (mm)	$Q_{turbine}$ (N-m)	$P_{turbine}$ (W)	P_{aero} (W)	$\eta_{aero-mech}$ (%)
4	0	20	63.5	0.00087	0.000	4.89	0.00
4.5	6,408	20	63.5	0.00098	0.109	4.89	2.24
5	10,060	20	63.5	0.00109	0.191	4.89	3.90
5.5	12,075	20	63.5	0.00120	0.252	4.89	5.15
6	15,057	20	63.5	0.00130	0.343	4.89	7.01
6.5	16,135	20	63.5	0.00141	0.398	4.89	8.14
7	17,175	20	63.5	0.00152	0.456	4.89	9.33
7.5	18,742	20	63.5	0.00163	0.533	4.89	10.90
8	21,762	20	63.5	0.00174	0.660	4.89	13.51
8.5	24,095	20	63.5	0.00185	0.777	4.89	15.89
9	26,303	20	63.5	0.00196	0.898	4.89	18.36
9.5	30,351	20	63.5	0.00207	1.094	4.89	22.37
10	33,193	20	63.5	0.00217	1.259	4.89	25.75
10.5	36,523	20	63.5	0.00228	1.455	4.89	29.75

Table B-77 Sample Data Recorded and Analyzed to Determine Turbine Shaft Power and Aero-Mechanical Efficiency for Run 7 ($A_e = 0.75A_{nominal}$ (0.298 μm^2), x=0 mm, y=33.3 mm, z=0 mm, α=0° & β=2.5°).

x (mm)	0	R (mm)	12.83
y (mm)	33.3	P_{in} (kPa)	683.27
z (mm)	0	T_{amb} (°C)	23.1
α (deg)	0	T_2 (°K)	295.91
β (deg)	2.5	P_{amb} (kPa)	105.7

Θ (deg)	RPM	W (g)	d (mm)	$Q_{turbine}$ (N-m)	$P_{turbine}$ (W)	P_{aero} (W)	$\eta_{aero-mech}$ (%)
2.5	0	20	63.5	0.000543	0.000	4.90	0.00
3	1,895	20	63.5	0.000652	0.022	4.90	0.44
3.5	5,249	20	63.5	0.000761	0.070	4.90	1.42
4	15,116	20	63.5	0.000869	0.229	4.90	4.68
4.5	20,064	20	63.5	0.000978	0.343	4.90	6.99
5	22,257	20	63.5	0.001087	0.422	4.90	8.62
5.5	25,637	20	63.5	0.001196	0.535	4.90	10.92
6	27,011	20	63.5	0.001304	0.615	4.90	12.55
6.5	30,836	20	63.5	0.001413	0.760	4.90	15.52
7	34,954	20	63.5	0.001522	0.928	4.90	18.95
7.5	37,185	20	63.5	0.001630	1.058	4.90	21.59
8	38,799	20	63.5	0.001739	1.178	4.90	24.03

Table B-78 Sample Data Recorded and Analyzed to Determine Turbine Shaft Power and Aero-Mechanical Efficiency for Run 8 ($A_e = 0.75A_{nominal}$ (0.298 μm^2), x=0 mm, y=33.3 mm, z=0 mm, α=0° & β=1.0°).

x (mm)	0	R (mm)	12.83
y (mm)	33.3	P_{in} (kPa)	681.89
z (mm)	0	T_{amb} (°C)	23.1
α (deg)	0	T_2 (°K)	295.35
β (deg)	1	P_{amb} (kPa)	105.7

Θ (deg)	RPM	W (g)	d (mm)	$Q_{turbine}$ (N-m)	$P_{turbine}$ (W)	P_{aero} (W)	$\eta_{aero-mech}$ (%)
2.5	0	20	63.5	0.00054	0	4.89	0.00
3	2,518	20	63.5	0.00065	0.029	4.89	0.59
3.5	8,840	20	63.5	0.00076	0.117	4.89	2.40
4	10,557	20	63.5	0.00087	0.160	4.89	3.28
4.5	12,947	20	63.5	0.00098	0.221	4.89	4.52
5	17,320	20	63.5	0.00109	0.329	4.89	6.73
5.5	20,332	20	63.5	0.00120	0.424	4.89	8.68
6	22,980	20	63.5	0.00130	0.523	4.89	10.71
6.5	25,474	20	63.5	0.00141	0.628	4.89	12.86
7	27,993	20	63.5	0.00152	0.743	4.89	15.22
7.5	29,850	20	63.5	0.00163	0.849	4.89	17.39
8	32,030	20	63.5	0.00174	0.972	4.89	19.90
8.5	33,414	20	63.5	0.00185	1.078	4.89	22.06

Table B-79 Sample Data Recorded and Analyzed to Determine Turbine Shaft Power and Aero-Mechanical Efficiency for Run 9 ($A_e = 0.75A_{nominal}$ (0.298 μm^2), x=0 mm, y=33.3 mm, z=0 mm, $\alpha=0^o$ & $\beta=-2.5^o$).

x (mm)	0	R (mm)	12.83	
y (mm)	33.3	P_{in} (kPa)	686.03	
z (mm)	0	T_{amb} (^oC)	23.1	
α (deg)	0	T_2 (^oK)	295.91	
β (deg)	-2.5	P_{amb} (kPa)	105.7	

Θ (deg)	RPM	W (g)	d (mm)	$Q_{turbine}$ (N-m)	$P_{turbine}$ (W)	P_{aero} (W)	$\eta_{aero-mech}$ (%)
4	0	20	63.5	0.00087	0.000	4.92	0.00
4.5	8,801	20	63.5	0.00098	0.150	4.92	3.05
5	12,993	20	63.5	0.00109	0.246	4.92	5.01
5.5	17,928	20	63.5	0.00120	0.374	4.92	7.60
6	20,975	20	63.5	0.00130	0.477	4.92	9.71
6.5	23,864	20	63.5	0.00141	0.588	4.92	11.96
7	25,557	20	63.5	0.00152	0.679	4.92	13.80
7.5	29,708	20	63.5	0.00163	0.845	4.92	17.18
8	31,161	20	63.5	0.00174	0.946	4.92	19.22
8.5	32,229	20	63.5	0.00185	1.039	4.92	21.13
9	33,446	20	63.5	0.00196	1.142	4.92	23.21
9.5	34,251	20	63.5	0.00207	1.234	4.92	25.09
10.5	37,611	20	63.5	0.00228	1.498	4.92	30.45

Table B-80 Sample Data Recorded and Analyzed to Determine Turbine Shaft Power and Aero-Mechanical Efficiency for Run 10 ($A_e = 0.75A_{nominal}$ (0.298 μm^2), x=0 mm, y=33.3 mm, z=0 mm, $\alpha=0^o$ & $\beta=-1.0^o$).

x (mm)	0	R (mm)	12.83	
y (mm)	33.3	P_{in} (kPa)	687.41	
z (mm)	0	T_{amb} (^oC)	23.1	
α (deg)	0	T_2 (^oK)	295.35	
β (deg)	-1	P_{amb} (kPa)	105.7	

Θ (deg)	RPM	W (g)	d (mm)	$Q_{turbine}$ (N-m)	$P_{turbine}$ (W)	P_{aero} (W)	$\eta_{aero-mech}$ (%)
3.5	0	20	63.5	0.00076	0.000	4.92	0.00
4	2,782	20	63.5	0.00087	0.042	4.92	0.86
4.5	8,645	20	63.5	0.00098	0.148	4.92	3.00
5	11,342	20	63.5	0.00109	0.215	4.92	4.37
5.5	13,803	20	63.5	0.00120	0.288	4.92	5.85
6	15,765	20	63.5	0.00130	0.359	4.92	7.29
6.5	18,704	20	63.5	0.00141	0.461	4.92	9.37
7	20,520	20	63.5	0.00152	0.545	4.92	11.07
7.5	22,547	20	63.5	0.00163	0.642	4.92	13.03
8	24,016	20	63.5	0.00174	0.729	4.92	14.80
8.5	27,306	20	63.5	0.00185	0.881	4.92	17.88
9	29,860	20	63.5	0.00196	1.020	4.92	20.70
9.5	30,934	20	63.5	0.00207	1.115	4.92	22.64
10	32,847	20	63.5	0.00217	1.246	4.92	25.30
10.5	34,443	20	63.5	0.00228	1.372	4.92	27.86

Table B-81 Sample Data Recorded and Analyzed to Determine Turbine Shaft Power and Aero-Mechanical Efficiency for Run 1 ($A_e = 0.5A_{nominal}$ (0.199 μm^2), x=12.8 mm, y=33.3 mm, z=0 mm, $\alpha=0^o$ & $\beta=0^o$).

x (mm)	12.8	R (mm)	12.83
y (mm)	33.3	P_{in} (kPa)	681.20
z (mm)	0	T_{amb} (^oC)	23.1
α (deg)	0	T_2 (^oK)	293.69
β (deg)	0	P_{amb} (kPa)	105.7

Θ (deg)	RPM	W (g)	d (mm)	$Q_{turbine}$ (N-m)	$P_{turbine}$ (W)	P_{aero} (W)	$\eta_{aero-mech}$ (%)
2	0	20	63.5	0.00043	0.000	3.24	0.00
2.5	8,032	20	63.5	0.00054	0.076	3.24	2.35
3	9,951	20	63.5	0.00065	0.113	3.24	3.49
3.5	12,069	20	63.5	0.00076	0.160	3.24	4.94
4	13,210	20	63.5	0.00087	0.200	3.24	6.18
4.5	15,402	20	63.5	0.00098	0.263	3.24	8.11
5	17,213	20	63.5	0.00109	0.327	3.24	10.07
5.5	19,524	20	63.5	0.00120	0.407	3.24	12.56
6	20,783	20	63.5	0.00130	0.473	3.24	14.58
6.5	21,031	20	63.5	0.00141	0.519	3.24	15.99
7	22,791	20	63.5	0.00152	0.605	3.24	18.66
7.5	24,596	20	63.5	0.00163	0.700	3.24	21.58
8	26,638	20	63.5	0.00174	0.808	3.24	24.92
8.5	30,680	20	63.5	0.00185	0.989	3.24	30.50
9	34,722	20	63.5	0.00196	1.186	3.24	36.55

Table B-82 Sample Data Recorded and Analyzed to Determine Turbine Shaft Power and Aero-Mechanical Efficiency for Run 2 ($A_e = 0.5A_{nominal}$ (0.199 μm^2), x=6.41 mm, y=33.3 mm, z=0 mm, $\alpha=0^o$ & $\beta=0^o$).

x (mm)	6.41	R (mm)	12.83
y (mm)	33.3	P_{in} (kPa)	685.34
z (mm)	0	T_{amb} (^oC)	23.1
α (deg)	0	T_2 (^oK)	293.69
β (deg)	0	P_{amb} (kPa)	105.7

Θ (deg)	RPM	W (g)	d (mm)	$Q_{turbine}$ (N-m)	$P_{turbine}$ (W)	P_{aero} (W)	$\eta_{aero-mech}$ (%)
1.5	0	20	63.5	0.00033	0.0000	3.26	0.00
2	3,242	20	63.5	0.00043	0.0246	3.26	0.75
2.5	6,955	20	63.5	0.00054	0.0660	3.26	2.02
3	8,236	20	63.5	0.00065	0.0937	3.26	2.87
3.5	10,258	20	63.5	0.00076	0.1362	3.26	4.17
4	11,168	20	63.5	0.00087	0.1695	3.26	5.19
4.5	12,601	20	63.5	0.00098	0.2151	3.26	6.59
5	13,789	20	63.5	0.00109	0.2616	3.26	8.01
5.5	15,662	20	63.5	0.00120	0.3268	3.26	10.01
6	18,753	20	63.5	0.00130	0.4269	3.26	13.08

Table B-82 Sample Data Recorded and Analyzed to Determine Turbine Shaft Power and Aero-Mechanical Efficiency for Run 2 ($A_e = 0.5A_{nominal}$ (0.199 μm^2), x=6.41 mm, y=33.3 mm, z=0 mm, $\alpha=0^o$ & $\beta=0^o$) (Cont'd).

Θ (deg)	RPM	W (g)	d (mm)	$Q_{turbine}$ (N-m)	$P_{turbine}$ (W)	P_{aero} (W)	$\eta_{aero-mech}$ (%)
6.5	20,957	20	63.5	0.00141	0.5168	3.26	15.84
7	22,239	20	63.5	0.00152	0.5906	3.26	18.10
7.5	24,145	20	63.5	0.00163	0.6870	3.26	21.05
8	27,378	20	63.5	0.00174	0.8309	3.26	25.46
8.5	29,611	20	63.5	0.00185	0.9549	3.26	29.26
9	30,844	20	63.5	0.00196	1.0532	3.26	32.27
9.5	32,077	20	63.5	0.00207	1.1561	3.26	35.43

Table B-83 Sample Data Recorded and Analyzed to Determine Turbine Shaft Power and Aero-Mechanical Efficiency for Run 3 ($A_e = 0.5A_{nominal}$ (0.199 μm^2), x=0 mm, y=33.3 mm, z=0 mm, $\alpha=-3.0^o$ & $\beta=0^o$).

x (mm)	0	R (mm)	12.83
y (mm)	33.3	P_{in} (kPa)	681.89
z (mm)	0	T_{amb} (^oC)	23.1
α (deg)	-3	T_2 (^oK)	293.13
β (deg)	0	P_{amb} (kPa)	105.7

Θ (deg)	RPM	W (g)	d (mm)	$Q_{turbine}$ (N-m)	$P_{turbine}$ (W)	P_{aero} (W)	$\eta_{aero-mech}$ (%)
3.5	0	20	63.5	0.000761	0.0000	3.24	0.00
4	7,561	20	63.5	0.000869	0.1147	3.24	3.54
4.5	10,559	20	63.5	0.000978	0.1803	3.24	5.56
5	14,102	20	63.5	0.001087	0.2675	3.24	8.25
5.5	17,768	20	63.5	0.001196	0.3707	3.24	11.43
6	20,655	20	63.5	0.001304	0.4702	3.24	14.49
6.5	22,921	20	63.5	0.001413	0.5652	3.24	17.42
7	25,828	20	63.5	0.001522	0.6859	3.24	21.14
7.5	29,854	20	63.5	0.001630	0.8495	3.24	26.19
8	32,911	20	63.5	0.001739	0.9989	3.24	30.79
8.5	34,533	20	63.5	0.001848	1.1136	3.24	34.33
9	35,738	20	63.5	0.001956	1.2203	3.24	37.62
9.5	36,743	20	63.5	0.002065	1.3243	3.24	40.82

Table B-84 Sample Data Recorded and Analyzed to Determine Turbine Shaft Power and Aero-Mechanical Efficiency for Run 4 ($A_e = 0.5A_{nominal}$ (0.199 μm^2), x=0 mm, y=33.3 mm, z=0 mm, α=-1.5^o & β=0^o).

x (mm)	0		R (mm)	12.83			
y (mm)	33.3		P_{in} (kPa)	683.27			
z (mm)	0		T_{amb} (^{o}C)	23.1			
α (deg)	-1.5		T_2 (^{o}K)	293.13			
β (deg)	0		P_{amb} (kPa)	105.7			

Θ (deg)	RPM	W (g)	d (mm)	$Q_{turbine}$ (N-m)	$P_{turbine}$ (W)	P_{aero} (W)	$\eta_{aero-mech}$ (%)
2	0	20	63.5	0.00043	0.000	3.25	0.00
2.5	4,460	20	63.5	0.00054	0.042	3.25	1.30
3	7,238	20	63.5	0.00065	0.082	3.25	2.53
3.5	10,059	20	63.5	0.00076	0.134	3.25	4.11
4	13,548	20	63.5	0.00087	0.206	3.25	6.32
4.5	17,974	20	63.5	0.00098	0.307	3.25	9.44
5	20,704	20	63.5	0.00109	0.393	3.25	12.08
5.5	22,056	20	63.5	0.00120	0.460	3.25	14.16
6	24,051	20	63.5	0.00130	0.547	3.25	16.84
6.5	26,909	20	63.5	0.00141	0.664	3.25	20.41
7	28,597	20	63.5	0.00152	0.759	3.25	23.36
7.5	29,575	20	63.5	0.00163	0.842	3.25	25.89
8	31,360	20	63.5	0.00174	0.952	3.25	29.28
8.5	32,693	20	63.5	0.00185	1.054	3.25	32.43
9	33,016	20	63.5	0.00196	1.127	3.25	34.68
9.5	35,339	20	63.5	0.00207	1.274	3.25	39.18

Table B-85 Sample Data Recorded and Analyzed to Determine Turbine Shaft Power and Aero-Mechanical Efficiency for Run 5 ($A_e = 0.5A_{nominal}$ (0.199 μm^2), x=0 mm, y=33.3 mm, z=0 mm, α=3.0^o & β=0^o).

x (mm)	0		R (mm)	12.83			
y (mm)	33.3		P_{in} (kPa)	699.13			
z (mm)	0		T_{amb} (^{o}C)	23.1			
α (deg)	3		T_2 (^{o}K)	295.91			
β (deg)	0		P_{amb} (kPa)	105.7			

Θ (deg)	RPM	W (g)	d (mm)	$Q_{turbine}$ (N-m)	$P_{turbine}$ (W)	P_{aero} (W)	$\eta_{aero-mech}$ (%)
1	0	20	63.5	0.00022	0.000	3.34	0.00
1.5	6,222	20	63.5	0.00033	0.035	3.34	1.06
2	12,322	20	63.5	0.00043	0.093	3.34	2.80
2.5	15,307	20	63.5	0.00054	0.145	3.34	4.34
3	19,890	20	63.5	0.00065	0.226	3.34	6.77
3.5	24,301	20	63.5	0.00076	0.323	3.34	9.66
4	26,073	20	63.5	0.00087	0.396	3.34	11.84
4.5	28,462	20	63.5	0.00098	0.486	3.34	14.54
5	30,401	20	63.5	0.00109	0.577	3.34	17.26

Table B-85 Sample Data Recorded and Analyzed to Determine Turbine Shaft Power and Aero-Mechanical Efficiency for Run 5 ($A_e = 0.5A_{nominal}$ (0.199 μm^2), x=0 mm, y=33.3 mm, z=0 mm, α=3.0° & β=0°) (Cont'd).

Θ (deg)	RPM	W (g)	d (mm)	$Q_{turbine}$ (N-m)	$P_{turbine}$ (W)	P_{aero} (W)	$\eta_{aero\text{-}mech}$ (%)
5.5	32,503	20	63.5	0.00120	0.678	3.34	20.30
6	33,153	20	63.5	0.00130	0.755	3.34	22.58
6.5	34,660	20	63.5	0.00141	0.855	3.34	25.58
7	36,327	20	63.5	0.00152	0.965	3.34	28.87
7.5	37,160	20	63.5	0.00163	1.057	3.34	31.64

Table B-86 Sample Data Recorded and Analyzed to Determine Turbine Shaft Power and Aero-Mechanical Efficiency for Run 6 ($A_e = 0.5A_{nominal}$ (0.199 μm^2), x=0 mm, y=33.3 mm, z=0 mm, α=1.5° & β=0°).

x (mm)	0	R (mm)	12.83
y (mm)	33.3	P_{in} (kPa)	683.96
z (mm)	0	T_{amb} (°C)	23.1
α (deg)	1.5	T_2 (°K)	295.35
β (deg)	0	P_{amb} (kPa)	105.7

Θ (deg)	RPM	W (g)	d (mm)	$Q_{turbine}$ (N-m)	$P_{turbine}$ (W)	P_{aero} (W)	$\eta_{aero\text{-}mech}$ (%)
1.5	0	20	63.5	0.00033	0.000	3.27	0.00
2	3,191	20	63.5	0.00043	0.024	3.27	0.74
2.5	7,494	20	63.5	0.00054	0.071	3.27	2.18
3.5	10,424	20	63.5	0.00076	0.138	3.27	4.24
4	13,181	20	63.5	0.00087	0.200	3.27	6.12
4.5	15,175	20	63.5	0.00098	0.259	3.27	7.93
5	17,329	20	63.5	0.00109	0.329	3.27	10.06
5.5	21,003	20	63.5	0.00120	0.438	3.27	13.42
6	23,580	20	63.5	0.00130	0.537	3.27	16.43
6.5	25,337	20	63.5	0.00141	0.625	3.27	19.13
7	28,330	20	63.5	0.00152	0.752	3.27	23.04
7.5	31,615	20	63.5	0.00163	0.900	3.27	27.54
8	33,483	20	63.5	0.00174	1.016	3.27	31.11
8.5	34,065	20	63.5	0.00185	1.099	3.27	33.63
9	36,083	20	63.5	0.00196	1.232	3.27	37.72

Table B-87 Sample Data Recorded and Analyzed to Determine Turbine Shaft Power and Aero-Mechanical Efficiency for Run 7 ($A_e = 0.5A_{nominal}$ (0.199 μm^2), x=0 mm, y=33.3 mm, z=0 mm, $\alpha=0^o$ & $\beta=2.5^o$).

x (mm)	0	R (mm)	12.83
y (mm)	33.3	P_{in} (kPa)	686.03
z (mm)	0	T_{amb} (^{o}C)	23.1
α (deg)	0	T_2 (^{o}K)	295.35
β (deg)	2.5	P_{amb} (kPa)	105.7

Θ (deg)	RPM	W (g)	d (mm)	$Q_{turbine}$ (N-m)	$P_{turbine}$ (W)	P_{aero} (W)	$\eta_{aero-mech}$ (%)
1	0	20	63.5	0.000217	0.000	3.28	0.00
1.5	5,856	20	63.5	0.000326	0.033	3.28	1.02
2	7,336	20	63.5	0.000435	0.056	3.28	1.70
2.5	9,708	20	63.5	0.000543	0.092	3.28	2.81
3	12,093	20	63.5	0.000652	0.138	3.28	4.20
3.5	14,387	20	63.5	0.000761	0.191	3.28	5.83
4	17,827	20	63.5	0.000869	0.271	3.28	8.26
4.5	21,185	20	63.5	0.000978	0.362	3.28	11.04
5	23,239	20	63.5	0.001087	0.441	3.28	13.46
5.5	24,669	20	63.5	0.001196	0.515	3.28	15.71
6	27,099	20	63.5	0.001304	0.617	3.28	18.83
6.5	29,783	20	63.5	0.001413	0.734	3.28	22.42
7	31,965	20	63.5	0.001522	0.849	3.28	25.91
7.5	34,330	20	63.5	0.001630	0.977	3.28	29.82

Table B-88 Sample Data Recorded and Analyzed to Determine Turbine Shaft Power and Aero-Mechanical Efficiency for Run 8 ($A_e = 0.5A_{nominal}$ (0.199 μm^2), x=0 mm, y=33.3 mm, z=0 mm, $\alpha=0^o$ & $\beta=1.0^o$).

x (mm)	0	R (mm)	12.83
y (mm)	33.3	P_{in} (kPa)	684.65
z (mm)	0	T_{amb} (^{o}C)	23.1
α (deg)	0	T_2 (^{o}K)	295.35
β (deg)	1	P_{amb} (kPa)	105.7

Θ (deg)	RPM	W (g)	d (mm)	$Q_{turbine}$ (N-m)	$P_{turbine}$ (W)	P_{aero} (W)	$\eta_{aero-mech}$ (%)
2	0	20	63.5	0.00043	0	3.27	0.00
2.5	2,570	20	63.5	0.00054	0.024	3.27	0.75
3	8,449	20	63.5	0.00065	0.096	3.27	2.94
3.5	10,983	20	63.5	0.00076	0.146	3.27	4.46
4	13,320	20	63.5	0.00087	0.202	3.27	6.18
4.5	16,649	20	63.5	0.00098	0.284	3.27	8.69
5	19,405	20	63.5	0.00109	0.368	3.27	11.26
5.5	22,992	20	63.5	0.00120	0.480	3.27	14.67
6	25,673	20	63.5	0.00130	0.584	3.27	17.87
6.5	27,993	20	63.5	0.00141	0.690	3.27	21.11
7	30,836	20	63.5	0.00152	0.819	3.27	25.05
7.5	32,229	20	63.5	0.00163	0.917	3.27	28.05
8	32,260	20	63.5	0.00174	0.979	3.27	29.95

Table B-89 Sample Data Recorded and Analyzed to Determine Turbine Shaft Power and Aero-Mechanical Efficiency for Run 9 ($A_e = 0.5A_{nominal}$ (0.199 μm^2), x=0 mm, y=33.3 mm, z=0 mm, $\alpha=0^o$ & $\beta=-2.5^o$).

x (mm)	0	R (mm)	12.83
y (mm)	33.3	P_{in} (kPa)	683.96
z (mm)	0	T_{amb} (^{o}C)	23.1
α (deg)	0	T_2 (^{o}K)	295.35
β (deg)	-2.5	P_{amb} (kPa)	105.7

Θ (deg)	RPM	W (g)	d (mm)	$Q_{turbine}$ (N-m)	$P_{turbine}$ (W)	P_{aero} (W)	$\eta_{aero-mech}$ (%)
2	0	20	63.5	0.00043	0.000	3.27	0.00
2.5	3,036	20	63.5	0.00054	0.029	3.27	0.88
3	5,906	20	63.5	0.00065	0.067	3.27	2.06
3.5	8,561	20	63.5	0.00076	0.114	3.27	3.48
4	12,643	20	63.5	0.00087	0.192	3.27	5.87
4.5	15,418	20	63.5	0.00098	0.263	3.27	8.06
5	18,629	20	63.5	0.00109	0.353	3.27	10.82
5.5	21,178	20	63.5	0.00120	0.442	3.27	13.53
6	24,752	20	63.5	0.00130	0.563	3.27	17.25
6.5	26,979	20	63.5	0.00141	0.665	3.27	20.37
7	28,271	20	63.5	0.00152	0.751	3.27	22.99
7.5	29,241	20	63.5	0.00163	0.832	3.27	25.47
8.5	30,015	20	63.5	0.00185	0.968	3.27	29.63
9	32,407	20	63.5	0.00196	1.107	3.27	33.88
9.5	33,684	20	63.5	0.00207	1.214	3.27	37.17

Table B-90 Sample Data Recorded and Analyzed to Determine Turbine Shaft Power and Aero-Mechanical Efficiency for Run 10 ($A_e = 0.5A_{nominal}$ (0.199 μm^2), x=0 mm, y=33.3 mm, z=0 mm, $\alpha=0^o$ & $\beta=-1.0^o$).

x (mm)	0	R (mm)	12.83
y (mm)	33.3	P_{in} (kPa)	686.03
z (mm)	0	T_{amb} (^{o}C)	23.1
α (deg)	0	T_2 (^{o}K)	295.35
β (deg)	-1	P_{amb} (kPa)	105.7

Θ (deg)	RPM	W (g)	d (mm)	$Q_{turbine}$ (N-m)	$P_{turbine}$ (W)	P_{aero} (W)	$\eta_{aero-mech}$ (%)
3	0	20	63.5	0.00065	0.000	3.28	0.00
3.5	4,910	20	63.5	0.00076	0.065	3.28	1.99
4	9,538	20	63.5	0.00087	0.145	3.28	4.42
4.5	12,764	20	63.5	0.00098	0.218	3.28	6.65
5	16,403	20	63.5	0.00109	0.311	3.28	9.50
5.5	18,008	20	63.5	0.00120	0.376	3.28	11.47
6	19,764	20	63.5	0.00130	0.450	3.28	13.73
6.5	22,208	20	63.5	0.00141	0.548	3.28	16.72
7	24,438	20	63.5	0.00152	0.649	3.28	19.81

Table B-90 Sample Data Recorded and Analyzed to Determine Turbine Shaft Power and Aero-Mechanical Efficiency for Run 10 ($A_e = 0.5A_{nominal}$ (0.199 μm^2), x=0 mm, y=33.3 mm, z=0 mm, $\alpha = 0^o$ & $\beta = -1.0^o$) (Cont'd).

Θ (deg)	RPM	W (g)	d (mm)	$Q_{turbine}$ (N-m)	$P_{turbine}$ (W)	P_{aero} (W)	$\eta_{aero\text{-}mech}$ (%)
7.5	27,257	20	63.5	0.00163	0.776	3.28	23.67
8	29,115	20	63.5	0.00174	0.884	3.28	26.97
8.5	30,695	20	63.5	0.00185	0.990	3.28	30.21
9	32,503	20	63.5	0.00196	1.110	3.28	33.88
9.5	33,216	20	63.5	0.00207	1.197	3.28	36.54

Table B-91 Coordinates, Offset Distances and Offset Angles Defined Matrix for Experimental Runs 1 through 10 with Planar Bladed Mini-Turbine Fixed at a distance of $y/D_e = 12.9$ from Ejector Nozzle Face ($D_e = 0.616$ mm).

Variables	Experimental Runs									
	1	2	3	4	5	6	7	8	9	10
x/D_e	20.8	10.4	0	0	0	0	0	0	0	0
y/D_e	12.9	12.9	12.9	12.9	12.9	12.9	12.9	12.9	12.9	12.9
z/D_e	0	0	0	0	0	0	0	0	0	0
α (deg)	0	0	-3	-1.5	3	1.5	0	0	0	0
β (deg)	0	0	0	0	0	0	2.5	1	-2.5	-1

Table B-92 Coordinates, Offset Distances and Offset Angles Defined Matrix for Experimental Runs 1 through 10 with Planar Bladed Mini-Turbine Fixed at a distance of $y/D_e = 33.4$ from Ejector Nozzle Face ($D_e = 0.616$ mm).

Variables	Experimental Runs									
	1	2	3	4	5	6	7	8	9	10
x/D_e	20.8	10.4	0	0	0	0	0	0	0	0
y/D_e	33.4	33.4	33.4	33.4	33.4	33.4	33.4	33.4	33.4	33.4
z/D_e	0	0	0	0	0	0	0	0	0	0
α (deg)	0	0	-3	-1.5	3	1.5	0	0	0	0
β (deg)	0	0	0	0	0	0	2.5	1	-2.5	-1

Table B-93 Coordinates, Offset Distances and Offset Angles Defined Matrix for Experimental Runs 1 through 10 with Planar Bladed Mini-Turbine Fixed at a distance of $y/D_e = 54.1$ from Ejector Nozzle Face ($D_e = 0.616$ mm).

Variables	Experimental Runs									
	1	2	3	4	5	6	7	8	9	10
x/D_e	20.8	10.4	0	0	0	0	0	0	0	0
y/D_e	54.1	54.1	54.1	54.1	54.1	54.1	54.1	54.1	54.1	54.1
z/D_e	0	0	0	0	0	0	0	0	0	0
α (deg)	0	0	-3	-1.5	3	1.5	0	0	0	0
β (deg)	0	0	0	0	0	0	2.5	1	-2.5	-1

Table B-94 Coordinates, Offset Distances and Offset Angles Defined Matrix for Experimental Runs 1 through 10 with Planar Bladed Mini-Turbine Fixed at a distance of $y/D_e = 15.8$ from Ejector Nozzle Face ($D_e = 0.503$ mm).

Variables	Experimental Runs									
	1	2	3	4	5	6	7	8	9	10
x/D_e	25.5	12.8	0	0	0	0	0	0	0	0
y/D_e	15.8	15.8	15.8	15.8	15.8	15.8	15.8	15.8	15.8	15.8
z/D_e	0	0	0	0	0	0	0	0	0	0
α (deg)	0	0	-3	-1.5	3	1.5	0	0	0	0
β (deg)	0	0	0	0	0	0	2.5	1	-2.5	-1

Table B-95 Coordinates, Offset Distances and Offset Angles Defined Matrix for Experimental Runs 1 through 10 with Planar Bladed Mini-Turbine Fixed at a distance of $y/D_e = 41.0$ from Ejector Nozzle Face ($D_e = 0.503$ mm).

Variables	Experimental Runs									
	1	2	3	4	5	6	7	8	9	10
x/D_e	25.5	12.8	0	0	0	0	0	0	0	0
y/D_e	41.0	41.0	41.0	41.0	41.0	41.0	41.0	41.0	41.0	41.0
z/D_e	0	0	0	0	0	0	0	0	0	0
α (deg)	0	0	-3	-1.5	3	1.5	0	0	0	0
β (deg)	0	0	0	0	0	0	2.5	1	-2.5	-1

Table B-96 Coordinates, Offset Distances and Offset Angles Defined Matrix for Experimental Runs 1 through 10 with Planar Bladed Mini-Turbine Fixed at a distance of $y/D_e = 66.2$ from Ejector Nozzle Face ($D_e = 0.503$ mm).

Variables	Experimental Runs									
	1	2	3	4	5	6	7	8	9	10
x/D_e	25.5	12.8	0	0	0	0	0	0	0	0
y/D_e	66.2	66.2	66.2	66.2	66.2	66.2	66.2	66.2	66.2	66.2
z/D_e	0	0	0	0	0	0	0	0	0	0
α (deg)	0	0	-3	-1.5	3	1.5	0	0	0	0
β (deg)	0	0	0	0	0	0	2.5	1	-2.5	-1

APPENDIX C: HAND CALCULATIONS

This Appendix section presents the sample calculations to the analysis of the results.

Mass Flow Rate Calculations

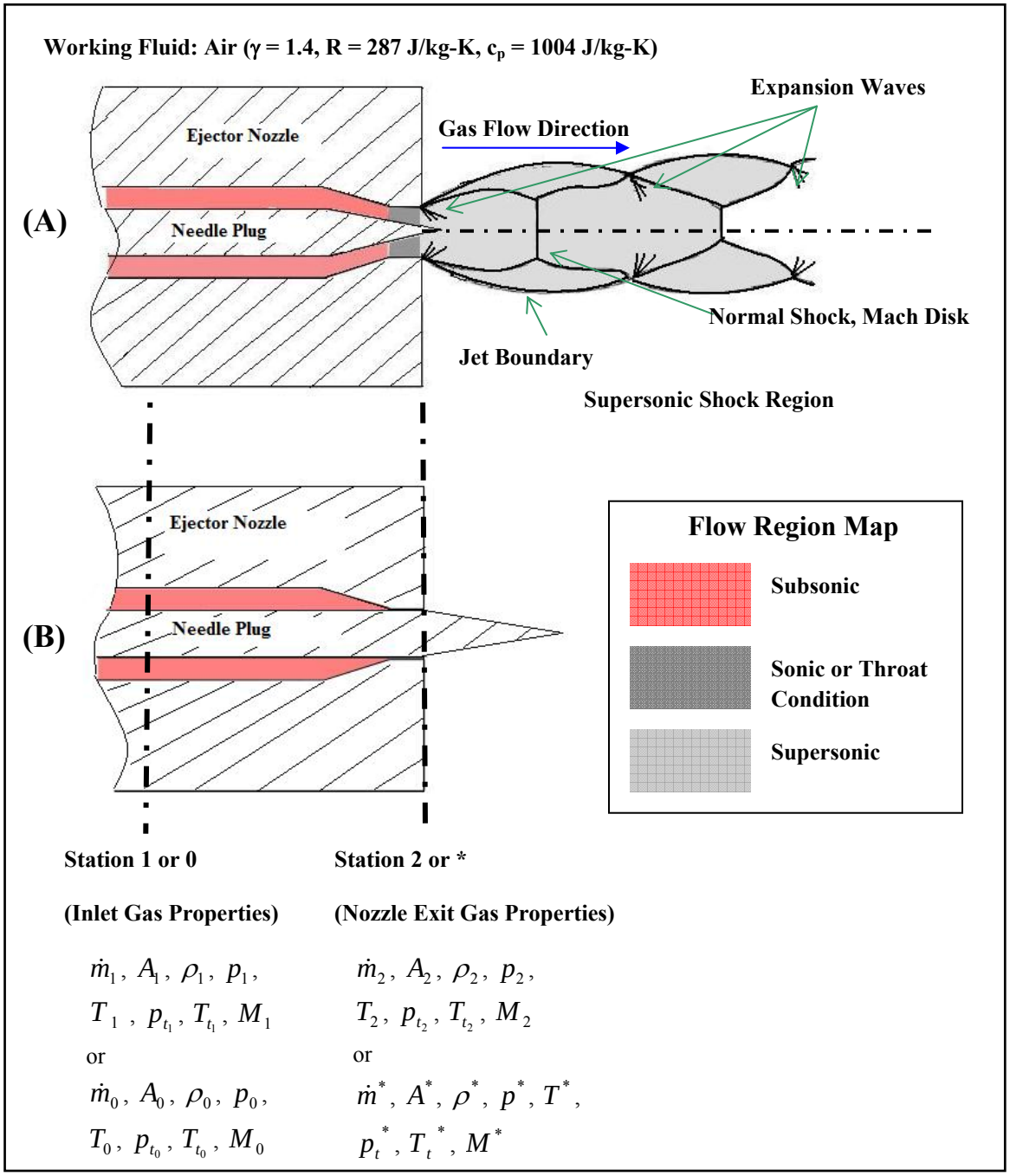

Figure C-1 Nozzle-Injector Configuration Showing Important Gas Parameters.

Exit flow is assumed to be choked, i.e. the gas is at sonic condition at the nozzle exit location. The mass flow rate of gas in the nozzle is maximized at sonic condition ($M_e = M_2 = M^* = 1.0$) as explained in Chapter 4. Also, note that nozzle exit area is the nozzle area for sonic condition to occur, $A_e = A_2 = A^*$.

The measured gas properties for air ($\gamma = 1.4$) are:

$$p_{t_1} = p_1 = 100.0 \ \ psi = 689.48 \ \ kPa \ or \ \frac{kN}{m^2}$$

$$T_2 = 69°F = 293.71 \ \ K$$

$$A_1 = \frac{\pi}{4}\left(3.175\times10^{-3} \ \ m\right)^2 = 7.92\times10^{-6} \ \ m^2, \text{ where } D_1 = 0.125 \ \ in = 3.175\times10^{-3} \ \ m$$

$$A_2 = \frac{\pi}{4}\left(7.11\times10^{-3} \ \ m\right)^2 = 3.97\times10^{-6} \ \ m^2, \text{ where } D_2 = 0.028 \ \ in = 7.11\times10^{-4} \ \ m$$

$$\frac{A_1}{A_2} = \frac{A_1}{A^*} = \frac{3.175\times10^{-3} \ \ m}{7.11\times10^{-4} \ \ m} = 19.95$$

Using Eq. 4.15 of Chapter 4, the upstream Mach number can be calculated for an area contraction ratio of $\frac{A_1}{A^*} = 19.95$:

$$\frac{A_1}{A^*} = 19.95 = \frac{1}{M_1}\left(\frac{\gamma+1}{2}\left[1+\frac{\gamma-1}{2}M_1^{\ 2}\right]\right)^{\frac{\gamma+1}{2(\gamma-1)}} \Rightarrow M_1 = 0.0291 \text{ (Subsonic solution)}$$

To solve for the static pressure ratio between the upstream gas flow properties and at the nozzle exit, Eq. 4.12 is used.

$$\frac{p_1}{p^*} = \frac{p_1}{p_2} = \left(\frac{\left(\frac{\gamma+1}{2}\right)}{\left[1+\left(\frac{\gamma-1}{2}\right)M_1^{\,2}\right]} \right)^{\frac{\gamma}{\gamma-1}} = \left(\frac{(1.2)}{\left[1+(0.2)(0.0291)^2\right]} \right)^{3.5} \Rightarrow \frac{p_1}{p_2} = 1.892$$

With knowledge of the upstream gas static pressure, the nozzle exit static pressure is given as:

$$\frac{p_1}{p_2} = 1.892 \Rightarrow p_2 = \frac{689.48\ \ kPa}{1.892} = 364.42\ \ kPa$$

The total to static temperature ratio relation of Eq. 4.5 can also be used to determine the total temperature of the nozzle exit flow,

$$\frac{T_{t_2}}{T^*} = \frac{T_{t_2}}{T_2} = \left(\frac{\gamma+1}{2}\right) = 1.2 \Rightarrow T_{t_2} = 1.2T_2 = 1.2(293.71\ \ K) = 352.45\ \ K$$

Similarly, the total pressure is calculated with the relation of Eq. 4.6:

$$\frac{p_t}{p^*} = \frac{p_{t_2}}{p_2} = \left(\frac{\gamma+1}{2}\right)^{\frac{\gamma}{\gamma-1}} = 1.2^{3.5} = 1.893 \Rightarrow p_{t_2} = 1.893(364.42\ \ kPa)$$

According to Chapter 4, the gas flow in the nozzle should account for the viscous effects at the wall boundary and an effective area is introduced in terms of nozzle discharge coefficients. For the sonic nozzle with nozzle exit Mach number of 1 and NPR > 2.0, a discharge coefficient, $C_d = 0.995$ is assumed for choked flow at the exit of a sonic orifice.

Using Eq. 4.16, the mass flow rate can be calculated as follows:

$$\dot{m}_2 = \sqrt{\frac{\gamma}{R}} \frac{p_{t_2}}{\sqrt{T_{t_2}}} C_D A_2 M_2 \left(\frac{1}{1 + \frac{\gamma - 1}{2} M_2^{\,2}} \right)^{\frac{\gamma+1}{2(\gamma-1)}}$$

$$\Rightarrow \dot{m}_2 = \sqrt{\frac{1.4}{0.287 \;\; J/kg-K}} \cdot \left(\frac{689.811 \;\; kPa}{\sqrt{352.45 \;\; K}} \right) \cdot (0.995) \cdot \left(3.97 \times 10^{-7} \;\; m^2 \right) \cdot 1 \cdot \left(\frac{2}{2.4} \right)^{\frac{2.4}{2(0.4)}}$$

Therefore, the mass flow rate at the nozzle exit is:

$$\dot{m}_2 = 0.019 \;\; \frac{kg}{s}$$

The mass flow rate can be calculated per unit area based on the exit nozzle area:

$$\frac{\dot{m}_2}{A_2} = \frac{0.019}{(0.995) \cdot \left(3.97 \times 10^{-7} \;\; m^2 \right)} = 46.73 \times 10^3 \; \frac{kg}{m^2 - s}$$

An estimate for the mass flow rate of nozzle exit flow for various nozzle exit areas based on the ratio determined above are given below:

$$A_2 = A_{nominal} = 3.97 \times 10^{-7} \;\; m^2$$

For various nozzle exit areas:

$$A_2 = 0.75 \cdot A_{nominal} = 2.98 \times 10^{-7} \;\; m^2 \Rightarrow \dot{m}_2 = 46.73 \times 10^3 \; \frac{kg}{m^2 - s} \cdot 2.98 \times 10^{-7} \;\; m^2 \approx 0.014 \;\; \frac{kg}{s}$$

$$A_2 = 0.5 \cdot A_{nominal} = 1.99 \times 10^{-7} \;\; m^2 \Rightarrow \dot{m}_2 = 46.73 \times 10^3 \; \frac{kg}{m^2 - s} \cdot 1.99 \times 10^{-7} \;\; m^2 \approx 0.0093 \;\; \frac{kg}{s}$$

Calculations for Fluid Aerodynamic Power of the Gas Flow at the Nozzle Exit

The fluid aerodynamic power for the gas flow at the nozzle exit is determined by Eq. 4.20 following a direct relation of mass flow rate and total enthalpy at the nozzle exit;

$$\wp_2 = \dot{m}_2 h_{t_2} = \dot{m}_2 c_p T_{t_2}$$

For $A_2 = A_{nominal} = 3.97 \times 10^{-7}\ m^2$, $\dot{m}_2 = 0.019\ \frac{kg}{s}$ and $T_{t_2} = 352.45\ K$, the aerodynamic power of the choked nozzle flow at the exit is given by:

$$\wp_2 = \dot{m}_2 c_p T_{t_2} = \left(0.019\ \frac{kg}{s}\right) \cdot \left(1.004\ \frac{J}{kg \cdot K}\right) \cdot \left(352.45\ K\right) \Rightarrow \wp_2 = 6.56\ W\ or\ \frac{J}{s}$$

The aerodynamic can be calculated per unit mass flow rate based on the exit nozzle areas:

$$\frac{\wp_2}{\dot{m}_2} = \frac{6.56}{0.019} = 353.85\ \frac{W}{kg/s}$$

An estimate for the aerodynamic power of nozzle exit flow for various nozzle exit areas based on the ratio determined above are given below:

For various nozzle exit areas:

$$A_2 = 0.75 \cdot A_{nominal} = 2.98 \times 10^{-7}\ m^2 \Rightarrow \dot{m}_2 \approx 0.014\ \frac{kg}{s}$$

$$\Rightarrow \wp_2 = \left(353.85\ \frac{W}{kg/s}\right) \cdot 0.014\ \frac{kg}{s} \approx 4.93\ W$$

$$A_2 = 0.5 \cdot A_{nominal} = 1.99 \times 10^{-7}\ m^2 \Rightarrow \dot{m}_2 \approx 0.0093\ \frac{kg}{s}$$

$$\Rightarrow \wp_2 = \left(353.85\ \frac{W}{kg/s} \right) \cdot 0.0093\ \frac{kg}{s} \approx 3.29\ W$$

Determination of Aero-Mechanical Efficiency of Power Conversion

The fluid power is calculated based on the gas properties at the nozzle exit and the shaft power is measured. The aero-mechanical efficiency of the power conversion is calculated for a gas flow that impinges on the blades of a turbine wheel to produce rotational motion using Eq. 4.22 for $\wp_{turbine} = \wp_{shaft} = 1.50\ W$:

$$\eta_{aero-mech} = \frac{\wp_{shaft}}{\wp_2} = \frac{\wp_{turbine}}{\wp_{aero}} = \frac{1.50\ W}{4.93\ W} = 0.304$$

APPENDIX D: DIMENSIONED DRAWINGS OF EXPERIMENTAL COMPONENTS

This appendix section presents the detailed dimensions and CAD drawings of the experimental components and assemblies.

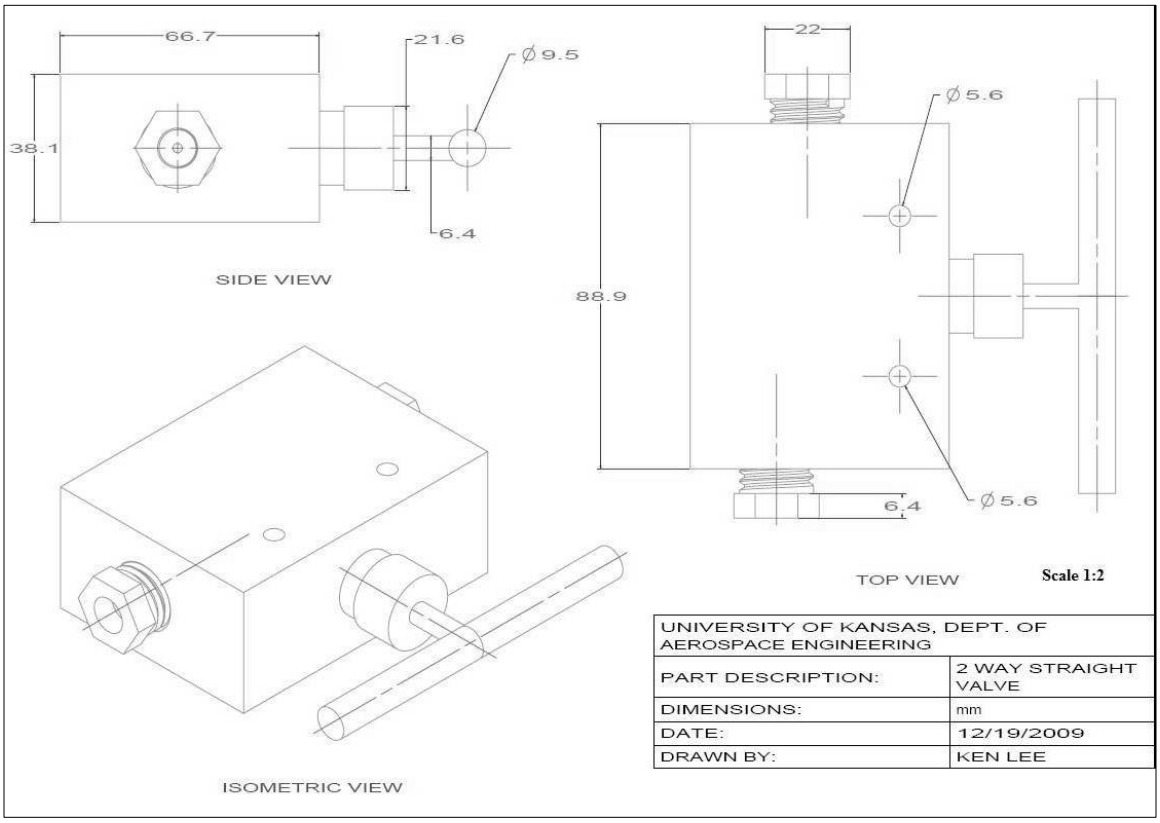

Figure D-1 Side, Top and Isometric CAD Views of the 2-Way Straight Valve Drafted in UG NX 6.0.

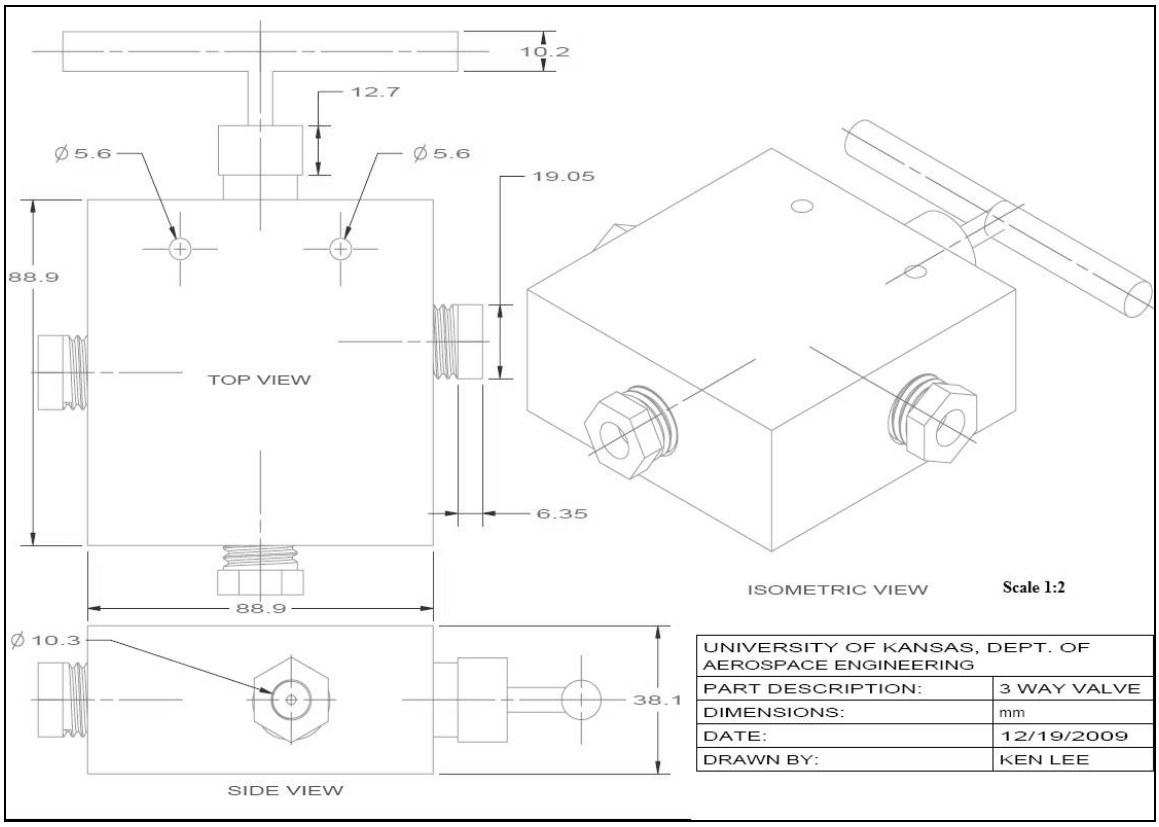

Figure D-2 Side, Top and Isometric CAD Views of the 3-Way Valve Drafted in UG NX 6.0.

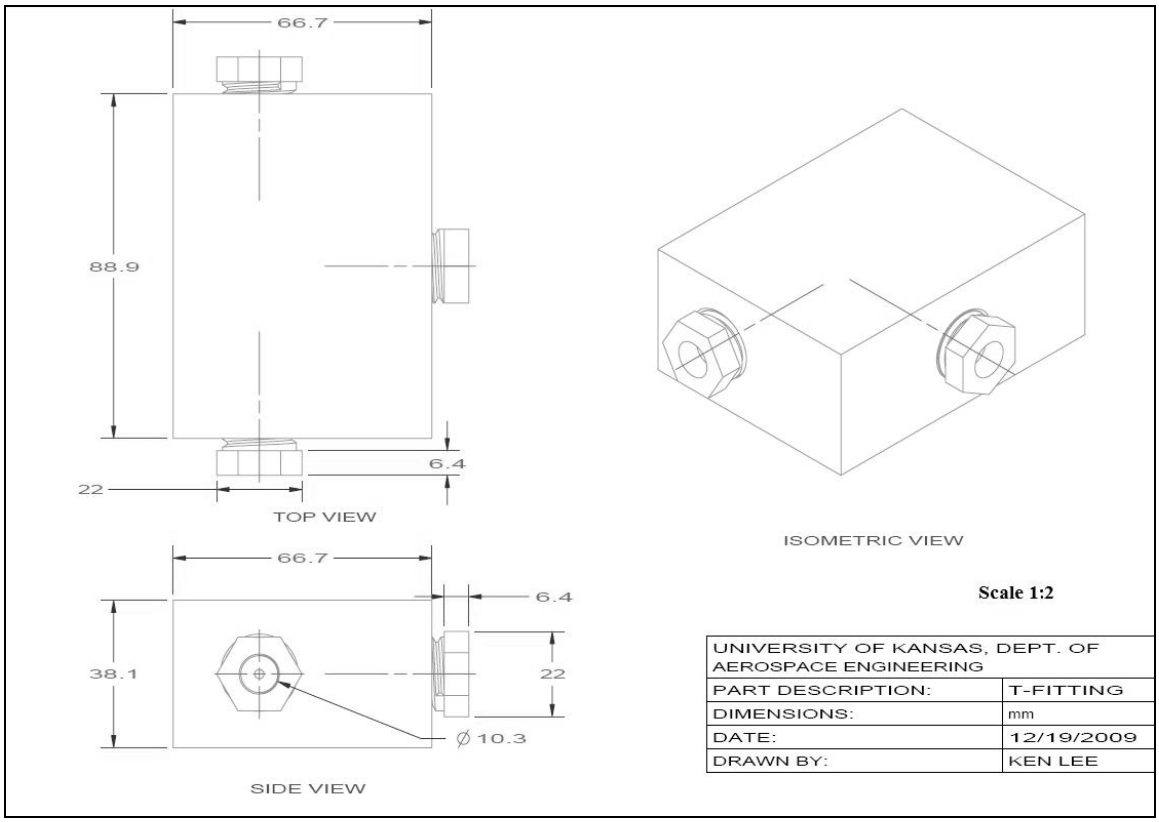

Figure D-3 Side, Top and Isometric CAD Views of the T-Fitting Drafted in UG NX 6.0.

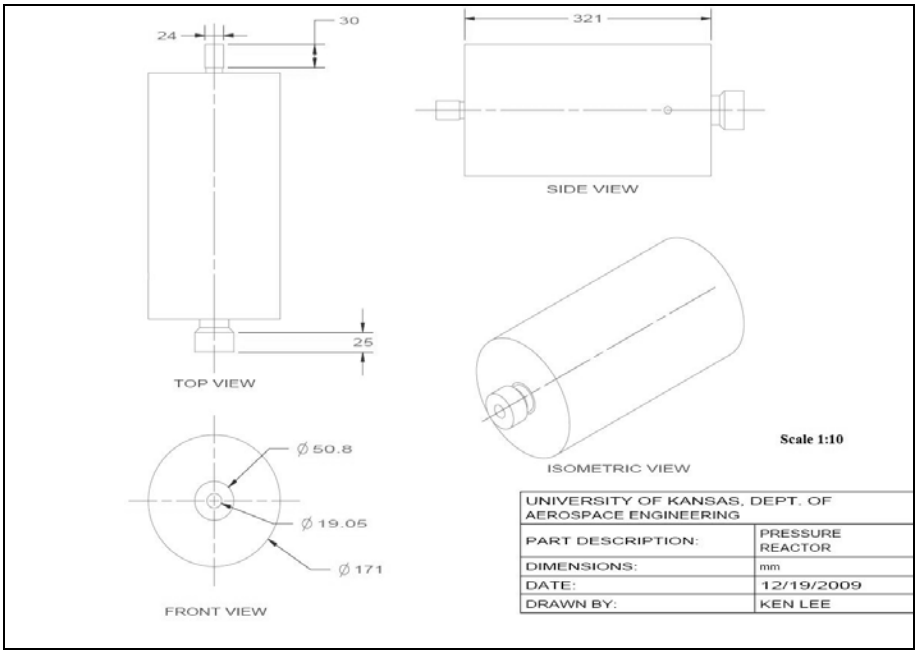

Figure D-4 Side, Top and Isometric CAD Views of the Pressure Reactor Drafted in UG NX 6.0.

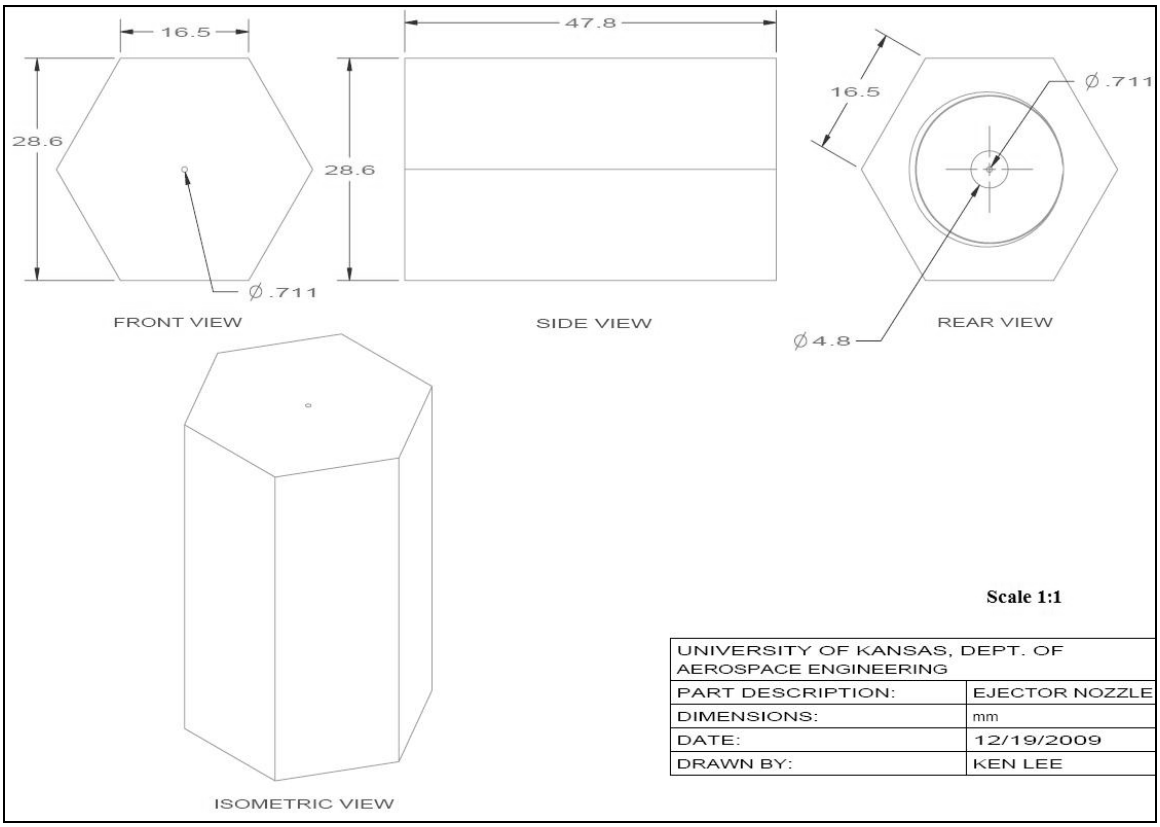

Figure D-5 Side, Front, Rear and Isometric CAD Views of the Pressure Reactor Drafted in UG NX 6.0.

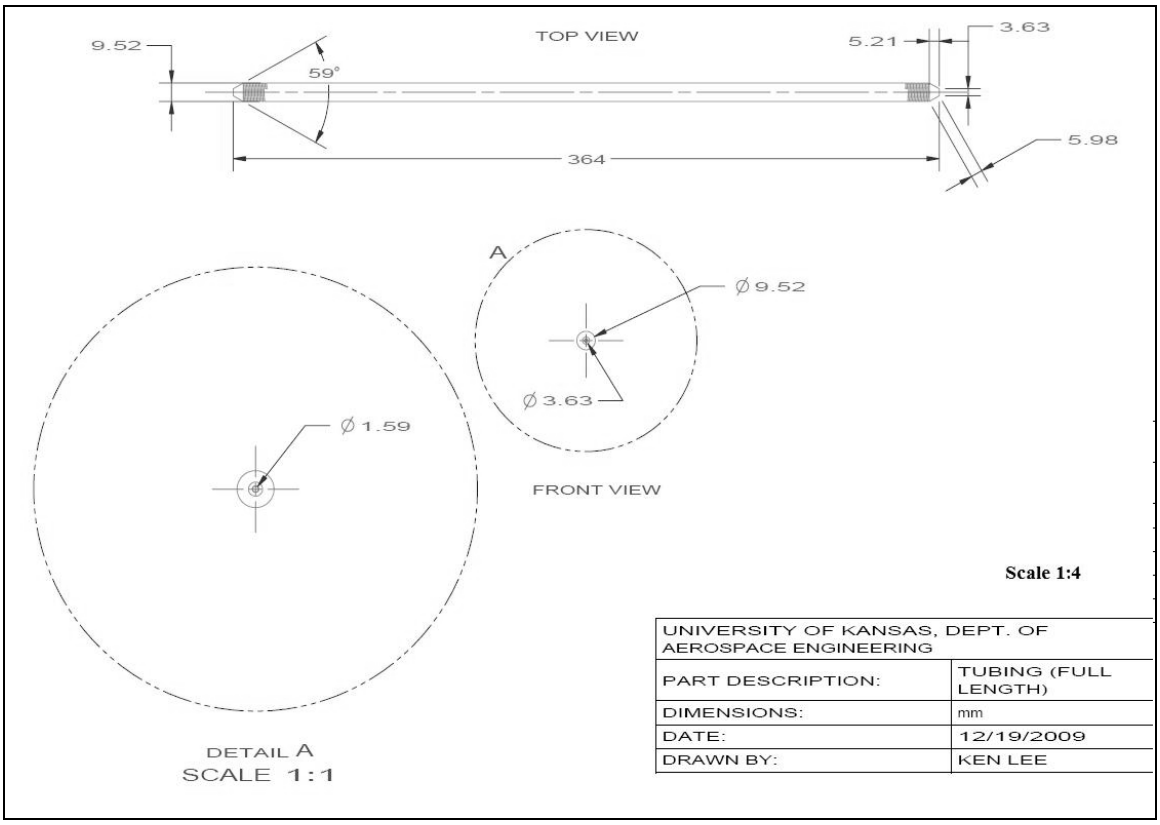

Figure D-6 Top and Front CAD Views of the Full-Length Tubing Drafted in UG NX 6.0.

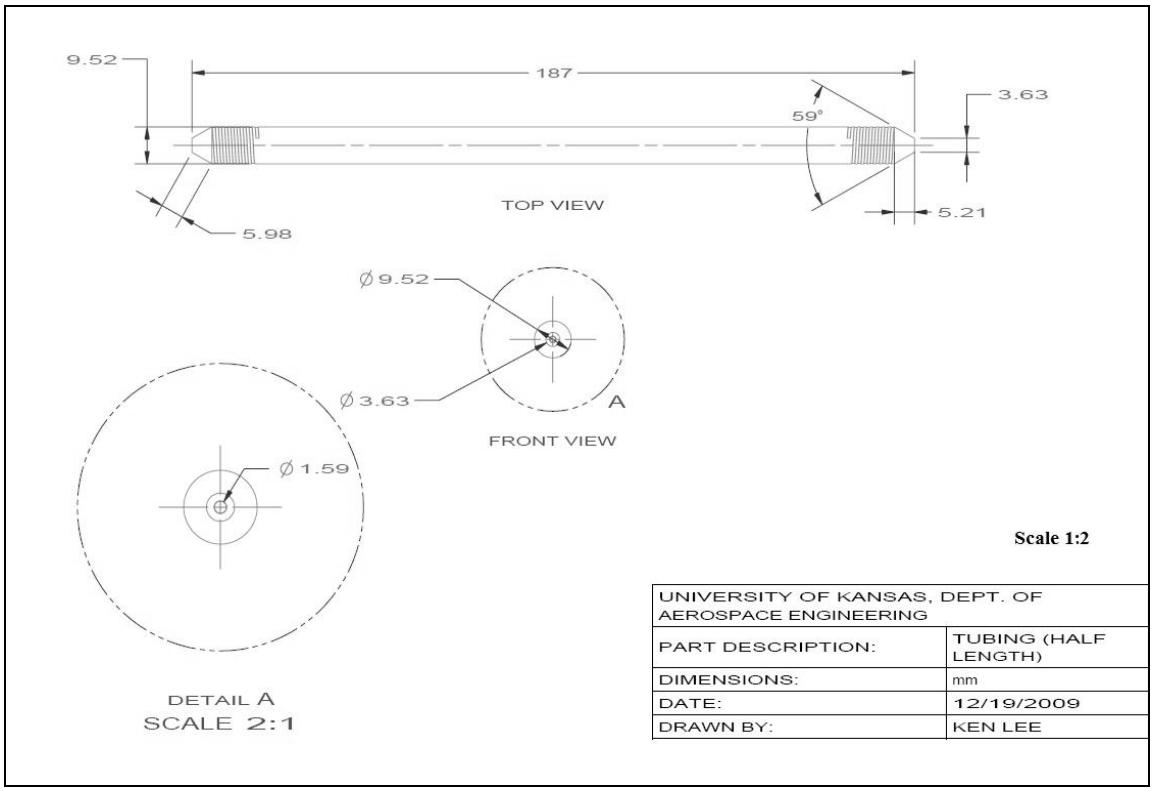

Figure D-7 Top and Front CAD Views of the Half-Length Tubing Drafted in UG NX 6.0.

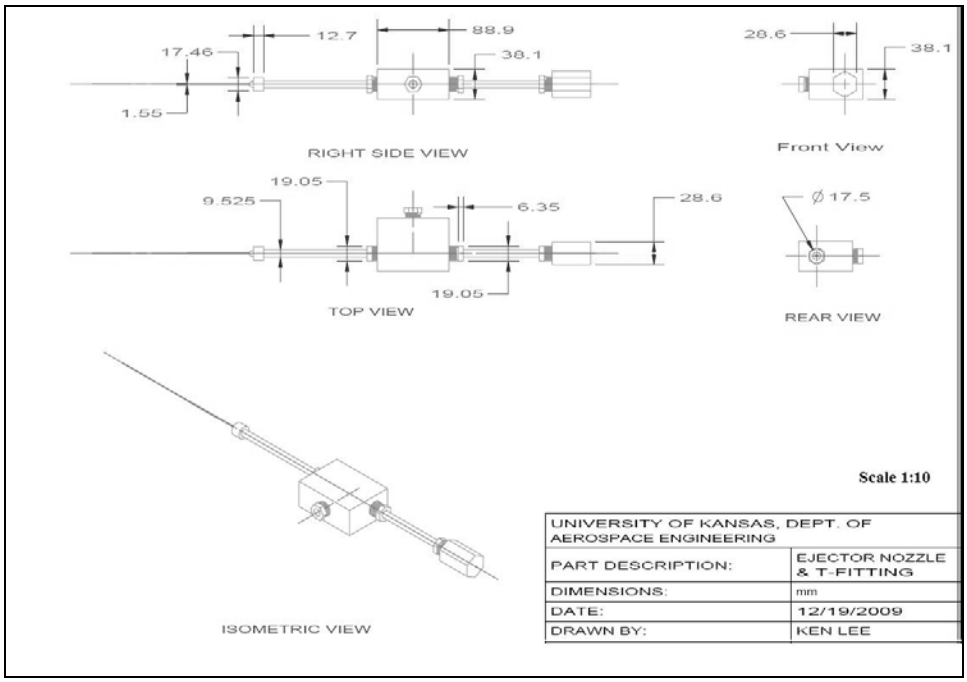

Figure D-8 CAD Diagram of the Ejector Nozzle and T-Fitting Assembly Drafted in UG NX 6.0.

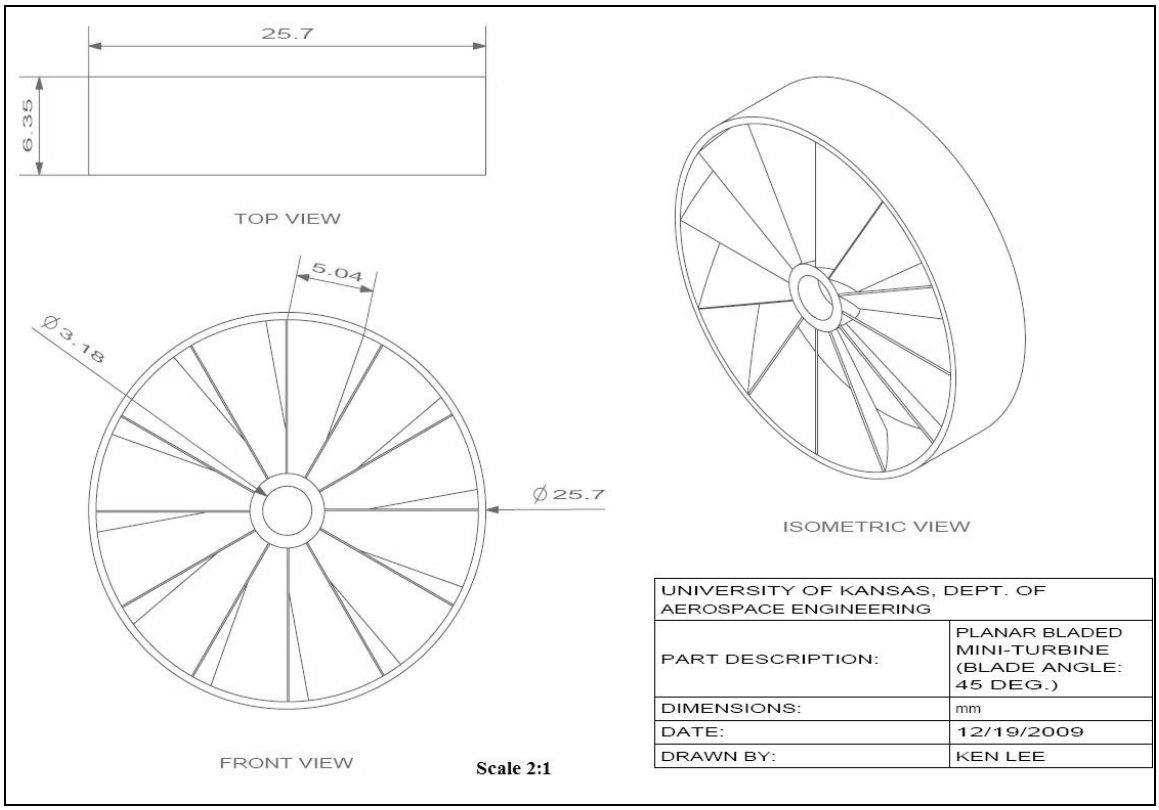

Figure D-9 CAD Diagram of the Planar Bladed Mini-Turbine Drafted in UG NX 6.0.

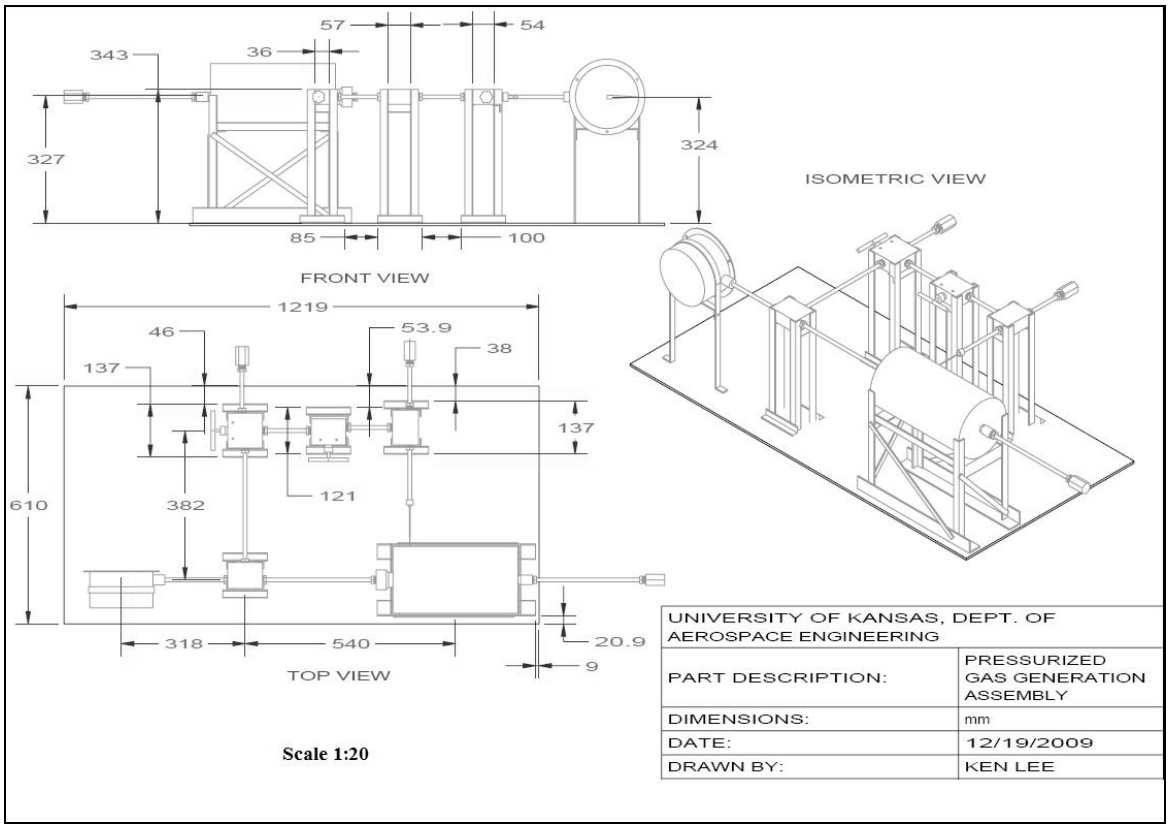

Figure D-10 Front, Top and Isometric CAD Views of the Pressurized Gas Generation Assembly Drafted in UG NX 6.0.

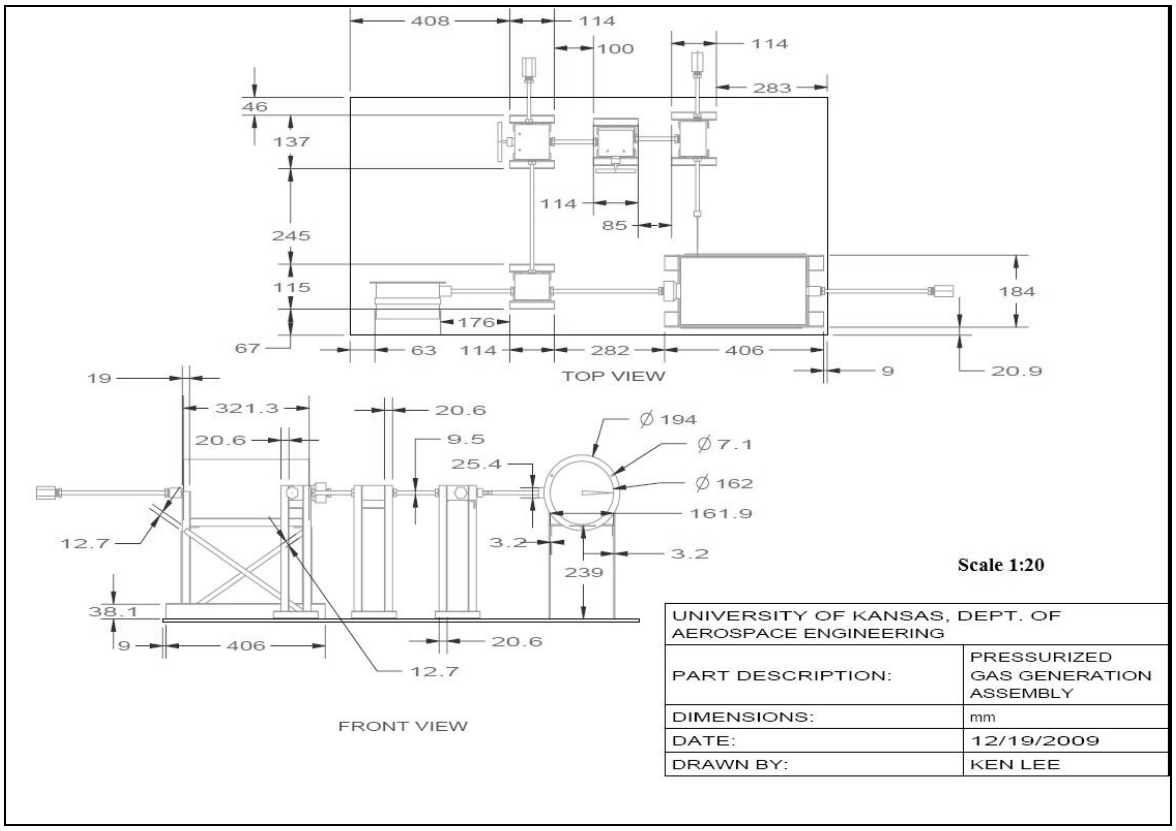

Figure D-11 Top and Front CAD Views of the Pressurized Gas Generation Assembly Drafted in UG NX 6.0.

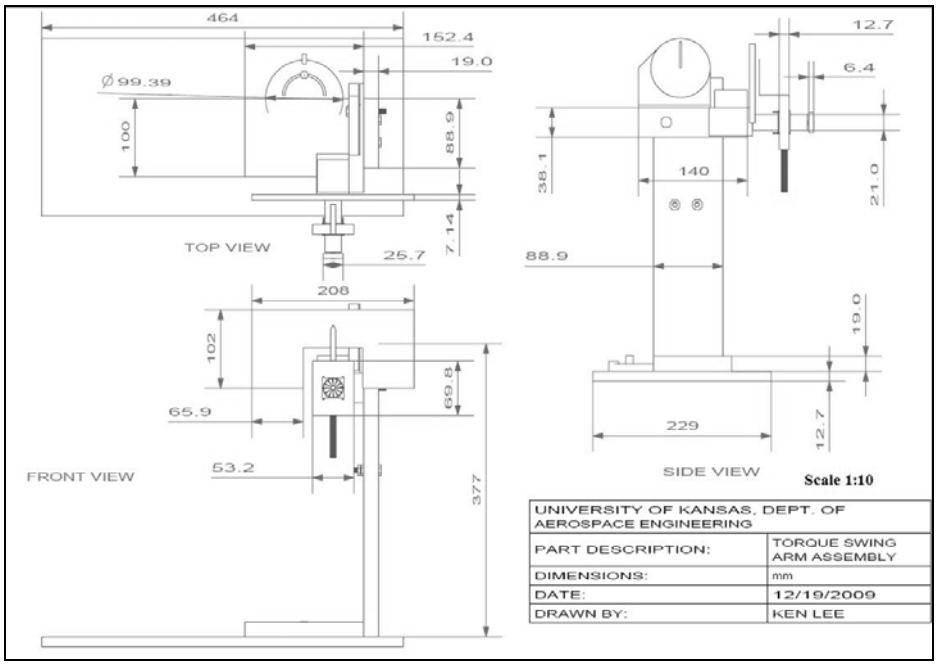

Figure D-12 Top, Front and Side CAD Views of the Torque Measurement Assembly Drafted in UG NX 6.0.

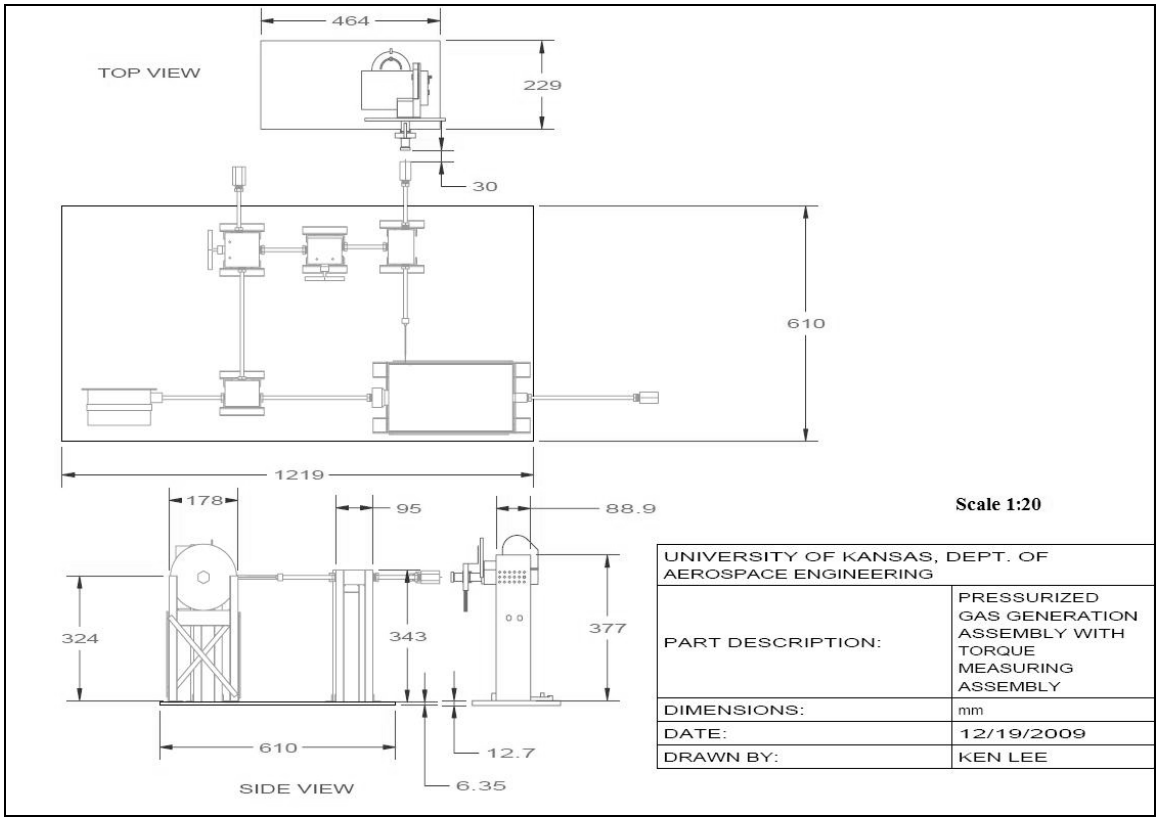

Figure D-13 Top and Side CAD Views of the Pressurized Gas Generation and Torque Measuring Assemblies Drafted.